Information Content Driven Model for Virtual Engineering Space

László Horváth, Imre J. Rudas

Óbuda University, Institute of Applied Mathematics and University Research and
Innovation Centre, Bécsi út 96/b, H-1034 Budapest, Hungary
horvath.laszlo@nik.uni-obuda.hu, rudas@uni-obuda.hu

Abstract: Engineering practice is increasingly relied upon virtual technologies. Recent virtual solutions ensure integration of all engineering activities using system level computer representation of complex multidisciplinary engineering product. The authors have provided research results in developing strategies for leading engineering virtual technology, for more than twenty years. They analyzed paradigm shifts on the way to present virtual engineering systems and organized their work around their formerly published concept of Virtual Engineering Space (VES). These were preliminaries of the reported work in this paper. New method is introduced for structuring and representation of active driving knowledge content background (KCB) in engineering model. The purpose of KCB is to drive entity generation in the KCB extended industrial engineering model of a product system. This paper introduces handling contextual initiatives and the application of them to define KCB structure for the generation of self-adaptive generic objects explaining role and structure of information content, as well as, the related model driving mechanism. Appropriately organized and configured engineering models offer a means for integration of engineering model based industrial, research and higher education applications in common VES. Recent industrial professional engineering modeling systems offer capabilities for implementation of KCB and application relevant configuration, of modeling capabilities for disciplines and human roles.

Keywords: virtual engineering space; system level product model; self-adaptive product object model; knowledge content background; multipurpose virtual engineering space

1 Introduction

Substantial changes in industrial products were followed by the dynamic development of virtual engineering methodologies and technology, over the previous decades. Development history of engineering modeling shows the way from the initial shape modeling to representation of generic industrial product system in virtual engineering space (VES). VES was a formerly published concept at the Laboratory of Intelligent Engineering Systems. The VES concept utilized

the product model principle, as it was standardized in ISO 13303 [1]. Concept VES was developed from the concept of intelligent virtual product space (IVPS) [8] The above laboratory was founded at the John von Neumann Faculty of Informatics, Óbuda University for research and higher education in VES relevant issues in 2005.

According to its definition, VES represents product as contextual segment of the physical world [8]. The VES represented product behaves similarly in virtual, as it will behave in the physical world, after its production and installation. Beyond product structure, VES includes objects for production, marketing, and application of the product. During its manufacturing, advanced product is converted from virtual (model) system to cyber-physical system (CPS). CPS is composed of cooperating physical and cyber units and it is highly contextual with VES.

Systems based architecture of multidisciplinary products essentially changed the engineering practice toward application of virtual technologies at all activities during the whole lifecycle of the product from the initial concept to the recycling. For this purpose, leading engineering systems organized engineering activities around complex model of multidisciplinary CPS product. Beyond development, production, marketing, and application of product this model could serve the whole innovation cycle including fundamental, general problem solving, and product related research. In this way, theory and practice were integrated in VES. Main advantages of engineering activity concentration around central model for the whole innovation cycle are realization of all contexts, real time propagation of new findings through existing results, and quick reaction to new theories and methods at practice intensive industrial companies. Proactive product support can be provided for engineers among others to prevent inappropriate or not allowed object parameters and repetition of obvious errors from the past.

New discipline areas, such as, systems engineering (SE), requirements engineering (RE), system of systems engineering (SoSE), and applied informatics for high abstraction engineering modeling were enforced by system based products to integrate in engineering modeling. New objectives established consistent contextual structure in the product model. This placed new emphasis on application specific but, highly scientific and advanced mathematics. The need for modeling of the product operated by cooperating systems it also placed new emphasis on a wide-ranging structure of contexts. Context structure acts as glue in the product model. Product wide contextual modeling is considered one of the main achievements in early 21st Century engineering systems.

Suddenly increasing complexity of engineering models resulted in a decreasing role of visualization by computer graphics. While human interaction with graphic visualization, in viewport, including dynamic navigation was still essential, emphasis was shifted to seeing and thinking in information space. This was inevitable because visualization capabilities of computer graphics proved to be inadequate for the information boom and deep knowledge. In this way, advances

in engineering modeling replaced the emphasis on human capability for high level abstraction to conceptualize, develop, survey and understand complex model systems.

Because connected cooperating systems typically come from different discipline areas, in the same product structure, contextually connected mechanical, electrical, electronic, hardware and software units must be engineered in the same product model system. It is foreseeable that application of conventional engineering model systems, which represent different discipline related units in separated or not contextually integrated models, will be over soon at leading industries. Inevitably, future engineering descriptions and representations will be organized in contextual multidisciplinary models [15]. It will be essential to apply and reuse active knowledge for driving multidisciplinary engineering model entities in consistent context system.

Recognizing the above, strong trend of development, the authors of this paper started research in relevant issues more than 20 years ago. They organized work around their VES concept. One of main contributions in this paper is a novel method to establish structure and representation of active driving knowledge content background (KCB) to support generation of engineering model entities. A survey of paradigm shifts and our own related results in engineering modeling are discussed as preliminaries of the reported work. Objectives and scenario of the reported research are outlined and a KCB extended industrial engineering model is introduced. Following this, organizing contextual engineering models into VES, the role of KCB structure in self-adaptive object generation, human and contextual contributions and model driving mechanism are explained. Another main contribution in this paper is the integration of engineering models for industrial, research, higher education activities in complex VES and possibilities for implementation of results in industrial professional engineering modeling system are proposed.

2   Paradigm Shifts and Preliminaries

Research in this paper is part of a long-term program. Beyond the main research, this program includes continuous recognition and characterization of paradigm shifts. Leading engineering modeling strategies, principles, methodologies and systemics in current engineering modeling systems have evolved through these paradigm shifts over the past decades. Therefore, paradigm shifts, and our own related research results are surveyed for previous decades in Fig. 1. Similarly to other areas of science and technology, current engineering modeling relies heavily on former achievements. Most of the content of former paradigm shifts can be recognized in current engineering modeling and CPS systems. However, it is also

important to recognize how things changed in the model environment of entities which contain former results.

Developments in factory automation needed geometric descriptions to generate programs for equipment and device control from the 70s. Typical results included symbolic descriptive language, geometric processing, and application related processing. Work in [19] can be considered as one of initial efforts in this area. Modeling of man-machine processes, served better communication between human and modeling procedures for better shape driven control [20].

The next paradigm shift introduced computer definition of engineering processes between the 70s and 90s. One of most advanced engineering process definition strategies was mixed application of variant and generative principles in the same solution [21]. Highly based on the result in [21], process and resource models were developed using vario-generative principle in the GLEDA system [22]. These models were extended to Quality Assurance [23] applications. One of the solutions for the connection of process and resource models with computer control of complex machine tools was introduced in [33] and an alternate method was applied in process plan definition and engineering system in [35].

The need for an engineer-understandable shape model was fulfilled by parametric solid form features in the 90s. Form feature modifies the previous shape and completes boundary representation of shape accordingly. Boundary representation (B-rep) is the prevailing geometric model which includes representations of surfaces and their intersection lines in boundary and places these geometric entities in Eulerian topology structure. The PRODES team joined early research in form feature based modeling and developed prototype modeling system in the 90s [30]. Advanced ideas and methodologies were applied at development of this system including object oriented form feature driven model and integration of form feature and manufacturing models. Our research was in associative modeling of industrial processes considering solid form features [24]. Shape modeling still relies upon boundary represented geometric and functional form features. Form feature based modeling supports advanced modeling concepts such as dynamic product reconfiguration [18].

One of the main contributions to engineering modeling was the integrated product information model (IPIM, ISO13303) [1] which provided a means for integration of formerly separated partial models using generic and application resources, application protocols, and object-oriented scenario in the 90s. Analysis of object connections in this scenario resulted in the concept of integrated model object (IMO) [25]. Work for IMO also emphasized the importance of communication between human and modeling process.

Dramatically increased complexity of product structures demanded self-modification product models capability of handling the propagation of extensive and frequent model changes during development, improving, correction, and variant creation activities.
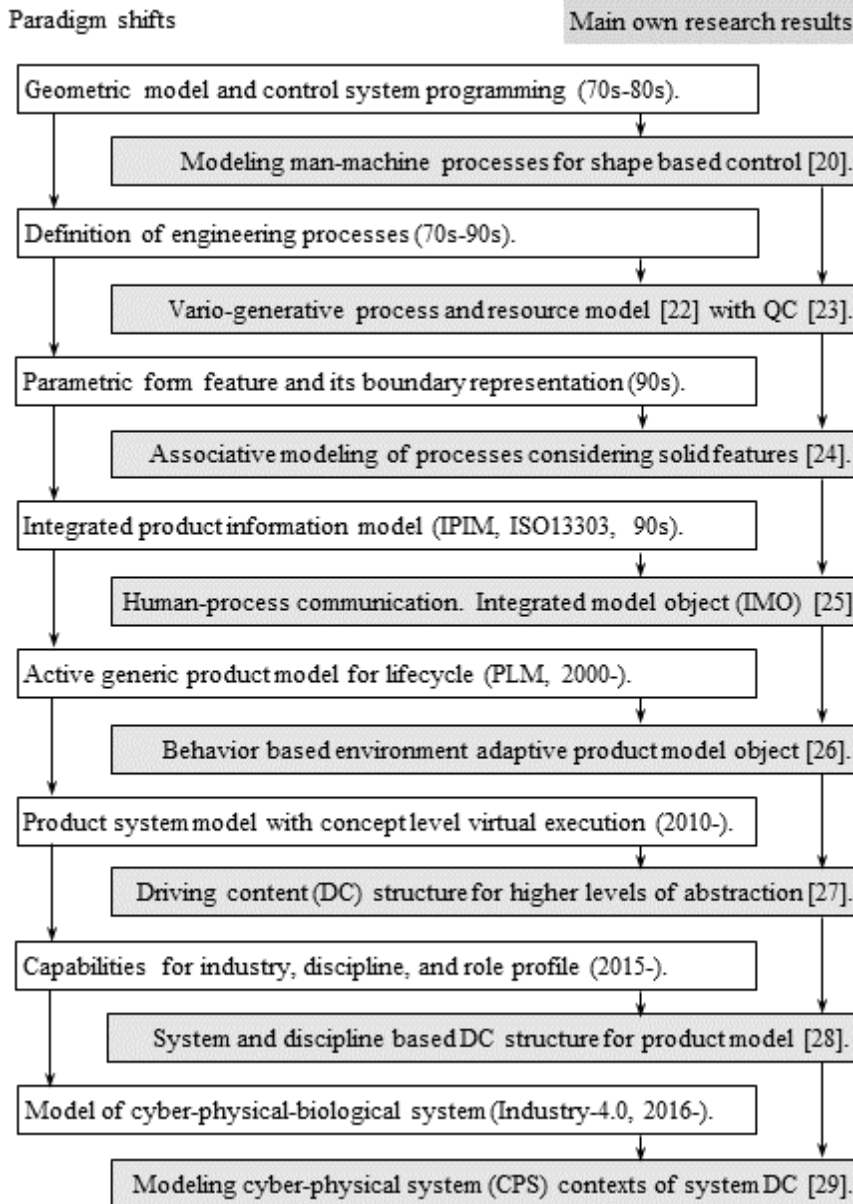
Paradigm shifts   Main own research results

Geometric model and control system programming (70s-80s).

Modeling man-machine processes for shape based control [20].

Definition of engineering processes (70s-90s).

Vario-generative process and resource model [22] with QC [23].

Parametric form feature and its boundary representation (90s).

Associative modeling of processes considering solid features [24].

Integrated product information model (IPIM, ISO13303, 90s).

Human-process communication. Integrated model object (IMO) [25]

Active generic product model for lifecycle (PLM, 2000-).

Behavior based environment adaptive product model object [26].

Product system model with concept level virtual execution (2010-).

Driving content (DC) structure for higher levels of abstraction [27].

Capabilities for industry, discipline, and role profile (2015-).

System and discipline based DC structure for product model [28].

Model of cyber-physical-biological system (Industry-4.0, 2016-).

Modeling cyber-physical system (CPS) contexts of system DC [29].

Figure 1
Paradigm shifts and relevant own research results in engineering modeling

An Active Knowledge Driven Contextual Generic Model was established for the above purpose at the beginning of the new century. Engineering activities served the entire lifecycle of product (PLM) [32]. As contribution to results in this area,

our own research aimed establishing behavior based environment adaptive product model object [26].

The spread of systems cooperating in product structures required system level product model. The requirements, functional, logical, and physical (RFLP) structure was implemented from the systems engineering (SE) for this purpose [2] around year 2010. As a main advancement, the product concept was modeled on functional and logical levels together with behavior representation allowing virtual execution of product concept model. Our research targeted joining to the work in system level engineering modeling by contributions such as multilevel abstraction and concept of information content. These contributions supported establishing driving content (DC) structure on higher levels of abstraction [27].

Establishing engineering modeling for multidisciplinary system based products required flexible configuration of capabilities available at engineering workstations. To fulfill this request, leading engineering systems include configuration capabilities for industry, discipline, and role profile from around 2015. Our result is system and discipline organized DC structure for system based product model [28].

Currently, actual paradigm shift is in engineering modeling for cyber-physical-biological system and Industry-4.0. Industry 4.0 means 4th generation of automation using CPS and its information technology background. Key elements of this information technology are Internet of things, cloud computing, and cognitive systems. Our work is concentrated in representation driving content (DC) structure for CPS [29].

Efforts are done to organize company and institutional knowledge in intellectual property (IP). Need for high level content exchange between organized IP and DC structures is anticipated for the future. For that reason, paper [29] proposed multilevel structured IP entity which was devoted to transfer IP content between IP and DC structures. It was considered that IP organizations also serve applications other than engineering modeling.

3   Objectives and Scenario

In the long-term personal research program, main issues relevant to results in this paper are survey of model based engineering problem solving strategies [6], integration of product model objects [7], concept of virtual engineering space (VES) [8], modeling engineering objects on high abstraction levels [9], representation of engineer intent [10], development of driving information content structures [11], and multipurpose virtual space for engineering [12]. Objectives of research in this paper are developing improved version of former [11] information content based model driving, placing information content in the VES concept,

defining the main driving context structure and driving mechanism, and integrating multiple applications in single VES.
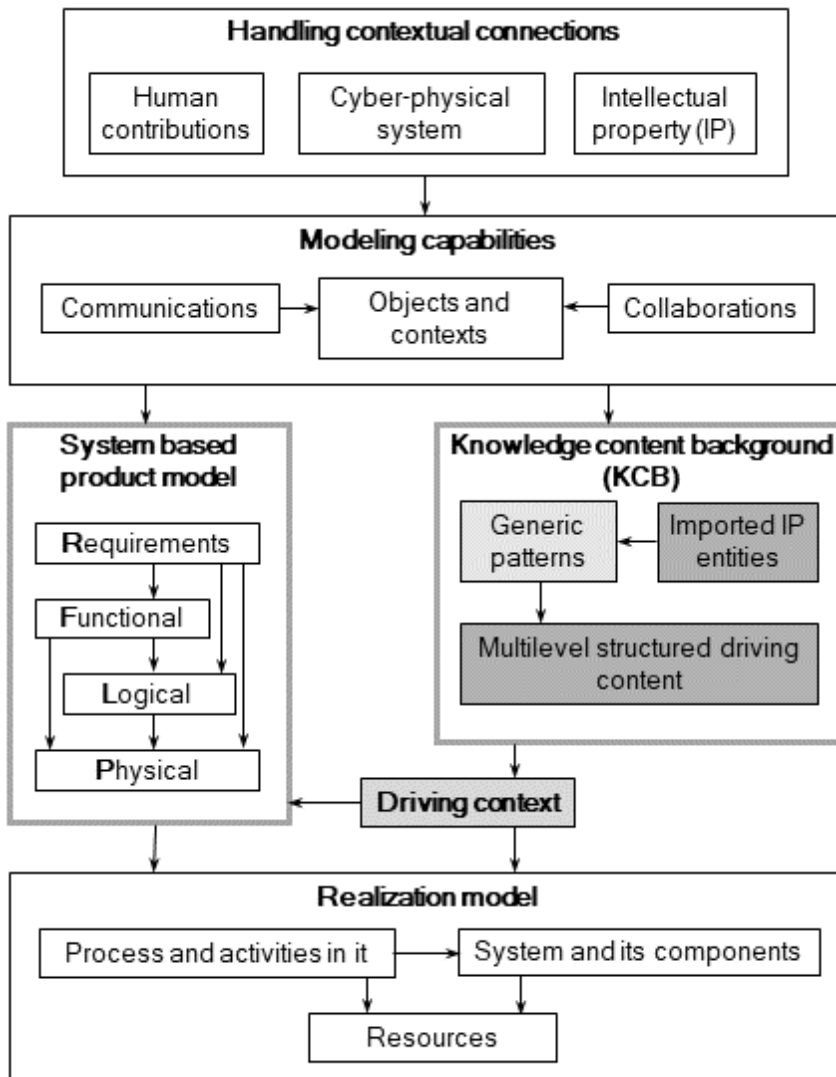

Figure 2
Scenario of modeling and subject of research

The main contributions of the research in this paper are the contextual structure of Knowledge Content Background (KCB); driving contexts from KCB structure elements to RFLP structured system level product model components, and integrated applications in VES. Term driving here means generation product

model object parameters under control from appropriately contextual KCB object parameters.

Modeling multidisciplinary product needs the development of a functional and logical level concept model, before the related physically visible objects are developed. This is due to the complex structure of components from various disciplinary areas and their relationships would be hard or even impossible to handle only in a physical level model. Complex contextual structure of product components in a physical level model is best defined under driving from logical model. In this way, a physical model is generated by execution of a logical model. At the same time, definition of logical model components and their connections demands functional product components which are connected in our structure. Functional and logical level models are virtually executable when behavior representations are available in their components [13]. Definition of behavior representation is often done using advanced software, which is outside of the actual RFLP structure enabled engineering system. An example for this solution is the definition of dynamic behavior of a heterogeneous physical system using the Modelica open object-oriented modeling language [34].

There are frequent changing requirements against the product demanded description of these requirements within product model. This is served by first level in the RFLP structure in current solutions. The requirements (R) level specifies requirements the product must fulfill and relies upon the dynamically developed area of requirements engineering (RE) [16]. Functions (F) level is functional decomposition of the product to fulfill requirements. On the logical (L) level components include information for how functions are achieved. Finally, physical (P) level is result of execution the logical model. P level is purposeful structure of real world product features. RFLP structure is well proven methodology in systems engineering (SE) and uses core elements from the IEEE/1220 Standard for Application and Management of the Systems Engineering Process.

KCB is contextual extension of the RFLP structured industrial product model. It consists of imported intellectual property, generic patterns for driving content, and structured driving content (Fig. 2). The driving content structure consists of four levels and substructures on each level. This structure and its contextual connections will be introduced in section 5 of this paper. Relevant entities from imported IP and generic patterns are included in the actual VES or cited from outside as context. They also can be collected in VES for future reuse. Generic pattern organizes a set of closely connected essential contexts. These contexts are mandatory to apply and assist to avoid erroneous content and context definitions. Generic patterns are developed with developing ideas, experiences, and expertise at companies and other organizations.

Definition, generation, and application of RFLP and KCB structure entities require appropriately configured sets of modeling capabilities. Capabilities are

considered as available at host engineering modeling system which is extended by KCB structure. Modeling capabilities are available for objects and contexts, as well as communication and collaboration processes.

The outside contextual connections of a product model system include human contributions, cyber-physical system (CPS) communications, and intellectual property (IP) import and export (Fig. 2). Human contributors are not only engineers on duty for actual engineering tasks but also other decision makers at application of standards, higher level decisions, law related affairs, etc. Advanced products can increasingly be regarded as CPSs [3]. The conventional connections with control units are being changed for increasingly smart communication between virtual and physical worlds. Cyber units in finished products can communicate with relevant VES representations for optimal operation and effective proactive malfunction handling. Intellectual property (IP) is established at a company or other organization not only to collect knowledge but also to make owning information clear.

Because a self-adaptive characteristic of the generic product model is relied upon, chains of contextual object parameters, context definitions have an exceptional role in VES [17]. Any object parameter has potential for participation, in one or more contexts. The engineering object parameter is modified only through a contextual chain, except for allowed exceptional manual interventions. The context is defined in object parameters or in the form of an individual object. Beyond its main content, context object includes time, variant, situation and event controlled activity parameters.

The realization model represents production related information. In recent advanced modeling systems, it has a three-level structure. Levels are for included manufacturing process and operational activities, the production system and its components and needed resources for realization. Recently, production systems increasingly adapt to CPS, in the scope of new paradigm Industry-4.0.

4 Organizing Engineering Models into Virtual Space

The next issue is how the complex product model in Fig. 2, can fulfill the criteria of virtual engineering space (VES). According to its definition in [8] VES represents a well-defined existing or planned segment of physical world together with its connections to all of the influencing outside virtual, physical and CPS environments. In engineering, the represented segment is a product, a prototype or an experimental object structure. The development process of VES includes model definition and integration activities to achieve the engineering requirements. The Model based Product Lifecycle Management (PLM) system [32] paved the way to VES level modeling. Unlike the previous product data management (PDM)

system, this PLM system handles product information in a set of contextual models. Areas of contribution to VES, in this paper, are shown as shaded boxes in Fig. 2 and Fig. 3.

VES is developed during controlled contributions from responsible engineers, other persons and outside contexts (Fig. 3). Contribution from other persons and outside contexts are reviewed then accepted or rejected by responsible engineers except for items which are already decided and thus enforced by the VES or its contextual environment. In this way, a quick reaction of VES to a changed specification, rule, legislation, standard and other attempts for contribution, is critical. Outside contexts must represent connections with trusted information sources. Dedicated VES procedures review contribution attempts from all of the three sources for breaking existing accepted results and content, as well as, feasibility. The accepted contribution is handled as an initiative and is applied at the generation of the KCB extension or direct generation of generic product model entities (Fig. 3). An element in KCB extension drives relevant generic product model entities. Consequences of new accepted and validated contexts are automatically enforced through the self-adaptive mechanism of VES. Any accepted interaction from outside is propagated in the model along chains of contexts while organized active simulations save consistency, suitability, and quality of the model. One of important applications of self-adaptive generic model is dynamic reconfiguration of product [18].

The main challenge is a stable tradeoff between the acceptance/rejection reaction of existing model and revision of the formerly accepted results or content when necessary. Although preference information can be correct in the KCB structure elements, handling these items often requires human interaction, in accordance with local engineering decision rules. Generic patterns include methods for handling argued cases as necessary. Anyway, reliable measures are necessary to protect correctness and consistency of models. It is obvious that the participants of the engineering project, who are eligible, authorized and responsible for contribution in an actual VES, try to enforce their intent, utilizing personal excellence.

The component model of the product model is created in its own model space to represent part, assembly, analysis, simulation, etc. The model in this space represents generic engineering objects and contexts of their parameters. The model which is defined in its' model space is in the possession of self-instancing capability and is contextually connected to related models in VES. Beyond requirements, functional, logical, and physical component structures, simulation and model generation process structures can be included as component models in VES. Real-time operated complex simulations provide advanced support for VES activities. Model generation processes are contextual with object representations and descriptions and serve regeneration of models when it is necessary. The generic characteristic of the model objects is essential to provide a capability for self-modification and self-instancing. To achieve this, the product model must

include proper active knowledge representation to generate modified or new entities.
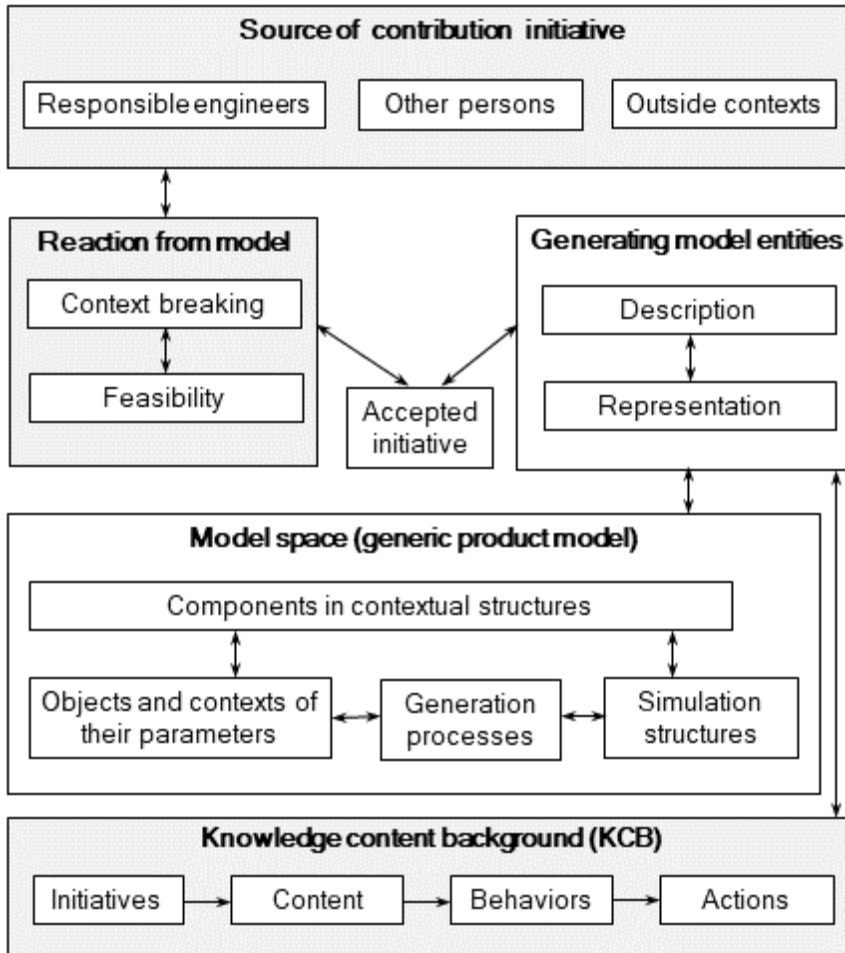

Figure 3
Contributions to VES

A four-level, product-wide, content element structure is proposed, for the knowledge content background (KCB) (Figs 3 and 4). Initiatives (I) level includes elements with personally represented information for accepted and processed contributions. Elements in the communicated content (C) level carry validated and accepted content. The acceptance process may result in an activated or deactivated element. A deactivated element is an option for later, changed circumstances. Behavior level (B) is an attempt to establish a product-wide contextual structure of the system and function-driven behavior content.

The actions (A) level includes elements to the drive P level entities, in the RFLP structure. Future development of level A elements is planned to serve their two-way connection with cyber units in CPS system. Development towards smart companies makes this feature of KCB more important and at the same time feasible for the future.

As the global integrator for a well-organized engineering model structure, VES is art of science, technology, and engineering. The sophisticated product model has a great impact on the effectiveness of advanced engineering activities. VES requires human background for collecting content and establishing the model structure. KCB was intended to provide a modeling environment which supports seeing and thinking in VES. Measures to check initiatives by VES content management are very important to avoid context breaking, infeasible tasks, mistaken representation and inconsistent object representation.

5 Information Content in Self-Adaptive Generic Driving Objects

As an organic extension of the driving mechanism in RFLP structured product model system, active KCB drives the product model entities through chains of contextual object parameter connections using knowledge representation as content. The RFLP structured product model definition currently applies very complicated dialogues between model generation procedures and collaborating humans. This definition of complex model entities and their relationships, need various contexts to consider as normal, during interactive human dialogues in collaborative engineering process. This problem motivated research, in raising human interactions to a higher-level abstraction, where better survey was provided and less contexts should be kept in mind during model definition. As result of this research, information content based driving [9] was conceptualized to replace dialogue definitions. Ackoff [35] classified content of the human mind into data, information, knowledge, understanding, and wisdom categories. Research in content kept this categorization in mind at analysis of higher level abstraction.

The Information content (or simply "The Content") describes and represents all information and knowledge in the background of coordinated decisions on information in generic product model entity (Fig. 3) parameters. Driving new and modified entities in RFLP structured model by active content provides new capability for the definition of consistent product model. In this way, driving by content can gradually replace complex dialogue definition of entities. Active content can flexibly represent and organize theoretical considerations, research findings, methodologies, experience, expertise, and intuition.

Increased complexity places high emphasis on consistency of model during the whole lifecycle of product. Product malfunctions are often caused by neglected or misleading context. To handle this problem, concept contextual consistency was included by the authors. A contextually consistent model includes proper set of organized contexts to ensure correct consideration of all influencing factors. Organized context set is revised during lifecycle of product when new context arises or existing content is abandoned at analysis, simulation, or physical product repair.

Shape representation applies concept topological consistency for decades. Consistent topology is assured by geometric modeling in engineering systems. Leaving assurance of topological consistency as separately handled in geometric modeling, topology of shape is not part of KCB context structure. At the same time, contexts of other model entities in RFLP and KCB structures with vertex, edge, and face topological entities must be included. Analysis and assurance of contextual consistency is planned as issue of future research at the Laboratory of Intelligent Engineering Systems. Thus, they are not issues in this paper.
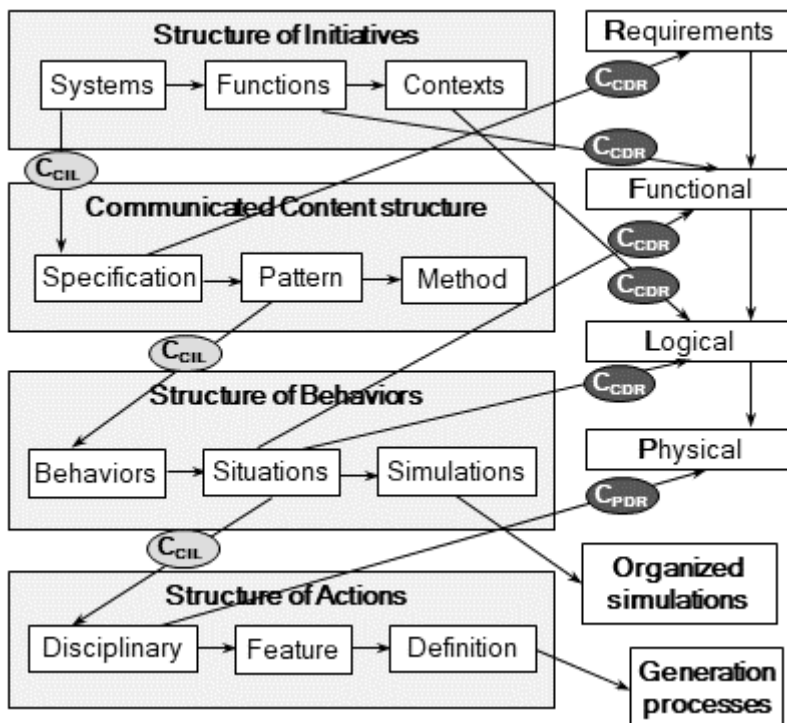

Figure 4
Main RFLP and KCB contexts

KCB level consists of contextually connected thematic substructures (Fig. 4) while substructure consists of contextually connected elements. KCB element drives one or more elements and components in KCB and RFLP structures, respectively. KCB elements and their connections are free to define under constraining by relevant active driving contextual definitions in the model. To ensure global consistency of model, some contextual connections (or simply contexts) are mandatory to include. Fig. 4 shows the set of mandatory contexts. These contexts form the main structure of model. They are inter-level context (C_{CIL}) between elements on different levels of KCB structure, concept driving context (C_{CDR}) between KCB element and R, F, or L level component, and physical driving context (C_{PDR}) between KCB element and P level component. Physical driving context was distinguished in KCB for applications where only the physical level exists in the product model, in the case of not RFLP enabled modeling system or model, which does not need concept level representation.

Although result of an engineering activity highly depends on the creativity of responsible engineers, contextual active knowledge items, represented in pattern and content entities, restrict role relevant human initiatives to avoid incomplete, erroneous, or contradictory representation. In default, KCB does not accept any contribution which contradicts any previously accepted active item. At the same time, any new contribution can create a debate result of which may be change or abandon formerly accepted KCB item. This evolution of KCB and RFLP model is essential during the whole lifecycle of product. Broken but abandoned higher level context is deactivated or deleted. This mechanism is enough flexible to accommodate situation dependent decisions on object parameters.

Initiatives are recorded and organized to accommodate and relate human intent in collaborative environment. Initiative (I) level substructures in the KCB structure organize systems, functions, and contexts for a generic product. Content in initiative is referred in elements of these substructures. "I" level makes discipline independent initiative definition possible. The systems-functions-context substructure chain allows for representation of main background content demanded by recent system-organized product structure.

The purpose of communicated content (C) level is to organize specifications which are active for the systems. Patterns and methods are organized for specification. Beyond the main contexts between systems and specification substructure elements, contexts are defined between elements in the rest substructures on "I" and "C" levels as required to transfer referred content. Consistent structure is checked for driving contexts. Context may also have a checking or an announcement status.

As it was emphasized previously, in this paper, behavior representations gained outstanding importance by their role at virtual execution of F and L level models in RFLP structure. It can be said that the representation of behavior brings life to the RFLP structured product concept model. Substructure chain on behaviors (B)

level of KCB structure provides structure of behaviors, structure of situations for behaviors, and simulations for situations. The Situation Element organizes circumstances. Some of recent modeling systems have capabilities for representation organized simulations in product model. These simulation entities can be driven by elements in the simulation substructure (Fig. 4).

The fourth (A) level of KCB structure organizes content for physical level driving actions. Because physical level engineering is divided to disciplines, disciplinary substructure organizes discipline related blocks of physical level product representation. This method is sufficiently flexible to handle disciplinary combinations in the engineering practice. The other two substructures organize features and their definition methods for discipline substructure elements.

As it was defined in [6], physical level engineering object fulfill eligibility criteria for its representation as feature in a feature driven product model. The "A" level of KCB structure assumes availability of feature definition to any physical level engineering object in the host modeling system. Element in definition substructure includes content for driving generation procedures of relevant physical level features in the host modeling system. Element also can be defined to drive model generation process entities where these entities are included in product model to capture engineering processes as knowledge representing proven practice for instant and future application. This advanced function was established at leading engineering systems on the way to automate engineering modeling. Process entity often serves set of procedures needed to generate physical level model of a well-defined product unit. Cross-disciplinary contexts can be placed in feature and definition substructure elements to connect features from different disciplinary areas. Cross-disciplinary modeling on physical level is an actual research issue [14] and future work will include further analysis at the Laboratory of Intelligent Engineering Systems.

6   Model Driving Mechanism

As it can be concluded from the above explanations, driving of the object parameter generation is critical in the proposed contribution to active adaptive product modeling for lifecycle of product. On one hand, the model must have the capability to modify itself automatically, using active contexts. On the other hand, using an active context set, which is not appropriate for the actual situation, can cause serious malfunctions in the operation of the represented product. Moreover, CPS product includes cyber units, which are created in virtual and may have VES connections, for control of physical product processes on the basis of actual sensor network information.

The organized driving of the RFLP model entity generation ensures consideration of all contexts using consistent context structure. The ad-hoc connection of the model object parameters is replaced by organized driving content structure. This means that object parameter is defined in the context of relevant parameters of relevant objects within the KCB structure or between KCB and RFLP structures. Context relevancy is important to make map for consistency analysis. However, it is impossible to prepare all driving contexts for automatic action along context chains. Regardless, responsible engineers must have role based means to sight into the modeling process at critical points. For the above purposes, role based, human interaction contexts are defined. When consistency analysis reveals a lack of context, a void context is generated and role based intervention is enforced by the modeling system. Driving RFLP structure components is like host modeling, system specific. Consequently, specialties of the connected RFLP structure must be considered at implementation of the KCB structure and its driving mechanism.
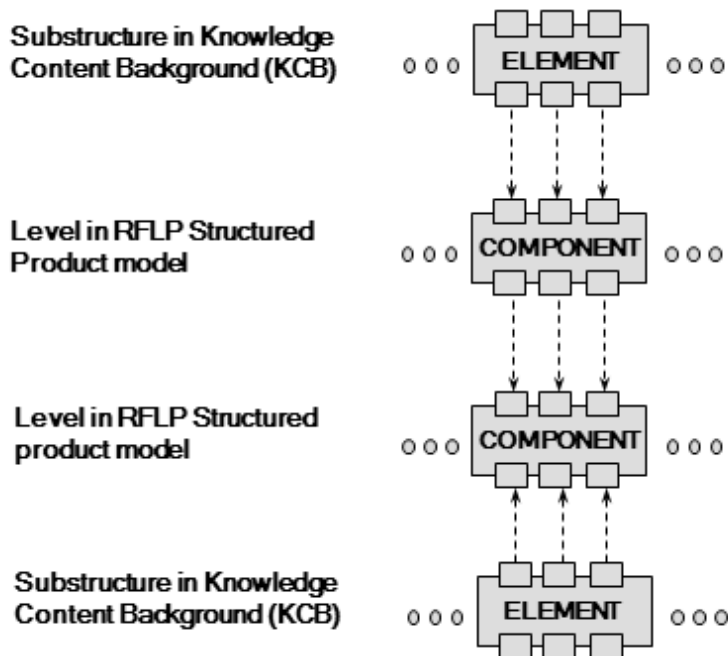
Figure 5
Communication through ports

Structural similarity between RFLP and KCB offers the benefit of application the same model construction methods and procedures. Consequently, KCB structure applies the same procedures and formats as management of RFLP structure in the host engineering system for the connection of model entities. Therefore, driving procedures and formats are RFLP modeling dependent. Known RFLP structure management systems apply ports on the component for communication with other

components. Ports are free to define, as demanded by the model under development. Port based connection is illustrated for two connected RFLP structure components and their KCB driving elements in Fig. 5. Elements and components in Fig. 5 apply three ports to establish connection between two entities, exchange information along this connection, and control of the connected element or component. A generic model is highly based on situation driven activity of elements and components using control port connections.

7   VES Integrates Application Areas

Developing strategies in engineering modeling highly relies upon four key concepts namely, integration, information space, multidisciplinary characteristic, and systems. Integration was continuous intention during long-term history of engineering modeling development. It was motivated by the need to replace manual and exchange types of data communication between separated units, objects and procedures by direct connection in computer based engineering systems. In this way, the integrating capabilities of models were extended continuously.

Information space accommodates, organizes and coordinates engineering resource originated information for the lifecycle of the product. It is an important concept for integration. In its generalized definition, the product is an organized structure of engineering objects. Engineering objects were analyzed and characterized in [8]. The main resources for information are human capabilities, modeling capabilities, control units, physical units, engineering objects, methodologies, processes, intellectual property and information handling related capabilities. Recently, information and other resources are available from the cloud as a service. The conventional option of premise installed resources does not provide sufficient capabilities and flexibility for VES installation.

The style, purpose, media and environment of engineering work has changed. This means there is a need for revision of classical organization, integration, methodology and activity in engineering. Spreading cyber-physical systems (CPSs) generated urgent need for extension of product and production modeling capabilities to multidisciplinary systems. CPS is inherently multidisciplinary, while industrial product and production systems are often handled as CPS, as their engineering. CPS requires integration of theory and practice within the same model and needs capabilities for fundamental, problem related and product related research, in the product modeling system [2].

Extensive involvement of industrial organizations in engineering related research forced the independent research organizations to consider integration of their industry related research projects with industrial projects. Separated modeling

installations at cooperating research and industrial organizations cannot provide real integration and generate a need for parallel installations of extended modeling capabilities and CPS laboratory equipment at the research organization. Cloud serviced VES offers a new chance for deep integration, using high level contextual driving between related models within the same VES. VES may consist of full value contextual component VESs in cloud environment, where work at research organization is still independent. The product model can be configured among others for experiments and engineering problem analysis. The Cloud also provides connection with outside CPS installations, including Industry-4.0 eligible smart factories.

It was recognized that the above joint VES can be extended to higher education organizations, where effective connection with outside research, industrial, and higher education organizations was a problem area for decades [36]. The Industry-4.0 paradigm shift and other changes have major impact on the requirements demanded of higher education programs in engineering. Undergraduate, Graduate, Postgraduate and Doctoral courses are forced to reorganize, for the new and changing issues, such as, multidisciplinary engineering, CPS, virtual space, advanced modeling; cloud serviced engineering and integrated theory/practice. It is not hard to anticipate that resources for changed programs can be provided only in virtual system in integration with cooperating industrial and research organizations. In virtual environment, effective industrial organization-higher education and research organization-higher education dual cooperation's can be configured and realized. High level and leading laboratory capabilities and capacities can be accessed as cloud based service from laboratory, experimental, or real industrial CPS systems.

The VES concept for multiple applications is summarized in Fig. 6 while Fig. 7 includes contextual information structures for industrial project, research program, and university course VES application types. Each application type uses an internal component-VES specific set of contextually integrated models within project organization in the host engineering modeling system. Component-VES applies type specific strategies, methods, communication, and representations. Component VESs are connected by driving contexts as demanded. These contexts can be applied at configuring "virtual" component-VES connecting units from different VES types. Modeling capabilities are configured for type specific profile of component-VES considering relevant disciplines and human roles.

The concept of VES, stand alone or component, can be followed in Fig. 6. VES objects are generated in the context of initiatives. Sources of initiative contexts are human interaction and trusted outside object connection. Initiative is contribution to define VES configuration, strategy, specification, and communication. The configuration is defined for application profile including application areas, disciplinary areas and roles and for capabilities in accordance with application profile. Definition of configuration drives the "work" in VES, to establish and develop configuration, handling of structures, product entities and communication.

This work is done using the configured capabilities in the host engineering system and it provides results for the VES model. VES model consists of VES administration, virtual spaces (or component-VESs), model objects and generated outside contexts.
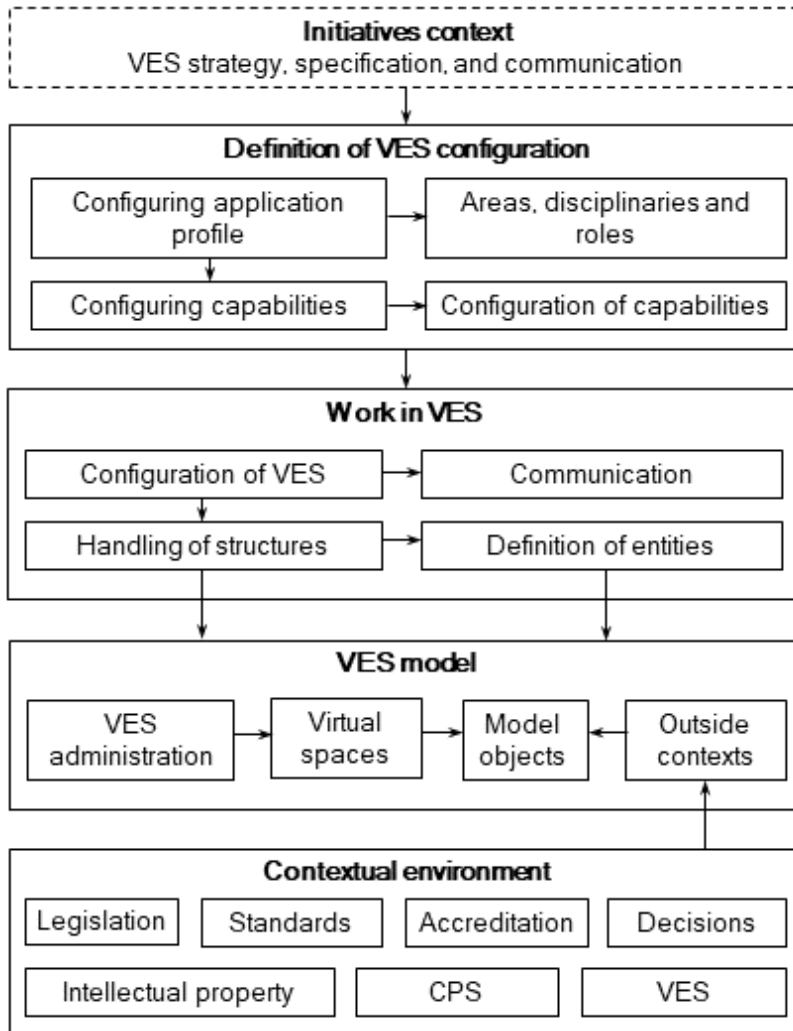

Figure 6
VES concept for multiple applications

While initial outside contexts are connections to control VES, generated outside contexts are connections which are decided in VES using recognized communication demand. VES entities are generated by relevant procedures in the host engineering modeling system. Because VES represents a separated segment

(or part) of physical world with connections with other related segments of this world, its connection with contextual environment is critical. Main units in the contextual environment are legislation, standard, accreditation, higher level decision, intellectual property, CPS and other VESs. In this way, VES must be fitted organically into its environment.

The VES type specific contextual information structures which are represented for activities in industrial, research, and academic applications are shown in Fig. 7. This allows for more sight into the proposed multipurpose VES. Information structures in Fig. 7 are results of initial analysis for the case where VES is based on KCB driven RFLP structured product model. This means that information units in Fig. 7 must be represented in the KCB-RFLP model structure. As it was noted above, product model sometimes is restricted to pure physical level. Owner related information for inventions, patents and know-how must be strictly included for any outside contextual connection of VES. Recently, in addition to product development, prototyping and application, industrial application may serve processes and activities at an Industry-4.0 eligible smart factory.

Industrial engineering activities start with a problem definition and its solution, which are served by collaborating human and intellectual property driven initiatives. Initiatives drive the definition of the problem to be solved and the process of solving. Problem solving works and produces results at the concept, physical and prototyping levels. CPS connections are required for physically produced and tested prototypes, application-ready products and the relevant production system. CPS physical units are connected and operated by cyber units. Nevertheless, physical units also have physical connections. Former concept of a virtual company needs reconsideration and application in this changed environment. Cyber elements of CPS can be configured within VES and they can be serviced from VES in the cloud.

Engineering, research type of VES application generally serves industrial problem solving, directly for engineering at a company or indirectly to produce general results. As it was explained herein, research activity is within an industrial or research application type of VES. In a research type VES application, activities start with definition and generation of objectives. This activity is driven by collaborating humans as well as resources and results (R&R). In this context, resources are utilized at research while results are referenced from work of others as initial conditions. Objectives, together with other initiatives, are applied at the generation of the research plan. Among others, initiatives drive principles and methods of research. Results of research are collected in experiments and findings. CPS connections are required for physical prototypes and laboratory installations.

Academic application serves higher education programs and includes specifics different from the other two applications. At the same time, the old problem is how to include industrial and research specifics in course programs. VES provides solution for this problem by offering an organic integration, of real industrial and

research units, into higher education programs in highly integrated model. Course programs, the knowledge in them, case studies, drills, assignments, assessment, laboratory tasks and teaching materials can be realized in the form of specific object models in active model system. Activities start with competences, which are driven by a collaborating Teaching Expert and Executive Human and Course Control (CC) initiatives.
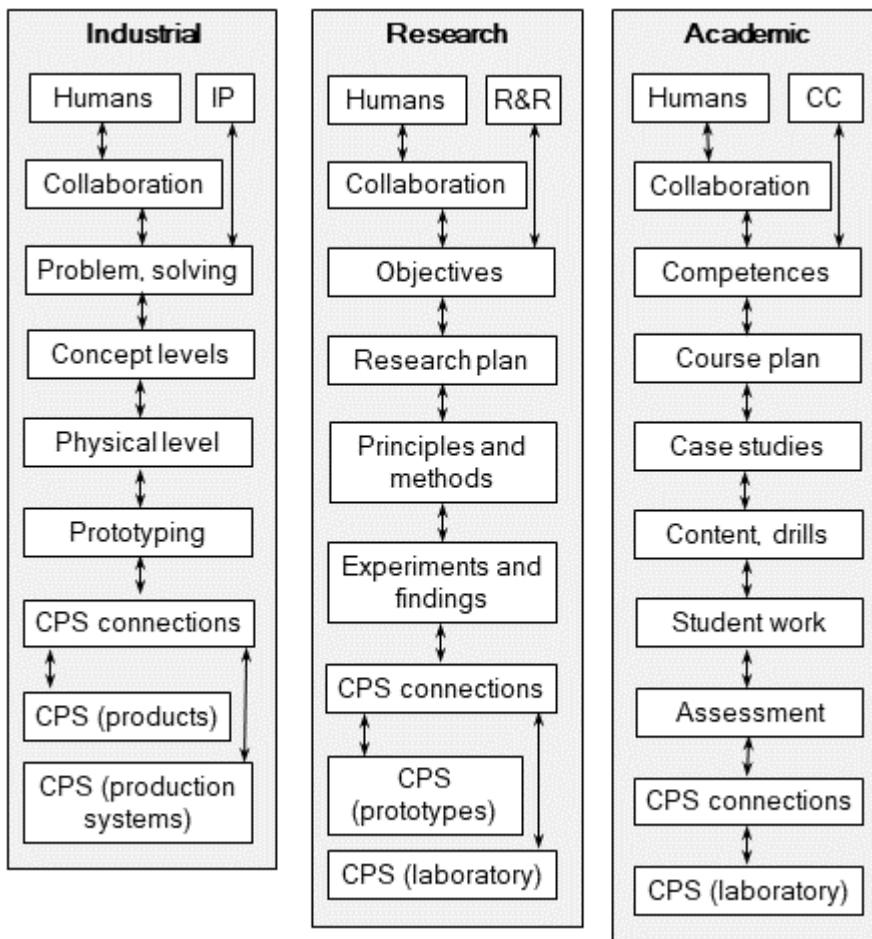

Figure 7
Information structures for VES applications

CC comes from, law, legislation, accreditation, teaching content, higher level decision and customer demand. In engineering education, the main customers are students and their potential employers. Initiatives and the resulted competences drive the course plan. Definition of competences must include information suitable for model generation. Course model can be considered as a very specific

product model, in which contextual engineering objects are represented to understand their systemics, principles, operation, characteristics, parameters and relationships. Active engineering objects represent a configuration of explanations, experiments, drills, assignments and assessment. Main contextual units of course information include, case studies, content and related drills, student work and assessment. CPS connections are required for laboratory installations.

8   Implementation Issues

The proposed KCB structure and multipurpose VES models are planned to integrate in an appropriately configured host industrial engineering modeling system product, where resources are accessed from the cloud as a service. It can be stated, that current advanced engineering systems, offer the demanded communication, modeling, development and management resources. Operation of KCB as an organic part of the product model uses the capabilities for model construction and configuration of the modeling environment. KCB definition, generation, and integration tasks can be realized by new object classes and related new procedures. Object handling and access to user surfaces and model structures are available, as open system functions in the host modeling system product. In this way, KCB related modeling capabilities, model object structures and model system management can be tailored. User defined model structures, algorithms; mathematical functions, etc. are included in actual and future models. The Application Programming Interface (API) is available for procedures which can use existing resources in the host modeling system.

Implementation of VES for multiple applications in industrial modeling systems needs future research and development in objects, communications, structures and the drives for research and academic applications using pilot VES. These applications demand much more specific objects, than the KCB structure. Model structures at these applications are different from the well proven product model structures. The main challenge is to transfer administrative, visualization and data transfer-centric processes to the world of contextual model structures. An experimental cloud based engineering environment configuration, is planned for development of integrated VES application areas, at the Laboratory of Intelligent Engineering Systems in the future.

Conclusions

This paper introduces some of the latest research results, in the information content supported driving of RFLP structured product model entities and multipurpose VES configurations, at the Laboratory of Intelligent Engineering Systems at Óbuda University. The work was motivated by new demands in engineering modeling, for the representation of cooperating multidisciplinary

systems, based on CPS products, self-adaptive generic knowledge driven contextual product models, highly integrated research, product development, manufacturing and application activities, development of product model towards virtual space and consideration of the new paradigm of Industry-4.0.

The above demands have brought new challenges for industrial engineering, engineering related research, operation of CPS installations and higher education in engineering. The study in the integration of model based activities required a historical survey of paradigm shifts and the relevant internal research results in engineering modeling in this paper. The main contributions of this paper are the updated scenario of engineering modeling, the new concept for organizing engineering models in VES including application oriented component-VES, the representation of information content as initiative based self-adaptive generic KCB driving structure and the information structures for application specific component-VESs. KCB driving content structure was conceptualized to fill the gap between contextual initiative sources and the RFLP structured product model.

Future research initiatives will include work on detailed driving structures, content entity structures, contextual consistency and integration of engineering models with Cyber Units of Cyber Physical Systems (CPS). The latter will be a contribution to CPS product related modeling for manufacturing, maintenance and optimized, malfunction-free operations.

Acknowledgement

References

[1]   R. Jardim-Goncalves, N. Figay, A. Steiger-Garcao: Enabling interoperability of STEP Application Protocols at meta-data and knowledge level, International Journal of Technology Management, 36(4) pp. 402-421, 2006

[2]   S. Kleiner, C. Kramer: Model Based Design with Systems Engineering Based on RFLP Using V6, in book Smart Product Engineering, Springer, pp. 93-102, 2013

[3]   A Canedo, E Schwarzenbach, E. M A Al Faruque: Context-sensitive synthesis of executable functional models of cyber-physical systems, In 2013 ACM/IEEE International Conference on Cyber-Physical Systems (ICCPS), Philadelphia, PA, USA, pp. 99-108, 2013

[4]   J. A. T. Machado, A. Babaei, B. P. Moghaddam: Highly Accurate Scheme for the Cauchy Problem of the Generalized Burgers-Huxley Equation, Acta Polytechnica Hungarica, 13(6), pp. 183-195, 2016

[5]   D. Wua, D. W. Rosena, L. Wangb, D. Schaefera: Cloud-based design and manufacturing: A new paradigm in digital manufacturing and design innovation" Computer-Aided Design, 59, pp. 1-14, 2015

[6]   L. Horváth and I. J. Rudas, Modeling and Problem Solving Methods for Engineers, Elsevier, Academic Press, New York, 2004

[7]   L Horváth: Towards Knowledge Driven Adaptive Product Representations, in book Advances in Soft Computing, Intelligent Robotics and Control. Heidelberg, London, New York, Springer, pp. 191-209, 2014

[8]   L. Horváth: Supporting Lifecycle Management of Product Data by Organized Descriptions and Behavior Definitions of Engineering Objects, Journal of Advanced Computational Intelligence and Intelligent Informatics, 11(9), pp. 1107-1113, 2007

[9]   L Horváth, I. J. Rudas: Multilevel Abstraction Based Self Control Method for Industrial PLM Model, 2014 IEEE International Conference on Industrial Technology, Busan, Korea, pp. 695-700, 2014

[10]   L. Horváth and I. J. Rudas: Human Intent Representation in Knowledge Intensive Product Model, Journal of Computers, 4(9), pp. 954-961, 2009

[11]   L Horváth: Towards Knowledge Driven Adaptive Product Representations, in Advances in book Soft Computing, Intelligent Robotics and Control. Springer, Heidelberg, London, New York, pp. 191-209, 2014

[12]   L. Horváth, I. J Rudas: Role of Information Content in Multipurpose Virtual Engineering Space, IEEE 15th International Symposium on Applied Machine Intelligence and Informatics, Herlany, Slovakia, pp. 99-104, 2017

[13]   K. Baughey: Functional and Logical Structures: A Systems Engineering Approach" SAE 2011 World Congress, SAE Technical Paper 2011-01-0517, 2011

[14]   G. Beier, A. Figge, R. Müller, U. Rothenburg, R. Stark: Supporting Product Development through Cross-Discipline Dependency-Modeling, Novel Approaches for Traceability-Usage, Lecture Notes on Information Theory, 1(1), 21-28, 2013

[15]   J Lefèvre, S Charles, M Bosch-Mauchand, B Eynard, É Padiolleau: Multidisciplinary modelling and simulation for mechatronic design, Journal of Design Research, 12(1-2), pp. 127-144, 2014

[16]   A, Sutcliffe, S. Thew, P. Jarvis: Experience with user-centered requirements engineering, Requirements Engineering, 16(4), pp. 267-280, 2011

[17]   A. Brière-Côté, L. Rivest, A. Desrochers: Adaptive generic product structure modelling for design reuse in engineer-to-order products, Computers in Industry, 61(1), pp. 53-65, 2010

[18]   J. Lee and D. Muthig: Feature-Oriented Analysis and Specification of Dynamic Product Reconfiguration, in book High Confidence Software Reuse in Large Systems, Springer Berlin, Heidelberg, pp. 154-165, 2008

[19]   M. Berta, I. Cser, Computer-aided operation planning and programming of machining on turning centers, in Proc. of SPIE 3832, Sensors and Controls for Intelligent Machining and Manufacturing Mechatronics, pp. 1-6, 1999

[20]   L. Horváth, I. J Rudas: Modeling Man-Machine Processes in CAD/CAM and Flexible Manufacturing Systems, in Proc. of the 1996 IEEE 22nd International Conference on Industrial Electronics, Control, and Instrumentation, Taipei, Taiwan, pp. 1484-1489, 1996

[21]   M. Horváth, Semi-generative process planning for part manufacturing, in proc. of the International IFIP/IFAC Conference on Programming Research and Operations Logistics in Advanced Manufacturing Technology (Ann Arbor, Mich., USA), North-Holland Pub. Co., Amsterdam, New York, Paper MS 79-153, pp. 1-9, 1979

[22]   L. Horváth, K. Szabó, GLEDA, A computer-aided Manufacturing Process Planning System for Parts to be Machined, in proc. of the APMS-COMPCONTROL' 85 conference, Budapest, pp. 618-629, 1985

[23]   I Cser, Gy Hermann, L Horváth, PC-based quality system for manufacturing of mechanical parts, in proc. of the 4th international conference on CAMP 94, CAD/CAM and multimedia, Budapest, Hungary, pp. 164-169, 1994

[24]   L. Horváth, I. J Rudas, G, Hancke: Associative Modeling of Machining Processes Using Feature Based Solid Part Models, in Proc. of the 2000 26th Annual Conference of the IEEE Industrial Electronics Society, Nagoya, Japan, pp. 1267-1273, 2000

[25]   L. Horváth, I. J. Rudas: An Integrated Description for Intelligent Processing of Closely Related Engineering Objects, in Proc. of the 2006 IEEE International Conference on Systems, Man & Cybernetics, Taipei, Taiwan, pp. 4886-4891, 2006

[26]   L. Horváth, I. J. Rudas:Human Intent Description in Environment Adaptive Product Model Objects, Journal of Advanced Computational Intelligence and Intelligent Informatics, Tokyo, 9(4), pp. 415-422, 2005

[27]   L. Horváth, I. J. Rudas: Filling the Gap between Human Thinking and Model Object Generation at Product Definition in Modeling Systems, in Proc. of the IEEE-ICIT 2010 International Conference on Industrial Technology, Viña del Mar, Chile, pp. 1012-1017, 2010

[28]   L. Horváth: Content for Context Structure in Multidisciplinary Engineering Model, in Proc. of the IEEE International Conference on Systems, Man, and Cybernetics Conference Budapest, Hungary, pp. 3824-3829, 2016

[29]   L. Horváth: New Method for Definition of Organized Driving Chains in Industrial Product Model, in Proc. of the 2017 IEEE International Conference on Industrial Technology, Toronto, Canada, pp. 1183-1188, 2017

[30]   I. Horváth, P. Kulcsár, Zs. Gábor, Z. Bagoly, A. Horváth, V. Thernesz: Implementation and Uniform Management of Modelling Entities in a Massively Feature-Object Oriented Advanced CAD Environment, in Periodica Polytechnica Ser. Mech. Eng., Vol. 39, No. 2, pp. 81-113, 1995

[31]   T. Tóth, D. Vadász: TAUPROG-T: Programsystem for Automatic Planning of Complete Technological Process of Rotation Symmetric Parts, in Proc of the COMPCONTROL'77 International Conference, Warsaw, Poland, pp. 194-202, 1977

[32]   Stark, J.: Product Lifecycle Management: 21st Century Paradigm for Product Realisation, Birkhäuser, Heidelberg, 2004

[33]   I. Cser, M. Juhász, K. Szabó, L. Horváth (I), L. Horváth (II), L. Tolnai: Computer-aided Planning of Machining Process. Preprints of the fifth international conference PROLAMAT'82, organized by IFIP and IFAC, Leningrad (now Saint Petersburg), 1982

[34]   R. Viruez, S. Machado, L. M. Zamarreno, G. León, F. Beaude, S. Petitrenaud, J.-B. Heyberger: A Tool to ease Modelica-based Dynamic Power System Simulations, in proc of the 12th International Modelica Conference, Prague, Czech Republic, pp. 235-239, 2017

[35]   Ackoff, R. L.: From Data to Wisdom, Journal of Applies Systems Analysis, Vol. 16, No 1, pp. 3-9, 1989

[36]   L. Horváth, I. J. Rudas: Multifunctional Engineering Space Supports Integration in Content Based Modeling, in proc. of the 11th IEEE International Symposium on Applied Computational Intelligence and Informatics, Timisoara, Romania, pp. 51-56, 2016

Infrastructural Model for the Healthcare System based on Emerging Technologies

Aleksandra Vukmirović[1], Zoltán Rajnai[2], Miroslav Radojičić[2], Jovanka Vukmirović[3], Marina Jovanović Milenković[3]

[1]Belgrade Business School Higher Education School for Applied Studies, Kraljice Marije 73, 11000 Belgrade, Serbia, aleksandra.vukmirovic@bbs.edu.rs

[2]Óbuda University, Bécsi út 96/b, 1034 Budapest, Hungary, rajnai.zoltan@bgk.uni-obuda.hu, dr.mradojicic@gmail.com

[3]Faculty of organizational sciences University of Belgrade, Jove Ilića 154, 11000 Belgrade, Serbia, vukmirovic.jovanka@fon.bg.ac.rs, marinaj@fon.bg.ac.rs

Abstract: Infrastructural model presented and developed in this paper represents a pillar for medical research and has a profound implication in the future of healthcare. The roposed model is based on Big Data concept that refers to technologies and techniques that consist of diverse data that changes rapidly and is too big and therefore cannot be efficiently processed by traditional computer technology and infrastructure. Components of this model are described in detail. In addition, this paper illustrates advantages, limitations, examples and recommendations for the use of Big Data in the healthcare system.

Keywords: Big Data; model; healthcare; Cloud technologies

1   Introduction

Thorough analysis of large amounts of data that is available, not only for healthcare system, but within the whole society, have shown that there are new possibilities for growth, which are eminent in many scientific disciplines, as well as in medicine [24]. This technological growth leads to a more efficient healthcare system: reduction in costs of treatments – faster and more precise diagnostics, better controlled use of prescribed medication, more effective monitoring of epidemics, pandemics and etc. [3] [5] [48].

The main problem considered in this paper is creation of a model based on emerging technologies and Big Data concept for improvement of the healthcare system. Focus is set on creating a reliable, distributive and scalable infrastructure

for managing, analysing, sharing, storing and sending large amounts of data. In medical research, available data are both structured and unstructured, stored in various formats: text, pictures, audio, video, clickstreams, log files, sensor files, etc. Data is often time sensitive and needs to be quickly delivered and analysed [17] [43].

The main goal that would be achieved by the implementation of a model developed in this paper is the emphasized importance for the introduction of emerging IT concepts in the process of medical research; which will significantly improve the output performance of healthcare system as a whole. This is primarily related to Big Data technologies and solutions; whose implementation will necessarily start methodological changes in the traditional research process that has been used for standard medical research so far.

Additional goals set in this paper are:

- Development of research methodology, which should lead to improvements in the data collection process by introducing the concept of Big Data, regarding timeliness, uniqueness and comprehensiveness of information related to medical research.

- Implementation of services and applications for medical research based on modern information technology,

- Optimal use of available IT resources,

- Pointing out the directions of further development in this area – especially in the field of research methodology and domain analytics.

This paper presents the benefits of implementing Big Data analytics in the field of medicine, the impact that emerging technologies have on preventing diseases, and describes examples reported in the literature [42]. The most important contribution of this paper is reflected in development of the infrastructure model based on new methodological assumptions. This model has solved problems such as collecting and storing large amounts of data, which creates conditions for their further analysis and presentation.

The main hypothesis that will be tested in this paper is: there are large amounts of available data (both structured and unstructured), from various sources that are not directly related to the healthcare system, but could be used for medical research.

The main hypothesis can be divided into two specific hypotheses:

H0.1. Emergence and implementation of Big Data necessarily leads to a change in the traditional methodology of processing, analysis and presenting data, and overall conducting medical research.

H0.2. Traditional statistical methods in the field of statistical inference (hypothesis testing) inevitably must adapt to the use of large amounts of data that are collected continuously in real-time.

The research methods used in developing this model are based on the existing theoretical approaches and on experimental work in this scientific field. Accordingly, scientific literature was consulted and referenced during the analysis phase of the model's content and systematization of knowledge. Implementation of the developed model should confirm the main hypothesis. The research methods implemented in this paper are data analysis methods: comparative and modelling methods.

2 The Importance of Emerging Technologies in Medicine

This paper provides a broad overview of Big Data technology for healthcare researchers and practitioners. The results of this research contribute to the accuracy of requirements necessary for the implementation of infrastructure in medical research [42].

Big Data technologies can be defined as datasets that are too large for traditional data-processing systems and thus require new technologies [39] [41]. In accordance with this general definition, Big Data can furthermore be defined as a set of data that overcomes the capabilities of typical software for databases management in the health care – data collection, storage, managing and analysing large amounts of data [7].

Big Data refers to the amount of data that is being produced on a daily basis, and describes the limits of existing data storages and computer power. It is a known fact that the healthcare system generates large amounts of data. Modern information technology has dramatically changed the landscape of how healthcare is delivered and studied. Per experts' estimation the worldwide digital healthcare data reached was 25,000 petabytes in 2014. According to the report of the Institute for Health Technology Transformation the U.S. healthcare system reached was 150 exabytes in 2011. It is estimated that at this growth rate, Big Data of the U.S. healthcare system will soon reach the petabyte scale and not long after, the yottabyte scale [42].

Aside from the volume, the Big Data concept is characterized by its velocity for information processing in real-time. It primarily assumes the time necessary to obtain a final result, which calls for action. The reasons for the imperative of the velocity in the healthcare are [15]:

- the very nature of medical activities, such as: the occurrence of an epidemic, diagnosis, response to therapy, the prognostics, etc.

- the medical data have short expiration dates and very quickly become obsolete due to the changes in the environment and the health status of patients.

In order to gain insight into the essence of the data as soon as possible all of the above facts confirm that the data must be collected, processed and analysed in real time. This also implies that the paradigm of the medical research is changing: data needs to be analysed from the moment of its collection [9] [44]. This means that the process of data collection is continuous in real time, because prompt actions are necessary in medicine, more than in any other field [6].

Big Data concept is based on another important characteristic – variety of data [42]. The development of information technology has led to the emergence of different types of data that could be collected [10] [11]. The structured data by simplest definition is all data collected, stored and presented by traditional methods, while all other data are defined as unstructured data. Big Data concept is based on the use of large quantities of unstructured data. When it comes to health care, these data sources can be internal (within the health institution) and external (coming from the environment).

The most common *Internal unstructured data* generated in the health care system are [23] [42]: Text (paper documents or electronic records: office medical records, handwritten nurse and doctor notes, hospital admission and discharge records, paper prescriptions, etc.), Medical Imaging Data (2D and 3D, x-ray films, MRI, CT and other images). Structural data consists of genetic data and data that represent regular monitoring, for example: multiple daily diabetic glucose measurements, blood pressure readings, EKGs, etc.

Internal and external structured data

Structural data in healthcare can be external and internal. External structured data comes from the environment while internal data is produced within the healthcare information system or clinical decision support systems. The electronic healthcare documentation in ideal conditions presents information about the patient since its birth and it is being collected from numerous healthcare institutions [25]. There are three major types of structured and semi-structured data in the healthcare sector as follows [14] [37]:

- Clinical data (electronic medical records, digital images, and information-sensing wireless medical devices),

- Various Medical research records,

- Business/organization operations records (data from administrative sources: financial, technical, etc.).

The structured data in electronic medical records includes: basic information about the patient (name, date of birth), physician's name, patient medical history, insurance information and any other information that is stored in existing

databases. As illustrated in the Figure 1, structured data is data that can be easily stored, queried, recalled, analysed and manipulated. This figure represents electronic healthcare documentation inside the healthcare system based on the example of the Republic of Serbia. Usually structured and semi-structured data in healthcare include instrument readings and data generated by the ongoing conversions from paper records into electronic health and medical records [10].
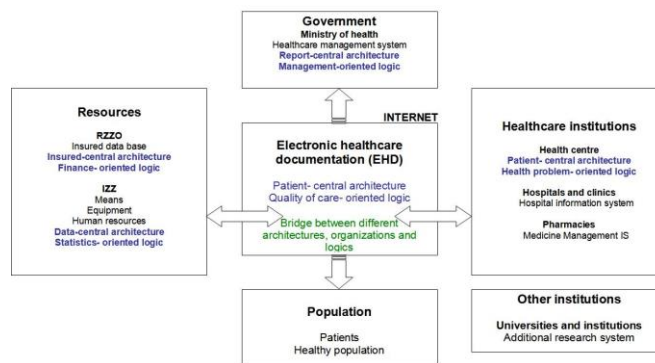

Figure 1

Electronic Healthcare Documentation inside the Healthcare System in Serbia [33]

A certain number of structured data exists in the external environment, such as data that is based on transactions in the field of insurance, health services, financial transactions, communications, etc. Accordingly, proposed model uses the data that is not essentially medical, but covers demographic, economic and lifestyle variables of individuals – patients. It is the use of new "medical" data that truly separates the proposed model from traditional solutions. This data is combined with the analysis of "classic" health data to improve health services, especially for prevention and diagnosis.

External unstructured data is being generated outside the healthcare system. Those are mostly nonmedical data such as data about demographic, financial and life style variables. External unstructured data are formatted in various forms, where the most common are text, figures, music and video.

There are many factors which are contributing to the volume increase of external unstructured data that becomes relevant to healthcare [29]:

- The increasing use of smartphones and specialized services, such as health applications, personal physical fitness tracking tools, GPS device, bar code reader, and QR reader.

- The number of unstructured data coming from the social media: social networks,

- Increased amounts of data gathered from reading sensors and similar devices like cameras, climate sensors, and chair and floor sensors.

- Extensive use of cloud technologies.

- The internet of the things concept – the introduction of smart devices in homes and smart meters that are based on Bluetooth technologies

Ericson company states in its annual Mobility report that in December 2015 there were as many mobile subscriptions as there were people in the world. Ericson estimates that by 2021, the increase of smartphone subscribers will double, considering the fact that in the third quarter of 2015 nearly 75% of mobile phones sold worldwide were smartphones. [12].

McKinsley & Co. acknowledged that the IoT (Internet of things) applications for health and fitness are very well adopted by the smartphone users. Based on current number of users of smart devices (phones, tablets, watches, wristbands, etc.) and projected growth of that number in the future, it is estimated that the economic income from the sold IoT applications for health and fitness will be between $170 billion to nearly $1.6 trillion globally in 2025. The largest source of value would be use of IoT devices for monitoring and treating illness [32]. Value would arise from improving quality of life and extending healthy life spans for patients with chronic illnesses, and reducing cost of treatment. Emerging applications have the potential to transform a wide range of health-care therapies. Ingestible and injectable – smart pills and nanobots—have the potential to replace many surgical interventions with less invasive approach that results in reduced medical costs, fast recovery and improved satisfaction of the patient [15].

Investments in IoT systems are proven to be justified, especially in the field of disease prevention, early diagnostics and cost reduction. One of the determinants that can be measured with more accuracy by the smart devices than with a physician appointment are the changes of human behaviour (for example, mood changes, routine changes, sleeping disorders, etc.) [28]. Often before the worsening of a patient's condition there is a period in which physiological data that now can be collected by smartphones, can also be used to determine whether patient is at risk for de-compensating. [2]

3 Model of Big Data Infrastructure as a Pillar of Technical Support for Medical Research

In a regular health analytics project, the analysis can be performed with a business intelligence tool installed on a stand-alone system, such as a desktop or laptop. Since Big Data is large by definition, processing is broken down and executed across multiple nodes. The concept of distributed processing has existed for

decades. What is relatively new is its use in analysing very large data sets as healthcare providers start to tap into their large data repositories to gain insight for making better-informed health-related decisions. [20] [35]

Especially, in case of science Big Data, scientists tend to move Big Data from the origin site of the Big Data to the nearest data centre because it is hard for scientists to analyse data remotely due to the long delay in time that occurs in the read/write process. After moving Big Data to the nearest data centre, scientists analyse it with thousands of CPUs that are connected by a very high-speed local network in the data centre. [38]

Open source platforms as Hadoop and MapReduce [49], available on the cloud, have encouraged the application of Big Data analytics in healthcare.

Suggested infrastructural model developed in this paper (Figure 2) cannot be integrated with existing management solutions (information system, CRM – applications, etc.) primarily due to the use of various definitions, and thus it was necessary to start modelling from the beginning.

Implementing the developed model of Big Data infrastructure for technical support in medical research (Figure 2) will lead to the real-time integrated management of the information. The main characteristics of this model are (Figure 2):

- Data that has been analysed are external secondary data,

- Collected data are poorly structured (located somewhere outside the organization and are not suitable for analysis without further processing),

- Model is not constructed to analyse past situations, but to predict the future.

Basic infrastructure model layers, shown in Figure 3 are the layers of software infrastructure and the layers of hardware infrastructure.

Software infrastructure component is based on the use of the concept of Big Data and Cloud Computing solutions, applied to the process of medical research. All software applications and services are implemented on the Cloud infrastructure [36].

Figure 4 illustrates the cyclical character of the developed model that enables one of the most important requirements of its design – reporting in real time.
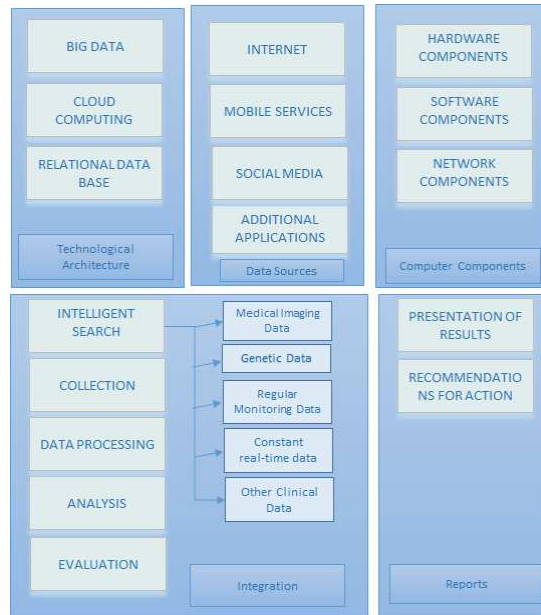
Figure 2

Developed general model of Big Data infrastructure for medical research technical support
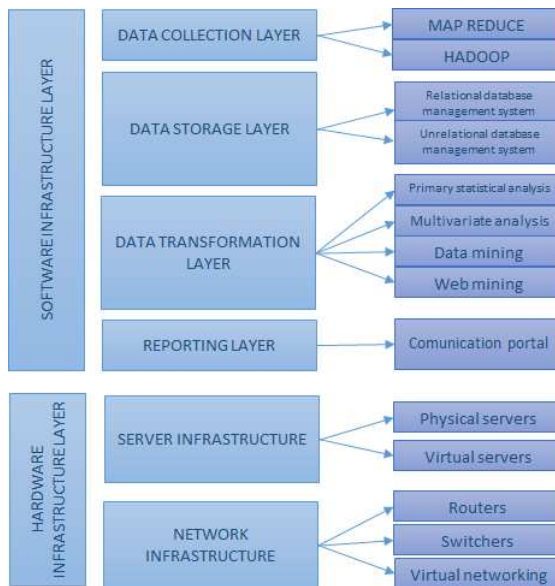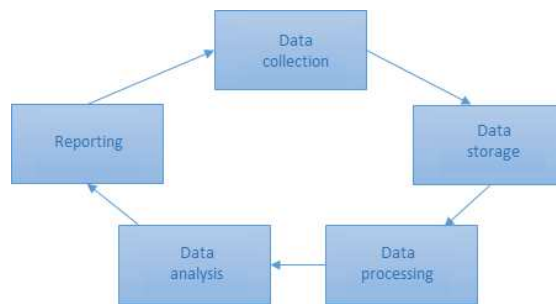

Figure 3

Multilayer infrastructural model

Figure 4

Cycle infrastructural model

Thanks to the "concept of a cycle" of this model and its dynamics, evaluation of results are being conducted automatically. Practically, every newly entered data entry is changing a previous report. This way, it meets the basic requirement of users – the real-time reporting.

From the standpoint of the infrastructure of the model, reporting component is being developed as the reporting portal consisted of two parts: Module for presenting the results and Module for forecasting.

Both modules are mutually connected and dynamically updated – as new data arrives in the model it is being stored, processed and analysed.

4   Discussion

In the previous sections of this paper, a model of Big Data infrastructure that can be used for medical research has been developed. This model generates and integrates various types of data that may have an impact on a person's health (demographic, financial, life style, etc.) and sends that data for analysis and reporting. The model opens the possibility for different devices to send data into the cloud which are then combined with different data and processed into medical information in real time. It is particularly important that this data can be combined with data from medical records, which offers the possibility of introducing new variables and measuring their impact in medical research. Further research will attempt to show how the model works in the case of establishing the early dementia.

Data will be collected from various sources provided by smart devices, mainly smartphones. Participants will be monitored in *in-house* and *out-house environment*. Collected data will be stored on the cloud server where it will be processed and paired with the existing EMRs (Electronic Medical Records) of the participants using Big Data technologies and Hadoop open source software [26].

Main data source is health application that collects: activity data using GPS and Bluetooth technologies (automatically), caffeine intake (by input), water intake (by input), heartbeat (measurement by the sensor implemented into the smartphone), nutrition (by input), sleep duration (automatically), stress amount (measurement by the sensor implemented into the smartphone). Data will be collected from other various mobile applications such as weather application (temperature, humidity, air pressure, UV index, noise level), and for female participant's period applications, agenda entry – in order to monitor the participants' focus on remembering daily tasks.

Monitoring the call logs, WhatsApp, Viber and messaging will provide data about socialization and human interaction, while microphone is being used for detecting voice changes. [51] In in-door conditions data can be collected by various sensors that monitor the participant's movement and position: intelligent chair sensor that detects posture [31], floor sensors for detecting falls [27], door sensors for detecting movement around home, *out-house environment:* For research purposes and maximizing of data collection, research will be conducted in urban environment. This data should represent the life style of the participants in outside environment. Primarily, the data collected using a smart phone that monitors their movement and activity (health applications + GPS) over hot-spots covered areas. Depending on the smart city development, the data can be combined with public transportation data (data provided by subway and/or bus cards).

Available data applicable in this research are credit card statements and list of groceries ordered online. Also, participants will be encouraged to scan the bills when shopping with the aim to identify a set of variables relating to food and financial status of the participants. Missing data that cannot be collected automatically using emerging technologies can be entered by participants on a daily basis through interactive questionnaires and reminders.

Most of the data that is collected from in-house and *out-house* environment are external unstructured data (data generated outside the healthcare system). The proposed infrastructure model allows this data to be collected and stored. This presents an opportunity for combining external with internal data (structured and unstructured), which is also stored in the same system and has already been collected within the health institution that takes care of the patient – research participant. Based on the database, healthcare institutions and care managers will monitor the patients' data. Real-time reporting is just one important future use of Big Data. Reporting may be displaying current results and forecasts. [12]

Until now, there could not be any forecasts analytics in healthcare because there was no data available. Applying this model of Big Data in healthcare fills-in the gap. Socioeconomic factors are an example in predictive analytics. This and similar data can help organizations to establish the exact diagnosis for the patient. Using this model, the report provides an analysis of data, noncompliance with medications, and more. That is just a small example of how Big Data can fuel predictive analytics. [18]

These predictive analytics predicts the state of health of a patient. Based on data from other patients with similar conditions, predictive algorithms can predict the state of health of patients over the time. [40]

Big Data technologies have the potential to transform the way healthcare providers use sophisticated technologies to gain insight from their clinical and other data repositories and make decisions based on collected information. In the future, we will see rapid, widespread implementation and use of Big Data analytics across the healthcare organization and the healthcare industry [42]. To that end, the several challenges highlighted above, must be addressed. As Big Data analytics becomes more mainstream, issues such as guaranteeing privacy, safeguarding security, establishing standards and governance, and continually improvement of the tools and technologies will garner attention. [2] Big Data analytics and applications in healthcare are at a nascent stage of development, but rapid advances in platforms and tools can accelerate their maturing process.

An additional challenge is the lack of experts – data scientists, experts not only in IT technologies, but also in the field of statistics, data mining and health statistics. It is important to emphasize that the research methodology and conclusion based on Big Data concept (and the proposed infrastructure model) must be developed in this field to ensure the verification of the results obtained on a scientific basis.

The benefits from implementing emerging technologies as a pillar of the healthcare system have been recognized by organisations world-wide. The USA National centre for scientific research has developed a project named City4Age that presents Ambient Assisted Cities for supporting older people with mild cognitive impairment to live independently. By collecting frequent data on behaviours, this project will alleviate the role of health services for older people that are at risk or have mild cognitive impairment. [45]

IBM and Microsoft have declared the partnership in developing the healthcare system based on Big Data technologies allowing iPhone and Apple Watch users to share the data from their devices to IBM's Watson Health cloud-based healthcare analytics service. [22]

University of Iowa is predicting that by year 2020, the amount of data available in healthcare will double every 73 days. [46] Therefore, the introduction of Big Data model into the health system is inevitable and has a great potential in improving healthcare.

Conclusions

This paper presents a comparative analysis of the possibilities and limitations of new technologies (ICT) applied in the healthcare system. The paper shows that this field of the medicine cannot remain on the side-lines when it comes to implementing new IT concepts, especially Big Data concept. Emerging ICT technologies have a direct impact on changing the current practice in the field of all types of research, including medical. In concrete terms, Big Data is not only

new technology; it is a new approach to medicine that requires improvement of research methodology, which has so far largely relied on classical statistical methods of inference.

Suggested model presents the first step in implementing this concept of adapting modern data warehousing solution to the concept of large amount of data. In the case of detection of dementia, benefits of technology developments were illustrated – enormous amount and variety of data is generated, but not yet fully available for implementation in healthcare. We pointed out the sustainability of the base hypothesis.

The main hypothesis tested in this paper: there are large amounts of available data (structured and unstructured) from various sources that can be used for medical purposes which are not directly related to the health system – was confirmed.

Also, first specific hypotheses was proven: Emergence and implementation of Big Data necessarily lead to a change in the traditional methodology of processing, analysis and presenting data, and overall conducting medical research. In addition to the manner of collection, the challenge is in processing and analysing the collected data. The second specific hypothesis goes beyond information frames and has yet to be demonstrated in future operations, primarily by statisticians, and data scientists.

The application of this model for medical purposes in Serbia is inevitable. In the past few years, informational scientists in Serbia have been working on introducing informational systems in healthcare facilities. However, the initial situational analysis shows that including Big Data technologies is essential for the growth of healthcare informational system. Introducing Bid Data technologies would present a qualitative leap in the effective use of information for the benefit of the patient and process management in the healthcare system.

Serbian Ministry of Health has announced that during the year 2016, healthcare will revitalize itself with a unique data centralization information system. However, without conducting the findings and knowledge that has been apprehended all around the world by applying Big Data technologies in the healthcare field, the results will be poor and the benefits negligible.

Further recommendation:

- Essentially educate medical experts about the importance of introducing new ICT, especially Big Data technologies into medical practice

- It is necessary to make and adopt a strategic and legal framework as a support system for Big Data technologies implementation in Healthcare that will provide a solution for overcoming problems of access and use of personal data by updating privacy and data ownership policies in a way to protect patients' rights and allowing the full potential of data collection and analysis.

- It is recommended for all states to adopt the form of academic-public-private partnerships, following the example of United Kingdom in 2012. [50]

- Adapting the curricula at universities, collages, and faculties in order to educate students about sciences in data field.

References

[1]   Barnett, M. L., Christakis, N. A., O'Malley, J., Onnela, J. P., Keating, N. L., Landon, B. E.: Physician patient-sharing networks and the cost and intensity of care in US hospitals. Med Care 2012; 50(2):152-60 (2012)

[2]   Bates, D. W., Saria, S., Ohno-Machado, L., Shah, A., Escobar, G.: Big Data in Health Care: Using analytics to identify and manage high-risk and high-cost patients. Health Affairs, 33, no. 7 (2014)

[3]   Beyer, M.A., Douglas, L.: The Importance of 'Big Data': A Definition. Available at: URL: http://www.gartner.com/it-glossary/big-data/ (2012)

[4]   Bollier, D.: The Promise and Peril of Big Data. The Aspen Institute (2010)

[5]   Bradley, P.: Implications of big data analytics of population health management. Big Data; 1(3): 152-159, DOI: 10.1089/big.2013.0019 (2013)

[6]   Bram, J. T., Warwick-Clark, B., Obeysekare, E., Khanjan, M.: Utilization and Monetization of Healthcare Data in Developing Countries. Big Data 2015; 3(2), DOI: 10.1089/big.2014.005 (2015)

[7]   Brown, B., Chui, M., Manyika, J.: Are you ready for the era of 'big data'? McKinsley Global Institute (2011)

[8]   Csubák, D., Szücs, K., Vörös, P., Kiss, A.: Big Data Testbed for Network Attack Detection. Acta Polytechnica Hungarica; Vol. 13, No. 2, DOI: 10.12700/APH.13.2.2016.2.3 (2016)

[9]   Davenport, T.: Big data @ work. Harvard Business School Publishing Corporation (2014)

[10]   Devdzic, V., Chaloub-Johansson, C., Weinhara, M.: Development of Health Information System for Basic Health and Pharmaceutical Services in Serbia. European Health Group, Copenhagen, Denmark (2008)

[11]   Dobrota, M., Jeremic, V., Markovic, A.: A new perspective on the ICT Development Index. Information Development 28(4): 271-280 (2012)

[12]   Ericsson Mobility Report November 2015. Available at: http://www.ericsson.com/res/docs/2015/mobility-report/ericsson-mobility-report-nov-2015.pdf

[13]   Foster P, Fawcett T. What you need to know about data mining and data-analytic thinking. O'Reilly Media, Inc. (2013)

[14]   Frost & Sullivan. Drowning in Big Data? Reducing Information Technology Complexities and Costs for Healthcare Organizations.

Available at: URL: http://www.emc.com/collateral/analyst-reports/frost-sullivan-reducing-information-technology-complexities-ar.pdf (2010)

[15]   Governemets Health – IT Staff. Is IoT potential understated? 2015. Available at: http://www.govhealthit.com/news/iot-potential-understated (2015)

[16]   Health Affairs. Big Data and New Knowledge in Medicine: The Thinking, Training, And Tools Needed For a Learning Health System; Available at: http://content.healthaffairs.org/content/33/7/1163.full.pdf+html (2014)

[17]   Heart, T., Kalderon, E.: Older adults: are they ready to adopt health-related ICT. International Journal of Medical Informatics. 82(11): 209-231 (2013)

[18]   Herland M., Khoshgoftaar TM., Wald, R.: A review of data mining using big data in health informatics. Big Data (2014)

[19]   Hersh, W., Jacko, J. A., Greenes, R., Tan, T., Janies, D., Embi, P. J., Payne, P.R.O.: Health-care hit or miss? The Ohio State University, College of Medicine; Nature 470, 327-329, DOI: 10.1038/470327a (2011)

[20]   Holmes, A.: Hadoop in practice. Manning Publications Co. (2012)

[21]   Huangb, T., Lanc, L., Fanga, X., Ana, P., Mind, J., Wanga, F.: Promises and Challenges of Big Data Computing in Health Sciences. Big Data Research (2015)

[22]   IBM Watson Health ©2015 International Business Machines Corporation. Available at: http://www-05.ibm.com/no/businessconnect/assets/files/IBMWatson-hjelper-leger-ta-beslutninger-StefanOhlsson.pdf (2015)

[23]   Jimeng, S., Chandan, K. R.: Big data analytics for healthcare. Proceedings of the 19th ACM SIGKDD international conference on Knowledge discovery and data mining; 1525-1525. DOI:10.1145/2487575.2506178 (2013)

[24]   Jovanovic Milenkovic, M., Jeremic, V., Martic, M.: Sustainable development in the e-health sector of the European Union. Journal of Environmental Protection and Ecology. 15(1): 248-256 (2014)

[25]   Jovanović Milenković, M., Radojičić, Z., Milenković, D., Vukmirović, D.: Applying electronic documents in development of the healthcare information system in the Republic of Serbia. Computer science and informational systems; 6(2), 111-126. DOI: 10.2298/csis0902111J (2009)

[26]   Lin, W., Dou, W., Zhou, Z., Liu, C.: A Cloud-based Framework for Home-diagnosis Service over Big Medical Data. The Journal of Systems and Software (2014)

[27]   Lustrek, M., Gjoreski, H., Kozina, S., Cvetkovi, B., Mirchevska, V., Gams, M.: Detecting Falls with Location Sensors and Accelerometers.

Proceedings of the Twenty-Third Innovative Applications of Artificial Intelligence Conference (2011)

[28]   Manyika, J., Chui, M., Bisson, P., Woetzel, J., Dobbs, R., Bughin, J., Aharon, D.: Unlocking the potential of the Internet of Things. McKinsley & Company; Available at: http://www.mckinsey.com/insights/business_technology/the_internet_of_things_the_value_of_digitizing_the_physical_world (2015)

[29]   Manyika, J., Chui, M., Bisson, P., Woetzel, J., Dobbs, R., Bughin, J., Aharon, D.: Unlocking the potential of the Internet of Things. McKinsley & Company; Available at: http://www.mckinsey.com/insights/business_technology/the_internet_of_things_the_value_of_digitizing_the_physical_world (2015)

[30]   Manyika, J., Chui, M., Brown, B., Bughin, J., Dobbs, R., Roxburgh, C., Hung Byers, A.: Big data: The next frontier for innovation, competition, and productivity. McKinsley & Company (2011)

[31]   Martins, L., Lucena, R., Belo, J., Santos, M., Quaresma, C., Jesus, A.P., Vieira, P.: Intelligent Chair Sensor. Engineering Applications of Neural Networks (2013)

[32]   McKinsey & Company. Internet of Things & Healthcare: two important reports; Available at: http://medgizmo.info/news/internet-of-things-healthcare-two-important-reports (2015)

[33]   Milenković, D., Jovanović Milenković, M., Vujin, M., Aleksić, A., Radojičić, Z.: Electronic health system – development and implementation into the health system of the Republic of Serbia. Vojnosanit Pregl 2012; 69(10): 880-890 (2012)

[34]   Milenkovic, N., Vukmirovic, J., Bulajic, M., Radojicic, Z.: A multivariate approach in measuring socioeconomic development of MENA countries. Economic Modelling; 38(C): 604-608 (2014)

[35]   Miner, D., Shook, A.: MapReduce design patterns. O'Reilly Media, Inc. (2012)

[36]   Narayanan, A., Greco, M., Powell, H., Coleman, L.: The reliability of Big "patient satisfaction" Data. Big Data; 1(3), 141-151, DOI: 10.1089/big.2013.0021 (2013)

[37]   Ozminkowski, R., Wells, T., Hawkins, K., Bhattarai, G., Martel, C., Yeh, C.: Big Data, Little Data, and Care Coordination for Medicare Beneficiaries with Medigap Coverage. Big Data; 3(2). DOI: 10.1089/big.2014.0034 (2015)

[38]   Park, H. W., Yeo, I. Y., Lee, J. R., Jang, H.: Study on Network Architecture of Big Data Centre for the Efficient Control of Huge Data Traffic.

Computer Science and Information Systems, Vol. 11, No. 3, 1113-1126 (2014)

[39] Pentland, A., Reid, T., Heibeck, T.: Big data and health, Revolutionizing medicine and Public Health. World Innovation Summit for Health (WISH), Big Data and Health Report. Available at: http://wish-qatar.org/big-data/big-data (2013)

[40] Poucke, S. V., Thomeer, M., Hadzic, A.: 2015, big data in healthcare: for whom the bell tolls? Critical Care (2015)

[41] Power, D.: Ask Dan! About DSS; Available at: http://dssresources.com/faq/index.php?action=artikel&id=263 (2014)

[42] Raghupathi, W., Raghupathi, V.: Big data analytics in healthcare: promise and potential. Health Information Science and Systems, 2(3), DOI: 10.1186/2047-2501-2-3 (2014)

[43] Seke, K., Petrovic, N., Jeremic, V., Vukmirovic, J., Kilibarda, B., Martic, M.: Sustainable development and public health: Rating European countries. BMC Public Health. 13(77), 1–7. DOI: 10.1186/1471-2458-13-77 (2013)

[44] Simon, P.: Too Big to ignore – the business case for big data. John Wiley & Sons, Inc. (2013)

[45] The National Centre For Scientific Research: Elderly-friendly city services for active and healthy ageing (2016) Avaiable at: http://www.ipal.cnrs.fr/project/eu-h2020-city4age

[46] University of Iowa Carver Collage of Medicine: MD Curriculum Renewal (2015) Avaiable at: http://www.healthcare.uiowa.edu/2020/

[47] Vukmirovic, A., Brbaklic Tepavac, M., Vukmirovic, J.: Virtual community research. XX Yu Info Conference Proceedings of the Association for Information Systems and Computer Networks; Kopaonik, Serbia (2014)

[48] Wang, W., Krishnan, E.: Big Data and Clinicians: A Review on the State of the Science. JMIR Medical Informatics, 2(1), doi:10.2196/medinform.2913 (2014)

[49] White, T. Hadoop – The definitive guide. O'Reilly Media Inc. (2012)

[50] Williams, L.: The power of information: Putting all of us in control of the health and care information we need, Department of Health, Avaiable at: https://data.gov.uk/sites/default/files/DH%20Open%20Data%20Strategy_1 0.pdf (2012)

[51] Yanga, J., Lic, J., Mulderd, J., Wange, Y., Chenf, S., Wug, H., Wangb, Q., Panf, H.: Emerging information technologies for enhanced healthcare. Computers in Industry (2015)

Hierarchical Histogram-based Median Filter for GPUs

Péter Szántó, Béla Fehér

Budapest University of Technology and Economics, Department of Measurement and Information Systems, Magyar tudósok krt. 2, 1117 Budapest, Hungary, {szanto, feher}@mit.bme.hu

Abstract: Median filtering is a widely used non-linear noise-filtering algorithm, which can efficiently remove salt and pepper noise while it preserves the edges of the objects. Unlike linear filters, which use multiply-and-accumulate operation, median filter sorts the input elements and selects the median of them. This makes it computationally more intensive and less straightforward to implement. This paper describes several algorithms which could be used on parallel architectures and propose a histogram based algorithm which can be efficiently executed on GPUs, resulting in the fastest known algorithm for medium sized filter windows. The paper also presents an optimized sorting network based implementation, which outperforms previous solutions for smaller filter window sizes.

Keywords: median; filter; GPGPU; CUDA; SIMD

1　Introduction

Median filtering is a non-linear filtering technique primarily used to remove salt-and-pepper noise from images. Compared to convolution-based filters, median filter preserves hard edges much better, therefore being a very effective noise removal filter used before edge detection or object recognition. For example, it is widely used in medical image processing to filter CT, MRI and PET images; in image capturing pipelines to remove the sensors' digital noise; or in biological image processing pipelines [14] [15] [17].

Median filter works basically replaces the input pixel with the median of the N=k*k surrounding pixels (Figure 1), which can be done by sorting these pixels and selecting the middle one. The figure also shows one of the possibilities for optimization: as the filter window slides with one pixel, only k pixels change in the k*k array.

The generalization of the median filter is the rank order filter [3], where the output is not the middle value, but the nth sample from the sorted list. Rank order filter

can be even more efficient in noise removal, also used in medical image processing [17]. Due to space limitation, rank order filtering is not discussed.

The main drawback of the median filter is the computational complexity. Linear filtering is based on sequential data access and multiply-and-accumulate operation that can be efficiently executed using CPUs, GPUs or FPGAs. On the other hand, implementing median filtering without data dependent operations is considerably less straightforward and most architectures are not tailored towards the efficient implementation of it.
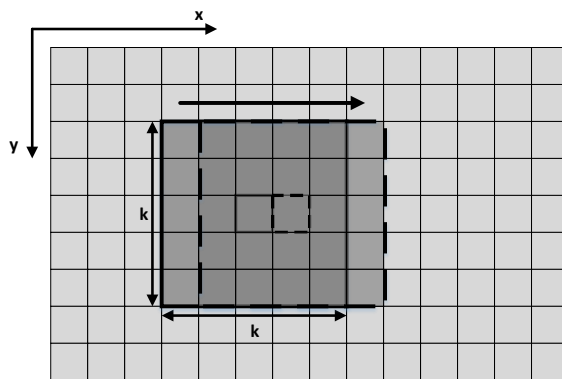
Figure 1

2D median filtering: computation of two consecutive pixels

Median filter implementations differ from each other by the applied sorting (or selection) algorithm. For small window sizes, $O(N^2)$ algorithms are good candidates, for larger window sizes $O(N)$ solutions are typically faster. Several research papers also presented $O(1)$ algorithms [5] [7], but these are typically highly sequential and only offer lower execution time than $O(N)$ algorithms if the window size is quite large (~25x25 pixels). We can conclude that there is no "best algorithm", the optimal solution depends on the window size.

This paper presents several algorithms, which can be efficiently used to execute low- and medium-sized median filtering on highly parallel architectures, like GPUs.

2   Architectures

Although there are many different computing architectures, the key in order to achieve high performance is parallelization. FPGAs offer fine-grained parallelism, where the computing elements and memory structures can be intensely tailored to the given application. Multi-core CPUs and many-core architectures, like GPUs,

share the basic idea of sequential instruction execution, but the level of parallelization is vastly different.

2.1 Parallel Execution on CPUs

Irrespectively of being embedded, desktop, or server products, CPUs offer two kinds of parallelization: the multi-threading and the vectorization. To be able to exploit the multi-core nature of processors, the algorithm should be able to run on multiple, preferably highly independent threads. For image processing, especially in case the resolution is high or there are lots of images in sequence, this is not an issue, as the number of cores in a single CPU is typically low (~32 for the largest server products). It is possible to separate input data temporally (by processing each image of the input sequence on different core) or within frames (by processing smaller parts of a single input image on different cores). This kind of multi-threading requires a minimum amount of communication between threads, and uniform memory access model – used by single multi-core CPUs – makes the data handling straightforward. Larger scale homogeneous CPU systems (such as High-Performance Computing centers) are quite different and are out of the scope of this paper.

The other parallelization method offered by CPUs is SIMD execution. Each modern CPU instruction set has its own SIMD extension: NEON for ARM [13], SSE/AVX for Intel [12] and AltiVec for IBM [9]. An important common feature of all SIMD instruction sets is the limited data loading/storing: one vector can be only loaded with elements from consecutive memory addresses and the elements of a vector can be written only to consecutive memory addresses. Beyond this limitation, in order to achieve the best performance, it is also beneficial to have proper address alignment. Regarding execution, obviously, it is not possible to have data dependent branches within one vector. The typical vector size is 128 or 256 bit and vector lanes can be 8, 16 or 32-bit integers or floats, so when processing 8-bit images 16 or 32 parallel computations can be done with one instruction. The nature of SIMD execution greatly reduces the type of algorithms which can be parallelized this way – with the notable exception of [5], most of them are based on the minimum and maximum instructions [8] [9].

Although the future of this product line seems to be questionable now, we should also mention Intel's many-core design: the Xeon Phi. In many ways, it is similar to standard Intel processors, as it contains x86 cores with hyper-threading and vector processing capabilities. The main differences are the number of cores in a single chip (up to 72); the wider vectors (512-bit); the mesh interconnect between the cores; and the presence of the on-package high-bandwidth MCDRAM memory.

2.2   Parallel Execution on GPUs

The computing model of GPUs is quite different from CPUs. First, the number of cores is much larger – e.g. 2560 in the high-end NVIDIA GTX 1080 [11]. To allow the efficient usage of these cores, the number of concurrently executed threads should be much larger (tens of thousands) than it is for a CPU. Execution is also different: basically, a GPU is a MIMD array of SIMD units.
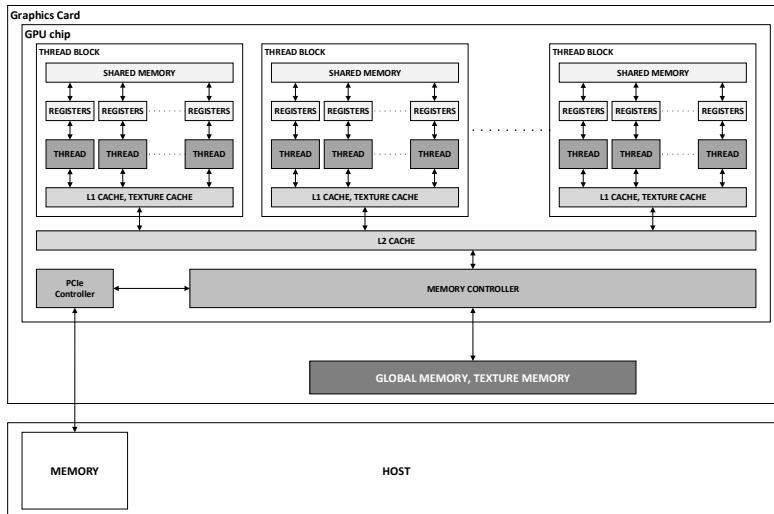

Figure 2

GPU thread hierarchy and accessible memories

Threads are grouped hierarchically, the lowest level being the warp (NVIDIA) or wavefront (AMD), which contains 32 or 64 threads, respectively. The threads within a warp always execute exactly the same instruction; therefore, they are SIMD in this respect. If threads within a warp execute different branches, all threads within the warp execute both branches – therefore data dependent branch divergence should be avoided within a warp unless one of the branches is empty. Memory access, however, is much less constrained compared to a CPU's SIMD unit: theoretically, there is no limitation on where the warp's threads read from or where they write to; practically to get good performance there are constraints, but it is still much freer than it is on CPUs. All threads have their own register space, which is the fastest on-chip storage that the GPU has. The number of registers allocated to a single thread is defined during compile time: the hardware maximum is 255, which is much more than the number of registers available in a CPU (though the number of concurrently scheduled threads decreases as the number of registers per thread increases, which may affect the performance).

The next hierarchy level is the Thread Block (TB): threads within a TB can exchange data through a local (on-chip) Shared Memory (SM) and they can be synchronized almost without overhead. Hardware-wise, threads within a TB are executed on the same Streaming Multiprocessor (SMP). If resource constraints – SM and register usage per TB – allow it, threads from multiple, independent TBs are scheduled on a single SMP.

TBs are grouped into Thread Grid, which is executed independently of each other. Data exchange between TBs is only possible through cached, off-chip Global Memory (GM) and synchronization is quite expensive in terms of performance.
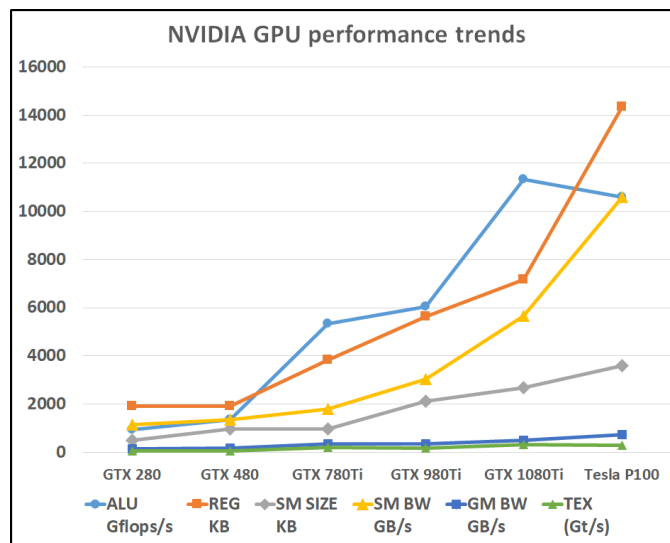
Figure 3
GPU performance trends

Beyond the computational capacity, another important factor that has a huge impact on performance is memory bandwidth. Just as in case of CPUs, the fastest storage is the register array. The second fastest memory is the on-chip SM, but in order to get the most performance out of it, there are restrictions to keep. SM is divided into 32 parallel accessible banks; each consecutive 32-bit word belongs to a different bank. As long as threads within a warp access different banks (or multiple threads access exactly the same word within a bank), SM access is parallel. However, if different threads within a warp access different words from the same bank, memory access is serialized, which heavily affects performance. GM bandwidth is considerably lower (see Figure 3). Since the Fermi architecture, access to off-chip memory is cached, thus performance impact of non-ideal transactions is considerably decreased, but it is still important to design for ideal read/write bursts.

Figure 3 shows the trends of the theoretical calculated performance of current and past NVIDIA GPUs. ALU performance is the number of floating point operations per second (other instructions may execute much slower, but it depends on GPU architecture); REG is the size of the register space on the whole chip; SM size is the size of the SM on the whole chip; SM BW is the cumulative bandwidth of all SM blocks; GM BW is the bandwidth of the off-chip GM; TEX is the texture read performance in GTexel/s.

Firstly, we can conclude: the increase in GM bandwidth is notably slower than the increase in computational performance (even for the P100, which uses HBM2 High Bandwidth Memory). Therefore, often used data should fit into on-chip memory otherwise the algorithm is not the best candidate for GPU acceleration. Second, SM bandwidth increases more or less in line with the computing performance, but this is not true for the size of this memory. Thus, memory bandwidth intensive algorithms may be relatively good candidates, but the algorithms requiring a large size of on-chip memory are not ideal.

2.3   Special Instructions

Creating branchless algorithms is a requirement for vectorization and it is also preferred for GPU acceleration. For median filtering, the most important instructions are the vector comparison instructions, the data selection instruction, and the minimum/maximum instructions.

All SIMD CPU and GPU architectures have comparison instructions for all data types: these instructions set a register either to a predefined value (if the comparison is true) or to zero. E.g. for Intel SSE the result is 1.0f and 0.0f for floating point data types and -1 and 0 for integer data types. For ARM NEON, the output is -1 or 0, irrespective of the input data type. NVIDIA GPUs has a more versatile SEL instruction: the result type can be set independently of the source operand type, therefore both (1.0f or 0.0f) and (-1 or 0) are supported. A slightly different version of the SEL instruction is SELP: instead of setting a general-purpose register, this instruction writes a special predicate register. Please note that comparison instructions are not always executed at full-speed: unlike the Fermi generation, in case of newer NVIDIA Maxwell and Pascal GPUs, the throughput is 0.5 operations per clock per ALU. The same is true for x86 SSE2, throughput is 0.5 or 1 depending on data type and CPU generation.

Another important instruction type is the selection. ARM NEON and IBM AltiVec natively supports 3-operand selection instruction. NVIDIA GPUs has a SELP instruction where the selection is based on the value of a predicate register and an SLCT instruction where selection between two operands is based on the sign of the third operand. SSE2 does not have dedicated selection instruction, but it can be implemented with several logical operations.

Minimum and maximum instructions are widely supported, all SIMD CPU instruction sets and all GPUs can execute them on all types of data, though – just like comparison and selection – throughput is typically lower than 1.

3   Grayscale Image Processing

In this chapter, we present several algorithms. Binary search (BS) is an optimized CUDA implementation of NVIDIA's OpenCL SDK sample [10]; Batcher's Odd-Even Merge Sort (BMS) implements the known algorithm [1] in CUDA; BMS2 is an optimized version of BMS; the counter based method (CNT) is the GPU implementation of our previous FPGA-based solution [3]; and finally hierarchical histogram (HH) is a novel histogram based solution for GPUs. Exactly the same implementations can be used to handle multiple color planes independently, e.g. to filter R, G and B channels independently. For biomedical image processing pipelines where the planes show different properties of the cell (e.g. fluorescence microscopy [16]) this is the required processing method. However, for natural color images, like photos, this is not an advisable method, as independent filtering may generate RGB combinations on the output, which were not present on the input. Chapter 4 presents a luminance based modification which can be used to filter photographs.

3.1   General Architecture

Similarly to most image processing functions, input data usage is very redundant in case of the median filter. For a $N=k*k$ window size, $N-k$ pixels are the same for two neighboring output pixel calculations (see Figure 1), which means that every input pixel is read several times. Therefore, appropriate caching is very important. Modern GPUs offer three alternatives: cached read access from GM; cached read from Texture Memory; software managed buffering in SM. Although every memory access is cached, efficiency is not the same – albeit it requires more instructions, typically an SM-based solution is considerably faster, thus this is the method used for the implementations discussed below.

Unless otherwise noted, the basic principle is that every thread computes one output pixel, which means that a thread block with a size of TX*TY requires $(TX+k-1)*(TY+k-1)$ input pixels. The 8-bit pixels are stored line by line in SM, so consecutive byte addresses belong to adjacent pixels, therefore one SM word stores four adjacent pixels. Using horizontal thread block size of 32, access to the adjacent pixels within a warp is free of bank conflict: at any given time the 32 threads of a warp access 32 adjacent pixels which reside in 32/4=8 banks. If a single thread computes S horizontally adjacent output pixels, the ith thread of a warp reads byte address $i*S$, which is bank $i*S/4$. To have a bank conflict-free

access, $(i*S/4)\%32$ should be different for $i=0\ldots31$, which limits the possible numbers to $O=\{1,2,3,4,12,\ldots\}$. Computing vertically adjacent pixels is free of bank conflict: at any given time the threads within a warp reads horizontally consecutive pixels from a single line. The drawback is GM read access: when loading input data into SM only $32+k-1$ bytes can be read from consecutive addresses.

3.2   Binary Search

Binary search (BS) is the algorithm employed by the 3x3 median filter example in NVIDIA's OpenCL SDK, therefore it is included as a reference [10]. It finds the median by counting the number of elements which are greater than the current median candidate (highcount); if the result is greater than $(N-1)/2$, there are more larger elements and less smaller elements than the median candidate, thus the candidate is increased with interval halving. Figure 4 shows the first three steps of the algorithm: the initial median candidate (128) is half of the absolute interval ($[0\ldots255]$). In the first step, there are 5 larger and 4 smaller elements than the median estimate. Therefore, the median estimate is moved to the middle of the upper half-interval: $(128+255)/2=192$. The new interval is $[128\ldots255]$. The maximum number of steps required to find the median is $b=\log_2 I$, where I is the range of the input data, e.g. 256 for 8-bit input.

A single step of an iteration is a comparison of the input data and the modification of the high-counter. This should be repeated for every input pixel, thus the complexity is $O(b*N)$, where b is the bit width of the input values. The algorithm is a good choice because it does not contain divergent branches and does not require an extensive amount of registers or memory (interval halving can be implemented branchless with comparison and selection instructions).

NVIDIA's original implementation was created for RGBA input images where every thread computes one pixel. The input components were stored in SM as 8-bit values per component, but computation (median estimate, interval ends) was done using float values. This is acceptable when the filter window is small because the compiled code reads input values from the SM only once and stores them in registers – conversion from uint8 to float takes place during the read. However, as the window size increases, there are not enough registers to store all N input pixels in registers, therefore every pixel is read and converted multiple times, which makes type conversion redundant (not to mention that this type of instruction is slow anyway). Although it requires more memory, performance wise it is a better approach to do the conversion when the SM is loaded – the speed of this process is limited by the GM bandwidth, so the relatively slow type conversion is almost free in terms of execution time.

By checking the generated assembly code, it can be noticed that the NVIDIA compiler generates a SETP and a SELP instruction from the C code which

implements the basic compare-increment functionality. This is unnecessary, as the SEL instruction can set a register to 1.0f or 0.0f based on the result of the comparison, thus one instruction can be saved. With the data type modification and inline assembly, the performance of the binary search method can be increased by 60% compared to the original code.
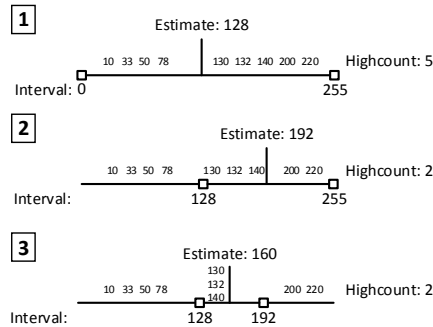

Figure 4

First three steps of the binary search

As the algorithm can be realized without branches, it can be vectorized when being implemented for CPUs. When SSE2 is used, a single vector register can be used to calculate the counter for 16 adjacent pixels. As the comparison returns -1 when true, the addition should be replaced with subtraction for the "larger than" counter and the selection operation should be implemented with logical operators.

3.3   Batcher Odd-Even Merge Sort

The Batcher Odd-Even Merge Sort (BMS) is a general sorting network introduced by Ken Batcher [1]. Although its $O(N*(logN)^2)$ complexity is not optimal, for reasonable input size it is better than any other sorting network [2]. Like other sorting networks it is based on comparison and element swapping, which is equivalent to executing min()/max() functions – therefore it can be implemented branchless. The algorithm completely sorts the N input elements, which is not necessary in the case of a median filter, so complexity can be slightly decreased by removing the unnecessary comparisons. Figure 4b shows the network for N=9. Generally, for $N=2^t$ inputs, the number of data swaps required to generate a sorted list [2]:

$$c(2^t) = (t^2 - t + 4) * 2^{t-2} - 1 \tag{1}$$

Therefore, complexity is $O(N*(logN)^2)$. Because of the relatively bad scaling and high register usage, the expectation is that a sorting network-based implementation can only be used for smaller (3x3 or 5x5) window sizes.
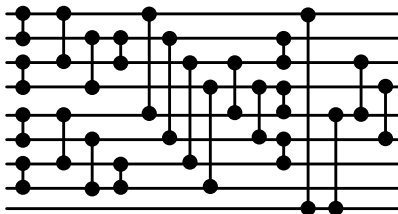
Figure 5
Batcher sorting network for N=9 median

The performance can be considerably increased by taking advantage of the common pixels in two adjacent filter windows: in a window of size N=k*k, there are CP=k*(k-1) common pixels. In the sorted list of the common pixels, the only median candidates are the (k+1) middle values. To compute the final median these candidates should be merged with the sorted list of the remaining k pixels, separately for each window. Therefore, to compute two outputs, we have to employ one CP-input sorting network and two additional merging steps using the (k+1) and k element sorted lists. Compared to performing two N-input sorting networks independently, this method greatly decreases the number of required instructions. Performance numbers achieved with this optimized version are denoted as BMS2 in Chapter 5.

3.5   Counter-based Method

The third algorithm (denoted with CNT) originates from our optimized FPGA implementation [3], but a slightly similar (less efficient) method was also used in [6]. The basic idea is to count the number of elements, which are greater than the current one for every pixel. At the end of the process, there will be N different counter values ranging from 0 to N-1; the median is the element which counter equals to (N-1)/2.

For the ith processed element, the initial value of its counter is set to i. Then the new element is compared with all the older elements (new<old); if the comparison is true, the counter of the older element is increased with one and the counter of the new element is decreased with one. If the comparison result is false, counters do not change. Figure 6 shows the steps of the algorithm for 5 elements.

The median element can be found by comparing all counter values with (N-1)/2 – the index of the median element is the index of the counter where the comparison is true. The already mentioned SETP and SELP instructions can be used to step through all the counter values and select the one with the appropriate value. As the GPU's registers cannot be indexed with a register, this should be done in an unrolled loop. A slightly faster version can be created using SEL and FMAD

(floating point multiply and add): the result of the SEL (1.0f or 0.0f) is multiplied with the index of the counter register and added to an accumulator. As all counter values are different, SEL returns 1.0f only once, thus the final accumulator value equals to the index. This is faster because the throughput of the FMAD instruction is 1.
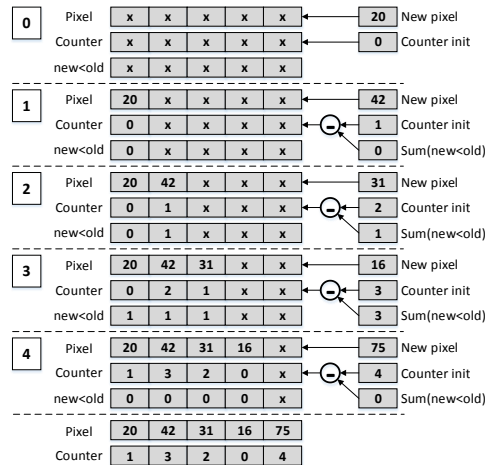

Figure 6
Counter based algorithm example

The basic step of the algorithm contains four arithmetic instructions: set initial counter value; compare the new value with the old one; increment and decrement the corresponding counters. The number of steps required for the full process equals to

$$c = \sum_{i=1}^{N-1} \sum_{j=0}^{i-1} 4 * j \tag{2}$$

so the algorithm is $O(N^2)$, meaning it is only a candidate for a window size of 3x3 pixels. Register usage also confirms this assumption: the number of counter registers required equals to the window size.

It is possible to exploit the benefits of the overlapping kernel windows: for two adjacent outputs, there are N-k common input pixels and k different pixels. This means that the first N-k computations are common. That is, the number of steps per output pixel can be decreased from 36 to 34 for the 3x3 window, and from 300 to 205 for the 5x5 window. On the other hand, register usage cannot be decreased, as all processed pixel should have their own counter.

3.6   Histogram-based Method

Histogram-based median filters are widely used in CPU implementations because of the achievable $O(N)$ or $O(N^{1/2})$ complexity. Moreover, several papers discussed $O(1)$ implementations [5] [7], but such algorithms are typically sequential, require a large amount of memory and, although $O(1)$ complexity is true, the large multiplication factor makes them a viable option only for extremely large window sizes. A conceptually similar method was also implemented for GPUs [5] with the conclusion that although $O(1)$ complexity can be approached, the $O(N)$ version is faster for reasonably sized windows.

Creating a simple histogram based median filter for uint8 data (referred as H256) is quite straightforward. After clearing the histogram, each pixel in the filter window is processed and the histogram bin corresponding to the given pixel's value is incremented. After all pixels are processed, the summation of the histogram bins equals to N. The median value can be found by accumulating histogram bin values starting with bin 0 – the median value is in the bin where the accumulator reaches $(N+1)/2$, because there are $(N+1)/2-1$ pixels which are smaller than the current bin index. Exploiting the advantages of a sliding window (see Figure 1) is also quite straightforward: as the filter window steps one column right, k pixels should be removed and k new pixels should be added to the histogram. For GPU implementation, the main drawback of the simple histogram algorithm is memory usage. Every thread should have its own histogram of the pixel(s) it processes. This limits the number of concurrently scheduled threads on an SMP to 384 (Maxwell and Pascal architectures) when using uint8 bins and to 192 when using uint16 bins (for windows which contain more than 255 pixels). Such a low level of occupancy can seriously decrease performance.

To reduce memory usage at the expense of increasing the instruction count, we propose a novel method, the Hierarchical Histogram (HH). The basic idea is to first create a histogram based on the MSB bits of the input and then create a histogram based on the LSB bits using the inputs whose MSB equals to the computed MSB median. Figure 7 demonstrates the operation using the following hexadecimal input values: 0x14, 0x44, 0x42, 0xA3, 0xA6, 0xAB, 0xC0, 0xE4, 0xFF. The MSB histogram is created from the 4 MSB bits of the input data set, then the median is found by accumulating the bin values until $(N+1)/2$ is reached – in this example this is bin 10, where the number of already counted elements equals to 6. The number of elements before the selected bin is 3 (bin 1 and bin 4). The LSB histogram is created using input data where MSB equals to 0xA. To find the LSB median, bin value accumulation should be started from 3, what was the number of elements before bin 10 in the MSB histogram. The process reaches $(N+1)/2$ at bin 6, therefore the median LSB value is 6, thus the full median value is 0xA6. For 8 bit inputs separating MSB and LSB processing requires only 16 bytes of histogram memory, which greatly increases GPU occupancy.

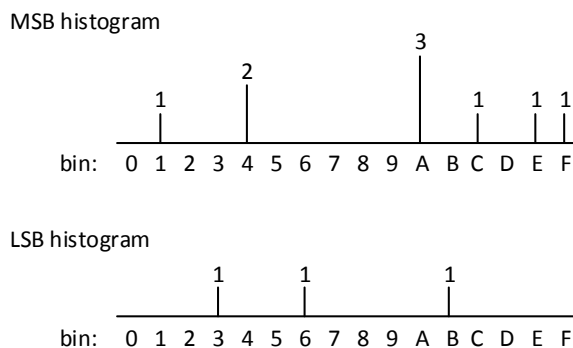MSB histogram

LSB histogram

Figure 7

Median filtering using Hierarchical Histogram

The main disadvantage is that in worst case every input pixel should be processed twice, which almost doubles SM bandwidth usage. The efficiency increase from incrementally processing adjacent pixels also decreases: although the MSB histogram can be updated by removing k old pixels and adding k new ones, the LSB histogram has to be cleared and recomputed for every new output. To be able to do this, the two histograms have to be stored in separate memories, which doubles the required space.

	Word address	Thread, Bin			
Bank 0, Word 0	0	0,0	32,0	64,0	96,0
Bank 1, Word 0	1	1,0	33,0	65,0	97,0
....	....	....	....	....	....
Bank 31, Word 0	31	31,0	63,0	95,0	127,0
Bank 0, Word 1	32	0,1	32,1	64,1	96,1
Bank 1, Word 1	33	1,1	33,1	65,1	97,1
....	....	....	....	....	....
Bank 31, Word 1	63	31,1	63,1	95,1	127,1
....	....	....	....	....	....
....	....	....	....	....	....
Bank 0, Word 15	480	0,15	32,15	64,15	96,15
....	....	....	....	....	....
Bank 31, Word 15	511	31,15	63,15	95,15	127,15

Figure 8

Histogram Shared Memory structure

For all histogram based filters bank conflict-free memory access is also an important design goal. As the threads within a warp access their histogram randomly, the histogram array should be constructed in a way that different bins of a histogram reside in the same bank and only bins from different warps may be placed in the same bank. For N<256 uint8 is enough to store a single bin, for larger N uint16 is necessary. Assuming uint8 bins, the most trivial way to avoid bank conflict is to place the first 4 bins of a thread into word W of bank B, and the ith 4 bin word into word W+i of bank B. The drawback of this method is that

histogram access requires additional bit selection from the input to determine word address and byte address. A better way is to make addressing data-independent and only related to the thread ID so it can be computed once. One general solution is to place 4 bins from 4 different warps into the same word and place the bins of a thread into the same bank, as Figure 8 shows. For window size N>256 only two uint16 bins are placed in a single word, but otherwise, the same memory structure can be used.

When using histogram-based median filters on CPUs, memory size is not the limiting factor – a 256-byte histogram easily fits into any CPU's L1 cache. On the other hand, searching the histogram may take up to 256 steps in the worst case. For reasonable window sizes (<15*15), this can require much more instructions than the histogram update itself, therefore accelerating the search gives a tremendous performance increase. Several SIMD instruction sets offer horizontal addition, which sums the elements of a single vector, e.g. 16 bins when the vector size is 128 bit. The downside is that the resolution of the resulting "sum of bins" is not one bin, but 16. Therefore, after the accumulated sum of 16 bins is larger or equal to $(N+1)/2$, single bin values should be subtracted until the accumulator becomes smaller than $(N+1)/2$. The bin subtracted, before this condition becomes true, is the median bin. In the worst case, the horizontally vectorized search requires (256/16) vector adds and 16 single bin subtractions, which is 8 times faster than the linear search. For SSE2, horizontal operations are very limited, only the sum-of-absolute–differences can be used to sum 8-8 elements of a 16 element vector. Most other instruction sets (SSE4, AVX, NEON) offer a wider range of horizontal add instructions.

4   Luminance-based Filtering

As it was mentioned earlier, to avoid mixing color planes from different input pixels, color images should be filtered using the luminance component (or a value similar to it). The additional work to be done compared to the grayscale version are the computation of luminance from RGB, and the selection of the full RGB values based on the luminance median value. The former is quite trivial: the input SM is filled with luminance values computed from the RGB components during the SM write. Storing only this value in SM is an appropriate compromise: the full RGB values are used only for computing the luminance value and during the final output RGB write. This degree of redundant read does not justify the memory size which would be required to store the luminance and all the RGB planes in internal memory. Even if only the luminance value is stored, its accuracy has an effect on the memory size required: storing only 8 bits requires similar memory size to the grayscale version, however using more bits doubles the input storage space required. Furthermore, in the case of the histogram-based algorithms, increasing

the accuracy of the luminance value exponentially increases the size of the required histogram memory.

Selecting the full RGB values from the computed luminance median is quite different for the algorithms discussed above.

The Counter based method does not require too much additional computation – searching is similar to the grayscale version with the only difference being that the output of the process is not the luminance value, but the linear index of the register (and thus the pixel) where the median value resides. This index – together with the thread IDs – clearly defines the input pixel, which should be written as an output.

Batcher Odd-Even Merge Sort (and any other algorithm based on min/max computation) can be easily modified by extending the values with the pixel indices. That is, when the luminance value is loaded from SM, a 32-bit value is generated by concatenating the luminance with the x and y pixel coordinates within the filter window. As the luminance is placed on the MSB, adding the indices does not affect the min/max computation. Final RGB values can be loaded based on the indices in the median value and the thread ID.

For the histogram based algorithms, there are two methods implemented. The first one simply compares all the luminance values of the filter window with the resulting median and stores the index of the pixel where the values are similar. This can be done branchless with SETP and SELP instructions. The other method requires an additional index memory. This index memory has as many bins as the LSB histogram and it is written with the pixel index whenever the LSB histogram is updated. When the LSB histogram update is finished, it is certain that the bin corresponding to the median value contains the index of the last pixel equals to the median. As this memory is never cleared, other bins of this index memory may contain outdated data (if multiple pixels are processed by a single thread), but this does not have any influence on the operation.

For the binary search algorithm, the only available option is the complete search method (the first alternative for the histogram based implementation).

5   Performance Results

For the benchmarks below a real-world 20 MPixel (4992x3774) photo was used – the histogram of the grayscale version is shown in Figure 9. With the exception of the histogram based methods, all other algorithms are data independent, thus execution time does not depend on the input data. For the HH version, the worst-case execution time can be measured when every pixel falls into the last bin. In this case, all pixels have to be processed both for the MS and the LS histograms

and the median search takes as many steps as many bins are used. For the vectorized H256 version the worst case is when all pixels are in bin 240 – this is the first bin of the last 16-bin part, so the median search is the slowest in this case. Measurements show that worst-case execution time is ~25% higher than the execution time presented.
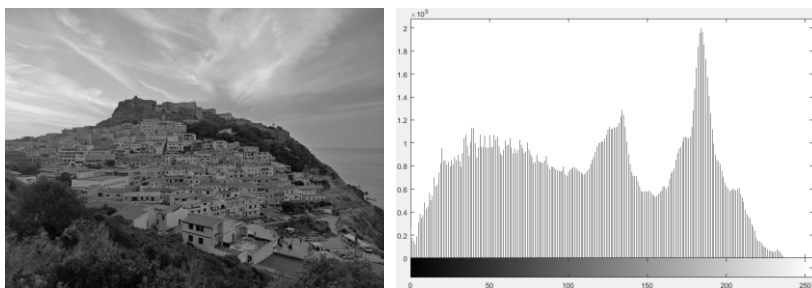

Figure 9

Image and its histogram used for the benchmarks

5.1 GPU Grayscale Results

To our knowledge, the fastest median algorithms for GPUs published to date are the Forgetful selection [4] and Parallel Ccdf-based Median Filter [5] (hereinafter FFUL and PCMF). Although our primary targets are modern desktop and embedded architectures (NVIDIA Maxwell, Pascal), to be comparable with previous work, the grayscale we also benchmarked on a Fermi GPU based Tesla 2070, which is the same card used in the above articles. In their article, the authors benchmarked PCMF for window sizes ranging from 3x3 to 15x15, while FFUL was benchmarked for 3x3, 5x5 and 7x7.

The performance numbers presented in Figure 10 differs from the numbers in the original articles. The mentioned articles measured the time of (host→GPU DMA + kernel runtime + GPU→host DMA) and calculated the MPixel/s numbers from this value, while the results in Figure 10 are calculated from the kernel runtime only. There are multiple reasons to do this. First of all, DMA speed is also affected by the capabilities of the PCIe root complex (chipset). Second, for several GPUs, DMA from/to the host can be overlapped with kernel execution, so as long as data movement takes less time than kernel runtime, it can be eliminated from the full runtime. Third, in the embedded Tegra SoC systems there is no separated GPU memory, therefore there is no need for data copy. For FFUL, kernel runtimes were presented in [4], for PCMF they were calculated by subtracting the two direction DMA times (which were measured with the same board and image size) from the runtimes published in [5].

Using the Tesla 2070, at 3x3 and 5x5 window sizes FFUL is slightly faster than the standard BMS implementation, but the optimized BMS2 has a substantial performance advantage over both. At sizes 7x7 and 9x9 BMS2 is still the fastest, though HH12 (Hierarchical Histogram, one thread computes 12 output pixels) is getting closer because of its lower complexity. The situation changes drastically when the number of registers required by the BMS2 increases too much – performance drops significantly and HH12 becomes the fastest solution for the larger windows. Although it scales worse than PCMF, it is still almost three times as fast even when the window size is increased to 15x15 pixels.
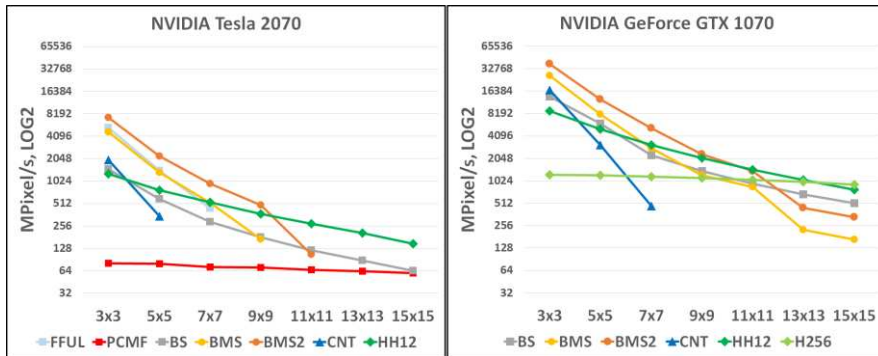
Figure 10
Performance using Tesla 2070 and GeForce GTX 1070

There are notable changes when we use the GTX 1070 with the most recent Pascal architecture (note: FFUL and PCMF were not re-implemented). Due to the increased register count, the larger performance drop of BMS2 happens only at larger window size. On the other hand, SM intensive algorithms also behave better, as the per-SMP SM size is increased from 48 kB to 96 kB, which allows higher occupancy for these implementations. Similarly to the case of the Tesla, the optimized BMS2 implementation is the fastest implementation up to window size 7x7. HH12 already performs on par with it at 9x9, however, the result is data dependent: HH12 can be up to 18% faster than BMS2, or can be up to 17% slower. For larger sizes, HH12 is data-independently faster. Due to the increased SM size, the trivial histogram based implementation (H256) also becomes a viable option – for the largest window size benchmarked, it is even faster than HH12.

Results differ noticeably when the algorithms are executed on NVIDIA's latest embedded GPU which can be found in the Tegra Parker SoC. Similarly to the GTX 1070, this chip is also based on the Pascal GPU architecture, but the SM size was decreased to 64 kB, while the per-SM register size remained the same. The impact is clearly visible in Figure 11: compared to the other solutions, the SM intensive HH4 (Hierarchical Histogram, one thread computes 4 output pixels) algorithm performs slightly worse. BMS2 is clearly the fastest solution up to 9x9

window size and it performs similarly to HH4 at 11x11. As the window size increases further, HH4 becomes the fastest method.
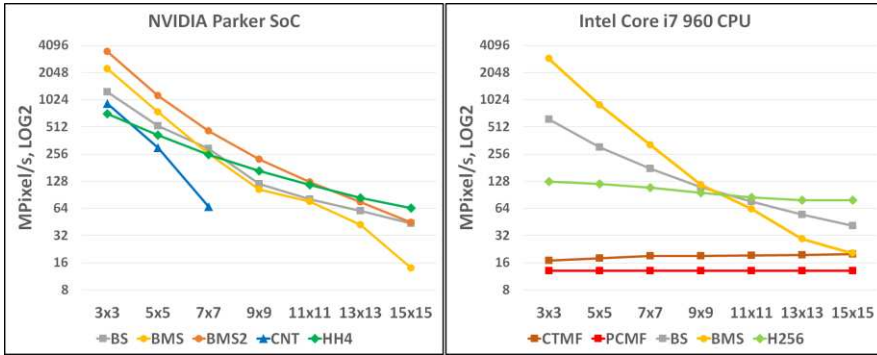

Figure 11
Tegra Parker and Intel Core i7 results

5.2 CPU Grayscale Results

For a complete picture, it is unavoidable to compare GPU filtering performance with CPU filtering performance. In [5] PCMF was also implemented for CPUs and compared to a histogram based O(1) algorithm (Constant Time Median Filtering - CTMF [7]), so these results are included as a reference. As these algorithms are more suitable for very large window sizes, to have comparable results, we have also implemented a multithreaded and vectorized version of BS, BMS, and H256 which takes advantage of Intel's SSE2 instruction set. The benchmarks were run on an Intel Core i7 960 CPU (4 cores, 8 threads, 3.2 GHz frequency, 17 GB/s memory bandwidth), which is similar to the CPUs used in [5], so the results are comparable.

As Figure 11. shows, the trends are quite similar to the GPU results. For window sizes below 11x11, the sorting network based BMS offers the best performance, while for larger windows H256 has the best throughput – at 15x15 it is 4 times as fast as CTMF and 6 times as fast as PCMF.

Conclusions

To give a comprehensive overview about GPU accelerated median filtering, we implemented several algorithms in CUDA and compared them to the fastest published solutions (FFUL, PCMF). BS and BMS are known branchless algorithms, which are good candidates for GPU implementation; CNT is a software implementation of our parallel method developed for FPGAs; BMS2 is our optimized version of the sorting network, while Hierarchical Histogram is our novel algorithm for GPUs. Based on the performance measurements done, we can

make the conclusion: the implementations we presented in the article are the fastest median filter solutions for GPUs. BMS2 offers the highest performance for smaller window sizes; it is faster than the FFUL [4] method even for a window size of 3x3. HH is suitable for larger windows, where it substantially outperforms previously published implementations.

To be able to compare the GPU performance to CPU performance, we also created optimized CPU-based solutions. We can conclude that the easily vectorizable sorting network-based method (BMS) is the fastest implementation up to 9x9 window size, but beyond that our partially vectorized histogram based algorithm becomes faster – at 15x15 window size it is 4 times as fast as the fastest O(1) algorithms published [5] [7].

We should also emphasize the benefits of GPU acceleration in this application. Compared to the CPU, not only the absolute performance is much higher, but also the energy efficiency is outstanding. Even if considering the actual CPU generation approximately doubles the performance per watt ratio, the GTX 1070 board is more than 5 times as efficient as a CPU. The situation is similar in case of the Tegra Parker. Whilst its performance is comparable to the Core i7 960 CPU, there is a huge difference in power consumption: the TDP of the CPU is 130 W, whereas the Tegra consumes less than 10 W.

References

[1]   K. Batcher: Sorting networks and their applications, AFIPS Spring Joint Computer Conference 32, 1968, pp 307-314

[2]   D. E. Knuth. The Art of Computer Programming, Volume 3: Sorting and Searching, Third Edition. Addison-Wesley, 1998. ISBN 0-201-89685-0. Section 5.3.4: Networks for Sorting, pp. 219-247

[3]   P. Szántó, G. Szedő, B. Fehér, Wilson Chung: Scalable architecture for rank order filtering, US Patent 8005881

[4]   G. Perrot, S. Domas, R. Couturier: Fine-tuned high-speed implementation of a GPU-based median filter, Journal of Signal Processing Systems, June 2014, Volume 75, Issue 3, pp. 185-190 [FFUL]

[5]   R. M. Sánchez, P. A. Rodríguez: Bidimensional median filter for parallel computing architectures, 2012 IEEE International Conference on Acoustics, Speech and Signal Processing (ICASSP)

[6]   P. S. Battiato: High Performance Median Filtering Algorithm Based on NVIDIA GPU Computing, International Symposium for Young Scientists in Technology, Engineering and Mathematics, 2016, pp. 1-10

[7]   S. Perreault, P. Hebert: Median Filtering in Constant Time, IEEE Transactions on Image Processing (Vol. 16, Issue 9, Sept. 2007), pp 2389-2394

[8]   M. Kachelrieß: Branchless Vectorized Median Filtering, Nuclear Science Symposium Conference Record (NSS/MIC), 2009 IEEE

[9]   P. Kolte, R. Smith, W. Su: A Fast Median Filter using AltiVec, Computer Design, 1999 IEEE International Conference on Computer Design: VLSI in Computers and Processors

[10]   NVIDIA OpenCL SDK, https://developer.nvidia.com/opencl

[11]   NVIDIA GeForce GTX 1080 Whitepaper, http://international.download.nvidia.com/geforce-com/international/pdfs/GeForce_GTX_1080_Whitepaper_FINAL.pdf

[12]   Intel Intrinsics Guide, https://software.intel.com/sites/landingpage/IntrinsicsGuide/

[13]   ARM NEON Intrinsics Reference, ARM Infocenter, Document IHI 0073A

[14]   B. Shinde, D. Mhaske, A. R. Dani: Study of Noise Detection and Noise Removal Techniques in Medical Images, International Journal of Image, Graphics and Signal Processing, 2012, 4(2):51-60

[15]   H. Zaidi: PET/MRI: Advances in Instrumentation and Quantitative Procedures, An Issue of PET Clinics, Volume 11-2, Elsevier 2016

[16]   H. M. Lodhi, S. H. Muggleton: Elements of Computational Systems Biology, 2010, Wiley

[17]   H. Pinkard, K. Corbin, M. F. Krummel: Spatiotemporal Rank Filtering Improves Image Quality Compared to Frame Averaging in 2-Photon Laser Scanning Microscopy, 2016, PLoS ONE 11(3)

The Impact of Data Representationson Hardware Based MLP Network Implementation

Norbert Ádám, Anton Baláž, Emília Pietriková, Eva Chovancová, Peter Feciľak

Faculty of Electrical Engineering and Informatics
Technical University of Košice
Letná 9, 042 00 Košice, Slovak Republic
norbert.adam@tuke.sk, anton.balaz@tuke.sk, emilia.pietrikova@tuke.sk, eva.chovancova@tuke.sk, peter.fecilak@tuke.sk

Abstract: Artificial neural networks are massively parallel systems containing large amounts of simple computing elements. Therefore, it is natural to try to implement them using parallel computing architectures. This paper deals with an implementation of a three layer multilayer perceptron artificial neural network. It summarises the impact of using various forms of data representation on the performance of the hardware implementation – a Kintex-7 XC7K325T-2FFG900C FPGA chip on a Xilinx Kintex KC705 board.

Keywords: fixed-point; floating-point; mlp; neural network; residue number system

1   Introduction

Artificial neural networks belong to the category of massively parallel architectures. Therefore, it is natural to try to implement these structures – interalia –as ASIC circuits (a notable example of this being the NI1000 architecture [1]), the CogniMem CM1K chip [2] or the SyNAPSE [3] chip with a brain-inspired non-von Neumann computer architecture with a million neurons and 256 million synapses. Most solutions provide high performance for the cost of lower flexibility. The change of structure of an artificial neural network (such as the number of neurons, the applied algorithm, etc.) requires to create a new block design, meeting the requirements for artificial neural networks [4]. Currently, significant effort is being invested in the implementations of artificial neural networks on re-configurable computer platforms [5]. The term 're-configurable' refers to the capability of achieving the required system properties [6] beyond those of the conventional architectures (such as the von-Neumann architecture).

Field Programmable Gate Arrays (FPGA) belong to the category of re-configurable hardware. They allow to designlogic circuits similarly to the way that programmers write programs and their performance is comparable to the performance of application-specific integrated circuits (ASIC).

When implementing artificial neural networks in FPGA chips, one has to take the limiting factors of this implementation into account. This factor is the relationship between area and precision. The issue is that greater precision requires a higher number of logical structures required for their implementation. Precision itself is a very important factor of the speed of convergence of the artificial neural network to the desired output. Single precision representation of numbers provides sufficient precision (i.e. in terms of minimal quantization error and minimal misclassification rate); however, due to the limited hardware resources of FPGA chips, it is less efficient than in case of fixed point numbers.

2   Multilayer Feedforward Networks

The basic architecture of the multilayer perceptron (MLP) feedforward artificial neural network consists of three layers of neurons: the input, hidden and output layers. In feedforward networks, the signal is led from the input of the unit to the output strictly only forward.

2.1   Structure of Feedforward Multilayer Artificial Neural Networks

Feedforward multilayer neural networks belong to the artificial neural networks, which are used most often as universal means of classification and prediction. A three-layer neural network (containing at least one layer of hidden neurons) can simulate an arbitrary function F of type

$$F\colon \mathbb{R}^n \to \,]0,1[\tag{1}$$

where F is a continuous function with the projection of n dimensional space $\mathbb{R}^n$ to the $]0,1[$ open interval.

With this, we have a universal tool for performing both regression analysis of functions defined by a training set and for extrapolation of functional values beyond the training set, i.e. a tool to solve generalisation problems (prediction and classification).

2.2   Backpropagation

The backward propagation of errors, or backpropagation (BP) proposed by Rumelhart, et al. [7], is a common method of training artificial neural networks and used in conjunction with an optimization method such as gradient descent.

The algorithm consists of two phases (Fig. 1): The forward phase where the activations are propagated from the input to the output layer, and the backward phase, where the error between the observed actual and the requested nominal value in the output layer (desired output) is propagated backwards in order to modify the weights and bias values.

The pseudocode of the algorithm is as follows:

```
Assign all network inputs and output
    Initialize network weights (small random values, typically between -1 and 1)
        do
            for every pattern in the training set
                Present the pattern to the network
                    //Propagated the input forward through the network:
                    for each layer in the network
                        for every node in the layer
                                1. Calculate the weight sum of the inputs to the node
                                2. Add the threshold to the sum
                                3. Calculate the activation for the node
                            end
                    end
                    //Propagate the errors backward through the network
                    for every node in the output layer
                        calculate the error signal
                    end
                    for all hidden layers
                        for every node in the layer
                                1. Calculate the node's signal error
                                2. Update each node's weight in the network
                        end
                    end
                    //Calculate Global Error
                        Calculate the Error Function
                end
        end
    while ((maximum number of iterations < than specified) AND (Error Function is > than specified))
```

Figure 1

Back-propagation algorithm

2.3   Activation Function

The individual neurons of the artificial neural networks use activation functions to calculate their own activation (i.e. output value). The argument of the activation function is the sum of the products of the weights and the outputs of the neurons of the preceding layer (or layers), connected to the particular neuron. In the

available literary sources, one may find multiple applicable activation functions. The choice of the activation function may significantly influence the speed of the learning phase. The choice of the activation function depends on the type of the task we want to solve by using the artificial neural network. For the purpose of the BP we may use functions, for which a first order derivative of the activation function may be produced. In this paper we decided to use the logistic function, the derivative of which is defined as $y' = f'^{(x)} = y \times (1 - y)$. This is the most commonly used soft-limiting activation function. Because it squashes the input range into $]0,1[$ output range.

3 Configuration of the Applied Artificial Neural Network

In addition to the applied target technology and platform, the overall performance of the artificial neural network is significantly influenced also by the applied algorithm, the form of data representation and the applied data structures. In this paper, when determining the overall performance of the proposed architecture, we will start out from the overall cost of implementing one forward and one backward phase of neural network training per epoch. For the configuration of the neural network, see Table 1.

The implemented neural network is aimed at the recognition of handwritten numbers, based on the MNIST database (Fig. 2). The MNIST database of handwritten digits has a training set of 60,000 samples (one epoch), and a test set of 10,000 samples. The digits have been size-normalized and centered in a fixed-size image.

The size of the individual figures – numbers ranging from 0 to 9 – is 28×28 pixels. Pixels are organized row-wise. Pixel values are 0 to 255. 0 means background (white), 255 means foreground (black). Figure 2 shows a sample of handwritten digits.

The pixel inputs were normalised into a $[2^{-6}; 1 - 2^{-6}]$ closed interval. The normalisation interval – other than $[0; 1]$ – was selected due to the applied activation function (sigmoid), the range of which is defined for the $]0; 1[$ open interval. These normalised values were then used as input values of the input layer neurons. The required output values were also subjected to normalisation. The output layer consisted of 10 neurons, representing digits 0 to 9.

We used one-hot encoding, i.e. only a single neuron shall have the maximum value of $1 - 2^{-6}$, the other neurons will be set to the lowest value 2^{-6}, since the extreme values of 0 and 1 were otherwise unachievable, due to the sigmoid function.

Figure 2

MNIST digits (illustration)

The error function for training pattern p is given by

$$E_p = \frac{1}{2}\sum_k \left(d_{p,k} - y_{p,o,k}\right)^2 \tag{2}$$

where $d_{p,k}$ is the target output, and $y_{p,o,k}$ is the output layer output. If the error is 0.125 per output unit, the pattern error becomes

$$E_p = \frac{1}{2}\sum_{k=1}^{10} \left(0.125\right)^2 = 0.078125 \tag{3}$$

And this value was used as a threshold for determining if a pattern is trained or not. Weight change values were accumulated for a pattern p having $E_p > 0.078125$, whereas a pattern is trained when $E_p \leq 0.078125$.

Table 1

Configuration of the artificial neural network

Number of layers	1 input layer, 1 hidden layer, 1 output layer
Connection of neurons between the hidden layers	Full connection
Number of neurons in the input layer	$28 \times 28 = 768$ neurons
Number of neurons in the hidden layer	500 neurons
Number of neurons in the output layer	10 neurons
Activation function applied to the neurons of the input layer	Linear mapping $y = f(x)$
Activation function applied to the neurons of the hidden and output layer	Sigmoid $y = f(x) = 1/\left(1 + e^{-x}\right)$
Activation function applied to the neurons of the output layer	Sigmoid $y = f(x) = 1/\left(1 + e^{-x}\right)$

4 Hardware Implementation of the Network

When designing the hardware, multiple aspects influencing the design have to be taken into account [8], [9]. These aspects are related to the structure of the artificial neural network, data representation, the set of operations, which have to be supported by the hardware [10], the choice and the method of implementation of the activation function, the method of storing and updating the data in the network and the algorithm used when training/testing the network [11].

Of the above aspects, the performance of the neurohardware is affected especially by the method of implementing the set of operations used in the learning phase of the network and the activation function. The implementation per se is affected also by the representation of the operands [12].

4.1 Floating Point Representation

Since the task described in section 3 deals with real numbers, it is natural to use floating point representation for the operands. In digital computers, real numbers are represented in accordance with standard IEEE-754, which defines three formats: single precision format (32-bit), double precision format (64-bit) and extended double format (80-bit).

The standard implementation of artificial neural networks uses the 32-bit floating point representation of data – the float data type. The advantage of the representation pursuant to standard IEEE-754 is the wide range of represented real numbers. The disadvantage is the inaccuracy of the real number representation. It's important to note that precision is about how exactly we can specify it (i.e. machine precision) an accuracy is about how close a value is to what it is meant to be; moreover, it is influenced by the applied rounding technique. A further disadvantage of the representation of real numbers pursuant to standard IEEE-754 is the time cost of implementation of the arithmetic operations.

4.2 Fixed Point Representation

Fixed point representation is used to represent real numbers in the way known from the decimal number system, ±integerPart.fractionalPart.

When using a binary number system, we let IP be the number of bits used to represent the integer part, including the sign bit. Let FP be the number of bits assigned to represent the fractional part of the number. Then, the total number of bits used to represent the real number may be expressed as $W = IP + FP$. The range of numbers equals to $- [-2^{IP-1}, 2^{IP-1} - 2^{-FP}]$, while machine precision ε equals to 2^{-FP} ($ulp = 2^{-FP}$).

There are numerous forms of notation applicable to the fixed point number representation. In this paper, we will use the Qw.i notation. In this notation, *w* represents the word length in bits, *i* is the number of bits used to represent the integer value. For example, Q32.9 describes a number with 9 integer bit and 23 fractional bits stored as a 32-bit 2's complement integer.

The disadvantage of the fixed point representation lies in the significantly lower range of numbers, which may be represented using this format, in comparison with the floating point representation, when using the same number of bits for representation. The advantage of the fixed point representation is that we may use integer arithmetic to implement operations on real numbers, which positively influences the requirements on hardware resources.

An interesting data representation category is the residue number system.

4.3   Residue Number System

Data representations described above employ a linear and positional number system, where the value of each symbol is influenced by the radix of the number system and the position of the symbol in the symbol series. Another group of numerical value representations are non-positional number systems. A significant non-positional number system is the residue number system.

If *q* and *r* are the quotient and remainder, respectively, of the integer division of *a* by *m*, that is, $a = q.m + b$, then, by definition, we have a ≡ b (mod m). The number *b* is said to be the residue of *a* with respect to *m*, and we shall usually denote this by $r = |a|_m$. The number *m* is a modulus (aka base). The set of *m* smallest values, $\{0, 1, 2, \ldots, m - 1\}$, that the residue may assume is called the set of least positive residues modulo *m*.

For example, numbers of the set $\{1, 3, 5, 7, \ldots, 2i + 1\}$ belong to the residue class mod 2, while for an arbitrary couple of numbers (a, b) of this set, the following applies: a ≡ b (mod 2).

Let $\{m_1, m_2, m_3, \ldots, m_N\}$ be a set of *N* pairwise relatively prime moduli. Let their product be *M*, i.e. $M = \prod_{i=1}^{N} m_i$. Then every number $X < M$ has a unique representation in the residue number system, which is the set of residues $\{|X|_{m_i} : 1 \leq i \leq N\}$. The number *M* is called the period (aka dynamic range) of the RNS, because the number of numbers that can be represented is *M*. For unsigned numbers, that range is [0, M-1]. For example, the decimal number *X*, represented in the conventionally weighted number system as *X* = 23 may be expressed as $\langle 1, 2, 3 \rangle_{2,3,5}$ in a system with a period of *M = 30* ($m_1 = 2, m_2 = 3, m_3 = 5$), where 1 is the result of the operation *X mod 2*, 2 is the result of the operation *X mod 3*, while 3 is the result of the operation *X mod 5*. Representations in a system in which the moduli are not pairwise relatively prime will be not be unique: two or more numbers will have the same representation (Tab. 2)

Number conversion to RNS and from RNS, the standard arithmetic operations of addition/subtraction and multiplication are easily implemented [13], depending on the choice of the moduli, but division is much more difficult.

In the error backpropagation algorithm, the operation of division is used only when evaluating the logical activation function. For the implementation of the activation function we used an approximation, eliminating the need of performing a division.

Table 2

The result of comparing in pairs with the final result

N	pairwise relatively prime moduli		relatively non-prime moduli	
	$m_1 = 2$	$m_2 = 3$	$m_1 = 2$	$m_2 = 4$
0	0	0	0	0
1	1	1	1	1
4	0	1	0	0
5	1	2	1	1

5   Neural Network Blockset Design

In this work, we decided to implement the artificial neural network on an FPGA chip. The following chapter contains the list of related works (partially in chronological order), aimed at the implementation of artificial neural networks in hardware.

5.1   Related Works

In [14], the authors researched whether FPGA chips were appropriate for speeding-up floating point calculations. They came to the following conclusion: „...*if we can achieve comparable performance from a pure floating-point application, it is a good indication that applications which require a few floating point operations intermixed with fixed-point computations can now be considered as implementation targets for reconfigurable computing. Furthermore, these results indicate that if device density and speed continue to increase, reconfigurable computing platforms may soon be able to offer a significant speedup to pure floating-point applications*".

Iwata, et al. [15] implemented a BP algorithm using a 24 bit floating point number representation.

The paper written by Holt & Hwang suggests, that an 8 and 16-bit number representation is sufficient for the implementation of BP in hardware [16].

For MLP networks using the BP algorithm, Holt and Baker [17] pointed out that in fixed point number representations, 16 bits are the least to maintain functionality of the network, on condition of normalising the input data to the interval [0,1] and using a sigmoid activation function.

Hammerstrom [18] proposed a neuro-architecture based on an 8 to 16-bit fixed point representation.

Aibe, et al. [19]implemented a probabilistic neural network (PNN). They used floating point representation of operands.

The ASIC implementation of an MLP network using floating point representation for weights and biases is the work of Ayela, et al. [20].

Moussa. et al. demonstrated implementations of MLP on FPGAs using fixed and floating point representations [21].

Wang, et al. [22] proposed a re-configurable architecture for the VLSI implementation of the BP algorithm based on systolic fields.

The authors of [23] focused on the efficient implementation of multiplication in a Maxout network. They trained a set of state-of-the-art neural networks (Maxout networks) on three benchmark datasets: MNIST, CIFAR-10 and SVHN. During the training, they used the following number representations: Goodfellow, et al. Format [24] (32 bits for propagations, 32 bits for parameter updates), single precision floating point (32 bits for propagations, 32 bits for parameter updates), half precision-floating point (16 bits for propagations, 16 bits for parameter updates), Fixed point (20 bits for propagations, 20 bits for parameter updates) and dynamic fixed point (10 bits for propagations, 12 bits for parameter updates). For each of those datasets and for each of those formats, they assess the impact of the precision of the multiplications on the final error after training. The authors of this work came to the conclusion that it is possible use a lower precision number representation not only during the life phase of the network, but also during the training phase. For example, their results achieved on the Startix V Altera FPGA chip suggest that a 10 bit number representation for propagation and a 12-bit representation for the parameter updates of the Maxout network are sufficient.

Gupta, et al [25] studied the effect of limited precision on neural network training and proposed a Xilinx Kintex325T FPGA based hardware accelerator. Their results showed that deep networks could be trained using only 16-bit wide fixed-point number representation with stochastic rounding.

Park & Sung, et al. [26] developed an FPGA based fixed-point deep neural network (DNN) system using only on-chip memory. They used Xilinx XC7Z045 for the implementation. They tested the solution to recognise MNIST handwritten digits. Due to the memory limitations, they used fixed pointrepresentation for data, 3 bits for the input and hidden layers, 8 bits for the output layer, more sensitive to quantisation.

In [27], the authors proposed a roofline-model-based method for FPGA acceleration of convolutional neural networks. In this method they first optimize CNN's computation and memory access. For data representation, they used 32-bit floats. They implemented the design using the Vivado HLS (v2013.4) environment on a Xilinx VC707 board.

Nakahara & Sasao [28] proposed a hardware implementation of a deep convolutional neural network (DCNN), based on a residue number system. Since the 2D convolutional operation performs massive multiply-accumulation, they propose to use nested RNS (NRNS), which recursively decompose the RNS. In the DCNN using the NRNS, a 48-bit multiply-accumulation unit is decomposed into 4-bit ones realized by look-up tables of the FPGA. The DCNN using the NRNS was implemented on a Xilinx Virtex VC707 evaluation board.

6   Our Proposal

The FPGA (Field Programmable Gate Array) is a kind of logical integrated circuits. It is a programmable gate array used to design digital systems [29]. FPGAs have a wide variety of uses [30]. The main idea is the use of programmable logic elements to perform simple logical functions. These elements are called look-up tables (LUTs) – they may perform arbitrary logical functions with a specific number of inputs and a single output.

Currently, there are many FPGA vendors. Xilinx, Altera, Actel and Atmel belong to the most popular. The FPGA structure depends on the vendor; however, the idea behind the FPGA remains the same – to use a logical block array based on look-up tables and registers. In this work, we used the Xilinx Kintex KC705 development board as an implementation platform.

In the sections below, we describe the implementation of a MLP network with error backpropagation in a Kintex-7 XC7K325T-2FFG900C FPGA chip [31], utilising a Xilinx Kintex KC705 [32] board.

The structure of the proposed neuro-accelerator is depicted in figure 3. In addition to the proposed (*ffnn*) IP module, the proposed hardware contains supporting components necessary for the following: to control the input and output of the IP module (microblaze_0 : MicroBlaze soft processor), to connect the *ffnn* module with the soft processor (microblaze_0_axi_periph : AXI Interconnect), to control interrupts (microblaze_0_axi_intc : AXI Interrupt Controller), to access memory (axi_dma_0 : AXI Direct Memory Access), module to control access to DDR3 SDRAM memory (mig_7series_0 : Memory Interface Generator), to measure the time required to perform the operations both on the soft processor and on the proposed module (axi_timer_0 : AXI Timer), to provide console access to the

system (axi_uartlite_0 : AXI Uartlite), a debugging module (mdm_1 : MicroBlaze Debug Module) and a local MicroBlaze memory (microblaze_0_local_memory).
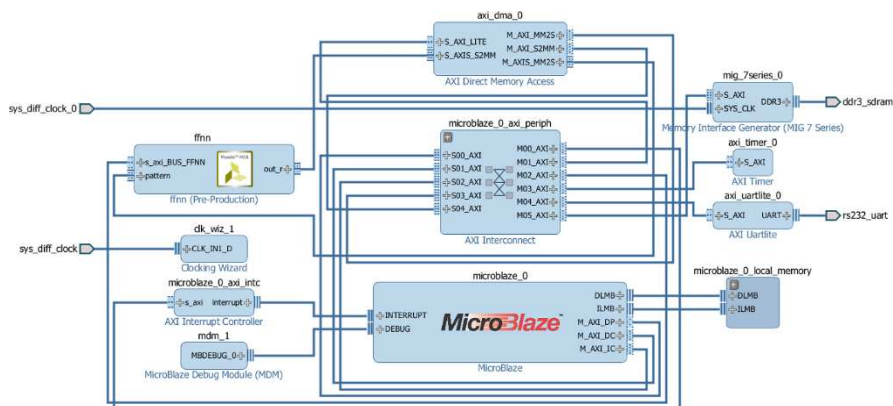

Figure 3
The NeuroAccelerator

6.1   Implementation using Floating Point Representation

Decreasing / increasing the number of bits used for number representation decreases / increases accuracy of the calculations [33]. The minimum bit count necessary to represent the numerical information – while maintaining the necessary level of accuracy and the meeting requirement of convergence of the artificial neural network to the solution – is significantly influenced by the type of the artificial neural network and its algorithm.

In this work, we used an MLP network with error backpropagation. We performed two experiments with the aim to find out the impact of using float and double data types on the overall performance of the artificial neural network.

For the purpose of implementing error backpropagation, we used the "Vivado(TM) HLS – High-Level Synthesis from C, C++ and System C Version 2016.3" tool. The source code of the hardware structure was created in C++. In the first experiment, we used the float (32-bit) data type. A summary of the results of the experiment is available in Table 3.

When using the float data type, due to the memory requirements of the algorithm and the resources of the FPGA chip available for the implementation of this IP, we could use at most 300 neurons in the hidden layer. The remaining hardware resources were used for the implementation of the support components of the chip. The misclassification rate for a network with this configuration, using the test set of 10,000 patterns was 3.76%.

Table 3

Hardware utilization of FFNN for data type Float

Timing [ns]	Hidden Layer [neurons]	BRAM_18K	DSP48E	FF	LUT
8.61 (116MHz)	200	525 (58%)	75 (8%)	8596 (2%)	88011 (43%)
	250	533 (59%)	75 (8%)	8604 (2%)	107227 (52%)
	300	533 (59%)	75 (8%)	8627 (2%)	126487 (62%)
	350	1045 (117%)	75 (8%)	8638 (2%)	145703 (71%)

In our second experiment we tried to find out: the impact of using the double data type on the network configuration; the performance of the hardware implementation; and the achievable misclassification rate. A summary of the results of the experiment is available in Table 4.

Table 4

Hardware utilization of FFNN for data type Double

Timing [ns]	Hidden Layer [neurons]	BRAM_18K	DSP48E	FF	LUT
8.68 (115MHz)	100	528 (59%)	158 (18%)	12583 (3%)	91477 (44%)
	150	536 (60%)	158 (18%)	12613 (3%)	129928 (63%)
	200	1048 (117%)	158 (18%)	12624 (3%)	168347 (82%)

In this case, the maximum number of neurons in the hidden layer was set to 150 neurons. The remaining hardware resources were used for the implementation of the support components of the chip. The misclassification rate for a network with this configuration amounted to 4.51%.

6.2   Implementation using Fixedpoint Representation

In this phase of the design we tried to find out what was the lowest bit count required to sufficiently train an MLP network, using floating point decimal data representation.

A summary of the results is available in the chart above (Fig. 4) – from this it is evident that up to 17 bits, the misclassification rate stays below 5%. Beyond this level, the misclassification rate grew fast. Another finding of the experiment was that when using 300 hidden neurons, the integer part of the fixed point representation did not exceed the value of 2. Therefore, in this implementation, we started out from the data representation using the Q17.2 two's complement form.
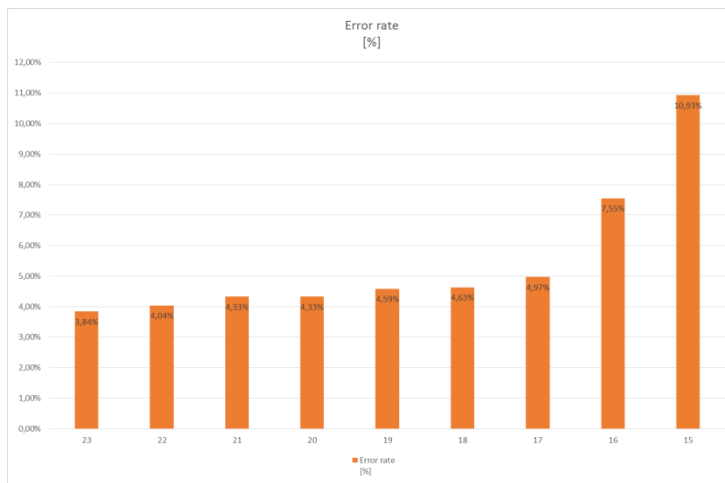
Figure 4

Misclassification rate

The overall hardware implementation costs are available in Table 5.

Table 5

Hardware utilization of FFNN for data type Q17.2

Timing [ns]	Hidden Layer [neurons]	Name	BRAM_18K	DSP48E	FF	LUT
8.58 (116MHz)	300	Utilization	555 (62%)	48 (5%)	5926 (3%)	11749 (5%)

The misclassification rate for a network with this configuration, using the test set of 10,000 patterns was 4.97%.

6.3 Implementation using the Residue Number System

Based on the results of the fixed pointdata representation experiment, we found that the lowest number of bits, which may be used to train the network with a misclassification rate below 5% was 17 bits. We used this information when implementing the *ffnn* IP module, based on calculations using the residue number system. As it is known, the operations of addition, subtraction and multiplication can be easily implemented in residue number systems. Due to the character of the residue number system and the aforementioned operations, these operations do not require carrybit propagation, therefore their execution is faster than the execution of these operations using fixed point number representation. Summaries of the time characteristics of selected mathematical operations using the residue number system and in a positional binary system were presented in [34].

However, division and comparison are more complex in this system. In the error backpropagation algorithm, the operation of division is used only to calculate the value of the logistic function. In the next chapter, we describe the solution to eliminate division from the error backpropagation.

6.3.1   Activation Function Implementation

It is important to note that the performance and precision of networks depend on the efficient implementation of the activation function on FPGA chips [35]. In MLP networks, the most common activation function is the sigmoid function. Direct implementation of sigmoid activation function on FPGA is difficult due to its division and exponential function. The operation of division and the implementation of an exponential function are time-consuming; moreover, they require also significant hardware resources [36].

According to [37], to decrease the requirements hardware resources and the time necessary to evaluate the function, the following may be used: uniform lookup table methods (LUT), linear approximation methods, piecewise linear approximation method (PWL), piecewise linear approximation of a nonlinear function (PLAN) approximation, A-law approximation, Allipi and Storti-Gajani approximation, piecewise second-order approximation and lookup table method with linear interpolation method. Compared to the approximation methods, solutions using LUT provide high speed, though at a cost of higher memory requirements.

Approximation methods have lower memory requirements. When combined with fixed point number representation, the speed differences are not as significant in comparison with the LUT methods [38].

In our proposal, we used the PLAN approximation of the sigmoid activation function, as published in [38]. To increase speed, we used only first-order functions for the approximation. The approximation of the function output was based on the evaluation of a linear function, used for the approximation of the sigmoid in a defined interval of input values (Table 6). We have set the coefficients with a precision of $ulp = 2^{-12}$.

Table 6

PLAN approximation of sigmoid activation function

Interval	Function Form	Absolute approximation error
$[2; 3[$	$y = f(x) = 0.07110596 * x + 0.74377441$	0.0051893
$[1; 2[$	$y = f(x) = 0.14950562 * x + 0.58935547$	0.0078025
$]-1; 1[$	$y = f(x) = 0.23828125 * x + 0.50000000$	0.0072125
$[-2; -1]$	$y = f(x) = 0.14950562 * x + 0.41058350$	0.0078635
$[-3; -2[$	$y = f(x) = 0.07110596 * x + 0.25610352$	0.0053031

6.3.2   Choice of the Residue Number System Parameters

The error backpropagation algorithm uses addition and multiplication operations. In the binary positional system, the result of adding two *n* bit numbers is a sum having at most *n+1* bits, the result of their multiplication is the product having *2n* bits. In a residue number system, carrybit propagation does not occur. The range and the precision of the calculation are functions of the period*M*. In the previous section we showed that when using 17 bits (1b sign + 16b modulus), the misclassification rate remains under 5%. The result of the multiplication of two 17-bit signed numbers is a 34-bit number (1b sign + 33b modulus).

To cover the required range of 34-bit signed numbers, we used the R residue number system with moduli $\{11,23,31,73,89,127,128\}$. Note that these moduli have to be pairwise relatively prime. The system period is $M = 828340264576,$, i.e. $M > 2^{34}$.

When transforming a binary number in fixed pointnumber representation Q17.2 to the residue number system, we used the properties of addition and multiplication in the residue number system. The following example shows the procedure of transforming a binary number into the R system with the set of moduli $\{5,7\}$.

Example: Consider the system R with the set of moduli $m_1 = 5, m_2 = 7$. M = 35. Let $X = (26)_{10}$. Then, by using binary decomposition: $X = 1 \times 2^4 + 1 \times 2^3 + 1 \times 2^1$ Moreover: $X =_R \langle 1 \times 2^4 + 1 \times 2^3 + 1 \times 2^1 \rangle = \langle 1 \times 2^4 \rangle + \langle 1 \times 2^3 \rangle + \langle 1 \times 2^1 \rangle = \langle 1 \rangle \times \langle 2^4 \rangle + \langle 1 \rangle \times \langle 2^3 \rangle + \langle 1 \rangle \times \langle 2^1 \rangle$ Thus $X =_R \langle |1|_5 \times |2^4|_5 + |1|_5 \times |2^3|_5 + |1|_5 \times |2^1|_5, |1|_7 \times |2^4|_7 + |1|_7 \times |2^3|_7 + |1|_7 \times |2^1|_7 \rangle = \langle 1 \times 1 + 1 \times 3 + 1 \times 2, 1 \times 2 + 1 \times 1 + 1 \times 2 \rangle = \langle |6|_5, 5 \rangle = \langle 1,5 \rangle$.

6.3.3   Implementation of BP Algoritm in Residue Number System

Residue number systems do not have metrics. Therefore, the comparison of two numbers represented in such a system is time-consuming. When comparing numbers, we may first transform the residue number system representation to a positional system, perform the comparison or – under certain circumstances – the comparison may be performed also by subtracting the two numbers and determining the sign of the operation [39]. Further algorithms are available in [13].

Table 7

Hardware utilization of FFNN for RNS R with moduli set $\{11,23,31,73,89,127,128\}$

Timing [ns]	Hidden Layer [neurons]	Name	BRAM_18K	DSP48E	FF	LUT
8.18 (122MHz)	300	Utilization	500 (56%)	336 (40%)	38519 (9,4%)	145337 (71%)

We chose to use the reverse transformation to a binary number system. The overall hardware implementation costs are available in Table 7.

With this solution, the misclassification rate amounted to 4.01%.

6.4   Comparison of the Solutions

We compared our solution with an implementation running on a desktop computer with an Intel(R) Core(TM) i7-4790 CPU @ 3.60GHz processor. In this paper, when determining the overall performance of the proposed architecture, we will start out from the overall cost of implementing one forward and one backward phase of neural network training per epoch.The results are available in Table 8.

If the sole criterion of performance is the speed of data training, the winner is the Desktop CPU. However, if we consider also energy efficiency, the winner is the MLP network implementation running on an FPGA chip. If we require higher overall recognition precision, the binary positional system using the float data type is a good candidate for representing data in the network, otherwise the use of a fixed pointnumber representation is advisable.

The residue number system falls back behind the solution using fixed pointnumber representation in terms of speed; however, it's misclassification rate is lower.

Table 8

Comparison of the solutions with an Intel i7-4790 CPU

	Clock frequency [MHz]	Power Consumption [W]	Timing (1 epoch, 1 iter) [s]	Overall Error-rate (requested < 5%)
Desktop CPU (float)	3.60GHz	84 (TDP)	28	3,76%
FPGA – float	116MHz	3.569	37	3,76%
FPGA – double	115MHz	7.298	52	4,51%
FPGA – fixed	116MHz	3.123	30	4,97%
FPGA – RNS	122MHz	4.560	36	4.01%

Conclusions

This paper deals with the implementation possibilities of multilayer neural networks aimed at the recognition of handwritten digits. The applied neural network belongs to the artificial neural networks with supervised learning. We used the error backpropagation algorithm as the training algorithm. The training and testing set was taken from the MNIST database. As the target platform for the hardware implementation, we used a Kintex-7 XC7K325T-2FFG900C FPGA chip on a Xilinx Kintex KC705 board. We researched the impact of the choice of number representation (floating point vs. fixed point decimal representation), the impact of the number of bits used to represent the numbers in fixed point notation

and the choice of the number system (conventionally weighted positional number system vs. residue number system) on both the utilisation of hardware resources and the neural network performance (training speed and misclassification rate). A summary of our findings is available in Table 8.

Acknowledgement

References

[1]   M. Perron and L. Cooper, "The Ni1000: High Speed Parallel VLSI for Implementing Multilayer Perceptrons," 1995.

[2]   K. Berkolds, "Image Recognition with Hardware Neural Networks," in *Engineering for Rural Development*, Jelgava, Latvia, 2016.

[3]   S. Esser, A. Alexander, R. Appuswamy, P. Datta, D. Barch, A. Amir, J. Arthur, A. Cassidy, M. Flickner, P. Merolla, S. Chandra, N. Basilico†, S. Carpin†, T. Zimmerman, F. Zee, R. Alvarez-Icaza, J. Kusnitz, T. Wong, W. Risk and McQui, "Cognitive computing systems: Algorithms and applications for networks of neurosynaptic cores," in *2013 International Joint Conference on Neural Networks (IJCNN)*, Dallas, 2013.

[4]   J. Ban, M. Féder, M. Oravec and J. Pavlovičová, "Non-Conventional Approaches to Feature Extraction for Face Recognition," *Acta Polytechnica Hungarica,* vol. 8, no. 4, 2011.

[5]   R. Lovassy, L. T. Kóczy and L. Gál, "Function Approximation Performance of Fuzzy Neural Networks," *Acta Polytechnica Hungarica,* vol. 7, no. 4, 2010.

[6]   G. Györök, "Reconfigurable Control in Robust Systems by FPAA," in *Intelligent Systems and Informatics, 2008: Proceedings of SISY 2008, 6th International Symposium.*, Subotica, Serbia, 2008.

[7]   D. Rumelhart, G. Hinton and R. Wiliams, "Learning internal representations by error propagation," in *Parallel distributed processing: explorations in the microstructure of cognition*, vol. 1, D. Rumelhart and J. McClelland, Eds., MA, USA, MIT Press Cambridge, MA, USA, 1986, pp. 318-362.

[8]   Š. Hudák, Š. Korečko and S. Šimoňák, "Reachability analysis of time-critical systems," in *Petri Nets Applications*, InTech, 2010, pp. 253-280.

[9]   M. Novák and M. Biňas, "An architecture overview of the smart-home

system based on OSGi," in *SCYR 2011*, Herľany, 2011.

[10] L. Vokorokos, B. Madoš, A. Baláž and N. Ádám, "Architecture of Multi-Core Computer with Data Driven Computation Model," *Acta Electrotechnica et Informatica,* vol. 10, no. 4, pp. 20-23, 2010.

[11] L. Vokorokos, N. Ádám and A. Baláž, "Training Set Parallelism In Pahra Architecture," *Acta Electrotechnica et Informatica,* vol. 7, no. 3, pp. 1-6, 2007.

[12] F. Silváši and S. Šimoňák, "Architecture Dependent Program Optimizations," in *Electrical Engineering and Informatics 4: Proceeding of the Faculty of Electrical Engineering and Informatics of the Technical University of Košice*, Košice, 2013.

[13] A. Omondi and B. Premkumar, Residue Number Systems : Theory and Implementation, Advances in Computer Science and Engineering: Texts – Vol. 2 ed., vol. 2, London: Imperial College Press, 2007.

[14] W. Ligon III, S. McMillan, G. Monn, K. Schoonover, F. Stivers and K. Underwood, "A Re-evaluation of the Practicality of Floating Point Operations on FPGAs," in *IEEE Symposium on FPGAs for Custom Computing Machines*, 1998.

[15] A. Iwata, Y. Yoshida, S. Matsuda, Y. Sato and N. Suzumura, "An artificial neural network accelerator using general purpose 24 bit floating point digital signal processors," in *International 1989 Joint Conference on Neural Networks*, 1989.

[16] J. L. Holt and J. N. Hwang, "Finite-precision error analysis of neural network hardware implementations," *IEEE Transactions on Computers,* vol. 42, no. 3, p. 280–290, 1993.

[17] J. L. Holt and T. Baker, "Backpropagation simulations using limited precision calculations," in *Proc. of International Joint Conference on Neural Networks (IJCNN-91)*, Seattle, WA, USA, 1991.

[18] D. Hammerstom, "A highly parallel digital architecture for neural network simulation," in *VLSI for Artificial Intelligence and Neural Networks*, J. Delgado-Frias and W. Moore, Eds., Plenum Press, 1991.

[19] N. Aibe, M. Yasunaga, I. Yoshihara and J. H. Kim, "A probabilistic neural network hardware system using a learning-parameter parallel architecture," in *Proceedings of the International Joint Conference on Neural Networks (IJCNN '02)*, Honolulu, Hawaii, 2002.

[20] J. L. Ayala, A. G. Lomeña, M. López-Vallejo and A. Fernández, "Design of a

pipelined hardware architecture for real-time neural network computations," in *Proceedings of the 45th Midwest Symposium on Circuits and Systems (MWSCAS '02)*, Tulsa, Okla, USA, 2002.

[21] M. Moussa, S. Areibi and K. Nichols, "On the arithmetic precision for implementing back-propagation networks on FPGA: a case study," in *FPGA Implementations of Neural Networks*, Berlin, Germany, Springer, 2006, pp. 37-61.

[22] Q. Wang, A. Li, Z. Li and Y. Wan, "A Design and Implementation of Reconfigurable Architecture for Neural Networks Based on Systolic Arrays," in *Advances in Neural Networks*, Lecture Notes in Computer Science ed., vol. Vol 3973, Berlin, Heidelberg, Springer, 2006.

[23] M. Courbariaux, J.-P. David and B. Y., "Training Deep Neural Networks With Low Precision Multiplications," *arXiv e-prints,* vol. 1412.7024, 2014.

[24] I. J. Goodfellow, D. Warde-Farley, M. Mirza, A. Courville and Y. Bengio, "Maxout networks," Universite de Montreal, 2013.

[25] S. Gupta, A. Agrawal, K. Gopalakrishnan and P. Narayanan, "Deep learning with limited numerical precision," in *Proc. of the 32nd International Conference on International Conference on Machine Learning*, 2015.

[26] J. Park and W. Sung, "Fpga based implementation of deep neural networks using on-chip memory only," in *IEEE International Conference on Acoustics, Speech and Signal Processing (ICASSP)*, 2016.

[27] C. Zhang, P. Li, G. Sun, Y. Guan, B. Xiao and J. Cong, "Optimizing FPGA-based Accelerator Design for Deep Convolutional Neural Networks," in *Proc. of the 2015 ACM/SIGDA International Symposium on Field-Programmable Gate Arrays*, Monterey, California, USA, 2015.

[28] H. Nakahara and T. Sasao, "A Deep Convolutional Neural Network Based on Nested Residue Number System," in *25th International Conference on Field Programmable Logic and Applications (FPL)*, Lausanne, Switzerland, 2015.

[29] L. Vokorokos, B. Madoš, J. Perháč and M. Chovanec, "Architecture of DFC-1 computer with data driven computation model," in *The 6th International Symposium on Applied Machine Intelligence and Informatics*, Herľany, Slovakia, 2008.

[30] O. Kainz, F. Jakab, M. Michalko a P. Feciľak, „Detection of Persons and Height Esatimation in Video Sequence," *International Journal of Engineering Sciences & Research Technology,* zv. 5, %1. vyd.3, 2016.

[31] „7 Series FPGAs Data Sheet: Overview," Xilinx, March 28, 2017.

[32] „KC705 Evaluation Board for the Kintex-7 FPGA - User Guide," Xilinx, July 8, 2016.

[33] L. Kónya and J. Kopják, PIC mikrovezérlők alkalmazástechnikája, PIC programozás C nyelven, Budapest: ChipCAD Elektronikai Disztribúció Kft., 2009.

[34] E. Olsen, „Introduction of the Residue Number Arithmetic Logic Unit With Brief Computational Complexity Analysis," 2015.

[35] L. D. J. Xiaobin, "A mixed Parallel Neural Networks Computing Unit Implemented in FPGA," in *IEEE Intl. Conference Neural Networks & Signal Processing*, China, 2003.

[36] A. Gomperts and A. Ukil, "Development and Implemenation of Parameterized FPGA-Based General Purpose Neural Networks for Online Applications," *IEEE Transaction on industrial informatics,* vol. 7, no. 1, 2011.

[37] K. Lakshmi and D. M. Subadra, "A Survey on FPGA based MLP Realization for On-chip Learning," *International Journal of Scientific & Engineering Research,* vol. 4, no. 1, pp. 1-9, 2013.

[38] M. Panicker and C. Babu, "Efficient FPGA Implementation of Sigmoid and Bipolar Sigmoid Activation Functions for Multilayer Perceptrons," *IOSR Journal of Engineering (IOSRJEN),* vol. 2, no. 6, pp. 1352-1356, 2012.

[39] L. Sousa, "Efficient Method for Magnitude Comparison in RNS Based on Two Pairs of Conjugate Moduli," in *18th IEEE Symposium on Computer Arithmetic (ARITH'07)*, Washington, DC, USA, 2007.

The Identification of Readiness in Implementating Business Intelligence Projects by Combining Interpretive Structural Modeling with Graph Theory and Matrix Approach

Vahid Farrokhi[1], László Pokorádi[2], Sahar Bouini[3]

[1]University of Debrecen, Doctoral School of Informatics, Kassai út 26, 4028 Debrecen, Hungary, vahid.farrokhi@inf.unideb.hu

[2]Óbuda University, Institute of Mechatronics and Vehicle Engineering, Népszínház u. 8, 1081 Budapest, Hungary, pokoradi.laszlo@bgk.uni-obuda.hu

[3]Institute for Advanced Studies in Basic Sciences,Department of Computer Science and Information Technology, Prof. Yousef Sobouti Blvd., Zanjan, Iran, s.bouini@iasbs.ac.ir

Abstract: In the past, decisions were made by senior management in organizations and they were based solely on personal experience, leading to increased risk in decision making. Nowadays, however, most companies are moving towards Business Intelligence (BI) systems. It is estimated that technology budgets dedicated to Business Intelligence in 2006, increased from $ 14 to $ 20 billion. Experiments have shown that the probability of failure in BI projects is high and evaluation before the start of implementation is important because if the company is not assessed, the implementation of BI projects can cause a waste of time and resources and the company will not achieve expected profits. The aim of this paper is to provide a method to evaluate the key factors for the successful implementation of BI projects and to determine the organization's index of assessing readiness before the implementation of BI projects. A series of technical and organizational key factors for the successful implementation of BI have been proposed in various literatures. These key factors will be evaluational ones for an organization. We apply a combination of Interpretive Structural Modeling (ISM) and Graph Theory and Matrix Approach (GTMA) on the factors to earn an indicator for evaluating the organization's readiness for implementing a BI project. We applied this method in two organizations for comparing and determined the organizations' readiness before the implementation of BI and found it to be very effective.

Keywords: Business Intelligence; Readiness Evaluation; Critical Success Factors; Interpretive Structural Modeling; Graph Theory and Matrix Approach

1   Introduction

Information and knowledge have become the main wealth of organizations in the third millennium [1]. Commercial institutes and production units trying to utilize as much of their wealth in their critical decisions to gain competitive advantages have placed Business Intelligence (BI) software at the top of the technology priority list [2].

Data Warehousing Institute (DWI) that works in the field of education data warehouse and BI, define BI as follows: processes, technology and tools needed to transform data into information, information into knowledge and knowledge into plans that lead to a lucrative business action [3]. Vodapalli in [4] says "BI brings people and data together, offering a variety of ways to see the information that backs fact-based decision making". In other words, BI uses a set of tools to collect different information about the organization in a data warehouse and to analyze the collected data. Employees and managers utilize the result of this analysis to make better decisions and to help the growth and profitability of their organization. In fact, BI is an analysis tool in order to automate decision making about business conditions, sales, customer demand, product preferences, etc. [3]. The key tasks of a BI system include smart exploration, defragmentation, aggregation and multidimensional analysis of data obtained from different information resources [2]. BI systems include two types of instruments; the tools of database management systems are the first group that analyze the databases and the second group as competitive intelligence tools, they help organizations in decision making of the market [5].

After having reviewed the literature, we came to the conclusion that we define BI as a solution which should be considered in both managerial and technical approaches in order to assist experts and all levels of managers in decision making and taking processes.

Although BI can help to improve the performance of organizations, according to different literature reviews there are many companies that have failed to successfully implement BI projects [6]. Hawking and Sellitto in [6], indicate that 60 percent of the BI projects fail due to poor planning, poor management of projects, undelivered business requirements or ones delivered with low quality.

Lukić et al., proposed a new methodology for building multi-dimensional data-warehousing and business intelligence systems for utility companies [7]. Their approach can be used by any utility company that wishes to take advantage of the principles.

Since these projects by nature have a high failure rate, the identification of Critical Success Factors (CSF) of the projects can be important and can have a valuable role in the successful implementation of the system and in reducing the failure rate [1]. CSFs are a set of conditions, characteristics and variables that are defined in

all fields and, if managed carefully, lead to organizational success. CSFs can help ensure the success of the BI implementation in an arbitrary organization.

In [2], Yeoh and Koronios said if BI shareholders reach an understanding of CSF, they can optimize their resources and efforts by focusing on critical factors that contribute to the successful implementation of the system. Farrokhi and Pokorádi [8] believed that these factors should be carefully considered by senior managers and BI project managers of companies that are evaluating the readiness of their organizations.

These factors will be much more effective, if used in accordance with their importance in various stages of implementation [8]. In this study, we used the factors presented in the paper of Farrokhi and Pokorádi [9] and listed in Figure 1. The authors in [9] have categorized the factors into both organizational and technical factors.
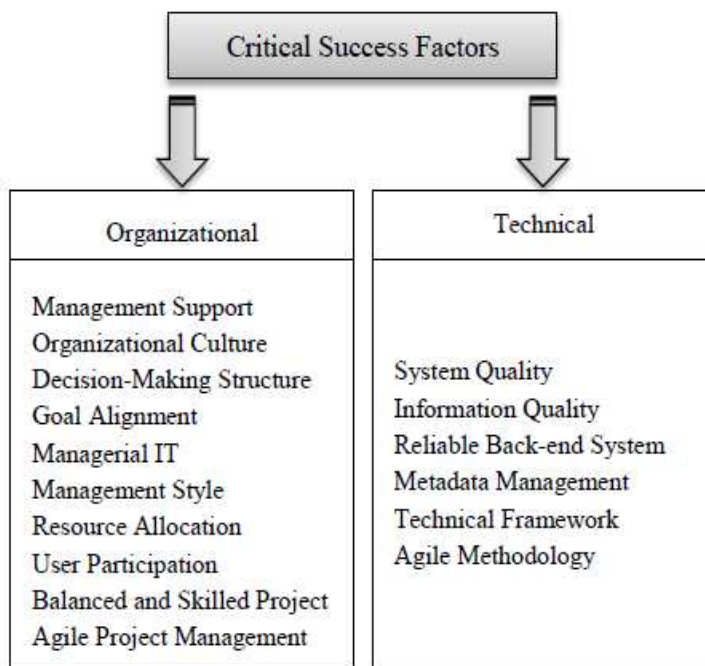
Figure 1
Critical Success Factors [8]

In [3] Farrokhi and Pokorádi reviewed the necessities for building a model to evaluate BI projects and they said that the BI readiness assessment had two main goals. Firstly, it shows the gap areas that are the reasons for the companyies not being ready to continue with the BI efforts. By identifying the BI readiness gaps, we will avoid wasting resources and time. Secondly, we can close these gaps by assessing and implementing BI with a high probability of success.

In the [10] Hidayanto et. al. Used the Analytic Hierarchy Process (AHP) method and surveys of experts in the field of BI to estimate the weight criteria. They have used an assessment model of the Electronic Government Procurement (e-GP) to determine the level of each criterion. Then, by multiplying the weight of each criterion at their level, the readiness of the organization from the perspective of each criterion before the implementation of BI can be determined. In [11] factors affecting the readiness of BI were examined in three different organizations: IT, education and commercial. In the paper, the partial least squares method was used for analysis and to model the readiness of the organization. They examined the positive and negative effects of criteria in these three organizations before implementing BI.

Farrokhi et al. in [12] examined various assessment methods of organization readiness to implement business intelligence. They divided the existing methods into three categories: probabilistic method, Multi Criteria Decision Making (MCDM) methods (such as fuzzy AHP, fuzzy ANP, fuzzy AHF, AHP, ANP and AHF) and hybrid methods. Hybrid methods, combine probabilistic and MCDM methods to benefit the advantages of both methods.Then, they compared all these methods through AHP. The results demonstrated that the hybrid methods are the better optionsto build evaluation models.

Rajesh Attri et al. in [13] provided a survey on Interpretive Structural Modeling (ISM) and says it is a suitable method to identify relationships between specific items that define a problem and Rao in [14] indicated that Graph Theory and Matrix Approach (GTMA) is a good method for the modeling of systems, network analysis, functional representation, conceptual modeling, diagnosis, etc.

In [12], the authors presented that the hybrid approach is the most appropriate method to assess the readiness of an organization before implementing BI. Also, according to the results of [13] and [14], the combination of ISM and GTMA are considered in this study for assessing the organization's readiness.

Overall, the main contribution of this paper is the usage of the ISM method to depict the relationship between the involved key factors in a successful implementation of BI projects. Then, by using the Graph Theory and Matrix Approach (GTMA), obtain an indicator to evaluate the organization's readiness before implementing BI projects.

The rest of this paper is organized as follows: In Section 2 the mathematical background is studied. More precisely the concepts of ISM and GTMA are introduced in Sections 2.1 and 2.2 subsequently. Section 3 defines the research process and works done. Section 4 is the conclusion of our research.

2   Mathematical Background

In this section the concepts of ISM and GTMA methods are presented. These concepts will be utilized in the research process and works done.

2.1   ISM Method

ISM is an appropriate technique to analyze the impact of an element on other elements. This methodology investigates respectively complex relationship directions between the elements of the system. In other words, the means by which, the system can overcome the complexity of the elements [15]. In this study, we need to determine the relationship between factors in a successful implementation of BI and convert them to a graph for further analysis. In this case, ISM comes to help. The implementation of ISM in accordance to [13] includes the following steps:

2.1.1   Structural Self Interaction Matrix (SSIM)

Primarily, utilizing the suggestions of experts from industry and academia, the relationships between components is defined. Four symbols are used to determine the relationship between two factors (i and j):

V: means factor i leads to factor j (factor i will influence factor j).

A: means factor j leads to factor i (factor i will be influenced by factor j).

X: for both direction relations (factors i and j will influence each other).

O: for no relation between the factors.

2.1.2   Reachability Matrix

To get a reachability matrix, the symbols of the SSIM matrix must be converted to zero and one. The reachability matrix is calculated according to the following rules:

  I.   If the (i,j) cell in the SSIM is V, then the (i,j) cell in the reachability matrix becomes 1 and the (j,i) cell becomes 0.

  II.   If the (i,j) cell in the SSIM is A, then the (i,j) cell in the matrix becomes 0 and the (j,i) cell becomes 1.

  III.   If the (i,j) cell in the SSIM is X, then the (i,j) cell in the matrix becomes 1 and the (j,i) cell also becomes 1.

  IV.   If the (i,j) cell in the SSIM is O, then the (i,j) cell in the matrix becomes 0 and the (j,i) cell also becomes 0.

After obtaining the primary reachability matrix, the property of transmissibility must be checked. This means that if (i,j) = 1 and (j,k) = 1, then (i,k) = 1.

2.1.3 Level Partitions

The Reachability set for a factor is a collection which includes the factor itself and the factors that can be reached through this factor and the Antecedent set is a collection that includes the factors which can be reached through them to this factor and the factor itself.

For level partitioning, first we determine the Reachability set and Antecedent set from the Reachability Matrix for any factor. After determining the Reachability set and Antecedent set, similar elements in both sets of factors are detected (named Similar set). In the first iteration, the factor with the same elements in the Reachability set and the Similar set is placed on the first level. Then, this factor is removed from consideration and the iteration is repeated to determine the factors of the second level. This process is continued until the levels of all the factors are defined.

2.1.4 Diagraph

According to the levels of each factor and the final Reachability Matrix, an initial model of ISM, with regard to the transmissibility is drawn. Then, the final version of ISM is computed by removing the transmissibility of nodes. This graph shows the relationships between different factors. High-level factors are placed on top of the graph and low-level factors at the bottom of the graph.Then the node contents are replaced with factors to obtain ISM model.

2.2 Graph Theory and Matrix Approach

A graph $G = [N,L,f]$ is a 3-tuple consisting of a set of nodes N, a set of links L, and a mapping function $f : L \rightarrow N \times N$ which maps links into pairs of nodes. Nodes directly connected by a link are called adjacent nodes [16]. When the node-pair order does not matter in linking the node pair, G is an undirected graph. In an undirected graph, $p_i \sim p_j$ is equivalent to $p_j \sim p_i$, But in direct graph, a link defined by the node pair $(p_i; p_j)$ is not the same as a link defined by node pair $(p_j; p_i)$. In fact, both links may exist in a directed graph [16]. Adjacency matrix **A** shows the number of links directly connecting node i to node j. This number is stored at row i, column j of the matrix [16].

In this section, we transform the ISM diagraph to a matrix and by analyzing it; we will obtain an index to assess the readiness of the organization for the successful implementation of BI. The routine for applying GTMA to the matrix is as follows:

first, the Relative Importance Matrix (RIM), **B** from ISM digraph is defined. **B** is a binary matrix (b_{ij}), where b_{ij} represents the relative importance between factors i and j such that [14]:

$$B = \begin{cases} b_{ij} = 1 & \text{if the } i-th \text{ factor is more important than the} \\ & j-th \text{ factor for a given machining operation.} \\ \\ \\ b_{ij} = 0 & \text{otherwise} \end{cases} \tag{1}$$

In other words, RIM is similar to the adjacency matrix in graph theory. In this matrix, all diagonal elements have a value of 0 and non-diagonal elements have a value of either 0 or 1. So, in this matrix only the relative importance among the factors is considered whilst the measures of the factors are not considered. To incorporate this, another matrix, called Characteristic Matrix (CM), is defined:

$$C = [\ AI - B] \tag{2}$$

Where **I** is an identity matrix, and **A** is a variable representing the measure of the factors. All diagonal elements of **C** are considered equal which means the measures of all factors are equal. But this is not true in the real world. In this formula, the relative importance of one factor to the second factor (b_{ij}) can adopt values greater than zero or one [15]. To solve this problem, another matrix (**D**) called Variable Characteristic Matrix (VCM), is developed:

$$D = [E - F] \tag{3}$$

In this equation, **E** is a diagonal matrix with diagonal elements e_i, which indicates the presence or size of factor *i*. If a factor is excellent, then it is assigned a maximum value. Also, for a very low significant factor, a minimum value is assigned [14]. **F** is a matrix of which the off-diagonal elements are represented as $f_{i,j}$, instead of 1, wherever the *i*-th factor has more relative importance than the *j*-th factor.

Due to the positive and negative values in matrix **D**, when calculating the matrix determinant, there may be a number of statements in the determinant formula of the calculation which become zero and so we lose some of the information. So, the Variable Permanent Function (VPF) is defined instead of the determinant. This function is derived from a new matrix called the Permanent Matrix [14]:

$$H = [E + F] \tag{4}$$

The Permanent function (Leibniz's formula) is as follows [17]:

$$Per(H) = \sum_{\pi \in \prod_n} a_{1\pi(1)} a_{2\pi(2)} \dots a_{n\pi(n)} \tag{5}$$

Where

$$\prod_n = \{\pi \mid \pi \text{ is permutation of } \{1,2,\dots,n\} \ \} \tag{6}$$

Permanent function is a standard matrix function that is used in combinatorial mathematics [14].

The index to assess the readiness of an organization for the successful implementation of BI is achieved by using the Permanent matrix, from the following equation:

BIIAR[1] = the numerical value of the Permanent matrix of factors.

The time complexity of this formula is O(N*N!) and it is not appropriate in cases where N is high. Therefore, we utilized the optimized algorithm from H. J. Ryser (1963) which has higher execution speed (O(N^2 2^N)) [17]. This formula is as follows:

$$per(A) = \sum_{t=0}^{n-1}(-1)^t \sum_{x \in \tau_{n-t}} r_1(X)r_2(X) \dots r_n(X) \tag{7}$$

where

$$\tau_k = \{X \epsilon R^{n \times k} \mid X \text{ consists of columns of } A\} \tag{8}$$

and

$$r_i(X) = sum \text{ of row } i \text{ of matrix } X \tag{9}$$

We adopted this algorithm from [17] and wrote it in C# and all the calculations were done.

3   Works Done

In this study, an index is achieved for evaluating the readiness of the organization to implement BI by combining ISM and GTMA methods and by taking into account the views of experts in the field of BI. Our research design is provided in Figure 2.

As it can be seen in Figure 2, we studied different literature and detected the critical factors that are involved in a successful implementation of BI. We used the technical and organizational factors for the successful implementation of BI that were presented by [8] and listed in Figure 1.

Two series of questionnaires were prepared according to these CSFs. The first questionnaire was related to the ISM and the second one is for GTMA. To check the reliability and validity of the questionnaires, we calculated Cronbach's alpha [18], which was 0.885 and also experts confirmed the accuracy of the questionnaires.

---

[1]**B**usiness **I**ntelligence **I**ndex of **A**ssess **R**eadiness
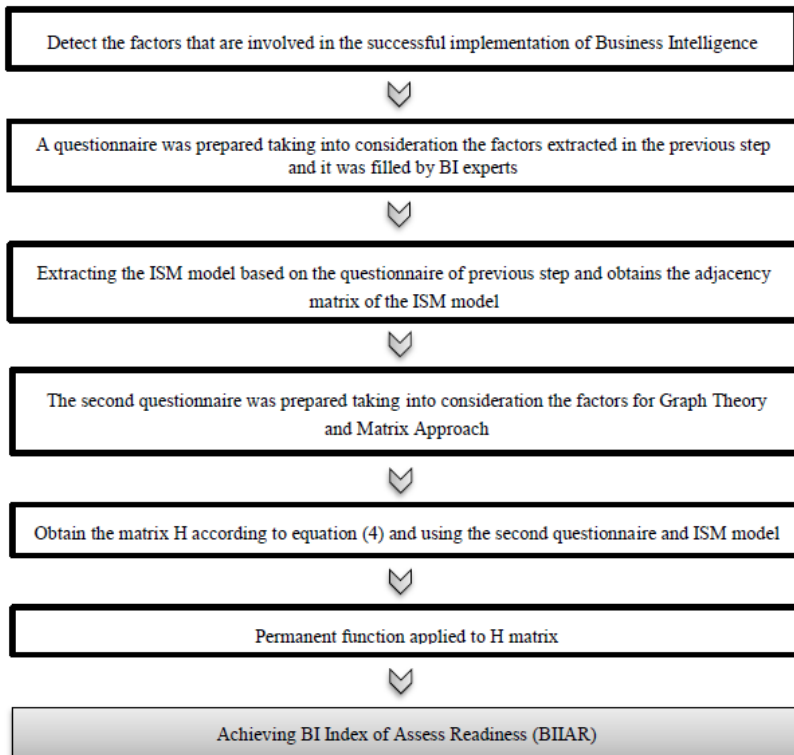
Figure 2

The block diagram of the proposed method

In the next phase questionnaires were completed by several specialists (five experts plus two academicians) in BI field. The relations between factors were extracted by applying ISM method and according to the experts' answers to the first questionnaire. In Table 2 the Final Reachability Matrix and in Table 3, Factor Levels resulted from ISM method are presented.

Table 2

Final Reachability Matrix for Sample Organization

CF→	1	2	3	4	5	6	7	8	9	10	11	12	13	14	15	16
CF1	1	1	1	1	1	1	1	1	1	1	1	1	1	1	1	1
CF2	1	1	1	1	1	1	1	1	1	1	1	1	1	1	1	1
CF3	1	1	1	1	0	1	1	1	1	1	1	1	1	1	1	1
CF4	1	1	1	1	0	1	1	1	1	1	1	1	1	1	1	1
CF5	1	1	1	1	1	1	1	1	1	1	1	1	1	1	1	1
CF6	1	1	1	1	1	1	1	1	1	1	1	1	1	1	1	1
CF7	1	1	1	1	0	1	1	1	1	1	1	1	1	1	1	1

CF8	1	1	1	1	0	0	0	1	1	1	1	1	1	1	1	1
CF9	1	1	1	1	0	1	1	1	1	1	1	1	1	1	1	1
CF10	1	1	1	1	1	1	1	1	1	1	1	1	1	1	1	1
CF11	1	1	1	1	0	1	0	1	0	1	1	1	1	1	1	1
CF12	1	1	1	1	0	1	1	1	0	0	1	1	1	1	1	1
CF13	1	1	1	1	0	1	1	1	0	0	1	1	1	1	1	1
CF14	1	0	1	1	0	0	1	1	0	0	1	1	1	1	1	1
CF15	1	1	1	1	0	1	1	1	0	1	1	1	1	1	1	1
CF16	1	1	1	1	0	1	1	1	1	1	1	1	1	1	1	1

Table 3

Factor Levels

Level	Factors
1	CF1,CF3,CF4,CF8,CF11,CF12,CF13,CF14,CF15,CF16
2	CF2,CF6,CF7, CF9, CF10
3	CF5

According to these two tables, the Interpretive Structural Model is achieved. This model will be the input for GTMA. As the graph of ISM in our study was large and complex, we brought only the adjacency matrix of this model in Table 4.

To apply GTMA, first we obtain the adjacency matrix of the ISM model. Then to create matrix **H** (equation 4), we form matrixes **E** and **F** by using the adjacency matrix of the ISM model and the results of the second questionnaire. **E** is a diagonal matrix with diagonal elements e_i, which indicates the importance of factors. The importance of factors was derived from the questionnaires completed by professionals. **F** is a matrix in which non-diagonal elements show the importance of one factor to another factor instead of 1 value in the adjacency matrix of ISM model. These values are derived from the second questionnaire too. Given the matrixes **E** and **F**, the matrix **H** is obtained according to Equation 4.

Table4

Adjacency Matrix of ISM Model for Sample Organization

CF→	1	2	3	4	5	6	7	8	9	10	11	12	13	14	15	16
CF1	9	4	0	5	0	4	4	4	2	3	3	2	0	2	3	0
CF2	4	8	3	2	0	3	0	4	3	2	0	0	0	0	0	0
CF3	3	0	7	2	0	0	3	2	3	4	2	3	0	0	3	3
CF4	4	3	4	8	0	0	0	3	0	2	0	0	0	0	0	0
CF5	4	0	0	0	7	3	3	0	3	2	3	4	3	3	0	2
CF6	0	2	3	2	3	7	2	3	3	4	3	3	0	0	0	3
CF7	0	3	0	4	0	0	9	3	0	3	4	4	4	3	2	0
CF8	0	0	0	2	0	0	0	8	3	0	5	4	0	3	0	0
CF9	4	4	5	0	0	0	4	5	8	3	4	3	3	3	4	4

CF10	0	4	4	3	0	5	4	4	5	6	3	3	3	2	3	4
CF11	0	3	0	0	0	0	0	3	0	0	7	4	4	0	5	4
CF12	4	5	4	3	0	0	0	0	0	0	4	8	0	0	2	0
CF13	4	0	3	2	0	0	0	2	0	0	3	2	7	3	4	0
CF14	3	0	4	0	0	0	0	0	0	0	3	5	4	6	0	0
CF15	4	0	3	0	0	0	0	0	0	0	2	0	5	3	8	4
CF16	4	3	4	0	0	0	3	4	0	4	3	2	2	0	3	6

We brought matrix **H** for both sample organizations in Tables 5 and 6.

Table5

Matrix H for First Organization

CF→	1	2	3	4	5	6	7	8	9	10	11	12	13	14	15	16
CF1	9	4	0	5	0	4	4	4	2	3	3	2	0	2	3	0
CF2	4	8	3	2	0	3	0	4	3	2	0	0	0	0	0	0
CF3	3	0	7	2	0	0	3	2	3	4	2	3	0	0	3	3
CF4	4	3	4	8	0	0	0	3	0	2	0	0	0	0	0	0
CF5	4	0	0	0	7	3	3	0	3	2	3	4	3	3	0	2
CF6	0	2	3	2	3	7	2	3	3	4	3	3	0	0	0	3
CF7	0	3	0	4	0	0	9	3	0	3	4	4	4	3	2	0
CF8	0	0	0	2	0	0	0	8	3	0	5	4	0	3	0	0
CF9	4	4	5	0	0	0	4	5	8	3	4	3	3	3	4	4
CF10	0	4	4	3	0	5	4	4	5	6	3	3	3	2	3	4
CF11	0	3	0	0	0	0	0	3	0	0	7	4	4	0	5	4
CF12	4	5	4	3	0	0	0	0	0	0	4	8	0	0	2	0
CF13	4	0	3	2	0	0	0	2	0	0	3	2	7	3	4	0
CF14	3	0	4	0	0	0	0	0	0	0	3	5	4	6	0	0
CF15	4	0	3	0	0	0	0	0	0	0	2	0	5	3	8	4
CF16	4	3	4	0	0	0	3	4	0	4	3	2	2	0	3	6

Table 6

Matrix H for Second Organization

CF→	1	2	3	4	5	6	7	8	9	10	11	12	13	14	15	16
CF1	7	4	0	4	0	4	3	3	5	3	4	4	0	3	3	0
CF2	2	7	3	4	0	4	0	4	3	3	0	0	0	0	0	0
CF3	2	0	6	3	0	0	3	3	5	4	3	3	0	0	4	3
CF4	2	2	3	5	0	0	0	3	0	3	0	0	0	0	0	0
CF5	1	0	0	0	7	4	3	0	4	4	4	4	3	3	0	4
CF6	0	2	2	2	2	7	4	4	4	3	3	4	0	0	0	4
CF7	0	3	0	3	0	0	5	4	0	3	3	3	3	2	2	0
CF8	0	0	0	3	0	0	0	6	4	0	4	3	0	2	0	0
CF9	1	3	1	0	0	0	2	2	8	4	3	3	3	3	4	3
CF10	0	3	2	3	0	3	3	3	2	6	4	4	3	4	4	4
CF11	0	3	0	0	0	0	0	2	0	0	7	4	4	0	4	3

CF12	2	2	3	2	0	0	0	0	0	0	2	6	0	0	3	0
CF13	3	0	3	4	0	0	0	3	0	0	2	2	6	3	3	0
CF14	3	0	3	0	0	0	0	0	0	0	3	3	3	5	0	0
CF15	3	0	2	0	0	0	0	0	0	0	2	0	3	4	6	4
CF16	3	3	3	0	0	0	3	5	0	2	3	4	3	0	2	6

Finally, permanent function applied to matrix **H** and BIIAR is obtained for both organizations. This index shows the readiness of each organization to implement BI.

Conclusion

Before the implementation of BI, the readiness of the organization must be evaluated to minimize waste of costs and resources. In this study, we examined two utility companies with about 1,000 and 1,200 employees, in which their tasks are electricity transmission and distribution.

We applied the Interpretive Structural Modeling (ISM), Graph Theory and Matrix Approach (GTMA) to derive a measure to check the readiness of two sample organizations before implementing BI. The research design is demonstrated in Figure 2.

The adjacency matrix of the ISM model was illustrated in Table 4 and shows the relationship between the factors. GTMA applied to the ISM and the BI Index of Assess Readiness (BIIAR) for each organization was obtained to show the readiness of the organization before implementing BI. The result of GTMA which were applied to both organizations in this research is as follows:

BIIAR for first organization = 21.348×10^{17}

BIIAR for second organization = 3.337×10^{17}

Beacuse of the BIIAR for the first organization is bigger, it will be relatively successful than the second organization in implementing BI project.

In an ideal situation, all values in matrix **H** will be maximum and so BIIAR will be 92.2337×10^{17}. But in the worst situation all values in matrix **H** will be minimum and BIIAR will be 6.3747×10^{8}. As you can see, the first organization is in better situation than second one, but still is far from the ideal.

The algorithm will produce different results according to society's culture and economy. Our suggestion is to implement the proposed algorithm in an organization that has already implemented BI successfully. Then the BIIAR rate obtained for that organization will be a standard for other organizations in the given society. Also, we can use an average from BIIARs of several successful organizations as a measure to obtain more accurate standards.

References

[1]   Zare Ravasan, A., & Rabiee Savoji, s. (2014) Identification and Classification of Business Intelligence System Implementation Projects' Critical Success Factors in Iran. International Journal of Business Intelligence Research (5)3, 41-57

[2]   Yeoh, W., & Koronios, A. (2010) Critical Success Factors for business intelligence systems. Journal of Computer Information Systems, 50(3) 23-32

[3]   Farrokhi, v., & Pokorádi, L. (2012) The Necessities for Building a Model to Evaluate Business Intelligence Projects- Literature Review. International Journal of Computer Science & Engineering Survey, 3, No. 2

[4]   Vodapalli, k. (2009) Critical Success Factors of BI Implementation (Master's Thesis) IT University of Copenhagen

[5]   Babazadeh sangar, A., & Noorminshah Binti Iahad, A. (2013) Critical Factors That Affect the Success of Business Intelligence Systems (BIS) Implementation in an Organization. International Journal of Scientific & Technology Research (2)2

[6]   Hawking, P., & Sellitto, C. (2010). Business Intelligence (BI) Critical Success Factors. 21st Australasian Conference on Information Systems. Brisbane

[7]   Lukić, J., Radenković, M., Despotović-Zrakić,M., Labus, A., Bogdanović, Z. (2016) A hybrid approach to building a multi-dimensional business intelligence system for electricity grid operators, Utilities Policy, Vol. 41, pp. 95-106

[8]   Farrokhi, v., & Pokorádi, L. (2013) Organizational and Technical Factors for Implementing Business Intelligence. Fascicle of Management and Technological Engineering, ISSUE #1

[9]   Naderinejad, M., Tarokh, M. J., & Poorebrahimi, A. (2014) Recognition and Ranking Critical Success Factors of Business Intelligence in Hospitals – Case Study: Hasheminejad Hospital. International Journal of Computer Science & Information Technology, 6, No 2

[10]   Achmad Nizar Hidayanto, & Robertus Kristianto, & Muhammad Rifki Shihab. (2012) Business Intelligence Implementation Readiness: A Framework Development and Its Application to Small Medium Enterprises (SMEs) International Research Symposium in Service Management (IRSSM-3) At Bejing, China

[11]   Hejazi, A., & Abdolvand, N., & Harandi, S. R. (2016) Assessing The Organizational Readiness For Implementing BI Systems. International Journal of Information Technology Convergence and Services (IJITCS) Vol. 6, No. 1

[12] Farrokhi, V., & Pokorádi, L. (2012) a comparative analysis of evaluation methods for readiness of business intelligence project. Proceedings of the 13th Conference on Mathematics and its Applications. University "Politehnica" of Timisoara, November, I3

[13] Rajesh Attri, Nikhil Dev, & Vivek Sharma (2013) Interpretive Structural Modelling (ISM) Approach: An Overview. Research Journal of Management Sciences, 2(2) 3-8

[14] Rao, RV. (2007) Decision Making in the Manufacturing Environment: Using Graph Theory and Fuzzy Multiple Attribute Decision Making Methods (pp. 7-24) Springer, London

[15] Alam Tabriz, A., Talai, H., & Moradi, E. (2013) Evaluating the Key Factors of Successful Implementation of World Class Manufacturing Using an Integrated Approach of Interpretive Structural Modeling(ISM), Graph Theory and Matrix Approach (GTMA): A Case Study for Iran Khodro and Saipa in Iran. Journal of Industrial Management (5)10, Number 1

[16] Pokorádi, L. (2013) Graph Theoretical Investigation of Network Structure System. 10th International Multidisciplinary Conference. 22-24

[17] RyserH. J. (1957) "Combinatorial properties of matrices of zeros and ones," Canadian Journal of Mathematics, Vol. 9, pp. 371-377

[18] Cronbach, L. J. (1951) ''Coefficient Alpha and the Internal Structure of Tests,'' Psychometrika, Vol. 16, pp. 97-334

Neural Network-based Adaptive Sliding Mode Control Method for Tracking of a Nonholonomic Wheeled Mobile Robot with Unknown Wheel Slips, Model Uncertainties, and Unknown Bounded External Disturbances

Tinh Nguyen[1], Kiem Nguyentien[2], Tuan Do[1], Tuan Pham[3]

[1]Institute of Information Technology, Vietnam Academy of Science and Technology, Hoang Quoc Viet street 18, 100000 Hanoi, Vietnam
e-mail: nvtinh@ioit.ac.vn; tuando@ioit.ac.vn

[2]Department of Electronics Power, Faculty of Electronics Engineering Technology, Hanoi University of Industry, Hanoi, Vietnam
e-mail: kiemnt@haui.edu.vn

[3]Space Technology Institute, Vietnam Academy of Science and Technology, Hoang Quoc Viet street 18, 100000 Hanoi, Vietnam, e-mail: pmtuan@sti.vast.vn

Abstract: This article represents a neural network-based adaptive sliding mode control (ASMC) method for tracking of a nonholonomic wheeled mobile robot (WMR) subject to unknown wheel slips, model uncertainties and unknown bounded disturbances. Self-recurrent wavelet neural networks (SRWNN) are employed in order to approximate unknown nonlinear functions due to the unknown wheel slips, model uncertainties, and unknown bounded external disturbances. By doing this, their harmful effects are compensated effectively. Thanks to this control method, a desired tracking performance of the closed-loop control system is achieved where the position tracking errors converge to an arbitrarily small neighborhood of the origin, regardless their initial values. According to Lyapunov theory and LaSalle extension, the stability of the whole closed-loop system is guaranteed to achieve the desired tracking performance. It is unnecessary to preliminarily offline train the neural network weights since they are easily initiated. Online tuning algorithms are established and used, for training the weights. Computer simulations are implemented to demonstrate the validity and efficiency of this proposed control method.

Keywords: Adaptive sliding mode control (ASMC); desired tracking performance; online tuning algorithm; unknown wheel slip; wheeled mobile robot (WMR)

1   Introduction

In recent years, control problems for wheeled mobile robots (WMR) are considered remarkable, due to their inherent nonlinear properties such as nonholonomic constraints and their wide applicability in various areas. Many researchers, all over the world, have paid attention to solving the tracking problems of WMRs by employing various techniques with the assumption "pure rolling without slip" being always satisfied. For example, an adaptive tracking controller in [1] employing a backstepping technique was developed for the dynamics of WMRs with unknown parameters. The content in [2] expressed a robust adaptive control method to cope with parametric uncertainties and external disturbances for nonholonomic WMRs. A wavelet-network-based control method was proposed in [3] for the dynamics of WMRs with unstructured unmodelled dynamics and unknown disturbance. Owing to having a fast response, good transient performance, and robustness against parameter variations, unstructured unmodelled dynamics, and unknown disturbances, the sliding mode control (SMC) technique has been applied widely for trajectory tracking problems of nonholonomic WMRs. For instance, the work in [4] proposed a tracking controller using the SMC technique for nonholonomic WMRs in polar coordinates. In addition, the authors in [5] also proposed an adaptive neural SMC method for trajectory tracking of nonholonomic WMRs with model uncertainties and external disturbances.

However, in practice, the assumption "pure rolling without slip" is often violated due to various factors such as slippery floor, external forces, and so on. The wheel slip is one of the reasons making the tracking performance of nonholonomic WMRs reduce considerably. Therefore, if one wants the tracking performance of the WMRs to be improved in such context, then control methods having the ability to overcome the undesired effects of the wheel slips must be taken into account.

Several research results have been published for trajectory tracking of nonholonomic WMRs subject to the wheel slips. In particular, an adaptive tracking control method by means of neural networks was proposed in [6] in order to overcome the harmful effect of the wheel slips. By employing gyro-sensors and encoders, the slip ratios were calculated in [7], [8]. Then the control approaches to compensate the wheel slips were proposed in these reports. The work in [9] developed a robust controller dealing with not only slip-kinematics but also slip-dynamics by employing the framework of differential flatness. The authors in [10] modeled overall the dynamics of a WMR subject to the wheel slips. Next, they proposed a discontinuous control technique for regulation control task and a SMC technique for sharp turning control task. The work in [11] proposed a feedback linearization control method for trajectory tracking of a WMR subject to both longitudinal and lateral slips between each driving wheel and the floor in an ideal condition where unknown bounded external disturbances, as well as, model

uncertainties did not exist. In addition, in this case, the values of the accelerations and velocities of the wheel slips could be measured precisely. On the contrary, such ideal condition barely exists in reality and it is difficult to exactly measure both the accelerations and the velocities of the wheel slips. Accordingly, it was impractical to employ this feedback linearization control method [11].

Therefore, most of these previous works assumed that the measurements of the wheel slips were made available by additional sensors such as global position systems (GPS), gyroscopes, accelerometers, etc. which are expensive and complex.

On the other hand, the neural network (NN) has been utilized as one of the intelligent techniques to enhance the performance of closed-loop control systems. Unlike classification applications, the NN in feedback control application seems to be part of the closed-loop control system. For this reason, it is useful in order to have a NN closed-loop control system with on-line learning algorithms [12] without the need of a preliminary off-line learning phase for the NN weights. In regard to the works in [5], [13], [14], and [15], the closed-loop control systems including self-recurrent wavelet neural networks (SRWNN) have been proposed. In fact, the SRWNN is a combination of the properties of a recurrent neural network (RNN) [16], [17], namely the attractor dynamics, and the fast convergence of a wavelet neural network (WNN) [18], [19]. As a consequence, the SRWNN includes a mother wavelet layer comprising self-feedback neurons being able to not only capture the past information of the NN but also adapt sharply to quick changes of the control environment.

These above research results have motived us to propose a neural network-based ASMC method for trajectory tracking of a nonholonomic WMR in the presence of the unknown wheel slips, model uncertainties, and unknown bounded external disturbances. In this work, the proposed controller is based on the SRWNNs to compensate the unknown wheel slips, model uncertainties, and unknown bounded external disturbances. Furthermore, the measurements of the wheel slips are unnecessary. In sense of Lyapunov and LaSalle extension, on-line tuning algorithms for all the weights of the SRWNNs are derived. The uniformly ultimately bounded property of all the signals in the closed-loop control system is also assured.

This paper is organized as follows. In Section 2, the kinematics and dynamics of a nonholonomic WMR subjected to the unknown wheel slips as well as the structure of a SRWNN are briefly introduced. Section 3 expresses the problem statement and then proposes an ASMC method using SRWNNs, following which the stability of the whole closed-loop system is proven by using standard Lyapunov theory and LaSalle extension. Finally, computer simulations illustrate the validity and efficiency of the proposed control method in Section 4.

2   Preliminaries

2.1   Kinematics of the Nonholonomic WMR with the Unknown Wheel Slips

Let us take into account a nonholonomic WMR comprising two driving wheels and a caster wheel as shown in Figure 1.

To be specific, point $G(x_G, y_G)$ is the center of mass of the WMR platform. Next, $M(x_M, y_M)$ is the midpoint of the wheel shaft and chosen as the reference point of the WMR. θ is the heading angle of the WMR. b expresses haft of the wheel shaft length. r illustrates the radius of each driving wheel. F_1 and F_2 reveal the total longitudinal friction forces at the right and left wheel, respectively. F_3 shows the totally lateral friction force along the wheel shaft. F_4 and ϖ describe external force and moment acting at G, respectively.

When there is no wheel slip, the linear velocity and the yaw rate of the WMR, computed at M, are represented respectively as follows:

$$\begin{cases} \Theta = \dfrac{r\left(\dot{\phi}_R + \dot{\phi}_L\right)}{2} \\ \mu = \dfrac{r\left(\dot{\phi}_R - \dot{\phi}_L\right)}{2b} \end{cases} \tag{1}$$

where $\dot{\phi}_R, \dot{\phi}_L$ denote the angular velocities of the right and left wheel about the wheel shaft, respectively.

Therefore, the kinematics of the WMR is written as follows:
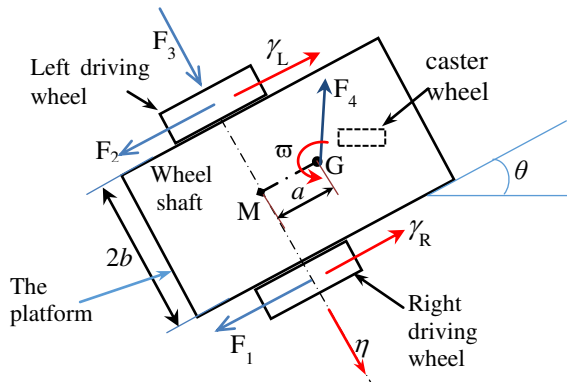
Figure 1

A nonholonomic WMR subject to unknown wheel slips

$$\begin{cases} \dot{x}_M = \Theta \cos \theta \\ \dot{y}_M = \Theta \sin \theta \\ \dot{\theta} = \mu \end{cases} \tag{2}$$

On the other hand, when the assumption of "pure rolling without slip" is violated, (1) and (2) are no longer true. Accordingly, let γ_R and γ_L be the coordinates of the longitudinal slip of the right and left wheels, respectively, and, η be the coordinate of the lateral slip along the wheel shaft (see Figure 1). In this case, the actual linear velocity of the WMR along the longitudinal direction is expressed in the following [11]:

$$\Omega = \frac{r(\dot{\phi}_R + \dot{\phi}_L)}{2} + \frac{\dot{\gamma}_R + \dot{\gamma}_L}{2} = \Theta + \frac{\dot{\gamma}_R + \dot{\gamma}_L}{2} \tag{3}$$

The actual yaw rate of the WMR is computed as follows [11]:

$$\omega = \frac{r(\dot{\phi}_R - \dot{\phi}_L)}{2b} + \frac{\dot{\gamma}_R - \dot{\gamma}_L}{2b} = \mu + \vartheta, \text{ with } \vartheta = \frac{\dot{\gamma}_R - \dot{\gamma}_L}{2b}. \tag{4}$$

Thus, the kinematics of this WMR can be expressed in term of the coordinates of M as follows [11]:

$$\begin{cases} \dot{x}_M = \Omega \cos \theta - \dot{\eta} \sin \theta \\ \dot{y}_M = \Omega \sin \theta + \dot{\eta} \cos \theta \\ \dot{\theta} = \omega \end{cases} \tag{5}$$

Due to the wheel slips, the perturbed nonholonomic constrains can be written as follows [20]:

$$\dot{\gamma}_R = -r\dot{\phi}_R + \dot{x}_M \cos \theta + \dot{y}_M \sin \theta + b\omega \tag{6}$$

$$\dot{\gamma}_L = -r\dot{\phi}_L + \dot{x}_M \cos \theta + \dot{y}_M \sin \theta - b\omega \tag{7}$$

$$\dot{\eta} = -\dot{x}_M \sin \theta + \dot{y}_M \cos \theta \tag{8}$$

2.2 Dynamics of the WMR with the Wheel Slips, the Model Uncertainties, and the Unknown Bounded External Disturbances

Let $\mathbf{q} = [x_G, y_G, \theta, \eta, \gamma_R, \gamma_L, \phi_R, \phi_L]^T$ show a Lagrange coordinate vector. The nonholonomic constrains (6), (7), and (8) can be shown in the following form:

$$\mathbf{A}(\mathbf{q})\dot{\mathbf{q}} = \mathbf{0}, \tag{9}$$

where $\mathbf{A}(\mathbf{q}) = \begin{bmatrix} \cos\theta & \sin\theta & b & 0 & -1 & 0 & -r & 0 \\ \cos\theta & \sin\theta & -b & 0 & 0 & -1 & 0 & -r \\ -\sin\theta & \cos\theta & a & -1 & 0 & 0 & 0 & 0 \end{bmatrix}$.

The dynamic equation of the WMR can be represented as follows:

$$\bar{\mathbf{M}}\ddot{\mathbf{q}} + \bar{\boldsymbol{\tau}}_{\mathrm{d}} = \mathbf{N}\boldsymbol{\tau} + \mathbf{A}(\mathbf{q})^{\mathrm{T}}\boldsymbol{\lambda}, \tag{10}$$

where $\boldsymbol{\lambda} = [\lambda_1, \lambda_2, \lambda_3]^{\mathrm{T}}$ is the vector of Lagrange multipliers to be considered as nonholonomic constraint forces. $\boldsymbol{\tau} = [\tau_{\mathrm{R}}, \tau_{\mathrm{L}}]^{\mathrm{T}}$ is the input vector with τ_{R} and τ_{L} being the torques at the right and left driving wheel about the wheel shaft, respectively. $\bar{\boldsymbol{\tau}}_{\mathrm{d}}$ is a vector illustrating the model uncertainties such as the unstructured unmodelled dynamic components and the unknown bounded external disturbances such as the unknown external forces such as F$_1$, F$_2$, F$_3$, F$_4$, ϖ (see Figure 1). $\mathbf{N}$ is the input transformation matrix shown as follows:

$$\mathbf{N} = \begin{bmatrix} 0 & 0 & 0 & 0 & 0 & 0 & 1 & 0 \\ 0 & 0 & 0 & 0 & 0 & 0 & 0 & 1 \end{bmatrix}^{\mathrm{T}}.$$

Furthermore, it is easy to develop the following equation:

$$\dot{\mathbf{q}} = \mathbf{S}_1(\mathbf{q})\mathbf{v} + \mathbf{S}_2(\mathbf{q})\dot{\boldsymbol{\gamma}} + \mathbf{S}_3(\mathbf{q})\dot{\eta}, \tag{11}$$

where $\mathbf{v} = [\dot{\phi}_{\mathrm{R}}, \dot{\phi}_{\mathrm{L}}]^{\mathrm{T}}$, $\boldsymbol{\gamma} = [\gamma_{\mathrm{R}}, \gamma_{\mathrm{L}}]^{\mathrm{T}}$,

$$\mathbf{S}_1 = \begin{bmatrix} \left(\frac{r}{2}\cos\theta - \frac{ar}{2b}\sin\theta\right) & \left(\frac{r}{2}\sin\theta + \frac{ar}{2b}\cos\theta\right) & \frac{r}{2b} & 0 & 0 & 0 & 1 & 0 \\ \left(\frac{r}{2}\cos\theta + \frac{ar}{2b}\sin\theta\right) & \left(\frac{r}{2}\sin\theta - \frac{ar}{2b}\cos\theta\right) & -\frac{r}{2b} & 0 & 0 & 0 & 0 & 1 \end{bmatrix}^{\mathrm{T}}$$

$$\mathbf{S}_2 = \begin{bmatrix} \left(\frac{1}{2}\cos\theta - \frac{a}{2b}\sin\theta\right) & \left(\frac{1}{2}\sin\theta + \frac{a}{2b}\cos\theta\right) & \frac{1}{2b} & 0 & 1 & 0 & 0 & 0 \\ \left(\frac{1}{2}\cos\theta + \frac{a}{2b}\sin\theta\right) & \left(\frac{1}{2}\sin\theta - \frac{a}{2b}\cos\theta\right) & -\frac{1}{2b} & 0 & 0 & 1 & 0 & 0 \end{bmatrix}^{\mathrm{T}},$$

$$\mathbf{S}_3 = [-\sin\theta \quad \cos\theta \quad 0 \quad 1 \quad 0 \quad 0 \quad 0 \quad 0]^{\mathrm{T}}$$

Subsequently, taking the time derivative of (11), we obtain:

$$\ddot{\mathbf{q}} = \dot{\mathbf{S}}_1(\mathbf{q})\mathbf{v} + \mathbf{S}_1(\mathbf{q})\dot{\mathbf{v}} + \mathbf{S}_2(\mathbf{q})\ddot{\boldsymbol{\gamma}} + \dot{\mathbf{S}}_2(\mathbf{q})\dot{\boldsymbol{\gamma}} + \dot{\mathbf{S}}_3(\mathbf{q})\dot{\eta} + \mathbf{S}_3(\mathbf{q})\ddot{\eta} \tag{12}$$

It is easy to show that $\mathbf{S}_1^\mathrm{T}\left(\mathbf{q}\right)\mathbf{A}^\mathrm{T}\left(\mathbf{q}\right)=\mathbf{0}_{2\times 3}$, $\mathbf{S}_1^\mathrm{T}\left(\mathbf{q}\right)\mathbf{N}=\mathbf{I}_{2\times 2}$, where $\mathbf{I}_{2\times 2}$ is an unit 2×2 matrix, and $\mathbf{0}_{i\times j}$ is an $i\times j$ zero matrix. Substituting (12) into (10), and then pre-multiplying the both sides of the new equation by $\mathbf{S}_1^\mathrm{T}\left(\mathbf{q}\right)$, we get:

$$\mathbf{M}\dot{\mathbf{v}}+\mathbf{B}\mathbf{v}+\mathbf{Q}\ddot{\mathbf{\gamma}}+\mathbf{C}\omega\dot{\eta}+\mathbf{G}\ddot{\eta}+\mathbf{\tau}_\mathrm{d}=\mathbf{\tau} \tag{13}$$

where $\mathbf{\tau}_\mathrm{d}=\mathbf{S}_1\left(\mathbf{q}\right)\bar{\mathbf{\tau}}_\mathrm{d}$ is a vector illustrating the total uncertainty consisting of the model uncertainties and the unknown bounded disturbances. The matrices in (13) are shown in detailed as follows:

$$\mathbf{M}=\mathbf{S}_1^\mathrm{T}\bar{\mathbf{M}}\mathbf{S}_1=\begin{bmatrix} m_{11} & m_{12}\\ m_{12} & m_{11}\end{bmatrix},\ \mathbf{Q}=\mathbf{S}_1^\mathrm{T}\bar{\mathbf{M}}\mathbf{S}_2=\begin{bmatrix} Q_1 & Q_2\\ Q_2 & Q_1\end{bmatrix},$$

$$\mathbf{C}\omega=\mathbf{S}_1^\mathrm{T}\mathbf{M}\dot{\mathbf{S}}_3=m_\mathrm{G}\frac{r}{2}\begin{bmatrix}1\\1\end{bmatrix}\omega,\ \mathbf{G}=\mathbf{S}_1^\mathrm{T}\mathbf{M}\mathbf{S}_3=m_\mathrm{G}\frac{ar}{2b}\begin{bmatrix}1\\-1\end{bmatrix},$$

$$m_{11}=m_\mathrm{G}\left(\frac{r^2}{4}+\frac{a^2r^2}{4b^2}\right)+\frac{r^2}{4b^2}\left(\mathrm{I}_\mathrm{G}+2\,\mathrm{I}_\mathrm{D}\right)+m_\mathrm{W}r^2+\mathrm{I}_\mathrm{W},$$

$$m_{12}=m_\mathrm{G}\left(\frac{r^2}{4}-\frac{a^2r^2}{4b^2}\right)-\frac{r^2}{4b^2}\left(\mathrm{I}_\mathrm{G}+2\,\mathrm{I}_\mathrm{D}\right),$$

$$Q_{1,2}=m_\mathrm{G}\frac{r}{4}\left(1\pm\frac{a^2}{b^2}\right)\pm\frac{r}{4b}\left(\mathrm{I}_\mathrm{G}+2\,\mathrm{I}_\mathrm{D}\right),\ \mathbf{B}=\mathbf{S}_1^\mathrm{T}\mathbf{M}\dot{\mathbf{S}}_1=m_\mathrm{G}\frac{ar^2}{2b}\omega\begin{bmatrix}0 & 1\\-1 & 0\end{bmatrix}.$$

The parameters of the WMR in the above matrices are illustrated in Table 1.

Table 1

The parameters of a WMR

Symbol	Quantity	Value
m_G	The mass of the platform of the WMR	10 (kg)
I_G	The inertial moment of the platform about the vertical axis through point G.	4 (kg.m^2)
a	The distance between G and M (see Figure 1).	0.2 (m)
C	The distance between P and M (see Figure 3)	0.5 (m)
m_W	The mass of each driving wheel	2 (kg)
I_W	The inertial moment of each driving wheel about the wheel shaft	0.1 (kg.m^2)
I_D	The inertial moment of each wheel about its diameter axis	0.05 (kg.m^2)
b	Half-distance between two the wheels	0.3 (m)
r	The radius of each driving wheel	0.15 (m)

2.3   Structure of SRWNN

Let us use SRWNNs [5], [13], [14], [15] with structure as shown in Figure 2 including N_i inputs, one output, and $N_i \times N_\upsilon$ wavelets in the mother layer as an estimator to compensate the unknown wheel slips, model uncertainties, and unknown bounded external disturbances.

The structure of the SRWNNs comprises 4 layers: one input layer, a mother layer, a product layer, and one output layer. The output of each SRWNN is expressed as follows:

$$y = \sum_{j=1}^{N_\upsilon} \upsilon_j \left(\prod_{k=1}^{N_i} \phi_{jk} \left(z_{jk} \left(N \right) \right) \right) + \sum_{k=1}^{N_i} a_k x_k \left(N \right) \tag{14}$$

Here, the subscript *jk* reveals the *k*-th term of the j-th wavelet, *N* shows the number of iterations; the output *y* approximates an uncertainty; x_k reveals the *k*-th input; a_k seems to be a weight connecting the corresponding input to the output directly; υ_j illustrates the connection weight from the product nodes to the output node, and $z_{jk} \left(N \right) = \left[x \left(N \right) + \rho_{jk} \phi_{jk} \left(N - 1 \right) - \beta_{jk} \right] / \varsigma_{jk}$ with β_{jk}, ς_{jk}, and ρ_{jk} corresponding to the translation factor, the dilation factor, and the weight of self-feedback loop, respectively. $\phi_{jk} \left(N - 1 \right)$ describes the one-step recurrent term of $\phi_{jk} \left(N \right)$.

Besides, the mother wavelets are selected as $\phi_{jk} \left(z_{jk} \right) = -z_{jk} \exp \left(-\dfrac{1}{2} z_{jk}^2 \right)$. In this work, all of a_k, β_{jk}, ς_{jk}, ρ_{jk}, and υ_j are trained online by using the on-line tuning algorithms to be discussed subsequently. For convenience, the vector of all the weights is defined in the following form:

$$\mathbf{w} = \begin{bmatrix} \mathbf{a}^{\mathrm{T}} & \boldsymbol{\beta}^{\mathrm{T}} & \boldsymbol{\varsigma}^{\mathrm{T}} & \boldsymbol{\rho}^{\mathrm{T}} & \boldsymbol{\upsilon}^{\mathrm{T}} \end{bmatrix}^{\mathrm{T}} \tag{15}$$

with
$$\mathbf{a}^{\mathrm{T}} = \begin{bmatrix} a_1, ..., a_k, ... a_{N_i} \end{bmatrix}, \ \boldsymbol{\beta}^{\mathrm{T}} = \begin{bmatrix} \beta_{11}, ..., \beta_{jk}, ... \beta_{N_i N_\upsilon} \end{bmatrix}, \boldsymbol{\varsigma}^{\mathrm{T}} = \begin{bmatrix} \varsigma_{11}, ..., \varsigma_{N_i N_\upsilon} \end{bmatrix},$$
$$\boldsymbol{\rho}^{\mathrm{T}} = \begin{bmatrix} \rho_{11}, ..., \rho_{jk}, ... \rho_{N_i N_\upsilon} \end{bmatrix}, \boldsymbol{\upsilon}^{\mathrm{T}} = \begin{bmatrix} \upsilon_1, ..., \upsilon_j, ..., \upsilon_{N_\upsilon} \end{bmatrix}, \text{with } 1 \le k \le N_i, \ 1 \le j \le N_\upsilon.$$
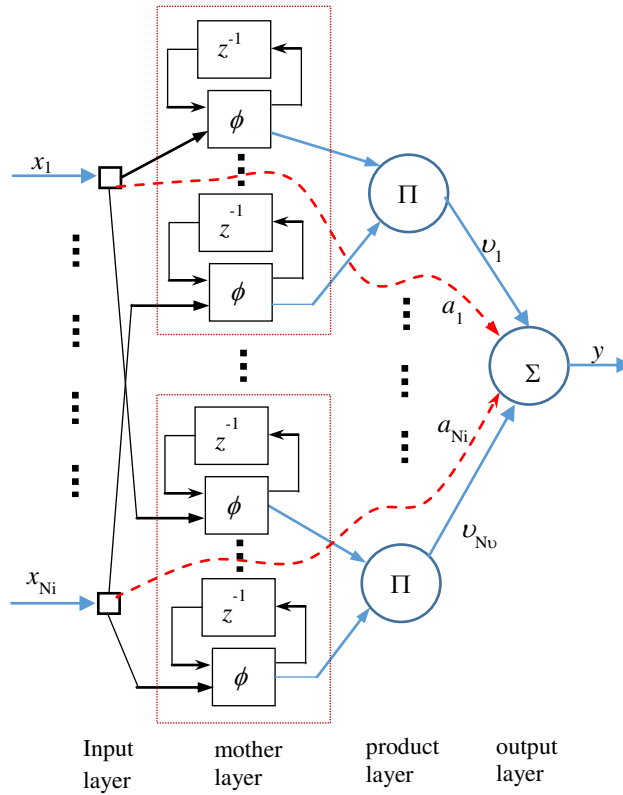
Figure 2
Structure of SRWNN

3 Problem Statement and Designing the Adaptive Sliding Mode Control

3.1 Problem Statement

The control objective is to design the ASMC method using SRWNN for trajectory tracking of the WMR in the presence of the unknown wheel slips, the model uncertainties, and the unknown bounded external disturbances so that the point P of the WMR (see Figure 3) tracks the desired point D without measuring the accelerations and velocities of the wheel slips.
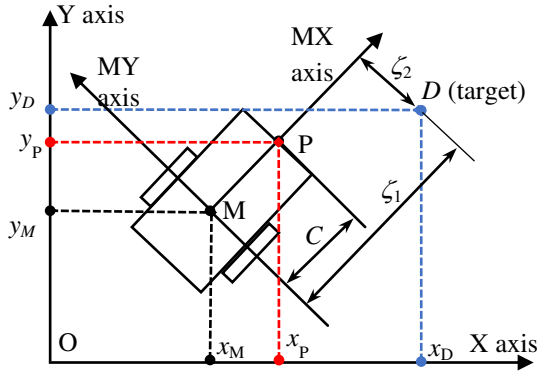
Figure 3
The coordinate of the target is represented in the body coordinate system M-XY

Remark 1: From Figure 3, we indicate (x_P, y_P, θ) as the actual posture of the WMR. Similarly, $(x_{Pd}, y_{Pd}, \theta_d)$ denotes the desired one of the WMR. It is impossible to achieve such an arbitrarily good tracking performance in a finite-time interval when controlling the WMR that the actual posture (x_P, y_P, θ) tracks the desired one $(x_{Pd}, y_{Pd}, \theta_d)$ successfully in the presence of both the longitudinal slip and the lateral slip. In contrast, it is completely possible to obtain the arbitrarily good tracking performance, in a finite-time interval if one wants to control the WMR so that the actual position (x_P, y_P) tracks the desired one (x_{Pd}, y_{Pd}) in such situations (see *Definition 1* and *Definition 2* in [21]).

3.2 Illustrating Sliding Surface

Let O-XY be the global coordinate system, M-XY be the body coordinate system which is attached to the platform of the WMR (see Figure 3). The coordinate vector of the target is represented in M-XY as follows:

$$\zeta = \begin{bmatrix} \zeta_1 \\ \zeta_2 \end{bmatrix} = \begin{bmatrix} \cos\theta & \sin\theta \\ -\sin\theta & \cos\theta \end{bmatrix} \begin{bmatrix} x_D - x_M \\ y_D - y_M \end{bmatrix}, \tag{16}$$

where (x_D, y_D) is the position coordinates of D (see Figure 3).

Computing the second order derivative with respect to time of (16) yields

$$\ddot{\zeta} = \mathbf{h}\dot{\mathbf{v}} + \mathbf{\Psi}_1 + \mathbf{\Psi}_2, \tag{17}$$

where $\mathbf{h} = \begin{bmatrix} \left(\zeta_2 \dfrac{1}{b} - 1\right)\dfrac{r}{2} & -\left(\zeta_2 \dfrac{1}{b} + 1\right)\dfrac{r}{2} \\ -\zeta_1 \dfrac{r}{2b} & \zeta_1 \dfrac{r}{2b} \end{bmatrix}$, $\mathbf{\Psi}_1$ and $\mathbf{\Psi}_2$ are nonlinear components revealed as follows:

$$\mathbf{\Psi}_1 = \dot{\mathbf{h}}\mathbf{v} + \begin{bmatrix} \ddot{x}_{\mathrm{D}}\cos\theta + \ddot{y}_{\mathrm{D}}\sin\theta - \dot{x}_{\mathrm{D}}\mu\sin\theta + \dot{y}_{\mathrm{D}}\mu\cos\theta \\ -\ddot{x}_{\mathrm{D}}\sin\theta + \ddot{y}_{\mathrm{D}}\cos\theta - \dot{x}_{\mathrm{D}}\mu\cos\theta - \dot{y}_{\mathrm{D}}\mu\sin\theta \end{bmatrix}, \text{ with } \mu = \frac{r\left(\dot{\phi}_R - \dot{\phi}_L\right)}{2},$$

and $\mathbf{\Psi}_2 = \begin{bmatrix} -\ddot{\chi} - \dot{x}_{\mathrm{D}}\vartheta\sin\theta + \dot{y}_{\mathrm{D}}\vartheta\cos\theta \\ -\ddot{\eta} - \dot{x}_{\mathrm{D}}\vartheta\cos\theta - \dot{y}_{\mathrm{D}}\vartheta\sin\theta \end{bmatrix}$, with $\chi = \dfrac{\gamma_R + \gamma_L}{2}$, $\vartheta = \dfrac{\dot{\gamma}_R - \dot{\gamma}_L}{2}$.

Remark 2: Owing to $\det(\mathbf{h}) = -\zeta_1 \dfrac{r^2}{2b}$, if $\zeta_1 \neq 0$, then $\mathbf{h}$ in (17) is invertible.

Then, we define the vector of the position tracking errors as $\mathbf{e} = [e_1, e_2]^{\mathrm{T}} = \zeta - \zeta_{\mathrm{d}}$, where ζ_{d} is the desired coordinate vector of the target D in M-XY. From the control objective mentioned in Sub-section 3.1 and Figure 3, one can easily express $\zeta_{\mathrm{d}} = [C, 0]^{\mathrm{T}}$.

A sliding surface is defined as follows:

$$\mathbf{s} = \dot{\mathbf{e}} + \mathbf{\Lambda}\mathbf{e}, \tag{18}$$

where $\mathbf{\Lambda}$ is a 2×2 diagonal, constant, positive definite matrix and can be chosen arbitrarily.

3.3   Structure of the Closed-Loop Control System

To begin with, let us propose the scheme of the whole closed-loop control system as shown in Figure 4.

Afterwards, since directly depending on the accelerations and velocities of the unknown wheel slips which are not measured in this work, $\mathbf{\Psi}_2$ in (17) is unknown. Therefore, let us define an auxiliary variable which can be measured easily as follows:

$$\mathbf{\kappa} = \mathbf{h}^{-1}\left(-\ddot{\zeta}_{\mathrm{d}} + \mathbf{\Lambda}\dot{\mathbf{e}} + \mathbf{\Psi}_1\right), \tag{19}$$

Alternatively, one can rewrite (13) as follows:

$$\mathbf{M}\dot{\mathbf{v}} = \mathbf{\tau} - \mathbf{B}\mathbf{v} - \mathbf{d}, \tag{20}$$

where $\mathbf{d} = \mathbf{Q}\ddot{\boldsymbol{\gamma}} + \mathbf{C}\omega\dot{\eta} + \mathbf{G}\ddot{\eta} + \boldsymbol{\tau}_{\mathrm{d}}$ shows all uncertainties because of the unknown wheel slips, the model uncertainties, and the unknown external disturbances.
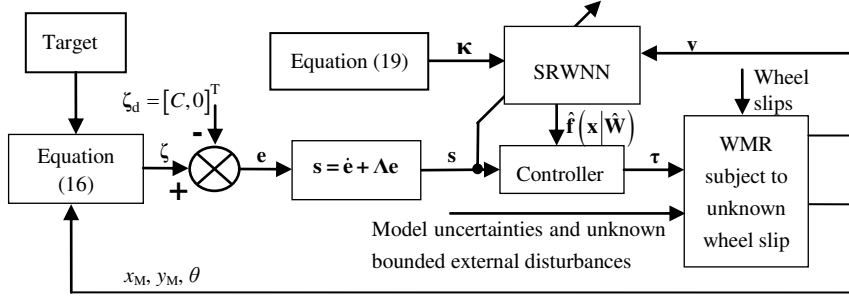
Figure 4
Scheme of the whole closed-loop control system

Adding $\mathbf{M}\boldsymbol{\kappa}$ to both of the sides of (20) and then combining the result with (17), (18), and (19) leads to

$$\mathbf{M}\mathbf{h}^{-1}\dot{\mathbf{s}} = \boldsymbol{\tau} + \mathbf{M}\boldsymbol{\kappa} - \mathbf{B}\mathbf{v} - \mathbf{d} + \mathbf{M}\mathbf{h}^{-1}\boldsymbol{\Psi}_2 \tag{21}$$

Conversely, it is not easy to exactly know dynamic parameters of this WMR such as mass, moments of inertia, etc. Accordingly, it is impossible in order to precisely express all expressions consisting of these quantities. Therefore, one can show (21) in the following form:

$$\hat{\mathbf{M}}\mathbf{h}^{-1}\dot{\mathbf{s}} = \boldsymbol{\tau} - \tilde{\mathbf{M}}\mathbf{h}^{-1}\dot{\mathbf{s}} + \mathbf{M}\boldsymbol{\kappa} - \mathbf{B}\mathbf{v} - \mathbf{d} + \mathbf{M}\mathbf{h}^{-1}\boldsymbol{\Psi}_2, \tag{22}$$

where $\tilde{\mathbf{M}} = \mathbf{M} - \hat{\mathbf{M}}$ with $\hat{\mathbf{M}}$ showing an approximation of $\mathbf{M}$.

Remark 3: both $\mathbf{M}$ and $\hat{\mathbf{M}}$ are always symmetric, invertible, positive definite matrices.

Multiplying both of the sides of (22) by $\mathbf{h}\hat{\mathbf{M}}^{-1}$ yields

$$\dot{\mathbf{s}} = \mathbf{h}\hat{\mathbf{M}}^{-1}\boldsymbol{\tau} + \mathbf{f}(\mathbf{x}), \tag{23}$$

where $\mathbf{f}(\mathbf{x}) = \mathbf{h}\hat{\mathbf{M}}^{-1}\left[-\tilde{\mathbf{M}}\mathbf{h}^{-1}\dot{\mathbf{s}} + \mathbf{M}\boldsymbol{\kappa} - \mathbf{B}\mathbf{v} - \mathbf{d} + \mathbf{M}\mathbf{h}^{-1}\boldsymbol{\Psi}_2 \right]$, $\mathbf{x} = \begin{bmatrix} \mathbf{v}^{\mathrm{T}} & \boldsymbol{\kappa}^{\mathrm{T}} \end{bmatrix}^{\mathrm{T}}$.

Clearly, $\mathbf{x}$ can be measured easily.

Thanks to the strong capability of the SRWNN for approximating unknown nonlinear functions [5], [13], [14], [15], it can be employed in order to approximate $\mathbf{f}(\mathbf{x})$ in (23) of the unknown wheel slips, the model uncertainties, and the unknown bounded external disturbances. By doing this, given a small

positive real number ε_M, there exists a vector of optimal weights $\mathbf{W}^* = \begin{bmatrix} \mathbf{w}_1^{*T} & \mathbf{w}_2^{*T} \end{bmatrix}^T$ such that:

$$\mathbf{f}(\mathbf{x}) = \hat{\mathbf{f}}(\mathbf{x}|\mathbf{W}^*) + \boldsymbol{\varepsilon} \tag{24}$$

Here, $\mathbf{x}$ is used as the input of the SRWNN; $\boldsymbol{\varepsilon}$ is the vector of reconstruction errors and bounded by $\|\boldsymbol{\varepsilon}\| \le \varepsilon_M$. Then, an estimation of $\hat{\mathbf{f}}(\mathbf{x}|\mathbf{W}^*)$ can be expressed as $\hat{\mathbf{f}}(\mathbf{x}|\hat{\mathbf{W}}) = \begin{bmatrix} y_{SRWNN1}, & y_{SRWNN2} \end{bmatrix}^T$ with $\hat{\mathbf{W}} = \begin{bmatrix} \hat{\mathbf{w}}_1^T, \hat{\mathbf{w}}_2^T \end{bmatrix}^T$ corresponding to an estimation of $\mathbf{W}^*$. Particularly, $\mathbf{w}_1^*, \mathbf{w}_2^*, \hat{\mathbf{w}}_1$, and $\hat{\mathbf{w}}_2$ are the weight vectors defined in (15). y_{SRWNN1} and y_{SRWNN2} are the outputs of the SRWNNs as shown in (14).

One can express (24) again in the following form:

$$\mathbf{f}(\mathbf{x}) = \hat{\mathbf{f}}(\mathbf{x}|\hat{\mathbf{W}}) + \left[\hat{\mathbf{f}}(\mathbf{x}|\mathbf{W}^*) - \hat{\mathbf{f}}(\mathbf{x}|\hat{\mathbf{W}})\right] + \boldsymbol{\varepsilon} \tag{25}$$

Let $\tilde{\mathbf{f}}(\mathbf{x}|\tilde{\mathbf{W}})$ be the functional deviation as follows:

$$\tilde{\mathbf{f}}(\mathbf{x}|\tilde{\mathbf{W}}) = \hat{\mathbf{f}}(\mathbf{x}|\mathbf{W}^*) - \hat{\mathbf{f}}(\mathbf{x}|\hat{\mathbf{W}}) \tag{26}$$

Here, $\tilde{\mathbf{W}} = \mathbf{W}^* - \hat{\mathbf{W}}$ is the weight deviation.

The Taylor series expansion of $\tilde{\mathbf{f}}(\mathbf{x}|\tilde{\mathbf{W}})$ around $\hat{\mathbf{W}}$ gives:

$$\tilde{\mathbf{f}}(\mathbf{x}|\tilde{\mathbf{W}}) = \mathbf{f}'(\hat{\mathbf{W}})\tilde{\mathbf{W}} + O(\tilde{\mathbf{W}}) \tag{27}$$

with $\mathbf{f}'(\hat{\mathbf{W}}) = \dfrac{\partial \mathbf{f}(\mathbf{x}|\mathbf{W}^*)}{\partial \mathbf{W}^*}\Big|_{\mathbf{W}^*=\hat{\mathbf{W}}}$, and $O(\tilde{\mathbf{W}})$ denoting higher-order terms in Taylor series expansion.

Due to (25), (26), and (27), we can rewrite (23) as follows:

$$\dot{\mathbf{s}} = \mathbf{h}\hat{\mathbf{M}}^{-1}\boldsymbol{\tau} + \hat{\mathbf{f}}(\mathbf{x}|\hat{\mathbf{W}}) + \mathbf{f}'(\hat{\mathbf{W}})\tilde{\mathbf{W}} + \boldsymbol{\delta}, \tag{28}$$

where $\boldsymbol{\delta} = O(\tilde{\mathbf{W}}) + \boldsymbol{\varepsilon}$.

Now, we propose the control input employing the SRWNNs as follows:

$$\boldsymbol{\tau} = \hat{\mathbf{M}}\mathbf{h}^{-1}\left[-\mathbf{K}\mathbf{s} - \hat{\mathbf{f}}(\mathbf{x}|\hat{\mathbf{W}})\right] \tag{29}$$

where $\mathbf{K}$ is a positive definition matrix and can be chosen arbitrarily.

Furthermore, the on-line tuning algorithms for all the weights are proposed as follows:

$$\dot{\hat{\mathbf{W}}} = \Gamma \left[\mathbf{f}'\left(\hat{\mathbf{W}} \right) \right]^{\mathrm{T}} \mathbf{s} - \sigma \Gamma \|\mathbf{s}\| \hat{\mathbf{W}}, \tag{30}$$

where Γ and σ are positive tuning gains and can be selected arbitrarily.

3.4   Stability

Assumption 1: the optimal weight vector $\mathbf{W}^*$ is bounded such that $\|\mathbf{W}^*\| \le \mathrm{W_M}$.

It is worth noting that $\mathrm{W_M}$ is not used to perform the proposed controller. It is, however, just employed with the purpose of analyzing the stability of the entire closed-loop control system.

Assumption 2: all of $x_\mathrm{D}, y_\mathrm{D}, \dot{x}_\mathrm{D}, \dot{y}_\mathrm{D}, \ddot{x}_\mathrm{D},$ and $\ddot{y}_\mathrm{D}$ are available and bounded.

Assumption 3: the accelerations and velocities of the unknown wheel slips are bounded.

Assumption 4: $\boldsymbol{\delta}$ in (28) is bounded such that $\|\boldsymbol{\delta}\| \le b_\delta$ with $b_\delta > 0$.

Theorem 1: *Let us consider the WMR subject to the unknown wheel slips, the model uncertainties, and the unknown bounded external disturbances with the kinematics (5) and the dynamics (13). If the control input using the SRWNN is proposed as (29), the weight vector is adjusted by (30), and Assumptions 1-4 are satisfied, then the errors,* $\mathbf{s}$ *and* $\tilde{\mathbf{W}}$, *of the closed-loop control system as shown in Figure 4 are uniformly ultimately bounded and further* $\mathbf{s}$ *can be kept arbitrarily small.*

Proof: Substitution of (29) into (28) results in the dynamics of the sliding vector as follows:

$$\dot{\mathbf{s}} = -\mathbf{K}\mathbf{s} + \mathbf{f}'\left(\hat{\mathbf{W}} \right) \tilde{\mathbf{W}} + \boldsymbol{\delta} \tag{31}$$

By contrast, a Lyapunov candidate function is chosen as follows:

$$V = \frac{1}{2}\mathbf{s}^{\mathrm{T}}\mathbf{s} + \frac{1}{2}\Gamma^{-1}\tilde{\mathbf{W}}^{\mathrm{T}}\tilde{\mathbf{W}} \tag{32}$$

Taking the first derivative of *V* with time leads to

$$\dot{V} = \mathbf{s}^{\mathrm{T}}\dot{\mathbf{s}} + \Gamma^{-1}\tilde{\mathbf{W}}^{\mathrm{T}}\dot{\tilde{\mathbf{W}}} \tag{33}$$

Because of $\dot{\tilde{\mathbf{W}}} = -\dot{\hat{\mathbf{W}}}$, substituting (30) and (31) into (33) achieves

$$\dot{V} = \mathbf{s}^{\mathrm{T}}\left(-\mathbf{Ks}+\boldsymbol{\delta}\right)+\sigma\|\mathbf{s}\|\,\tilde{\mathbf{W}}^{\mathrm{T}}\left(\mathbf{W}^{*}-\tilde{\mathbf{W}}\right), \tag{34}$$

According to Assumption 1, it is useful to point out the following inequality:

$$\tilde{\mathbf{W}}^{\mathrm{T}}\left(\mathbf{W}^{*}-\tilde{\mathbf{W}}\right) \le \mathrm{W_M}\left\|\tilde{\mathbf{W}}\right\| - \left\|\tilde{\mathbf{W}}\right\|^{2} \tag{35}$$

Substitution of (35) into (34) leads to

$$\dot{V} \le -K_{\min}\left\|\mathbf{s}\right\|^{2} + \left\|\mathbf{s}\right\|\left\|\boldsymbol{\delta}\right\| + \sigma\|\mathbf{s}\|\left(\mathrm{W_M}\left\|\tilde{\mathbf{W}}\right\| - \left\|\tilde{\mathbf{W}}\right\|^{2}\right) \tag{36}$$

here $K_{\min}$ is the minimum singular value of $\mathbf{K}$.

Due to $\mathrm{W_M}\left\|\tilde{\mathbf{W}}\right\| \le \dfrac{1}{2}\left(\mathrm{W_M}\right)^{2} + \dfrac{1}{2}\left(\left\|\tilde{\mathbf{W}}\right\|\right)^{2}$, we have

$$\dot{V} \le -\|\mathbf{s}\|\left(K_{\min}\left\|\mathbf{s}\right\| + \dfrac{1}{2}\sigma\left\|\tilde{\mathbf{W}}\right\|^{2} - b_{\delta} - \dfrac{1}{2}\sigma\,\mathrm{W_M^{2}}\right) \tag{37}$$

Observing (37) reveals that $\dot{V}$ is guaranteed to be negative definite as long as the term in the braces seems to be positive, that is, the following inequality is correct:

$$K_{\min}\left\|\mathbf{s}\right\| + \dfrac{1}{2}\sigma\left\|\tilde{\mathbf{W}}\right\|^{2} > b_{\delta} + \dfrac{1}{2}\sigma\,\mathrm{W_M^{2}} \tag{38}$$
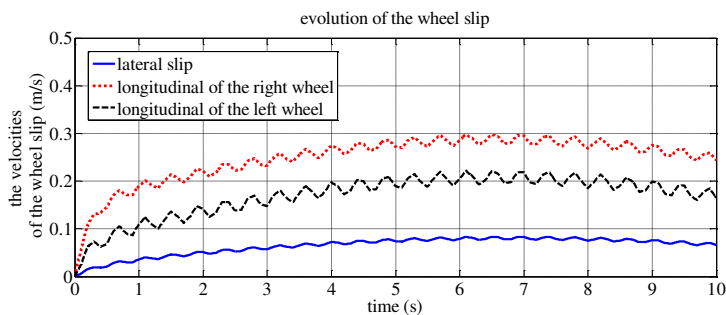
Figure 5
Evolution of the wheel slips
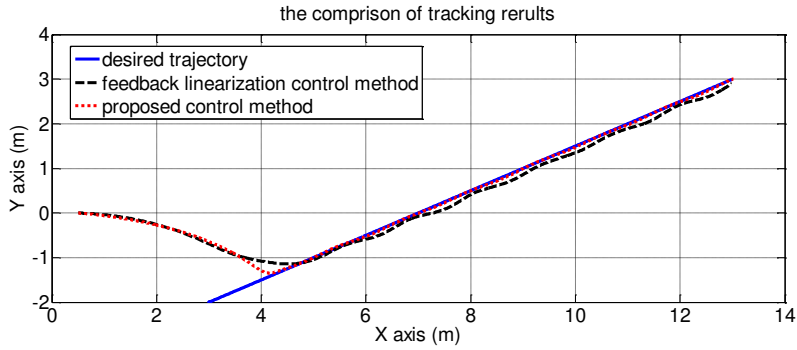
Figure 6

Comparison of tracking performances in Example 1
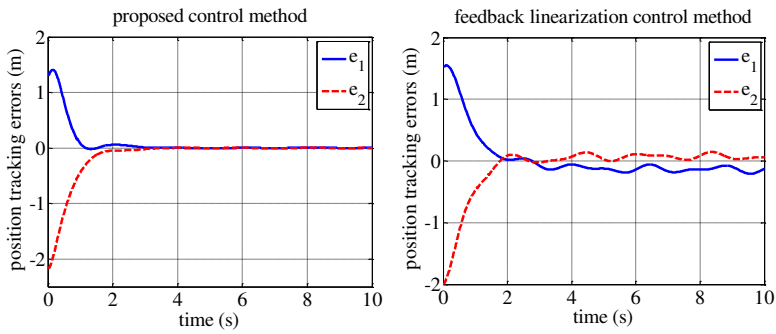
Figure 7

Comparison of position tracking errors in Example 1
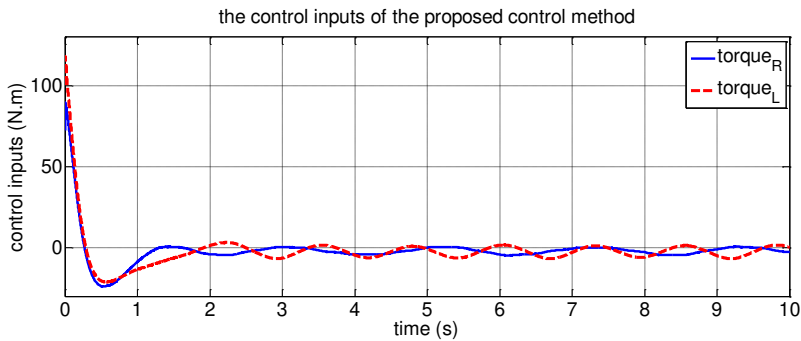
Figure 8

Control inputs of the proposed control method in Example 1

As a consequence of this, according to Lyapunov theory and LaSalle extension, the error vectors, both $\mathbf{s}$ and $\tilde{\mathbf{W}}$, are uniformly ultimately bounded in a compact set as follows:

$$\mathbf{U_B} = \left\{ \mathbf{s}, \tilde{\mathbf{W}} \left| K_{\min} \|\mathbf{s}\| + \frac{1}{2}\sigma \|\tilde{\mathbf{W}}\|^2 \le b_\delta + \frac{1}{2}\sigma \, W_M^2 \right. \right\} \tag{39}$$

As can be seen from (39), $\mathbf{s}$ can be kept as small as possible by increasing $K_{\min}$ suitably.

4   Simulation Results

In this section, computer simulations for trajectory tracking of the WMR were implemented to verify the correctness and effectiveness of the proposed control method. Moreover, a comparison between the tracking performance of this proposed control method and that of the feedback linearization control method [11] was executed to confirm the strong points of this proposed control method.

For comparison, both of the two methods were performed under the same condition that there existed the model uncertainties and the unknown bounded external disturbances, and the accelerations and velocities of the unknown wheel slips were not measured. Namely, without loss generality, it was assumed that $\boldsymbol{\tau}_d = \begin{bmatrix} 3 + \sin(0.5t), & 2.5 + \cos(0.4t) \end{bmatrix}^T$ (N.m), and the unknown wheel slips between the floor and the driving wheels are illustrated as Figure 5. Furthermore, the estimation of the matrix $\mathbf{M}$ was assumed as $\hat{\mathbf{M}} = 0.8\mathbf{M}$.

The control parameters were chosen as K = diag([6, 6]), $\boldsymbol{\Lambda} = diag\left([2, \quad 2]\right)$. For simplicity, there was only one product node in each SRWNN. The weight tuning gains were set as $\Gamma = 0.005$, and $\sigma = 0.15$. The initial values of the weight matrices were chosen to random numbers in [0, 1], other than that the weights of the self-feedback loops were chosen as 0. The initial posture of the WMR was assumed as $x_P = C = 0.5$ (m), $y_P = 0$ (m), and $\theta = 0$ (rad).

For illustration, two the following examples were carried out by Matlab/Simulink software.

Example 1: the target D was on a straight line with the following motion equation:

$$\begin{cases} x_D = 4 + t, \\ y_D = -2 + 0.5t \end{cases}. \tag{40}$$

Simulation results are shown in Figure 6, Figure 7, and Figure 8.
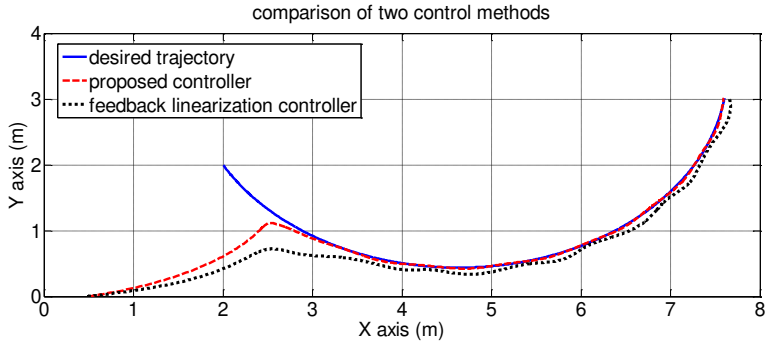
Figure 9

Comparison of tracking performances in Example 2
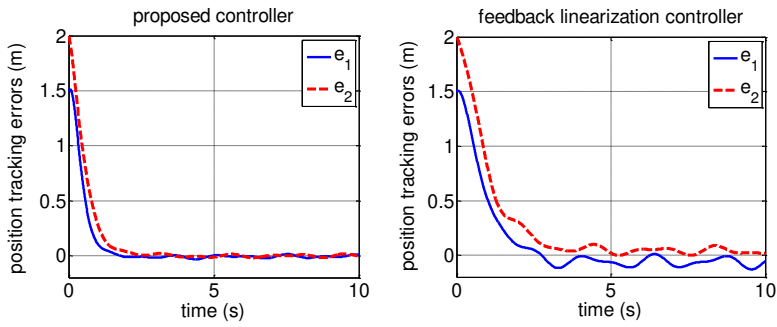
Figure 10

Comparison of position tracking errors in Example 2
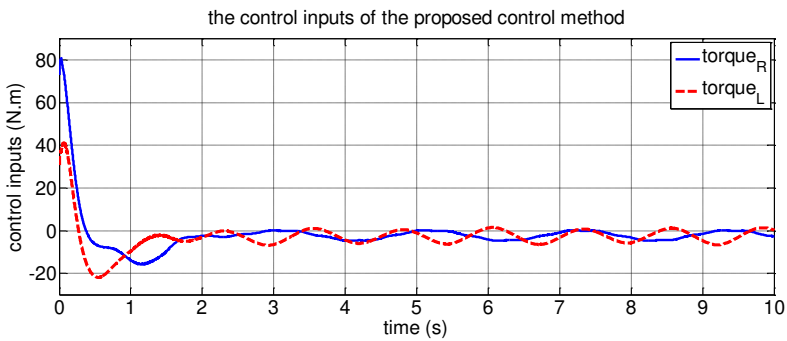
Figure 11

Control inputs of the proposed control method in Example 2

It is obvious from Figure 6 and Figure 7 that when the accelerations and velocities of the unknown wheel slips were not measured, and there existed the model uncertainties and the unknown bounded external disturbances; the approach in [11] could not overcome their undesired effects, whereas the proposed control method managed to effectively compensate the undesired effects. In addition, the control inputs of the latter were bounded as shown in Figure 8.

Example 2: the target D moved on a circular trajectory expressed as follows:

$$\begin{cases} x_D = 5 - 3\cos(0.25t), \\ y_D = 2 - 3\sin(0.25t) \end{cases}. \tag{41}$$

The tracking performance is shown in Figure 9, Figure 10, and Figure 11.

Noticeably, regardless of the unknown wheel slips, the model uncertainties, and the unknown bounded disturbances, the proposed control method managed to compensate their effects very effectively whereas the approach in [11] could not. Furthermore, the control inputs of the proposed method were bounded as illustrated in Figure 11.

It should also note that in Figure 7 and Figure 10 the position tracking errors of the proposed control method almost converged to zero, but that of the approach in [11] did not. In general, the tracking performance of the former is better than that of the latter in both the above examples.

It is clear that the vector of the position tracking errors, **e** in (18), converged to an arbitrarily small neighbourhood of the origin, thus, ζ_1 converged to an adjustable small neighbourhood of C. Consequently, according to Remark 2, one can easily conclude that **h** in (17), (19), (21), (22), and (29) is invertible.

From these simulation results, we can draw a conclusion that Theorem 1 is true and the proposed control method is robust against the unknown wheel slips, the model uncertainties, and the unknown bounded external disturbances.

Conclusion

In this work, an ASMC method based on SRWNN, with the online tuning algorithms has been developed, to allow the WMR to track a desired trajectory with the desired tracking performance, in the presence of the unknown wheel slips, model uncertainties and unknown bounded external disturbances. It is unnecessary for initial offline training for the weights of the SRWNN, since they can be initialized without difficulty. The online tuning algorithms are established from standard Lyapunov theory and LaSalle extension. It has been shown that not only the position tracking errors, but also, the neural network weight errors, are uniformly, ultimately bounded, via standard Lyapunov theory and LaSalle extension. The former can be kept arbitrarily small, by choosing the control gains appropriately. The results of the computer simulation confirmed the veracity and effectiveness of the proposed controller.

References

[1]   T. Fukao, H. Nakagawa, and N. Adachi: Adaptive tracking control of a nonholonomic mobile robot, *IEEE Trans. Robot. Automat*., Vol. 16, No. 5, pp. 609-615, Oct. 2000

[2]   M. S. Kim, J. H. Shin, S. G. Hong, and J. J. Lee: Designing a robust adaptive dynamic controller for nonholonomic mobile robots under modeling uncertainties and disturbances, *Mechatronics*, Vol. 13, No. 5, pp. 507-519, 2003

[3]   D. Sousa, E. M. Hemerly, and R. K. H. Galvao: Adaptive control for mobile robot using wavelet networks, *IEEE Trans. Syst., Man, Cybern. B, Cybern*, Vol. 32, No. 4, pp. 493-504, Aug. 2002

[4]   D. K. Chwa: Sliding-mode tracking control of nonholonomic wheeled mobile robots in polar coordinates, *IEEE Trans. Control Syst. Technol*., Vol. 12, No. 4, pp. 637-644, Jul. 2004

[5]   B. S. Park, S. J. Yoo, J. B. Park, and Y. H. Choi: Adaptive neural sliding mode control of nonholonomic wheeled mobile robots with model uncertainty, *IEEE Trans. Control Syst. Technol*., Vol 17, No. 1, pp. 207-214, Jan. 2009

[6]   H. Gao, X. Song, L. Ding, K. Xia, N. Li, Z. Deng: Adaptive motion control of wheeled mobile robot with unknown slippage," *Int. J. Control*, Vol. 87, No. 8, pp. 1513-1522, Feb, 2014

[7]   M. Seyr, S. Jakubek, Proprioceptive Navigation: Slip Estimation and Slip Control for Autonomous Wheeled Mobile Robots, in: *Proc. RAM*, Bangkok, Thailand, 2006, pp. 1-6

[8]   L. Chang Boon, W. Danwei: Integrated Estimation for Wheeled Mobile Robot posture, velocities, and wheel skidding perturbations, in: *Proc. ICRA*, Roma, Italy, 2007, pp. 2355-2360

[9]   J.-C. Ryu, S.K. Agrawal: Differential flatness-based robust control of mobile robots in the presence of slip, *Int. J. Robot. Res.* Vol 30, pp. 463-475, 2011

[10]   Y. Tian, N. Sarkar: Control of a mobile robot subject to wheel slip," *J. Intell. Robot. Syst*., Vol. 74, pp. 915-929, 2014

[11]   N. V. Tinh, N. T. Linh, P. T. Cat, P. M. Tuan, M. N. Anh, N. P. Anh: Modeling and Feedback Linearization Control of a Nonholonomic Wheeled Mobile Robot with Longitudinal, Lateral Slips, In: *Proc. CASE*, Fort Worth, TX, USA., 2016, pp 996-1001

[12]   F. L. Lewis, A. Yesildirek, and K. Liu: Multilayer neural-net robot controller with guaranteed tracking performance, *IEEE Trans. Neural Networks*, Vol. 7, pp. 1-12, 1996

[13]   S. J. Yoo, Y. H. Choi, and J. B. Park: Generalized predictive control based on self-recurrent wavelet neural network for stable path tracking of mobile robots: Adaptive learning rate approach, *IEEE Trans. Cir-cuit Syst. I, Reg. Papers*, Vol. 53, No. 6, pp. 1381-1394, Jun. 2006

[14]   S. J. Yoo, J. B. Park, and Y. H. Choi: Adaptive dynamic surface control of flexible-joint robots using self-recurrent wavelet neural network, *IEEE Trans. Syst., Man, Cybern. B, Cybern*., Vol. 36, No. 6, pp. 1342-1355, Dec. 2006

[15]   S. J. Yoo, J. B. Park, and Y. H. Choi: Indirect adaptive control of nonlinear dynamic systems using self recurrent wavelet neural network via adaptive learning rates, *Inf. Sci*., Vol. 177, No. 15, pp. 3074-3098, 2007

[16]   C. C. Ku and K. Y. Lee: Diagonal recurrent neural networks for dy-namic systmes control, *IEEE Trans. Neural Netw*., Vol. 6, No. 1, pp. 144-156, Jan. 1995

[17]   F. J. Lin, T. S. Lee, and C. H. Lin: Robust controller design with recurrent neural network for linear synchronous motor drive, *IEEE Trans. Ind. Electron*., Vol. 50, No. 3, pp. 456-470, May/Jun. 2003

[18]   B. Delyon, A. Juditsky, and A. Benveniste: Accuracy analysis for wavelet approximations, *IEEE Trans. Neural Netw*., Vol. 6, No. 2, pp. 332-348, Mar. 1995

[19]   Y. Oussar, I. Rivals, L. Personnaz, and G. Dreyfus: Training wavelet networks for nonlinear dynamic input-output modeling, *Neuro-comput*., Vol. 20, pp. 173-188, 1998

[20]   S. J. Yoo: Approximation-based adaptive control for a class of mobile robots with unknown skidding and slipping, *Inter J Contr, Autom, Syst,* Vol. 10, No. 4, pp. 703-710, 2012

[21]   D. Wang and C. B. Low: Modeling and analysis of skidding and slipping in wheeled mobile robots: control design perspective, *IEEE Trans. on Robotics*, Vol. 24, No. 3, pp. 676-687, Jun, 2008

Dynamic Stability of a Thin Plate Subjected to Bi-Axial Edged Loads

Abbas Talimian, Péter Béda

Department of Vehicle Elements and Vehicle-Structure Analysis, Budapest University of Technology and Economics, Műegyetem rakpart 3, 1111 Budapest, Hungary; talimian@kme.bme.hu, bedap@kme.bme.hu

Abstract: The first dynamic stability of a thin rectangular plate made from linear elastic material and subjected to a bi-axial time dependent load is discussed in this study. The plate carries a combination of loads that are changing linearly with respect to the length of its edges. It is also supposed that its boundary conditions on the edges are simply supported. Relevant inertia, elastic stiffness, and stability matrices are derived by applying Finite Difference Method from a differential motion equation of the plate. Subsequently, Mathieu-Hill equation form is obtained for the plate and the first dynamic stability boundaries of the plate are elaborated for using specified load parameters.

Keywords: rectangular plate; Finite Difference Method (FDM); bi-axial load; Dynamic stability; Mathieu-Hill equations

1 Introduction

Thin plates are used in several structures as elements for different applications such as aerospace, civil structures, containers, ships, and machinery parts. These elements are subjected to various loading types, e.g. statics, dynamic and thermal as well. Sometimes these loads are reactions from other elements. The present study models a situation when a rectangular plate as a structure's element is subjected to loads acting on its edges. Loads are in-plane and vary along the length of the edge as a general condition. Loads' effect on an element behaviour is crucial, especially when these parts are subjected to time-dependent loading. In the designing procedure of a machine's elements, determining buckling load (static stability) and doing dynamic stability analysis can give a better overview of either a structure or its elements while it is loaded with different force types. Up to now, numerous literature has been discussed concerning these fields of study.

A rectangular plate with localised zones of damage and loaded by either uni- or bi-axial compressive uniform edge load(s) was considered by Prabhakara and Datta for studying the free vibration and static stability analysis by application of finite

element analysis. The plate was discussed while parameters such as damage size, its position, boundary condition and aspect ratio were changing [1]. They worked on the tension and compression buckling of a square plate with localised zones of damage and loaded partially on its edge by using finite element method. A plate stability was discussed with respect to damage location and its size as well as the position of load [2]. Their study was extended for a plate with internal opening while in-plane compressive or periodic tensile loading acted on the plate's edge. The study was done for different shapes and cut-out sizes [3].

Deolasi and Datta studied a plate subjected to localised in-plane either compressive or tensile periodic edge loads for finding buckling loads and parametric instability analysis. The transverse shear deformation and rotary inertia were considered as well. The load type, its band and location effect on vibration and parametric instability were elaborated [4]. They also applied finite element method to obtain the equilibrium equation of a simply supported rectangular plate subjected to partially in-plane periodic loading for investigating the damping effect on the behaviour of simple and combination resonances. The method of multiple scales was applied for obtaining boundaries of parametric instability region's relations [5].

A research was done on a rectangular plate with completely elastically restrained boundaries by application of the variational method for governing equations. The plate rested on the non-homogeneous foundation as well and was subjected to a uniform compressive in-plane bi-axial time-dependent load. The foundation has two regions with different stiffness, but symmetric about the centre lines of the plate. The method of multiple scales was applied for analysing Mathieu-Hill equations and elaborating stability boundaries [6]. Sahu and Datta used the first order shear deformation theory for modelling the doubly curved panels to consider the effects of transverse shear deformation and rotary inertia. They used finite element analysis application for obtaining parametric instability characteristics of the panels. It was supposed loads on edges are various in-plane static and periodic compressive, including partial and concentrated type [7]. The study was continued for studying parametric instability behaviour of curved panels with cut-outs with in-plane static and periodic compressive edge loadings [8]. Kumar et al. investigated vibration and dynamic instability behaviour of laminated composite plates subjected to partially distributed non-conservative follower forces and uniaxial in-plane point and patch tensile edge loadings by consideration of finite element method and first order shear deformation theory for modelling laminated composite plates and doubly curved panels [9, 10]. Dynamic instability analysis was done for stiffened plates carried in-plane partial and concentrated edge loadings by Srivastava et al. The plate and the stiffeners were modelled as separate elements and the compatibility between these two types of elements is maintained [11]. Tensile buckling, vibration, and parametric instability behaviour of doubly curved panels with central circular cut-out regarding uniaxial in-plane partially distributed tensile edge loadings were studied by Ravi Kumar et al. [12]. They

also expanded their research to laminated composite doubly curved panels, subjected to non-uniform follower load. Their formulation was based on the extension of dynamic, shear deformable theory according to Sanders' first approximation for doubly curved laminated shells [13]. Static and dynamic instability analysis were done for stiffened shell panels with a uniform in-plane harmonic edge by Patel et al. [14]. They used eight-node isoparametric degenerated shell element for shell panels and three-node curved beam element for stiffeners.

Whenever the loading types are not constant or a structure is complex, solving the partial differential equation of motion will be impossible from analytical methods point of view and a numerical solution technique such as finite element method has to be applied to estimate a solution and studying free vibration and static stability analysis of thin isotropic plates [15, 16].

There are also some suggestions on the basis of either exact or numerical method for seeking a solution for deriving the partial differential equation of motion. The majority of these studies focused on either uniaxial constant in-plane loads or pressure acts perpendicular to the plate face leading to a constant coefficient differential motion equation (i.e. some of the most recent studies are [17-21]). The buckling load was derived by the help of Differential Quadrature Method (DQM) for a thin rectangular plate while it was loaded by either uni- or bi-axial concentrated loads meanwhile different combination of simply supports and clamped boundary conditions were involved [22].

Another possible numerical method for estimating solutions is the Finite Difference Method (FDM), which is based on replacing differential equations with corresponding difference equations (see [23, 24]). Using FDM makes solving the differential form of motion equation straightforward. Werfalli and Karoud studied free vibration of thin isotropic rectangular plates having various boundary conditions [25]. They used a Galerkin-based finite element method for deriving a mathematical model represents the vibration behaviour of the plate. Cubic quadrilateral serendipity elements with twelve degrees of freedom were considered in their analysis. An available Modified Discrete Kirchhoff Quadrilateral (MDKQ) element that is developed based on Classical Plate Theory (CPT) by using discrete Kirchhoff technique is applied by Patil in free vibration response analysis of a thin isotropic rectangular plate [26]. This method had just considered only for static analysis of plate formerly. It was also tried to assess the accuracy of the developed finite element formulation in analysing the vibration response of a thin isotropic rectangular plate that has different boundary conditions and geometrical dimensions ratios. An Ordinary Finite Difference Method (OFDM), was applied in pure bending and free vibration analysis of a thin flat rectangular plate by Ezeh, et al. [27, 28].

To our best knowledge, there has been no study for considering the influence of linear bi-axial loading effect on the dynamic stability of a thin plate.

A Ph.D. dissertation was written on the investigation of parametric instability of thin plates [29]. The motion equation of the plate was derived on basis of the first order shear theory by using the FEM. However, the author just discussed the axial loading effect on the dynamic stability regions. Here, we have a thin plate as a simplification model. It is supposed the displacement field is continuous and its derivatives exist for sufficient times, hence applying FDM helps to derive inertia, elastic stiffness and stability matrices for the plate from a differential motion equation easily. As a consequence, the dynamic stability analysis is done for linear bi-axial loading.

2   Problem Formulation

Here a thin rectangular plate that is made from a linear elastic material is considered. a and b are plate's width and height along the x_1- and x_2- axes respectively, Figure 1. h is the thickness of the plate along the x_3- axis. While a thin plate is selected for the study, it is supposed the ratio of thickness to the smallest dimension is lower than five percent ($h/b \leq 0.05$). The plate is subjected to different linearly in-plane bi-axial loads on its edges as shown in Figure 2. The following assumptions, which are fundamental points in the small-deflection plate theory, are valid here as well [24].
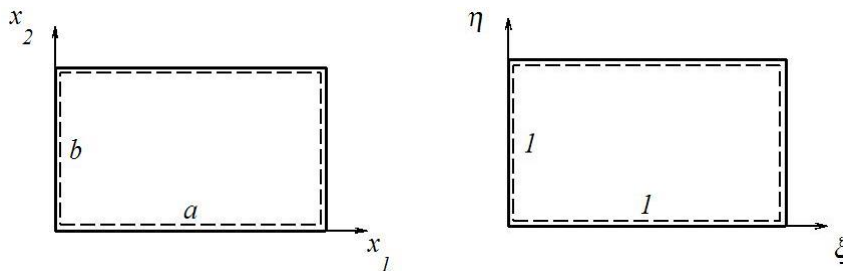
Figure 1

Plate Dimensions

It is supposed that: (1) There is no deflection in the plate's mid-surface in comparison with its thickness and, consequently, the square of the slope can be omitted compared to unity. (2) Plane sections normal to mid-surface initially remain plane and normal to the surface after bending. (3) The translation's component along to the normal axis to the mid-surface is independent of x_3-.

The differential motion equation of a thin plate subjected to bi-axial in-plane load is given by [24, 30],

$$D\nabla^4\tilde{w}+\rho h\frac{\partial^2\tilde{w}}{\partial t^2}=q+N_{x_1}\frac{\partial^2\tilde{w}}{\partial x_1^2}+2N_{x_1x_2}\frac{\partial^4\tilde{w}}{\partial x_2^2\partial x_1^2}+N_{x_2}\frac{\partial^2\tilde{w}}{\partial x_2^2}. \tag{1}$$

where ρ represents density per unit volume and time is given by t. Normally distributed load per unit area on the plate surface, in-plane forces per unit length acting on plate's edges in the direction of x_1- and x_2- axes are q, N_{x_1}, N_{x_2} respectively. The shearing force per unit length in the $x_1\,x_2$- the plane is $N_{x_1x_2}$. The *Flexural rigidity* of a plate is E and v are *Young's modulus* and *Poisson's ratio* respectively. $\tilde{w}$, is the time-dependent displacement, with angular speed of ω, along the axis perpendicular to the plate's plane,

$$\tilde{w}=w(x_1,x_2,t). \tag{2}$$

Assume that there is no shear load ($N_{x_1x_2}=0$) and normally distributed load ($q=0$) acting on the plate. In-plane forces (N_{x_1} and N_{x_2}) acting on the plate's edges that varying along a length, are:

$$N_{x_1}=-N_0\left(1-\frac{\alpha x_2}{b}\right), \quad N_{x_2}=-N_0\left(1-\frac{\beta x_1}{a}\right). \tag{3}$$

In-plane load intensity is N_0. α and β are selected numbers (α, β={1,2}) and are called load parameters. The possible bi-axial loading is given in Figure 2. Substituting (2) and (3) to the differential motion equation of plate (1) gives the following equation

$$D\nabla^4 w+\rho h\frac{\partial^2 w}{\partial t^2}+N_0\left(1-\frac{\alpha x_2}{b}\right)\frac{\partial^2 w}{\partial x_1^2}+N_0\left(1-\frac{\beta x_1}{a}\right)\frac{\partial^2 w}{\partial x_2^2}=0, \tag{4}$$

It is supposed here the plate has *simply supported* boundary conditions on its edges which prevent transverse deflection and allows rotations. These boundary conditions equations are given as,

$$\begin{cases} w(0,x_2)=0, \ w(a,x_2)=0, \\ w(x_1,0)=0, \ w(x_1,b)=0. \end{cases}$$

$$\begin{cases} \left.\dfrac{\partial^2 w(x_1,x_2)}{\partial x_1^2}\right|_{x_1=0}=0, \quad \left.\dfrac{\partial^2 w(x_1,x_2)}{\partial x_1^2}\right|_{x_1=a}=0, \\[2mm] \left.\dfrac{\partial^2 w(x_1,x_2)}{\partial x_2^2}\right|_{x_2=0}=0, \quad \left.\dfrac{\partial^2 w(x_1,x_2)}{\partial x_2^2}\right|_{x_2=b}=0. \end{cases} \tag{5}$$

The non-dimensional parameters for the horizontal, ξ and vertical axes, η (see Figure 1) are introduced as,

$$x_1=\xi a, \quad \begin{cases} for \ x_1=0, \ \xi=0. \\ for \ x_1=a, \ \xi=1. \end{cases} \quad and \quad x_2=\eta b, \quad \begin{cases} for \ x_2=0, \ \eta=0. \\ for \ x_2=b, \ \eta=1. \end{cases} \tag{6}$$

Hence the equation of motion of the plate (4) is written in non-dimensional form,

$$\zeta^2 \frac{\partial^2 w}{\partial t^2} + \left(\frac{\partial^4 w}{\partial \xi^4} + 2r^2 \frac{\partial^4 w}{\partial \xi^2 \partial \eta^2} + r^4 \frac{\partial^4 w}{\partial \eta^4} \right) + \bar{N} \left((1-\alpha\eta)\frac{\partial^2 w}{\partial \xi^2} + r^2(1-\beta\xi)\frac{\partial^2 w}{\partial \eta^2} \right) = 0. \quad (7)$$

$$N_{x_1} = -N_0\left(1-\frac{x_2}{b}\right) , \ N_{x_2} = -N_0\left(1-\frac{x_1}{a}\right). \qquad N_{x_1} = -N_0\left(1-\frac{x_2}{b}\right) , \ N_{x_2} = -N_0\left(1-\frac{2x_1}{a}\right).$$

$$N_{x_1} = -N_0\left(1-\frac{2x_2}{b}\right) , \ N_{x_2} = -N_0\left(1-\frac{x_1}{a}\right). \qquad N_{x_1} = -N_0\left(1-\frac{2x_2}{b}\right) , \ N_{x_2} = -N_0\left(1-\frac{2x_1}{a}\right).$$
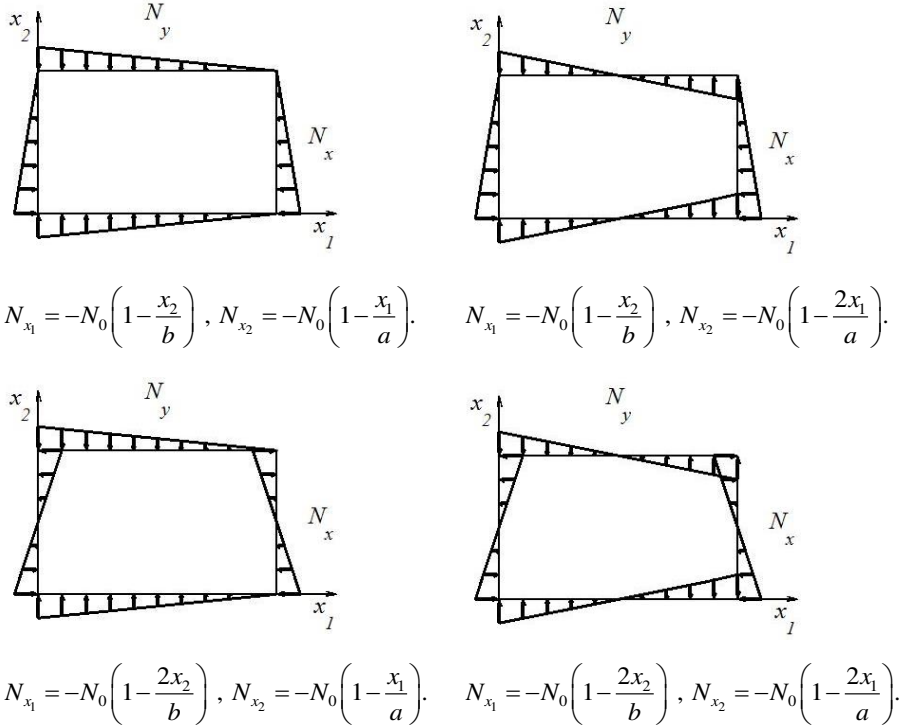
Figure 2

Loading types

r, is a geometrical aspect that represents the ratio of plate's length over its height. Buckling load and frequency factors are $\bar{N} = N_0 a^2 \big/ D$ and $\zeta^2 = \rho h a^4 \big/ D$ respectively. Boundary conditions (5) are also given as non-dimension equations,

$$\begin{cases} w(0,\eta)=0, \ w(1,\eta)=0, \\ w(\xi,0)=0, \ w(\xi,1)=0. \end{cases} \ and \ \begin{cases} \left.\dfrac{\partial^2 w(\xi,\eta)}{\partial \xi^2}\right|_{\xi=0} = 0, \quad \left.\dfrac{\partial^2 w(\xi,\eta)}{\partial \xi^2}\right|_{\xi=1} = 0, \\[2mm] \left.\dfrac{\partial^2 w(\xi,\eta)}{\partial \eta^2}\right|_{\eta=0} = 0, \quad \left.\dfrac{\partial^2 w(\xi,\eta)}{\partial \eta^2}\right|_{\eta=1} = 0. \end{cases} \quad (8)$$

3 Discretization of the Problem: Finite Difference Method

Finite difference method as a numerical method is used in solving a differential equation. Here the motion equation of the plate (7) is given by a fourth order differential equation. For approximating each term of it with difference equation on solution's domain the plate's surface is uniformly discretized to $N{\times}N$ equal sub-domain rectangular meshes. The length and width of each mesh's grid equal to $1/N$, Consequently, each node's abscissa and ordinate are,

$$\begin{cases} \xi_i = i/N, & i = 1...N. \\ \eta_j = j/N, & j = 1...N. \end{cases} \tag{9}$$
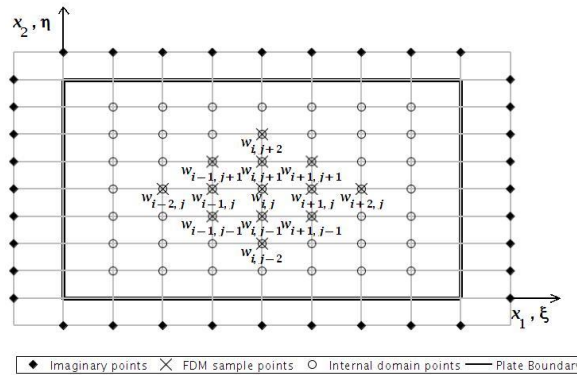
Figure 3

Internal, boundary and imaginary points of a plate

The second and fourth derivatives of displacement field respect to the selected non-dimensional parameters for the horizontal and vertical axes are defined subsequently on the basis of central difference formulas for node $w_{i,j}(\xi,\eta)$ (i.e. [24, 27, 28]),

$$\frac{1}{N^2}\left(\frac{\partial^2 w(\xi,\eta)}{\partial \xi^2}\right) = \left(w_{i-1,j} + w_{i+1,j}\right) - 2w_{i,j},$$

$$\frac{1}{N^2}\left(\frac{\partial^2 w(\xi,\eta)}{\partial \eta^2}\right) = \left(w_{i,j-1} + w_{i,j+1}\right) - 2w_{i,j}. \tag{10}$$

$$\frac{1}{N^4}\left(\frac{\partial^4 w(\xi,\eta)}{\partial \xi^4}\right) = \left(w_{i-2,j} + w_{i+2,j}\right) - 4\left(w_{i-1,j} + w_{i+1,j}\right) + 6w_{i,j},$$

$$\frac{1}{N^4}\left(\frac{\partial^4 w(\xi,\eta)}{\partial \xi^2 \partial \eta^2}\right) = \left(w_{i-1,j+1} + w_{i+1,j+1} + w_{i-1,j-1} + w_{i+1,j-1}\right)$$

$$- 2\left(w_{i-1,j} + w_{i+1,j} + w_{i,j-1} + w_{i,j+1}\right) + 4w_{i,j},$$

$$\frac{1}{N^4}\left(\frac{\partial^4 w(\xi,\eta)}{\partial \eta^4}\right) = \left(w_{i,j-2} + w_{i,j+2}\right) - 4\left(w_{i,j-1} + w_{i,j+1}\right) + 6w_{i,j}. \tag{11}$$

The plate's differential equation of motion (7) terms is replaced with relevant difference equations (10) and (11). Boundary conditions have to be also modified with consideration of (10) and are written as,

$$\begin{cases} w_{0,j} = w_{N,j} = 0, & j = 1\ldots N. \\ w_{i,0} = w_{i,N} = 0, & i = 1\ldots N. \end{cases}$$
$$\begin{cases} w_{-1,j} = -w_{1,j}, & w_{N+1,j} = -w_{N-1,j}, & j = 1\ldots N. \\ w_{i,-1} = -w_{i,1}, & w_{i,N+1} = -w_{i,N-1}, & i = 1\ldots N. \end{cases} \tag{12}$$

A set of algebraic equations is derived for every internal point of a plate, Figure 3. These equations are collected in a matrix equation,

$$\underline{\underline{M}}\, \ddot{\underline{w}} + \left(\underline{\underline{K}} + \bar{N}\underline{\underline{S}}\right)\underline{w} = \underline{0}. \tag{13}$$

$\underline{\underline{M}}$, is a diagonal matrix and called either mass or inertia matrix as its elements are mass properties. Elastic stiffness and stability matrices are given by $\underline{\underline{K}}$ and $\underline{\underline{S}}$ respectively. They are band matrices and their elements are computed from second and third group equations in (7). Elastic behaviour of the plate is affected by $\underline{\underline{K}}$'s elements while loading terms are collected in $\underline{\underline{S}}$. $\underline{w}$ is a nodal displacement vector contains internal points' displacements of the plate, Figure 3, along with normal axis x_3- perpendicular to the mid-surface plane of the plate.

4 Dynamic Stabiliy Analysis, the Basic Solution

The plate is subjected to in-plane time-dependent loads on its edges. External loads (3) on the plate's edges are,

$$N_0(t) = N_s + N_d \cos(\Omega t), \tag{14}$$

as a function of time. N_s and N_d are the static and dynamic amplitude of time-dependent load respectively.

Ω represents an *excitation frequency*, (14) is simplified in the form of,

$$N_0(t) = \frac{1}{2} N_{cr0}\left(\lambda + \mu \, cos(\Omega t)\right). \tag{15}$$

N_{cr0}, represents the critical buckling load and can be calculated by solving the eigenvalue problem (13) for $\bar{N}$ if stability analysis at static loads is considered. Static load factor, λ, and dynamic load factor, μ, are defined by comparing (14) and (15).

$$\lambda = \frac{2N_s}{N_{cr0}}, \qquad \mu = \frac{2N_d}{N_{cr0}}. \tag{16}$$

Substituting in-plane time-dependent load (15) in plate's motion equation(13), one has,

$$\underline{\underline{M}}\ddot{\underline{w}} + \left(\underline{\underline{K}} + \frac{1}{2}N_{cr0}\left(\lambda + \mu\,cos(\Omega t)\right)\underline{\underline{S}}\right)\underline{w} = \underline{0}. \tag{17}$$

The latter equation is *Mathieu-Hill* [31]. Some methods have been advised for solving these type of equations, as the experimental solutions, i.e. Bolotin monograph, Galerkin, Lyapunov's second method, asymptotic techniques, perturbation and iteration [32-36]. There exists no analytic solution for (17), second order differential equations with a periodic coefficient in general. Hence, an approximated time-dependent periodic function is used as a trial solution based on a method advised and applied in [31] with a *2T* period (a first approximation of the first region of stability) for (17).

$$\underline{w} = \sum_{k=1,3,5,\cdots}^{\infty} \underline{a_k} \sin\left(\frac{k\Omega t}{2}\right) + \underline{b_k} \cos\left(\frac{k\Omega t}{2}\right),$$

$$\ddot{\underline{w}} = -\left(\frac{k\Omega}{2}\right)^2 \underline{w}. \tag{18}$$

Introducing (18) into (17) returns the motion equation of the plate as

$$\sum_{k=1,3,5,\cdots}^{\infty} \left[-\underline{\underline{M}}\left(\frac{k\Omega}{2}\right)^2 + \underline{\underline{K}} + \frac{1}{2}\lambda N_{cr0}\underline{\underline{S}}\right]\left(\underline{a_k}\sin\left(\frac{k\Omega t}{2}\right) + \underline{b_k}\cos\left(\frac{k\Omega t}{2}\right)\right)$$

$$+ \frac{1}{2}\mu\cos(\Omega t)N_{cr0}\underline{\underline{S}}\left(\underline{a_k}\sin\left(\frac{k\Omega t}{2}\right) + \underline{b_k}\cos\left(\frac{k\Omega t}{2}\right)\right) = \underline{0}. \tag{19}$$

From the mathematics point of view of trigonometric relations in sine and cosine multiplication (19) can be simplified. (19) is easily separated by sine and cosine terms as far as they are linearly independent mathematical functions. The final form of motion equation of the plate is,

$$\sum_{k=1,3,5,\cdots}^{\infty} \sin\left(\frac{k\Omega t}{2}\right)\left[-\underline{\underline{M}}\left(\frac{k\Omega}{2}\right)^2 + \underline{\underline{K}} + \frac{1}{2}\lambda N_{cr0}\underline{\underline{S}}\right]\underline{a_k}$$

$$+\frac{1}{4}\mu N_{cr0}\underline{\underline{S}}\left[\sin\left((k+2)\frac{\Omega t}{2}\right) + \sin\left((k-2)\frac{\Omega t}{2}\right)\right]\underline{a_k}$$

$$+\cos\left(\frac{k\Omega t}{2}\right)\left[-\underline{\underline{M}}\left(\frac{k\Omega}{2}\right)^2 + \underline{\underline{K}} + \frac{1}{2}\lambda N_{cr0}\underline{\underline{S}}\right]\underline{b_k} \qquad (20)$$

$$+\frac{1}{4}\mu N_{cr0}\underline{\underline{S}}\left[\cos\left((k+2)\frac{\Omega t}{2}\right) + \cos\left((k-2)\frac{\Omega t}{2}\right)\right]\underline{b_k} = \underline{0}.$$

Selecting just first two counters in (20) (*k=1, 3*) to obtain the first dynamic stability regions leads (21). It has to be solved for having a non-trivial solution, hence each matrix's determinant has to be zero. These equations are separated into two independent eigenvalue problems regarding the linear independence of the unknown constant in (18), $\underline{a_k}$ and $\underline{b_k}$.

$$\begin{bmatrix} \boxed{-\left(\frac{\Omega}{2}\right)^2\underline{\underline{M}} + \underline{\underline{K}} + \frac{1}{2}N_{cr0}\left(\lambda - \frac{\mu}{2}\right)\underline{\underline{S}}} & \frac{1}{4}N_{cr0}\mu\underline{\underline{S}} \\ \frac{1}{4}N_{cr0}\mu\underline{\underline{S}} & -\left(\frac{3\Omega}{2}\right)^2\underline{\underline{M}} + \underline{\underline{K}} + \frac{1}{2}N_{cr0}\lambda\underline{\underline{S}} \end{bmatrix}\begin{bmatrix} \underline{a_1} \\ \underline{a_3} \end{bmatrix} +$$

$$\begin{bmatrix} \boxed{-\left(\frac{\Omega}{2}\right)^2\underline{\underline{M}} + \underline{\underline{K}} + \frac{1}{2}N_{cr0}\left(\lambda + \frac{\mu}{2}\right)\underline{\underline{S}}} & \frac{1}{4}N_{cr0}\mu\underline{\underline{S}} \\ \frac{1}{4}N_{cr0}\mu\underline{\underline{S}} & -\left(\frac{3\Omega}{2}\right)^2\underline{\underline{M}} + \underline{\underline{K}} + \frac{1}{2}N_{cr0}\lambda\underline{\underline{S}} \end{bmatrix}\begin{bmatrix} \underline{b_1} \\ \underline{b_3} \end{bmatrix} = \underline{0}. \qquad (21)$$

The first elements of the eigenvalue problem (22) are just selected for analysing the dynamic stability of the plate and returns the first dynamic stability boundaries. Dynamic stability analysis of a structure, here a thin plate, is closely related to changing in parameters such as *Ω*, N_{cr0}, *λ* and *μ*. The excitation frequency is supposed to be a ratio of the natural frequency of the plate ($\Omega = \phi\,\omega$). Here, ϕ is *Excited Frequency Ratio*. While no load acts on the plate ($\bar{N} = 0$) the natural frequency of the plate, *ω*, can be calculated from (13).

$$\det\left(-\frac{\varphi^2\omega^2}{4}\underline{\underline{M}} + \underline{\underline{K}} + \frac{1}{2}\bar{N}_{cr0}\left(\lambda - \frac{\mu}{2}\right)\underline{\underline{S}}\right) = 0,$$

$$\det\left(-\frac{\varphi^2\omega^2}{4}\underline{\underline{M}} + \underline{\underline{K}} + \frac{1}{2}\bar{N}_{cr0}\left(\lambda + \frac{\mu}{2}\right)\underline{\underline{S}}\right) = 0. \qquad (22)$$

5   Results and Calculations

The first dynamic stability boundaries, show domains where the plate goes to be either stable or lose its stability respect to time-dependent excitation load, are plotted from (22) and illustrated in Figure 4. Plots are drawn here for three different static load factors (λ={0.3,0.6,0.9}). If effective parameters, ϕ, and μ, are selected from inside boundaries' region, the plate loses its stability. On the other hand, whenever latter parameters are chosen from these boundaries' outside, the plate's motion regarding assumed load (15) remains stable.

(α=1, β=1, λ=0.3)   (α=1, β=1, λ=0.6)   (α=1, β=1, λ=0.9)

(α=2, β=1, λ=0.3)   (α=2, β=1, λ=0.6)   (α=2, β=1, λ=0.9)

(α=1, β=2, λ=0.3)   (α=1, β=2, λ=0.6)   (α=1, β=2, λ=0.9)

(α=2, β=2, λ=0.3)   (α=2, β=2, λ=0.6)   (α=2, β=2, λ=0.9)
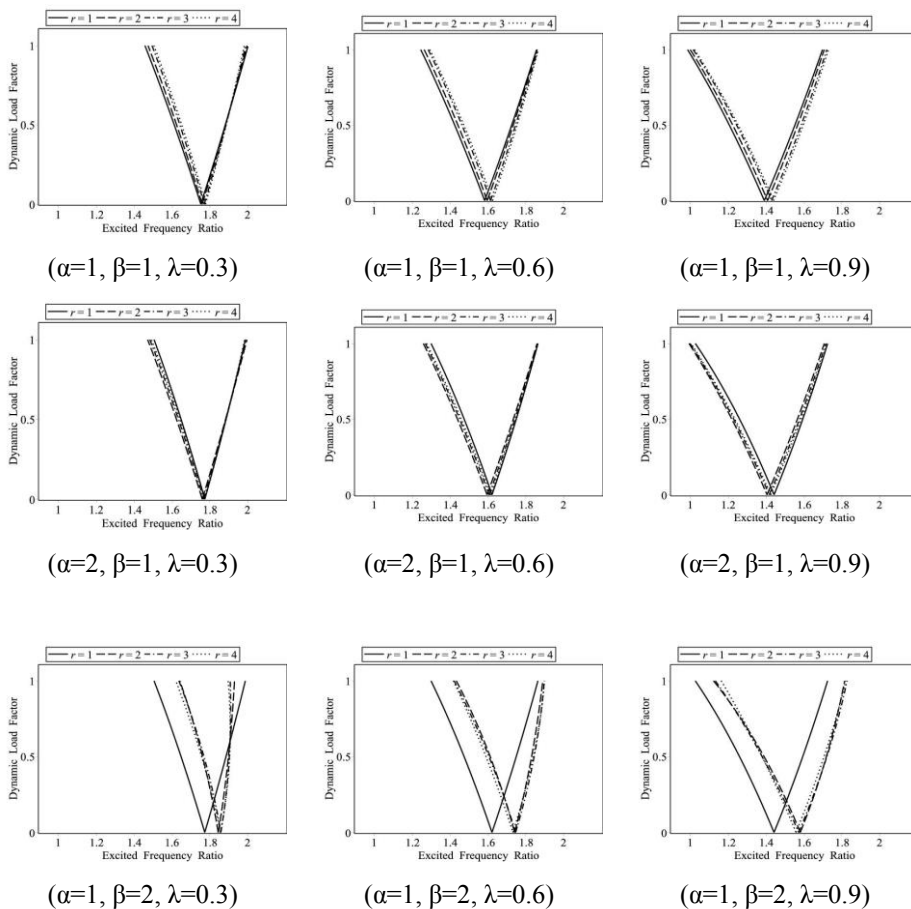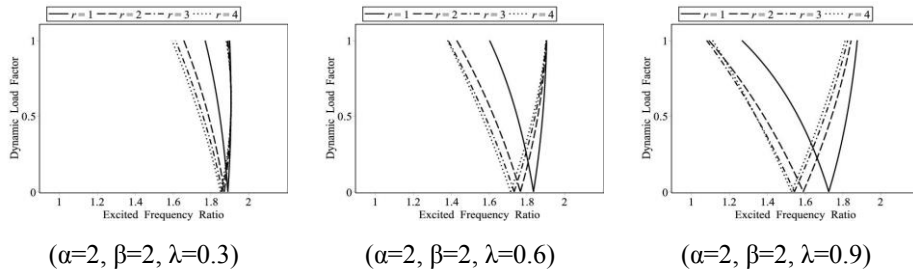
Figure 4
Dynamic Stability Diagrams

Conclusions

In this study, a thin rectangular plate is made from linear elastic material subjected to bi-axial time dependent loads was supposed. A combination of two in-plane load act on edges, changing linearly respect to the length, was considered. The plate has simply supported boundary conditions on its edges. The plate's displacement field is continuous and can be differentiated sufficient time hence the Finite Difference Method is applied for solving the fourth order differential equation of the motion. The first dynamic stability boundaries of the plate respect to load parameters and static load factor are illustrated in Figure 4. According to these results, following points can be obtained.

Increasing the share of the static load factor λ causes the first stability range of the plate regardless any combination of load types being decreased (borders' gap are going to be wider).

Generally, the plate loses its stability around lower excited frequency ratios whenever greater numbers are selected for the static load factor.

Whenever in-plane loads acting on the plate's edges have same shapes, enlarging the geometrical aspect ratio leads the plate loses its stability in wider ranges.

References

[1]   D. L. Prabhakara and P. K. Datta, Vibration and static stability characteristics of rectangular plates with a localized flaw, *Computers & Structures,* 49 (5) (1993) 825-836

[2]   D. L. Prabhakara and P. K. Datta, Static and dynamic elastic behaviour of damaged plates subjected to local inplane loads, *Marine Structures,* 9 (8) (1996) 811-818

[3]   D. L. Prabhakara and P. K. Datta, Vibration, buckling and parametric instability behaviour of plates with centrally located cutouts subjected to in-plane edge loading (Tension or compression), *Thin-Walled Structures,* 27 (4) (1997) 287-310

[4]   P. J. Deolasi and P. K. Datta, Parametric instability characteristics of rectangular plates subjected to localized edge loading (compression or tension), *Computers & Structures,* 54 (1) (1995) 73-82

[5]   P. J. Deolasi and P. K. Datta, Simple and combination resonances of rectangular plates subjected to non-uniform edge loading with damping, *Engineering Structures,* 19 (12) (1997) 1011-1017

[6]   K. N. Saha, R. C. Kar, and P. K. Datta, Dynamic stability of a rectangular plate on non-homogeneous winkler foundation, *Computers & Structures,* 63 (6) (1997) 1213-1222

[7]   S. K. Sahu and P. K. Datta, Parametric Instability of Doubly Curved Panels Subjected to Non-Uniform Harmonic Loading, *Journal of Sound and Vibration,* 240 (1) (2001) 117-129

[8]   S. K. Sahu and P. K. Datta, Dynamic Stability of Curved Panels With Cutouts, *Journal of Sound and Vibration,* 251 (4) (2002) 683-696

[9]   L. R. Kumar, P. K. Datta, and D. L. Prabhakara, Dynamic instability characteristics of laminated composite plates subjected to partial follower edge load with damping, *International Journal of Mechanical Sciences,* 45 (9) (2003) 1429-1448

[10]   L. R. Kumar, P. K. Datta, and D. L. Prabhakara, Tension buckling and dynamic stability behaviour of laminated composite doubly curved panels subjected to partial edge loading, *Composite Structures,* 60 (2) (2003) 171-181

[11]   A. K. L. Srivastava, P. K. Datta, and A. H. Sheikh, Dynamic instability of stiffened plates subjected to non-uniform harmonic in-plane edge loading, *Journal of Sound and Vibration,* 262 (5) (2003) 1171-1189

[12]   L. Ravi Kumar, P. K. Datta, and D. L. Prabhakara, Tension buckling and parametric instability characteristics of doubly curved panels with circular cutout subjected to nonuniform tensile edge loading, *Thin-Walled Structures,* 42 (7) (2004) 947-962

[13]   L. Ravi Kumar, P. K. Datta, and D. L. Prabhakara, Dynamic instability characteristics of laminated composite doubly curved panels subjected to partially distributed follower edge loading, *International Journal of Solids and Structures,* 42 (8) (2005) 2243-2264

[14]   S. N. Patel, P. K. Datta, and A. H. Sheikh, Buckling and dynamic instability analysis of stiffened shell panels, *Thin-Walled Structures,* 44 (3) (2006) 321-333

[15]   R. I and S. C. Mohanty, Study on Free Vibration Analysis of Rectangular Plate Structures Using Finite Element Method, *Procedia Engineering,* 38 (2012) 2758-2766

[16] B. C. L. Vanam, M. Rajyalakshmi, and R. Inala, Static analysis of an isotropic rectangular plate using finite element analysis (FEA), *Journal of Mechanical Engineering Research,* 4 (4) (2012) 148-162

[17] L. V. Kurpa and A. B. Linnik, Studying The Vibrations of In-Plane Loaded Plates of Variable Thickness, *International Applied Mechanics,* 41 (1) (2005) 62-69

[18] M. Bodaghi and A. R. Saidi, Buckling analysis of functionally graded Mindlin plates subjected to linearly varying in-plane loading using power series method of Frobenius, *International Journal of Engineering, Transactions B: Applications,* 25 (1) (2011) 89-106

[19] S. Hosseini-Hashemi, M. Fadaee, and S. R. Atashipour, A new exact analytical approach for free vibration of Reissner–Mindlin functionally graded rectangular plates, *International Journal of Mechanical Sciences,* 53 (2011) 11-22

[20] A. R. Pouladkhan, J. Emadi, and M. Safamehr, Numerical Study of Buckling of Thin Plates, *World Academy of Science, Engineering and Technology,* 78 (2011) 152-157

[21] A. J. Wilson and S. Rajasekaran, Elastic stability of all edges simply supported, stepped and stiffened rectangular plate under uniaxial loading, *Applied Mathematical Modelling,* 36 (2012) 5758-5772

[22] X. Wang and Y. Wang, Buckling analysis of thin rectangular plates under uniaxial or biaxial compressive point loads by the differential quadrature method, *International Journal of Mechanical Sciences,* 101-102 (2015) 38-48

[23] Ć. B. Dolićanin, V. B. Nikolić, and D. Ć. Dolićanin. (2010) Application of Finite Difference Method to Study of the Phenomenon in the Theory of Thin Plates. *Applied Mathematics, Informatics and Mechanics*. 29-43

[24] A. C. Ugural, *Stresses in Beams, Plates, And Shells*, Third ed.: CRC Press, Taylor and Francis Group, 2011

[25] N. M. Werfalli and A. A. Karoud, Free Vibration Analysis of Rectangular Plates Using Galerkin-Based Finite Element Method, *International Journal of Mechanical Engineering,* 2 (2) (2012) 59-67

[26] A. S. Patil, Free Vibration Analysis of Thin Isotropic Rectangular Plate, *International Journal of Innovative Research in Science, Engineering and Technology,* 3 (4) (2014) 77-80

[27] J. C. Ezeh, O. M. Ibearugbulem, and C. I. Onyechere, Free-Vibration Analysis of Thin Rectangular Flat Plates Using Ordinary Finite Difference Method, *Academic Research International,* 4 (2) (2013) 187-192

[28] J. C. Ezeh, O. M. Ibearugbulem, and C. I. Onyechere, Pure Bending Analysis of Thin Rectangular Flat Plates Using Ordinary Finite Difference

Method, *International Journal of Emerging Technology and Advanced Engineering,* 3 (3) (2013) 20-23

[29]   S. S. Kolukula, Investigation of parametric instability in elastic structures, 2013

[30]   A. W. Leissaa and J.-H. Kang, Exact solutions for vibration and buckling of an SS-C-SS-C rectangular plate loaded by linearly varying in-plane stresses, *International Journal of Mechanical Sciences,* 44 (2002) 1925-1945

[31]   W. Chau Xie, *Concept of Stability*: Cambridge University Press, 2010

[32]   P. Pedersen, Stability of the solutions to Mathieu-Hill equations with damping, *Ingenieur-Archiv,* 49 (1) (1980) 15-29

[33]   E. Grebenikov, Y. A. Mitropolsky, and Y. A. Ryabov, *Asymptotic Methods in Resonance Analytical Dynamics*: CRC Press, 2004

[34]   F. Verhulst, Methods and Applications of Singular Perturbations: Boundary Layers and Multiple Timescale Dynamics: Springer New York, 2006

[35]   M. Bessa, Perturbations of Mathieu equations with parametric excitation of large period, *Advances in Dynamical Systems and Applications,* (2010)

[36]   M. Gadella, H. Giacomini, and L. Lara, Periodic analytic approximate solutions for the Mathieu equation, *Applied Mathematics and Computation,* 271 (2015) 436-445

Multilevel Inverter Topology with Modified Pulse Width Modulation and Reduced Switch Count

Thiyagarajan Venkatraman[1], Somasundaram Periasamy[2]

[1] Dept. of Electrical and Electronics Engineering, SSN College of Engineering, Chennai, Tamilnadu, India (thiyagarajanv@ssn.edu.in)

[2] Dept. of Electrical and Electronics Engineering, Anna University, Chennai, Tamilnadu, India (mpsomasundaram@annauniv.edu)

Abstract: This paper proposes a new inverter topology with minimum switches, which generates a larger numbers of output voltage levels. The major advantages of the presented topology are minimum number of power switches, minimum cost, reduction in installation area and less switching losses. Different algorithms for determination of the magnitude of voltage sources are presented. Digital based switching scheme has been proposed for low switching frequency operation. Comparative analysis of the proposed inverter topology with earlier presented topologies shows that the performance of the proposed topology is improved as compared with conventional and other recently developed topology. The performance of the presented inverter has been analyzed by simulation, using MATLAB and also the feasibility of the topology has been validated experimentally.

Keywords: multilevel inverter; symmetric inverter; asymmetric inverter; total harmonic distortion

1 Introduction

Multilevel inverter (MLI) plays a crucial role in the field of power electronics and widely been employed in high power low voltage applications [1, 2]. It synthesizes a desired staircase output voltage waveform from multiple input DC voltage sources [3]. The DC sources used for MLI may be capacitors, batteries, photovoltaic, wind and fuel cell. Conventional multilevel inverters such as diode-clamped [4, 5], flying capacitor [6, 7] and cascaded H-bridge (CHB) inverters [8, 40] have widely been used over last few decades. Among these topologies, CHB MLI has received more attention because of its simple structure and modularity. It consists of several isolated DC sources and H-bridge units. Based on the magnitude of these isolated DC voltage sources, CHB MLI has been classified as

symmetric and asymmetric [9]. In symmetric type inverter, the magnitudes of DC sources are equal which offers superior modularity, whereas the magnitude of DC voltage sources are not equal in the asymmetric type inverter [10]. It is possible to achieve higher number of output levels during asymmetric operation as compared with symmetric operation for the same amount of switches and DC sources. To achieve large number of output levels, CHB requires increased number of components which increases the complexity and cost. Many researchers proposed new inverter topologies with reduced switch count [9-29]. However, the reduction in the switch count increases the number of sources and power rating of the switching devices [11].

Coupled inductors based 9-level inverter is proposed in [1]. But this topology does not reduces the number of switching components compared to conventional CHB MLI. A generalized topology of the multilevel inverter with coupled inductors is presented in [2]. In order to minimize the size of the inductors, the DC component in the corresponding voltage and current waveforms are eliminated by proper switching strategy. This inverter topology reduces the number of DC sources, however fails to minimize the number of switches. Multicarrier sinusoidal PWM based multilevel inverter is presented in [11]. A fuzzy logic controller [49] based multilevel converter for photovoltaic systems is proposed in [50] This system does not require any optimal PWM switching-angle generator and proportional–integral controller. The cascaded inverter with regeneration capability is proposed in [12]. However, the number of switches is same as CHB MLI. A symmetrical type inverter with reduced switching components is proposed in [13]. In this topology, when the magnitude of DC voltages are not same, it is difficult to achieve all possible output levels. A 5-level inverter topology is presented in [14]. In this, each basic unit consists of conventional H-bridge, one bidirectional switch and two DC sources. In [15], modular current source inverter is presented which operates in both symmetric and asymmetric modes. This topology requires proper current control to achieve all possible output levels. A T-type inverter with modified multiple reference multicarrier based PWM technique is presented in [16]. In [17], a modified modular MLI using series-parallel conversion of DC sources is proposed. This topology requires two independent sources to achieve same number of voltage levels as compared with conventional CHB MLI. A transformer based symmetric and asymmetric type CHB MLI is presented in [18]. In this topology, the peak inverse voltage of the switching devices is reduced considerably. However, the inverter size is bulky because of the presence of transformer. Another topology of multilevel inverter is presented in [19]. This topology reduces the voltage sources and the number of switches compared to CHB MLI. But, it is not possible to achieve all possible levels of output voltage. Also, this topology needs more number of bidirectional switches for achieving the constant number of output voltage levels. The multilevel inverter topology proposed in [20] operates in both symmetric and asymmetric mode. It also reduces the number of switches to achieve higher output levels. The major drawback of this topology is its complex control algorithm to control the switching operations.

A 4-level inverter is presented in [21]. This topology uses single DC source to achieve the required output levels. The drawback of this inverter topology is it fails to achieve zero level voltage which results in increased switching losses. As compared with the inverter topology presented [36, 48], the proposed topology synthesizes larger number of output levels for the same number of switching components and DC sources.

This paper presents a new inverter topology with a high number of steps associated with a minimum number of power switches. The operation of the proposed inverter topology and different algorithms for the determination of the DC voltage magnitude is presented in Section 2. A brief comparison study is presented in Section 3. The digital based modulation scheme with low switching frequency is explained in Section 4. Simulation results for a symmetrical 9-level and asymmetrical 31-level inverter are presented in Section 5. Section 6 presents the experimental results which show the practicality of the proposed inverter topology and the conclusions are given in Section 7.

2   Proposed Inverter Topology

The proposed structure of the new inverter topology with polarity changing unit is shown in Fig. 1. This topology consists of basic unit and H-bridge unit. The basic unit of the proposed structure is made of two DC voltage sources and four main switches. This inverter topology operates in both symmetric and asymmetric operation.

(a)   (b)
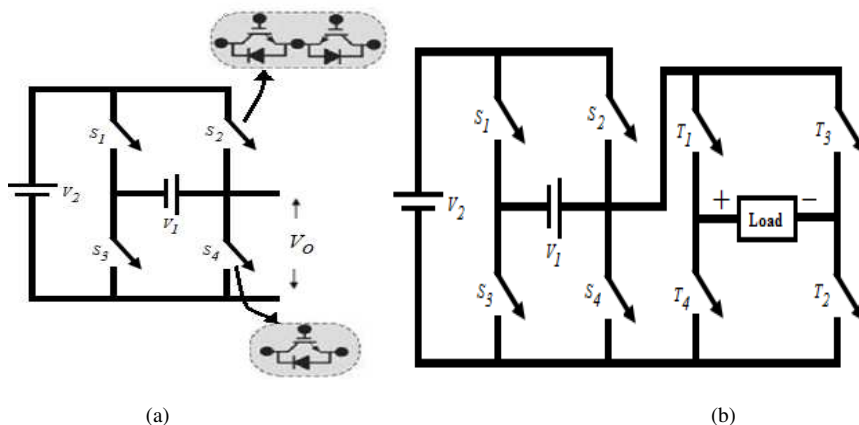
Figure 1

Proposed inverter topology (a) Basic unit (b) With H-bridge inverting unit

2.1   Operation

The different operating modes of the proposed inverter is shown in Fig. 2. The switches T_1, T_2 and T_3, T_4 helps to reverse the polarity of the output voltage of the basic unit. In this, the switch S_4 is used to achieve the zero voltage across the load.

(a) V_1

(b) V_2

(c) $V_1 + V_2$

(b) $-V_1$

(e) $-V_2$

(f) $-(V_1 + V_2)$

(g) 0 (During Positive cycle)

(h) 0 (During Negative cycle)
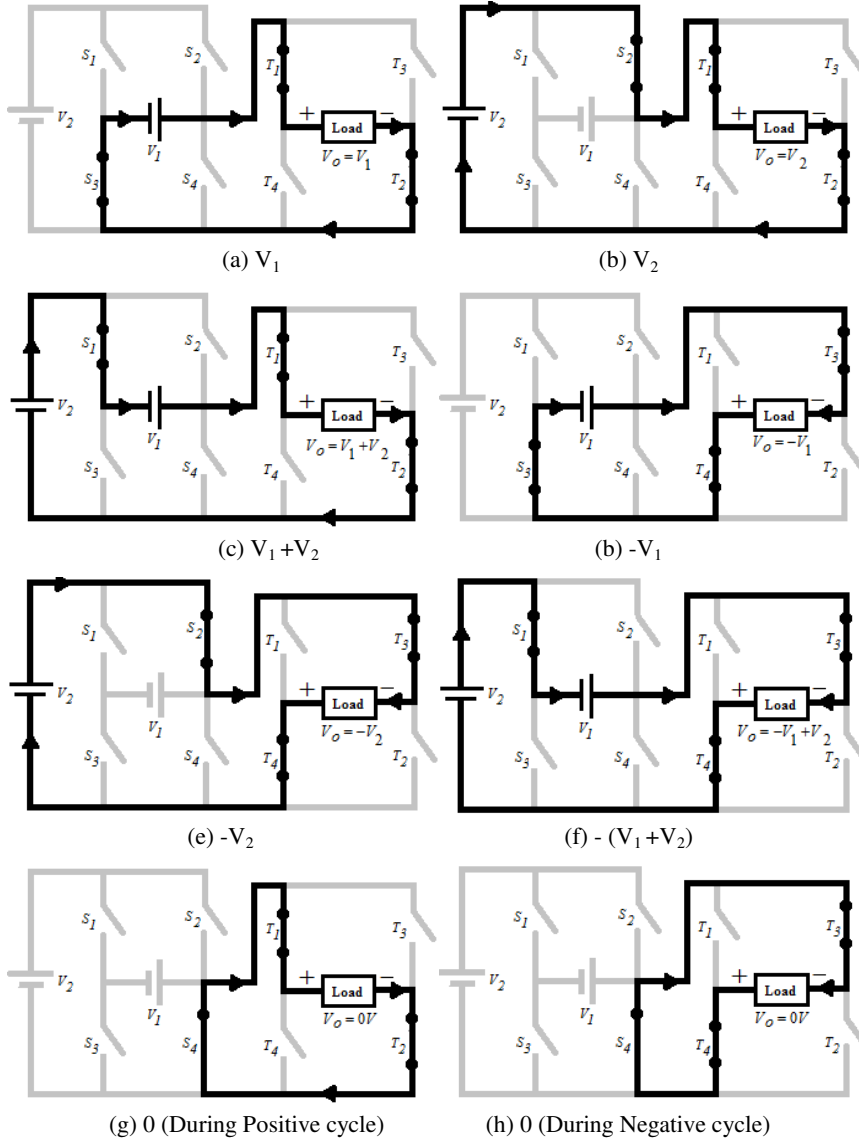
Figure 2

Different modes of operation

A rectifier unit with an isolation transformer and a capacitor filter forms the DC voltage sources. The proposed inverter can generate five level output during symmetric condition and seven level output during asymmetric condition. The operating modes during symmetric and asymmetric operation of the proposed inverter for obtaining the alternating output voltage across the load are given in Table 1 and Table 2 respectively. It is seen that the switches T_1 and T_2 were ON during positive cycle of operation while the switches T_3 and T_4 are ON during negative cycle of operation.

Table 1
Switching table for symmetric five level inverter

Output Level	ON state switches	Voltage Sources
1	(S_3, T_1, T_2) or (S_2, T_1, T_2)	V_1 or V_2
2	(S_1, T_1, T_2)	V_1+V_2
0	(S_4, T_1, T_2) or (S_4, T_3, T_4)	0
-2	(S_1, T_3, T_4)	$-(V_1+V_2)$
-1	(S_3, T_3, T_4) or (S_2, T_3, T_4)	$-V_1$ or $-V_2$

Table 2
Switching table for asymmetric seven level inverter

Output Level	ON state switches	Voltage Sources
1	(S_3, T_1, T_2)	V_1
2	(S_2, T_1, T_2)	V_2
3	(S_1, T_1, T_2)	V_1+V_2
0	(S_4, T_1, T_2) or (S_4, T_3, T_4)	0
-3	(S_1, T_3, T_4)	$-(V_1+V_2)$
-2	(S_2, T_3, T_4)	$-V_2$
-1	(S_3, T_3, T_4)	$-V_1$

2.2   Determination of Voltage Magnitude

To achieve higher number of output levels, the basic unit can be added in series. The generalized topology of the proposed inverter with an H-bridge inverting unit is shown in Fig. 3. The general structure is made of 'p' number of basic units connected in series. For the simulation analysis, the switches are assumed as ideal and hence, the drop across each switches has been neglected. Therefore, the maximum voltage across the load is synthesized by adding the magnitude of all DC voltage sources and is given by:

$$V_o = \sum_{i=1}^{p}(V_{1i} + V_{2i}) \tag{1}$$

If the magnitude of all DC sources are same i.e.:

$$V_{1i} = V_{2i} = V_{dc} \quad where \ i = 1,2,..., p \tag{2}$$

then the maximum voltage magnitude obtained across the load is given by:

$$V_o = 2pV_{dc} \tag{3}$$

Since each individual basic unit consists of two voltage sources, the relation between the number of voltage sources 'n' and the number of basic units connected in series 'p' is given by:

$$n = 2p \tag{4}$$
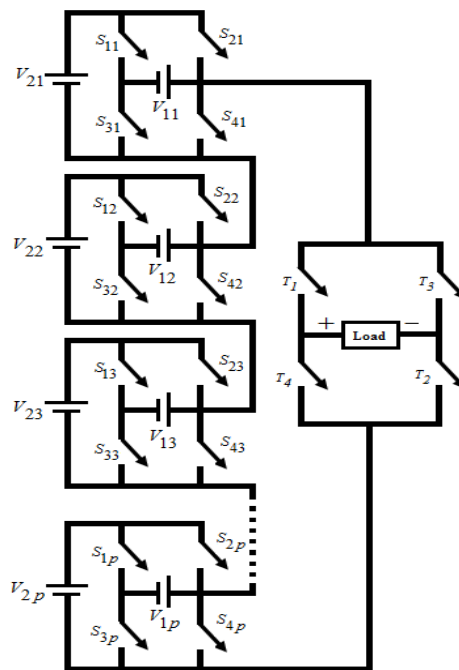
Figure 3
Generalized inverter topology

The relationship between the number of voltage sources '*n*' and the number of levels '*m*' during symmetric operation is given by:

$$n = \frac{m-1}{2} \tag{5}$$

Similarly, the relationship between the number of voltage sources '*n*' and the total number of switches 'N_{switch}' during symmetric operation is given by:

$$N_{switch} = 2(n+2) \tag{6}$$

From (5) and (6), the relation between 'N_{switch}' and 'm' is obtained as:

$$N_{switch} = m + 3 \tag{7}$$

It is known that the number of output levels and their corresponding magnitude depends on the magnitude of the different voltage sources. It is also know that the higher output level is achieved during asymmetric operation as compared with symmetric. Therefore, the magnitude of DC sources has to be chosen differently to achieve larger output levels. This paper proposes six algorithms to determine the magnitude of each DC sources. Table 3 shows the comparison of different algorithms of determining the output levels of the proposed inverter.

Table 3
Comparison of the proposed algorithms

Algorithm	Magnitude of voltage sources	Number of switches	Maximum Voltage	Number of levels
Algorithm - 1	$V_{1,i} = V_{2,i} = V_{dc}$ where, $i = 1, 2, 3. . . .,p$	$4(p+1)$	$2pV_{dc}$	$4p+1$
Algorithm - 2	$V_{1,i} = V_{2,i} = iV_{dc}$ where, $i=1, 2, 3. . .,p$	$4(p+1)$	$p(p+1)V_{dc}$	$2p^2+2p+1$
Algorithm - 3	$V_{1,i} = V_{2,i} = (2)^{i-1}V_{dc}$ where, $i=1, 2, 3. . .,p$	$4(p+1)$	$2(2^P - 1)V_{dc}$	$2^{p+2} - 3$
Algorithm - 4	$V_{1,i} = V_{2,i} = (3)^{i-1}V_{dc}$ where, $i=1, 2, 3. . .,p$	$4(p+1)$	$(3^P - 1)V_{dc}$	$2(3^p) - 1$
Algorithm - 5	$V_{1,i} = (2i-1)V_{dc}$ $V_{2,i} = (2i)V_{dc}$ where, $i=1, 2, 3. . .,p$	$4(p+1)$	$p(2p+1)V_{dc}$	$4p^2+2p+1$
Algorithm - 6	$V_{1,i} = (4)^{i-1}V_{dc}$ $V_{2,i} = (2)^{2i-1}V_{dc}$ where, $i=1, 2, 3. . .,p$	$4(p+1)$	$(2^{2p} - 1)V_{dc}$	$2^{2p+1} - 1$

The number of output voltage levels, magnitude of the DC voltage sources and the maximum obtained voltage across the load are different for each algorithm. The comparison of different algorithms with respect to the number of levels are given in Table 4. The algorithm-1 is corresponding to the symmetric operation of the inverter where the magnitude of all DC voltage sources are same. The remaining algorithms are corresponding to the asymmetric operation of the inverter where each DC voltage sources have different magnitude. It is clear that the maximum magnitude of the output voltage is achieved during asymmetric mode as compared with symmetric mode of operation with same number of DC voltage sources and power switches.

Table 4

Comparison of the proposed algorithms for 'm' level

Algorithm	Number of basic units	Number of switches	Number of voltage sources
Algorithm - 1	$\dfrac{m-1}{4}$	$m+3$	$\dfrac{m-1}{2}$
Algorithm - 2	$\dfrac{(2m-1)^{1/2}-1}{2}$	$2\left((2m-1)^{1/2}+1\right)$	$(2m-1)^{1/2}-1$
Algorithm - 3	$\log_2(m+3)-2$	$4(\log_2(m+3)-1)$	$2(\log_2(m+3)-2)$
Algorithm - 4	$\log_3(\dfrac{m+1}{2})$	$4\left(\log_3(\dfrac{m+1}{2})+1\right)$	$2\log_3(\dfrac{m+1}{2})$
Algorithm - 5	$\dfrac{(4m-3)^{1/2}-1}{4}$	$(4m-3)^{1/2}+3$	$\dfrac{(4m-3)^{1/2}-1}{2}$
Algorithm - 6	$\dfrac{\log_2(m+1)-1}{2}$	$2(\log_2(m+1)+1)$	$\log_2(m+1)-1$

The comparison of the number of voltage sources with the output levels in the different algorithms is shown in Fig. 4(a). Fig. 4(b) shows the comparison of the number of switches with the output levels for the different algorithms.
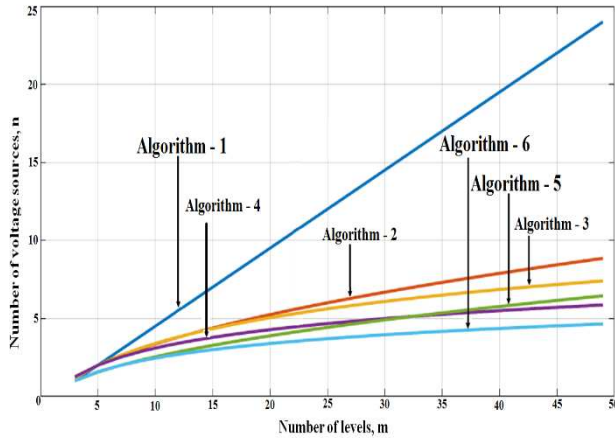
(a)
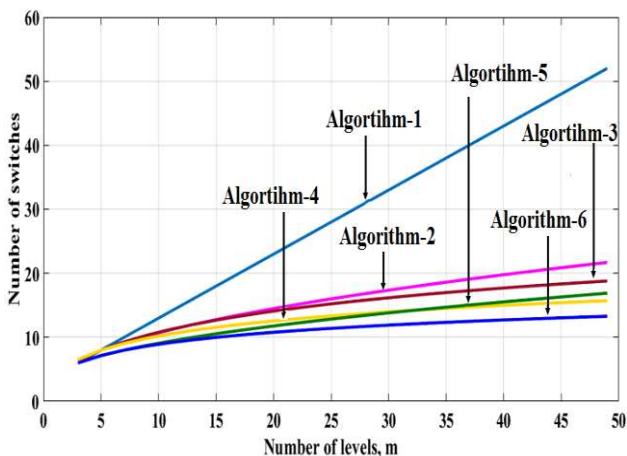
(b)

Figure 4

Comparison (a)Number of levels vs DC voltage sources (b) Number of levels vs number of switches

It is observed that the algorithm-6 requires minimum number of switches and voltage sources to achieve required output levels as compared with other algorithms. However, the drawback of using algorithm-6 is that it requires larger magnitude of DC voltage. It is also observed that the algorithm-5 shows better reduction in the switching devices and the voltage sources during the minimum output levels as compared with algorithm-4. With increase in output level greater than 40, algorithm-4 gives better reduction in the switching components as compared with algorithm-5.

3   Comparison between the Proposed Topology with other Recent Inverter Topologies

In this section, the proposed inverter topology is compared with conventional CHB inverter and other existing multilevel inverter topologies during both symmetrical and asymmetrical modes of operation. Comparison indices used in this paper are number of switching devices, number of DC sources and number of ON-state switches (i.e., conducting switches) required to synthesize any required voltage level. The proposed inverter topology is compared with the symmetrical inverter topologies presented in [13, 22], asymmetrical inverter topologies presented in [19, 23, 24] and other recent topologies which operates in both symmetric and asymmetric mode presented in [11, 15, 20, 25, 36].

3.1   DC Sources

With 'n' DC sources, the proposed inverter achieves 2n+1 levels during symmetric mode which is same as the conventional CHB inverter and other symmetric topologies presented in [11, 15, 20, 23, 25]. It means that this topology achieves 5 level with 2 DC sources, 9 level with 4 DC sources and so on. During asymmetrical modes of operation, the number of levels can vary with respect to the magnitude and number of the DC voltage sources. Fig. 5 shows the comparison of number of levels with the number of DC sources during asymmetrical modes of operation of the proposed inverter topology. It is important to note that the proposed inverter topology achieves higher number of output levels with minimum number of DC voltage sources as compared with topologies presented in [23] and [25].
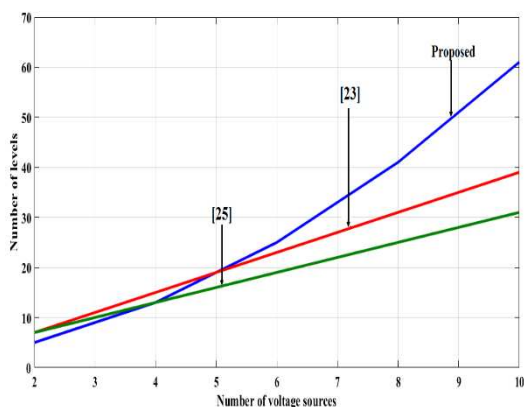
Figure 5
Levels vs DC sources in asymmetrical mode

3.2   Switches

Fig. 6 shows the comparison of number of levels with the number of switching devices during symmetrical and asymmetrical modes of operation of the proposed inverter topology. It is seen that the proposed inverter topology utilizes minimum number of switching components as compared with conventional CHB, and other topologies presented in [11, 19, 23-25]. For example, to achieve 9-level output voltage during symmetric mode, the proposed topology requires 12 switches which is same as in [25]. Whereas, the conventional CHB and the topology in [11] requires 16 switches which shows that the number of switching components is reduced by 25%. To achieve 31 level during symmetric operation, the proposed topology requires 34 switches only. However, the required switch count is increased to 60 for CHB and topology presented in [11]. Similarly, the switch

count is increased to 45 for the inverter topology presented in [25] to achieve 31 level during symmetric operation. This shows that the switch count is reduced by 43.33% compared with CHB, [11] and 24.44% compared with [25]. It is also observed that the proposed topology during asymmetrical mode achieves 14.28% reduction in number of switching components compared with the topology presented in [23], 25% reduction compared with CHB and [24] while synthesizing 31 level output voltage.
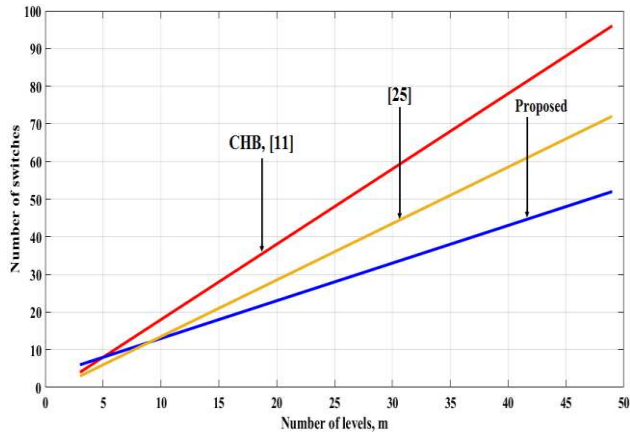
(a)
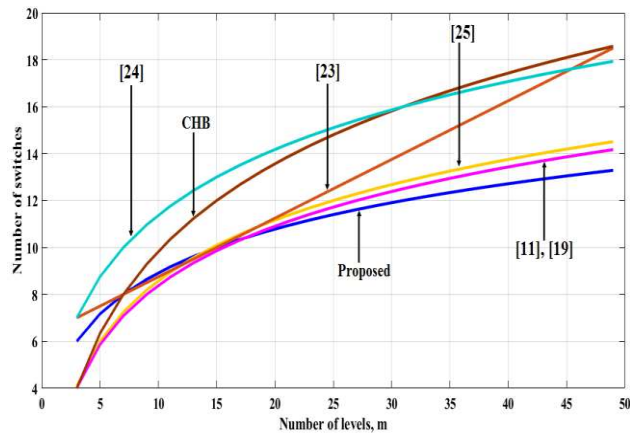
(b)

Figure 6
Levels vs switches (a) Symmetrical mode (b) Asymmetrical mode

3.3 ON-state Switches

The number of switches in the conduction path is another important parameter to compare the different topologies. The total power loss of the switches depends on the total number of switches in the current conduction path. From Table 1, it is seen that for the proposed inverter topology with single basic unit and H-bridge inverting unit, three switches will be conducting one from the basic unit and two from the H-bridge inverting unit to achieve any desired output levels. The number of on-state switches at any time will depend on the number of basic units connected in series '*p*' and is equal to *p+2*. With '*n*' DC voltage sources, the number of switches in the conduction path is $\frac{n}{2}+2$ whereas for conventional CHB MLI, it is equal to *2n*. Fig. 7 shows the comparison of the number of on-state switches against the number of DC voltage sources. It is seen that the on-state switches for the proposed inverter is lower than the conventional CHB inverter and other topologies presented in [26-29]. This will reduces the number of associated gate driver circuits, installation area and overall cost of the proposed inverter topology. Therefore it is concluded that the conduction losses of the proposed topology will be very less as compared with other presented topologies.
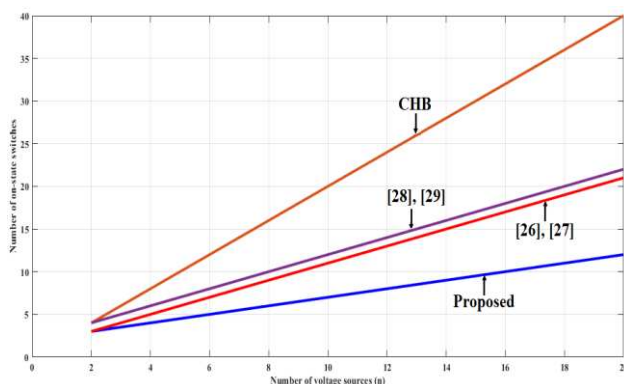
Figure 7

On state switches

4 Modified PWM Technique

In MLI, many methods such as pulse width modulation (PWM) [30, 35, 37, 38, 43], selective harmonic elimination (SHE) [31, 41, 52], space vector modulation [32, 42, 44] and active harmonic elimination [33] have been used for modulation control. The PWM governs the consistent conduction of switching devices in the MLI to achieve a preferred output levels. In this paper, a modified multicarrier

based digital PWM technique is used to generate required pulses. In this technique, the generation of the switching signals involves three stages. In stage-1, the reference sinusoidal signal is compared with multiple number of constant amplitude carrier signals to generate the stage-1 signals. The number of carrier signals depends on the number of levels of the inverter and the number of stage-1 signals generated will be equal to the number of carrier signals. For 'm' level inverter, the required number of carrier signals is (m-1)/2. The amplitudes of the different carrier signals are determined using the formula,

$$V_{Ci} = V_{\max}\left(\frac{2i-1}{m-1}\right) \quad i = 1,2,3....,\left(\frac{m-1}{2}\right) \tag{8}$$

where $V_{\max}$ is the maximum voltage of the reference sinusoidal signal. The stage-2 involves the process of state assignment. In this stage, the state assignment is done for digital values of each generated stage-1 signals during each level of the output voltage. During stage-3, the switching states are obtained against each assigned states. On simplifying the resultant table using reduction techniques, the final switching signals were obtained. During simplification, the unused states are treated as don't cares 'x'. To illustrate this, consider a 9-level symmetrical topology of the proposed inverter. It consists of 4 DC voltage sources and 8 main switches.

Stage-1

For 9-level inverter, four carrier signals were required and these signals were compared with sinusoidal reference signal to generate stage-1 signals C_1, C_2, C_3 and C_4 as shown in Fig. 8(a). Since the output voltage waveform is symmetrical, it is enough to consider the signals till $\pi/2$. The maximum voltage of the reference sinusoidal signal is 4V and hence, the amplitudes of the carrier signals are determined as 0.5V, 1.5V, 2.5V and 3.5V respectively. The frequency of the reference signal is 50 Hz.

Stage-2

The stage -2 is the process of assigning the states to the stage-1 signals during each interval. The state assignment process is shown in Fig. 8(b). It is important to note that only one bit changes at a time during each state transition. During period 0 to $\pi/2$, the state transits from state-1 to state-4 and during period $\pi/2$ to π, the state transits from state-4 to state-1.

Stage-3

Table 5 shows the switching conditions of the proposed 9-level inverter for different states. On simplification, the final switching signals were obtained as,

$$
\begin{aligned}
&S_{11} = A + B &\qquad &S_{21} = 0 \\
&S_{31} = \overline{B}C &\qquad &S_{41} = \overline{A}\,\overline{B}\,\overline{C} \\
&S_{12} = A &\qquad &S_{22} = 0 \\
&S_{32} = B\overline{C} &\qquad &S_{42} = \overline{A}\,\overline{B} + \overline{C}
\end{aligned}
\tag{9}
$$

Table 5

Switching conditions during Stage-3

S. No	States	Signals			Switches							
		A	B	C	S_{11}	S_{21}	S_{31}	S_{41}	S_{12}	S_{22}	S_{32}	S_{42}
1	State-0	0	0	0	0	0	0	1	0	0	0	1
2	State-1	0	0	1	0	0	1	0	0	0	0	1
3	State-2	0	1	1	1	0	0	0	0	0	0	1
4	State-3	0	1	0	1	0	0	0	0	0	1	0
5	State-4	1	0	0	1	0	0	0	1	0	0	0
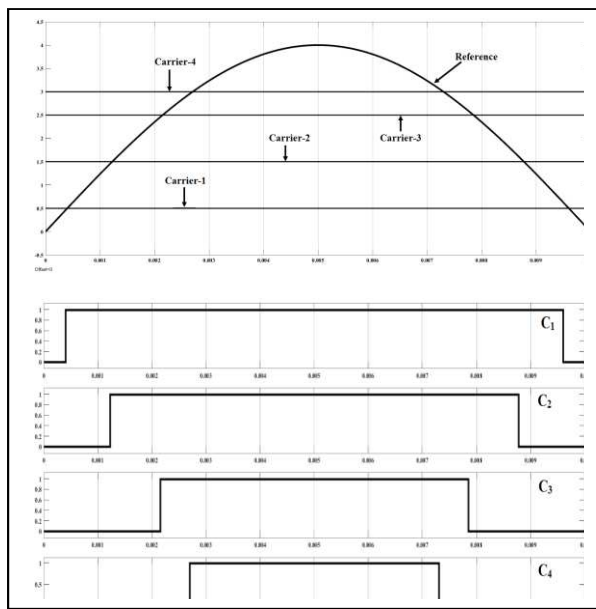
(a)
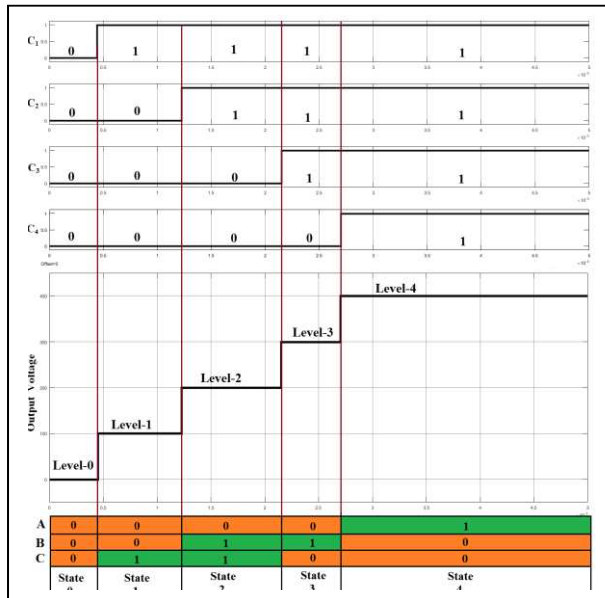
(b)

Figure 8

PWM generation stages (a) Stage-1 (b) Stage-2

5   Simulation Results

To analyze the performance of the proposed inverter topology during the symmetric and asymmetric operation, simulation is carried out. A series connected two basic units with a H-bridge as shown in Fig. 9 is developed using MATLAB/SIMULINK software. The developed model consists of four DC voltage sources and eight main switches. It achieves 9-level during symmetric operation and 31-level during asymmetric operation. A series RL load with magnitudes R= 75 Ω and L = 30 mH are considered as load parameters.
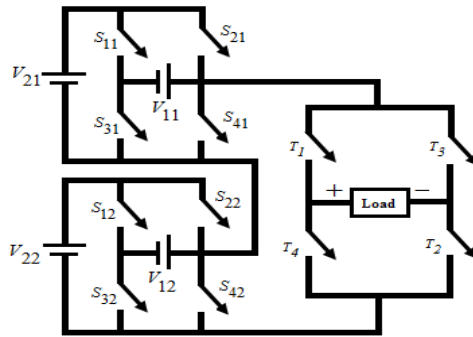
Figure 9

Proposed inverter topology with series connected two basic units

5.1   Symmetric -9-level

During symmetric operation, the magnitude of all DC voltage sources are equal i.e., $V_{11} = V_{21} = V_{12} = V_{22} = V_{dc} = 60$ V. The required PWM signals are generated as explained in section-4 and is shown in Fig. 10.
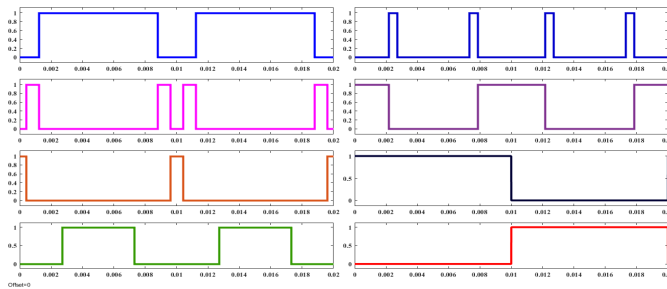
Figure 10

Switching pulses for 9-level inverter

The output voltage obtained across each basic unit of the proposed inverter topology during the symmetric operation is shown in Fig. 11 and Fig. 12 respectively. During symmetrical operation, the total voltage stress on switches is calculated as $16V_{dc}$.
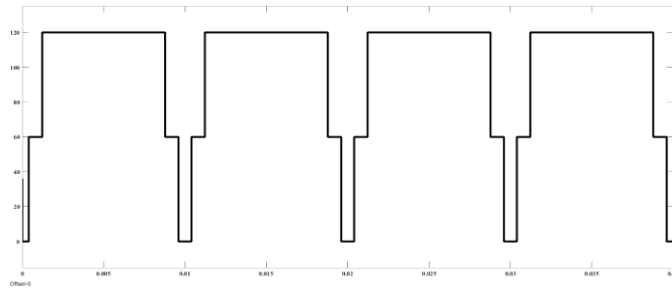
Figure 11
Output voltage across unit-1 during symmetric operation
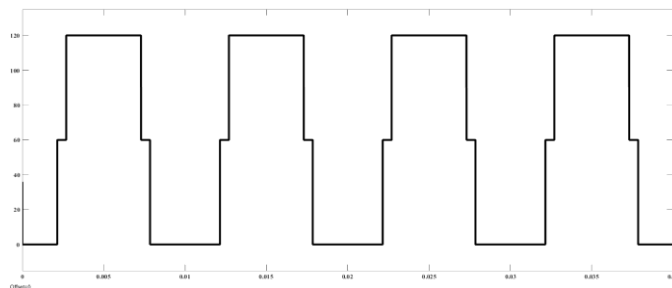
Figure 12
Output voltage across unit-2 during symmetric operation

The measured input and output powers are about 440 W and 420 W, respectively with the loss of 20 W. Therefore, the efficiency of the proposed inverter topology during 9-level symmetric operation is about 95.45%. However, the efficiency of the multilevel inverter topology presented in [39] is about 93%. The 9-level output voltage and the corresponding THD are given in Fig. 13. It is observed that the THD of the 9-level output voltage waveform is 10.47% with the fundamental value of the output voltage as 257.6V. The THD comparison of 9-level output voltage waveform for different inverter topologies is given in Table 6. It is observed that the proposed topology achieves minimum THD for the 9-level output voltage waveform.

Table 6
Comparison of THD for 9-level inverter

Topology	[29]	[45]	[46]	[11]	**Proposed**
THD (%)	16.20	13.45	12.75	11.41	**10.47**
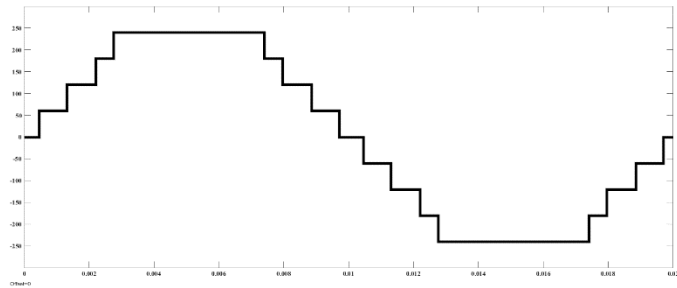
(a)
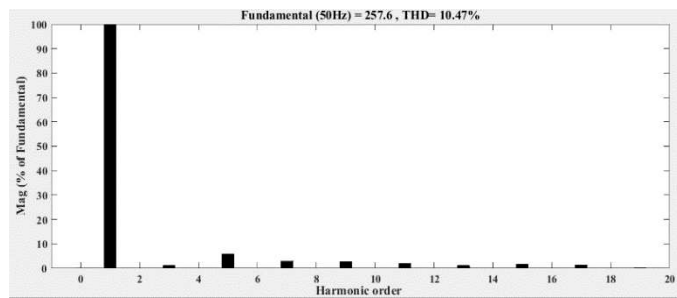
(b)

Figure 13

Symmetric 9-Level (a) Output Voltage and (b) THD

5.2   Asymmetric -31-level

During asymmetric operation, the magnitude of all DC voltage sources are different. The magnitude of each DC voltage sources can be determined using algorithm-6 and are given as $V_{11} = V_{dc} = 16$ V, $V_{21} = 2V_{dc} = 32$ V, $V_{12} = 4V_{dc} = 64$ V and $V_{22} = 8V_{dc} = 128$ V. For 31-level inverter, fifteen carrier signals were required and these signals were compared with sinusoidal reference signal to generate fifteen stage-1 signals C_1 to C_{15}. The amplitude of these carrier signals were determined using equation (8). The stage-2 signals were determined with an assumption that only one bit changes at a time using the following relation,

$$A = C_8$$
$$B = C_4 - C_{12}$$
$$C = C_2 - C_4 + C_6 - C_8 + C_{10} - C_{12} + C_{14}$$
$$D = C_1 - C_3 + C_5 - C_7 + C_9 - C_{11} + C_{13} - C_{15}$$

$$(10)$$

On simplification, the switching signals for the 31-level asymmetric inverter were obtained as

$$S_{11} = C\overline{D} \qquad S_{21} = A\overline{B}$$
$$S_{31} = CD \qquad S_{41} = AB$$
$$S_{12} = \overline{C}D \qquad S_{22} = \overline{A}B \qquad\qquad (11)$$
$$S_{32} = \overline{C}\,\overline{D} \qquad S_{42} = \overline{A}\,\overline{B}$$

The required PWM signals are generated as explained in section-4 and is shown in Fig. 14. The output voltage obtained across each basic unit of the proposed inverter topology during the asymmetric operation is shown in Fig. 15 and Fig. 16 respectively.
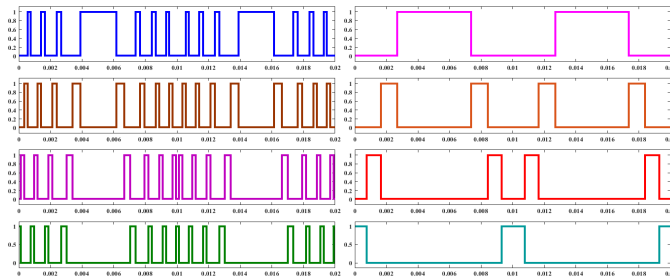
Figure 14
Switching pulses for 31-level inverter
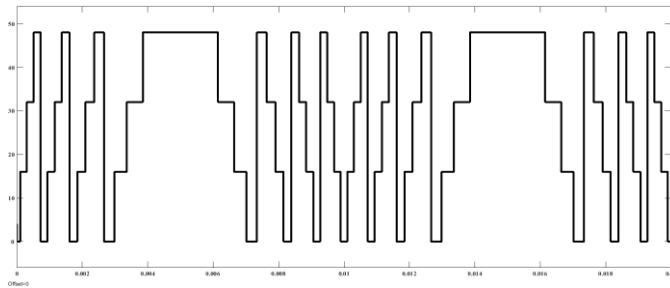
Figure 15
Output voltage across unit-1 during asymmetric operation
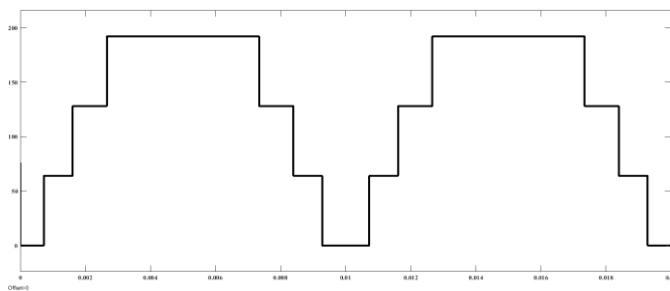
Figure 16
Output voltage across unit-2 during asymmetric operation

During asymmetrical operation, the total voltage stress on switches is calculated as $50V_{dc}$. The efficiency of the proposed inverter topology during 31-level asymmetric operation is about 96.32% with the power loss of around 14.85 W. The 31-level output voltage and the corresponding THD are given in Fig. 17. It is observed that the THD of the 31-level output voltage waveform is 2.70% with the fundamental value of the output voltage as 246.3 V.

(a)

(b)
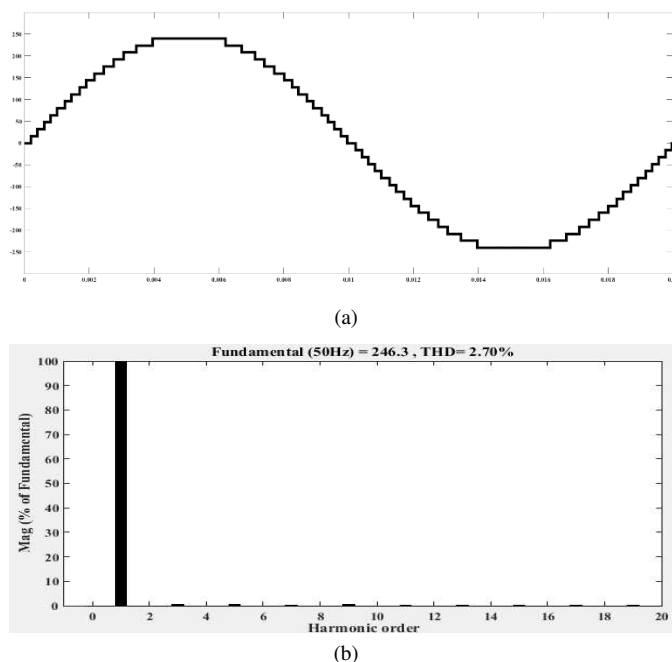
Figure 17

Asymmetric 31-Level (a) Output Voltage and (b) THD

The THD comparison of 31-level output voltage waveform for different inverter topologies is given in Table 7. It is observed that the proposed topology achieves minimum THD for the 31-level output voltage waveform. Fig. 18 shows the %THD value for different modulation indices during symmetrical and asymmetrical operation of the proposed inverter. From the graph, it is clearly shown that %THD decreases with increase in the modulation index and it is also shown that %THD for the proposed inverter topology during the asymmetric operation is lesser that of symmetric operation for the same modulation index.

Table 7

Comparison of THD for 31-level inverter

Topology	[46]	[26]	[34]	**Proposed**
THD (%)	4.66	4.04	3.26	**2.70**
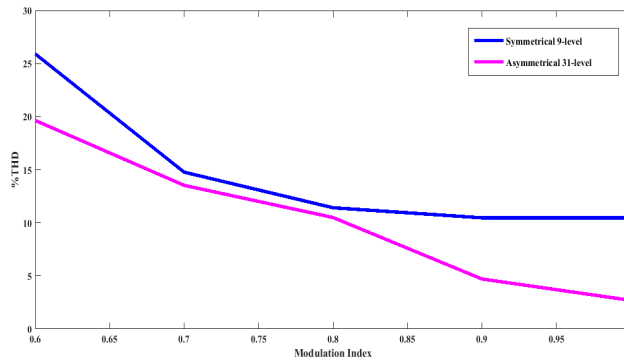
Figure 18
%THD for different modulation indices

6 Hardware Results

To show the feasibility of the proposed inverter topology, a hardware setup of 9-level symmetrical topology is considered. The experimental setup consists of two basic blocks connected in series with each block consists of two DC sources with equal magnitude as 16V. A rectifier unit with an isolation transformer and a capacitor filter forms the DC voltage sources. The diode IN4007 acts as a bridge rectifier unit. To get the constant voltage to the controller, IC7805 acts as a voltage regulator. The gate signals for driving the power switches has been generated with the help of 16-bit digital signal controller dsPIC30F2010. As seen from Table 5, the switches S_{21} and S_{22} were neglected and therefore 10 MOSFET (IRF840N) power switches were employed in the hardware setup. Fig. 19 shows the experimental results for the symmetric 9-level inverter. It is observed that the THD of the 9-level output waveform is achieved as 11%.
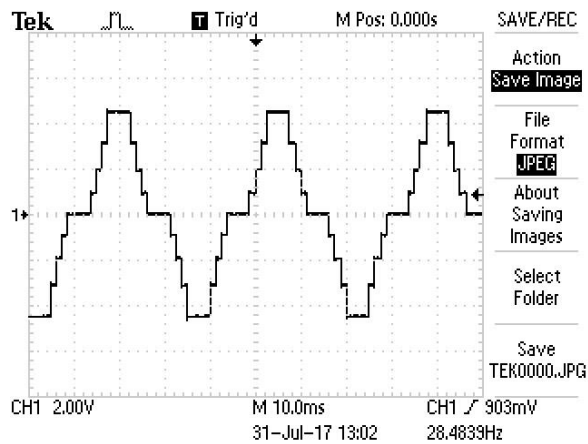
(a)
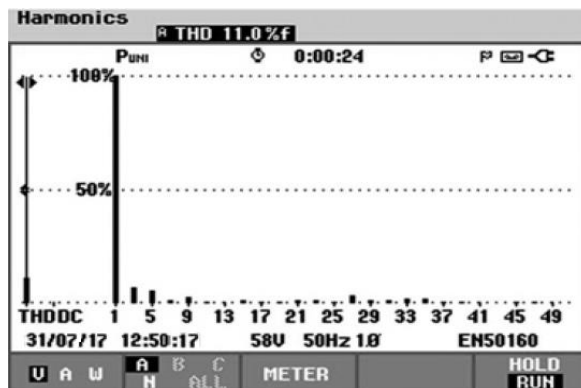
(b)

Figure 19
Hardware results (a) 9-level Output Voltage and (b) THD

Conclusions

In this paper, a new topology of a symmetrical and asymmetrical type, multilevel inverter, with reduced switch count, is proposed. Different algorithms for the determination of the magnitude of the DC voltage sources are analyzed. The comparative analysis of the proposed inverter topology with other recent topologies show that the proposed topology significantly reduces the number of DC voltage sources and power switches. The advantages of the proposed topology include simple construction, ease of control, a reduced number of components, lower THD and a minimized cost. The number of on-state switches in the conduction path, are also reduced, as compared with other existing topologies. The performance of the proposed inverter topology is analyzed for 9-level symmetrical and 31-level asymmetrical cases. Finally, the feasibility of the proposed inverter

topology for 9-level symmetrical operation has been tested experimentally. The experimental results are in good agreement with the simulation results.

References

[1]   S. H. Ashan and M. Monfared: Design and comparison of nine-level single-phase inverters with a pair of coupled inductors and two dc sources, IET Power Electronics, Vol. 9, No. 11, pp. 2271-2281, 2016

[2]   S. H. Ashan and M. Monfared: Generalised single-phase N-level voltage-source inverter with coupled inductors, IET Power Electronics, Vol. 8, No. 11, pp. 2257-2264, 2015

[3]   E. Zamiri, N. Vosoughi, S. H. Hosseini, R. Barzegarkhoo and M. Sabahi: A New Cascaded Switched-Capacitor Multilevel Inverter Based on Improved Series–Parallel Conversion With Less Number of Components, IEEE Transactions on Industrial Electronics, Vol. 63, No. 6, pp. 3582-3594, 2016

[4]   A. Nabae, I. Takahashi and H. Akagi: A New Neutral-Point-Clamped PWM Inverter, IEEE Transactions on Industry Applications, Vol. IA-17, No. 5, pp. 518-523, 1981

[5]   J. Rodriguez, S. Bernet, P. K. Steimer and I. E. Lizama: A Survey on Neutral-Point-Clamped Inverters, IEEE Transactions on Industrial Electronics, Vol. 57, No. 7, pp. 2219-2230, 2010

[6]   C. Feng, J. Liang and V. G. Agelidis: Modified Phase-Shifted PWM Control for Flying Capacitor Multilevel Converters, IEEE Transactions on Power Electronics, Vol. 22, No. 1, pp. 178-185, 2007

[7]   T. A. Meynard, H. Foch, F. Forest, C. Turpin, F.Richardeau, L.Delmas, G. Gateau and E. Lefeuvre: Multicell converters: derived topologies, IEEE Transactions on Industrial Electronics, Vol. 49, No. 5, pp. 978-987, 2002

[8]   F. Z. Peng and J. S. Lai: Multilevel cascade voltage source inverter with separate DC sources, U.S. Patent 5 642 275, 1997

[9]   K. K. Gupta, A. Ranjan, P. Bhatnagar, L. K. Sahu and S. Jain: Multilevel Inverter Topologies With Reduced Device Count: A Review, IEEE Transactions on Power Electronics, Vol. 31, No. 1, pp. 135-151, 2016

[10]   S. P. Gautam, L. Kumar and S. Gupta: Hybrid topology of symmetrical multilevel inverter using less number of devices, IET Power Electronics, Vol. 8, No. 11, pp. 2125-2135, 2015

[11]   K. K. Gupta and S. Jain: Topology for multilevel inverters to attain maximum number of levels from given DC sources, IET Power Electronics, Vol. 5, No. 4, pp. 435-446, 2012

[12] P. Lezana, J. Rodriguez and D. A. Oyarzun: Cascaded Multilevel Inverter With Regeneration Capability and Reduced Number of Switches, IEEE Transactions on Industrial Electronics, Vol. 55, No. 3, pp. 1059-1066, 2008

[13] M. F. Kangarlu, E. Babaei and S. Laali: Symmetric multilevel inverter with reduced components based on non-insulated dc voltage sources, IET Power Electronics, Vol. 5, No. 5, pp. 571-581, 2012

[14] C. I. Odeh and D. B. N. Nnadi: Single-phase 9-level hybridised cascaded multilevel inverter, IET Power Electronics, Vol. 6, No. 3, pp. 468-477, 2013

[15] E. S. Najmi and A. Ajami: Modular symmetric and asymmetric reduced count switch multilevel current source inverter, IET Power Electronics, Vol. 9, No. 1, pp. 51-61, 2016

[16] H. P. Vemuganti, D. Sreenivasarao and G. Siva Kumar: Improved pulse-width modulation scheme for T-type multilevel inverter, IET Power Electronics, Vol. 10, No. 8, pp. 968-976, 2017

[17] M. Kaliamoorthy, V. Rajasekaran, I. G. Christopher Raj and L. Hubert Tony Raj: Generalised hybrid switching topology for a single-phase modular multilevel inverter, IET Power Electronics, Vol. 7, No. 10, pp. 2472-2485, 2014

[18] A. Farakhor, R. R. Ahrabi, H. Ardi and S. N. Ravadanegh: Symmetric and asymmetric transformer based cascaded multilevel inverter with minimum number of components, IET Power Electronics, Vol. 8, No. 6, pp. 1052-1060, 2015

[19] E. Babaei, S. H. Hosseini, G. B. Gharehpetian, M. T. Haque, M. Sabahi: Reduction of dc voltage sources and switches in asymmetrical multilevel converters using a novel topology, Electric Power Systems Research, Vol. 77, pp. 1073-1085, 2007

[20] A. Mokhberdoran and A. Ajami: Symmetric and Asymmetric Design and Implementation of New Cascaded Multilevel Inverter Topology, IEEE Transactions on Power Electronics, Vol. 29, No. 12, pp. 6712-6724, 2014

[21] G. S. Perantzakis, F. H. Xepapas and S. N. Manias: A Novel Four-Level Voltage Source Inverter—Influence of Switching Strategies on the Distribution of Power Losses, IEEE Transactions on Power Electronics, Vol. 22, No. 1, pp. 149-159, 2007

[22] M. R. J. Oskuee, E. Salary and S. N. Ravadanegh: Creative design of symmetric multilevel converter to enhance the circuit's performance, IET Power Electronics, Vol. 8, No. 1, pp. 96-102, 2015

[23] M. Jayabalan, B. Jeevarathinam and T. Sandirasegarane: Reduced switch count pulse width modulated multilevel inverter, IET Power Electronics, Vol. 10, No. 1, pp. 10-17, 2017

[24]   E. Babaei: A Cascade Multilevel Converter Topology With Reduced Number of Switches, IEEE Transactions on Power Electronics, Vol. 23, No. 6, pp. 2657-2664, 2008

[25]   E. Babaei, S. Laali and S. Alilu: Cascaded Multilevel Inverter With Series Connection of Novel H-Bridge Basic Units, IEEE Transactions on Industrial Electronics, Vol. 61, No. 12, pp. 6664-6671, 2014

[26]   M. R. Banaei, M. R. J. Oskuee and H. Khounjahan: Reconfiguration of semi-cascaded multilevel inverter to improve systems performance parameters, IET Power Electronics, Vol. 7, No. 5, pp. 1106-1112, 2014

[27]   M. R. Banaei and E. Salary: Verification of New Family for Cascade Multilevel Inverters with Reduction of Components, Journal of Electrical Engineering and Technology, Vol. 6, No. 2, pp. 245-254, 2011

[28]   E. Babaei, S. H. Hosseini: New cascaded multilevel inverter topology with minimum number of switches, Energy Conversion and Management, Vol. 50, pp. 2761-2767, 2009

[29]   A. Ajami, M. R. J. Oskuee, A. Mokhberdoran and A. Van den Bossche: Developed cascaded multilevel inverter topology to minimise the number of circuit devices and voltage stresses of switches, IET Power Electronics, Vol. 7, No. 2, pp. 459-466, 2014

[30]   B. P. McGrath and D. G. Holmes: Multicarrier PWM strategies for multilevel inverters, IEEE Transactions on Industrial Electronics, Vol. 49, No. 4, pp. 858-867, 2002

[31]   H. Lou, C. Mao, D. Wang, J. Lu and L. Wang: Fundamental modulation strategy with selective harmonic elimination for multilevel inverters, IET Power Electronics, Vol. 7, No. 8, pp. 2173-2181, 2014

[32]   O. Lopez, J. Alvarez, J. D. Gandoy and F. D. Freijedo: Multilevel Multiphase Space Vector PWM Algorithm, IEEE Transactions on Industrial Electronics, Vol. 55, No. 5, pp. 1933-1942, 2008

[33]   Z. Du, L. M. Tolbert and J. N. Chiasson: Active harmonic elimination for multilevel converters, IEEE Transactions on Power Electronics, Vol. 21, No. 2, pp. 459-469, 2006

[34]   R. S. Alishah, S. H. Hosseini, E. Babaei and M. Sabahi: Optimal Design of New Cascaded Switch-Ladder Multilevel Inverter Structure, IEEE Transactions on Industrial Electronics, Vol. 64, No. 3, pp. 2072-2080, 2017

[35]   S. F. Ahmed, C. F. Azim, H. Desa and A. S. T. Hussain: Model Predictive Controller-based, Single Phase Pulse Width Modulation (PWM) Inverter for UPS Systems, Acta Polytechnica Hungarica, Vol. 11, No. 6, pp. 23-38, 2014

[36]   V. Thiyagarajan and P. Somasundaram: Modeling and Analysis of Novel Multilevel Inverter Topology with Minimum Number of Switching

Components, CMES: Computer Modeling in Engineering and Sciences, Vol. 113, No. 4, pp. 461-473, 2017

[37] I. Vajda, Y. N. Dementyev, K. N. Negodin, N. V. Kojain, L. S. Udut, I. A. Chesnokova: Limiting Static and Dynamic Characteristics of an Induction Motor under Frequency Vector Control, Acta Polytechnica Hungarica, Vol. 14, No. 6, pp.7-27, 2017

[38] V. Thiyagarajan and P. Somasundaram: Analysis of Multicarrier PWM techniques for Photovoltaic fed Cascaded H-Bridge Multilevel Inverter, Journal of Electrical and Electronics Engineering, Vol. 10, No. 1, pp. 85-90, 2017

[39] K. Boora and J. Kumar: General topology for asymmetrical multilevel inverter with reduced number of switches, IET Power Electronics, Vol. 10, No. 15, pp. 2034-2041, 2017

[40] M. Saeedian, J. Adabi and S. M. Hosseini: Cascaded multilevel inverter based on symmetric–asymmetric DC sources with reduced number of components, IET Power Electronics, Vol. 10, No. 12, pp. 1468-1478, 2017

[41] P. L. Kamani and M. A. Mulla: Middle-Level SHE Pulse-Amplitude Modulation for Cascaded Multilevel Inverters, IEEE Transactions on Industrial Electronics, Vol. 65, No. 3, pp. 2828-2833, 2018

[42] B. Kirankumar, Y. V. Siva Reddy and M. Vijayakumar: Multilevel inverter with space vector modulation: intelligence direct torque control of induction motor, IET Power Electronics, Vol. 10, No. 10, pp. 1129-1137, 2017

[43] S. K. Sahoo and T. Bhattacharya: Phase-Shifted Carrier-Based Synchronized Sinusoidal PWM Techniques for a Cascaded H-Bridge Multilevel Inverter, IEEE Transactions on Power Electronics, Vol. 33, No. 1, pp. 513-524, 2018

[44] J. S. Hu, J. N. Lin and H. C. Chen: A Discontinuous Space Vector PWM Algorithm in abc Reference Frame for Multilevel Three-Phase Cascaded H-Bridge Voltage Source Inverters, IEEE Transactions on Industrial Electronics, Vol. 64, No. 11, pp. 8406-8414, 2017

[45] N. Arun and M. M. Noel: Crisscross switched multilevel inverter using cascaded semi-half-bridge cells, IET Power Electronics, Vol. 11, No. 1, pp. 23-32, 2018

[46] A. Ajami, M. R. J. Oskuee, M. T. Khosroshahi and A. Mokhberdoran: Cascade-multi-cell multilevel converter with reduced number of switches, IET Power Electronics, Vol. 7, No. 3, pp. 552-558, 2014

[47] F. Chabni, R. Taleb and M. Helaimi: ANN-based SHEPWM using a harmony search on a new multilevel inverter topology, Turkish Journal of

Electrical Engineering and Computer Sciences, Vol. 25, No. 6, pp. 4867-4879, 2017

[48]   M. Ramya and P. Usha Rani: Asymmetrical Cascaded Twenty Seven level Inverter based STATCOM, Rev. Roum. Sci. Techn.–Électrotechn. etÉnerg., Vol. 62, No. 4, pp. 411-416, 2017

[49]   R. E. Precup, S. Preitl and P. Korondi: Fuzzy Controllers With Maximum Sensitivity for Servosystems, IEEE Transactions on Industrial Electronics, Vol. 54, No. 3, pp. 1298-1310, 2007

[50]   C. Cecati, F. Ciancetta and P. Siano: A Multilevel Inverter for Photovoltaic Systems With Fuzzy Logic Control, IEEE Transactions on Industrial Electronics, Vol. 57, No. 12, pp. 4115-4125, 2010

[51]   V. Thiyagarajan and P. Somasundaram: Modified Seven Level Symmetric Inverter with Reduced Switch Count, Advances in Natural and Applied Sciences, Vol. 11, No. 7, pp. 264-271, 2017

[52]   F. Chabni, R. Taleb, M. Helaimi: Output voltage waveform improvement of modified cascaded H-bridge multilevel inverter using selective harmonic elimination technique based on hybrid genetic algorithm, Rev. Roum. Sci. Techn.–Électrotechn. etÉnerg., Vol. 62, No. 4, pp. 405-410, 2017

Conceptual Models of Information Content for Product Modeling

Yatish Bathla

Óbuda University, Doctoral School of Applied Informatics and Applied
Mathematics, Bécsi út 96/b, H-1034 Budapest, Hungary
e-mail: yatish.bathla@phd.uni-obuda.hu

Abstract: Modeling of product as a system is the new era of virtual product development. Requirement, Functional, Logical, and Physical (RFLP) structure provides system engineering based product definition in product modeling which allows to more effectively translate requirements of the customers into the physical form. But, it is difficult in RFLP structure to store and organize the knowledge of product model in a generic format so that engineers of different disciplines gain detailed knowledge of participating components in order to make the most effective decision. In this paper, a conceptual model is proposed by classifying the information content. This is done in context of the engineering discipline and system behavior. Info-Chunk is proposed in the logical level of RFLP structure. They are mapped with the information content and describe the parameters of the model for representing the engineering object. The models are used to guide the engineer to a precise correlating decision.

Keywords: RFLP structure; Product modeling procedures; Information content of product model; Engineering objects management; Life cycle management of product information; Engineering discipline; System behavior

1 Introduction

A complex product model generally faces difficulties in making decisions when there is a large number of engineering objects participating in the product modeling. The level of complexity increases in the case of high number of dependencies among the engineering objects. In a complex multi-discipline product, the difficulty level is higher because there is a vast collection of data gathered from the various engineering disciplines participating in product modeling. In the virtual environment, some of the challenging tasks need definite and correlated information of an engineering discipline, tracking activities of the system behavior, amongst others. Hence, the establishment of effective assistance of engineering decisions is quite impractical. To cope with the issue, information content was defined to control the engineering object and related engineering

activities. However, the information content is in the unfledged stage and needs to be enhanced in terms of human-computer interaction and structured processing of interrelated engineering objects to obtain coordinated decisions. This paper proposes classification of information content by classifying the intent so that the decision processes can take place efficiently. These are discipline based content and behavior based content respectively. Based on the classification, a different number of conceptual models are generated to store the knowledge of engineering discipline and system behavior. This knowledge is stored and applied to take effective decisions so that the complex product model is represented in a simplified manner. Info-Chunk is introduced in the logical component and logical level of RFLP (requirement, functional, logical and physical) structure. This entity is mapped with the information content to control the activities of the product model. In the present situation, RFLP structure requires a sector that can store and organize knowledge of the product model in generic format for the engineering discipline to gain knowledge of product model and provide the guidance toward the most effective decision. Community diagrams [10] are used to represent the parameters of information content that provide assistance to the engineering discipline and system behavior. The rest of the paper is discussed as follows: It starts with the preliminary work. Information content is then classified by engineering discipline and system behavior. After the classification, Info-Chunk is defined for the conceptual model. Later, the configuration of info chunk in the logical component and logical level is explained which drives the conceptual model. Next, the decision strategy of the conceptual models are discussed. After that, a practical approach of conceptual model in the real world is explained. Finally, the conclusion and future work are discussed.

2 Preliminaries and Purpose

Classical Product Model (CPM) [13] represents engineering objects with certain types of attributes and their relationships. CPM, however, doesn't provide sufficient information to analyze or upgrade the current product model. To fill the gap between the engineer and information based product modeling procedures, information content [1] was proposed. It is an interactive media to transfer the content information from human to data based computers. It is suitable for better explanation and evaluation for the making of an interrelated decision on product objects [7]. Here, the term *information content* is used related to the technical process of the system. To calculate an engineering object related data, information content sector is interconnected with data oriented product model sector. The data oriented sector consists of the engineering objects' description, their attributes and information about their functions and activities. In other words, knowledge of the engineering object is stored in the data-oriented sector. In the context of this research, a mathematical model is used in the RFLP structure to obtain the

information about a system. Artifacts represented by the mathematical models are called virtual prototypes [3] that can optimize the product properties without a physical prototype. Info-Chunk is an entity [2] that transfers the knowledge of the product model to the conceptual model of Information content. Likewise, there are different kinds of entities used in the conceptual model. It can be based on type, shape, size or property of a system. Engineering objects and entities define a product in the virtual environment. These terms are related to each other but not the same. High-level entities use low-level entities as a parameter of model creating procedures. It could be an engineering object [15], a component [10] or a process [6]. Information content is a sector, which is used to control the system in the virtual environment. The controlling data can be input manually or automatically. In the case of manual information content, the engineer can initialize the parameter of info chunks using the specialized knowledge. Whereas, in case of self-adaptive information content, the parameter of Info-Chunk is initialized automatically by the intelligent space called Intelligent Virtual Product Space (IVPS) [3] where the development sector, interface sector, behavior sector and learning sector are used to store the knowledge of the system.

3   Current Practice

To analyze the behavior of a product, RFLP structure considers the product as a system [9]. It can consider all aspects of the virtual prototype of a product before manufacturing the first physical prototype. It is a framework that supports the MBSE (Model Based Systems Engineering) process [10]. There are numerous companies investing in the product modeling like Dassault Systèmes, Synopsys, Autodesk, Siemens amongst others. In the context of research, the author considers RFLP structure of CATIA V6 and 3DEXPERIENCE (3DXP) platform by Dassault Systèmes. In this software, Dymola [14] is used to analyze the dynamic logical behavior of a product and Modelica [5] is used for logical and physical modeling of the technical system. Modelica is a multi-domain modeling language for component-oriented modeling of complex systems and based on the object-oriented principles. To generate the executable code, Modelica uses Dymola compiler, which generates C code [12]. This code can run on the hardware and can possibly be modified manually to implement the interfaces of controller API.

4   Classification of Information Content

The role of information content in the product model is to store the relevant information of a system. Information must be pertinent and precise so that the engineers can understand every aspect of a system and take the literal decision. The conceptual model of information content can control the product model by accessing the parameters of Info-Chunk in the RFLP structure. Classification of information content is based on the engineering discipline and system behavior by using the information stored in the info chunk. It is categorised as discipline-based content and behavior-based content as shown in Fig. 1 respectively [1]. Discipline based content stores the knowledge of various engineering disciplines while behavior based content stores knowledge of the system behavior. It can also be used for upgrading the product version by adding new features, parts or subsystems.

The RFLP structure is compliant with the IEEE1220 standard. It is based on the V-cycle design process and allows concurrent engineering to coordinate the separate activities of a distributed design team. The conceptual models of Information content are mapped with logical and physical levels of the RFLP structure as shown in Fig. 2 [11]. Here, both contents are inter-connected with each other so that any changes made in content affects other content. Furthermore, a different number of models can be constructed for a system based on the classification. To explain the concept of the content, let's consider: number of disciplines in discipline based content = N_d, number of behaviors in behavior based content = N_b, number of disciplines participated in the engineering activities = D, number of expected behaviors of a system = B.
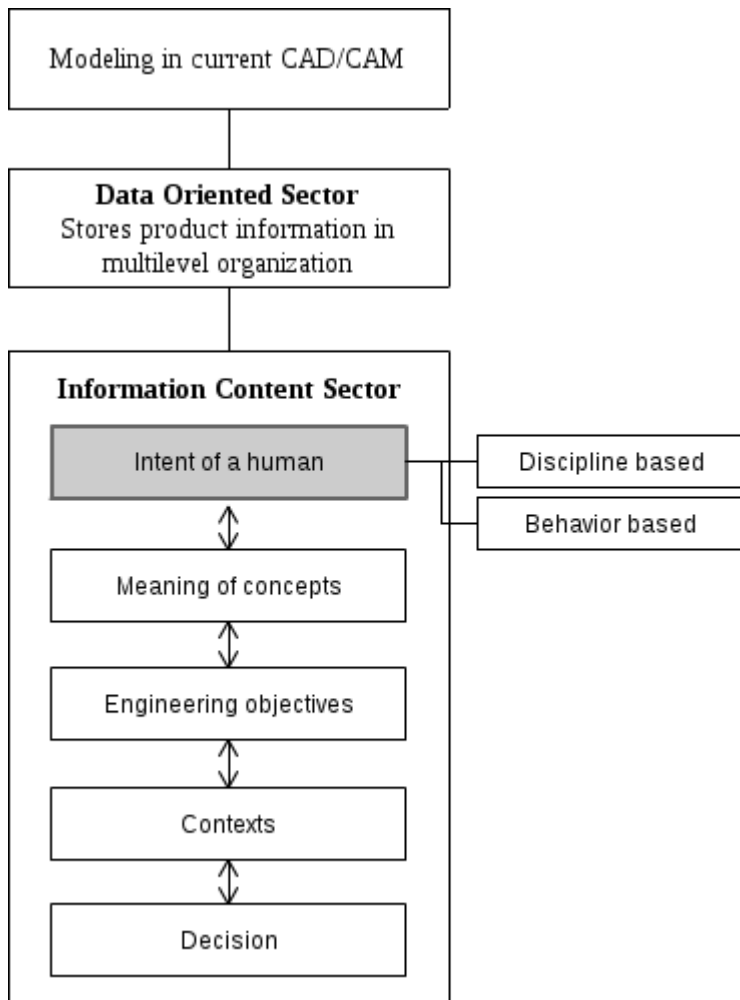
Figure 1
Category of content in the information content sector
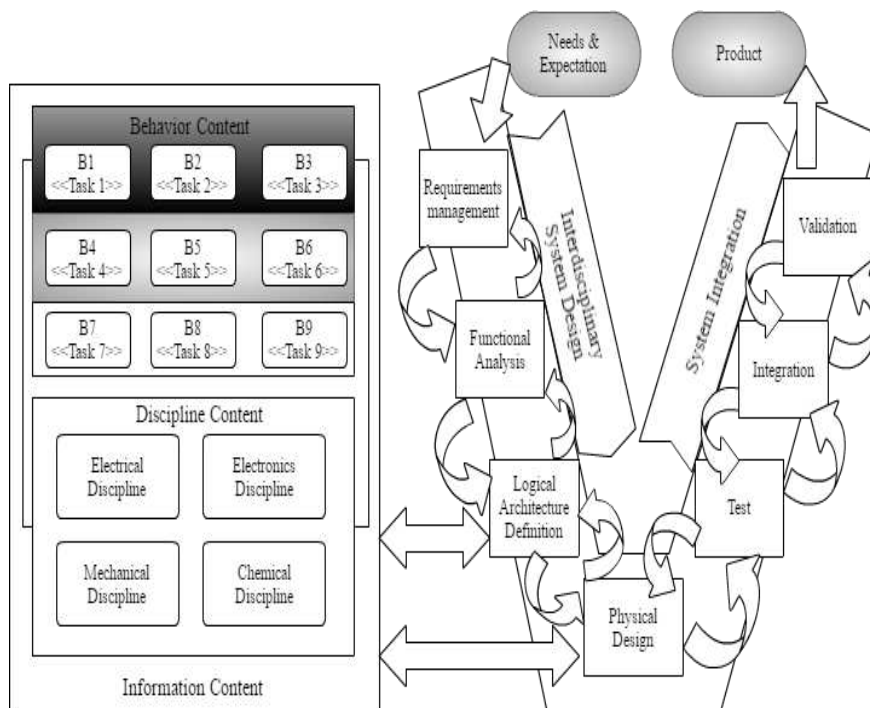
Figure 2
Relation between proposed information content and RFLP structure

4.1 Behavior based Content

The intent of behavior-based content is defined based on system behavior. The engineering objective is to view the system within the context of expected behavior. Behavior based content is the collection of expected behaviors based on the requirement. Priority [8] is assigned to a behavior in the content and arranged in descending order as shown in Fig. 2. In terms of expression, $N_b <= B$, as some behaviors of a product are more mandatory to implement than others in the real world. Here, low priority behavior could be implemented in a future version of the system.

4.2 Discipline based Content

Discipline based content is defined by intializing the intent based on the number of participating engineering disciplines within the system. The engineering objective is to view the system in the context of a discipline as shown in Fig. 2.

Engineers can store the knowledge of a discipline in the Info-Chunk which will be discussed in the next section. This information is used by various engineering disciplines for the depth of knowledge of a system. This content is used to display the activity of a discipline in the product model. In terms of expression, $N_d = D$.

5 Info-Chunk

Info-Chunk acts as a tunnel between information content and the RFLP structure. It stores the correlated knowledge of logical and physical components that participate in the product modeling. It is defined manually by the engineer or automatically by the virtual space during the system design phase. Info-Chunk is placed in the logical component and logical layer of RFLP structure. The knowledge of a system is distributed in the small portions of information in the form of an Info-Chunk in RFLP structure and stored in the data-oriented sector. The main goal of Info-Chunk is to deliver the RFLP structure's component knowledge to the Information Content in context of engineering discipline and system behavior. It is categorised into Component Info-Chunk and Layer Info-Chunk explained in the following subsections.

5.1 Component Info-Chunk

Component Info-Chunk (CiC) is a low-level entity and placed in the logical component of the RFLP structure. It can store the knowledge of the logical component. The parameters that describe the CiC are demonstrated in Fig. 3. In Catia V6, CiC is used to store the knowledge of a modelica component based on the configuration. According to the proposed rule, if there is one CiC, then the component name is the modelica component name defined in the library otherwise initialized either by an engineer or by the intelligent virtual space. Here, the component description parameter is optional and defined to store the component name and component number in the case of more than one CiC. The LiC description stores the information of Logical Info-Chunk. It will be described briefly in the next subsection. The community name stores the engineering discipline name of the modelica component. It is the main parameter of discipline based content. The contribution in the product parameter stores the role of Component Info-Chunk in Layer Info-Chunk for the expected result. The connector parameter stores the knowledge of the inner connector and the stream connector. Here, the inner connector is concerned with the knowledge of input port and output port type while the stream connector is concerned with knowledge of the material flow in the component as explained in [5]. The behavior parameter stores the role of component behavior contributing to a behavior of system. It is the main parameter for the behavior based content.
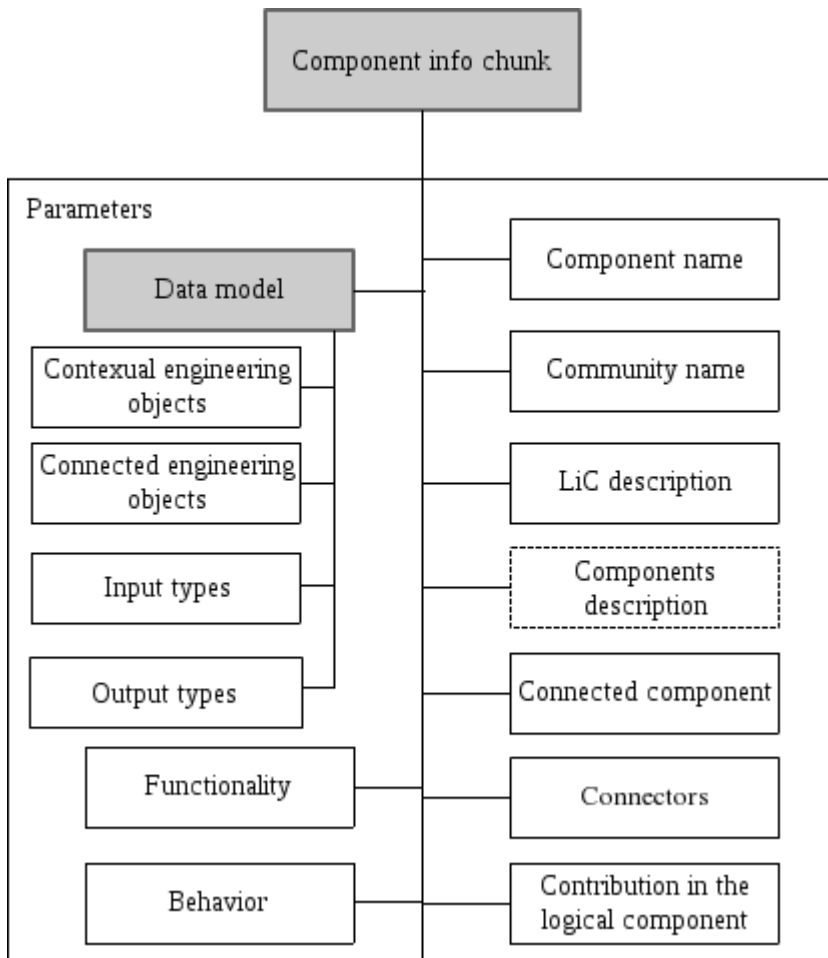
Figure 3
Parameter of Component Info-Chunk

The functionality parameter stores the feature of the component. The data model stores knowledge of the contextual engineering object for the physical level of a system. The contextual engineering object parameter stores knowledge of the engineering object within context of influenced engineering objects and relates to the component. The connected engineering object parameter stores the knowledge of engineering object in the context of connected engineering objects.
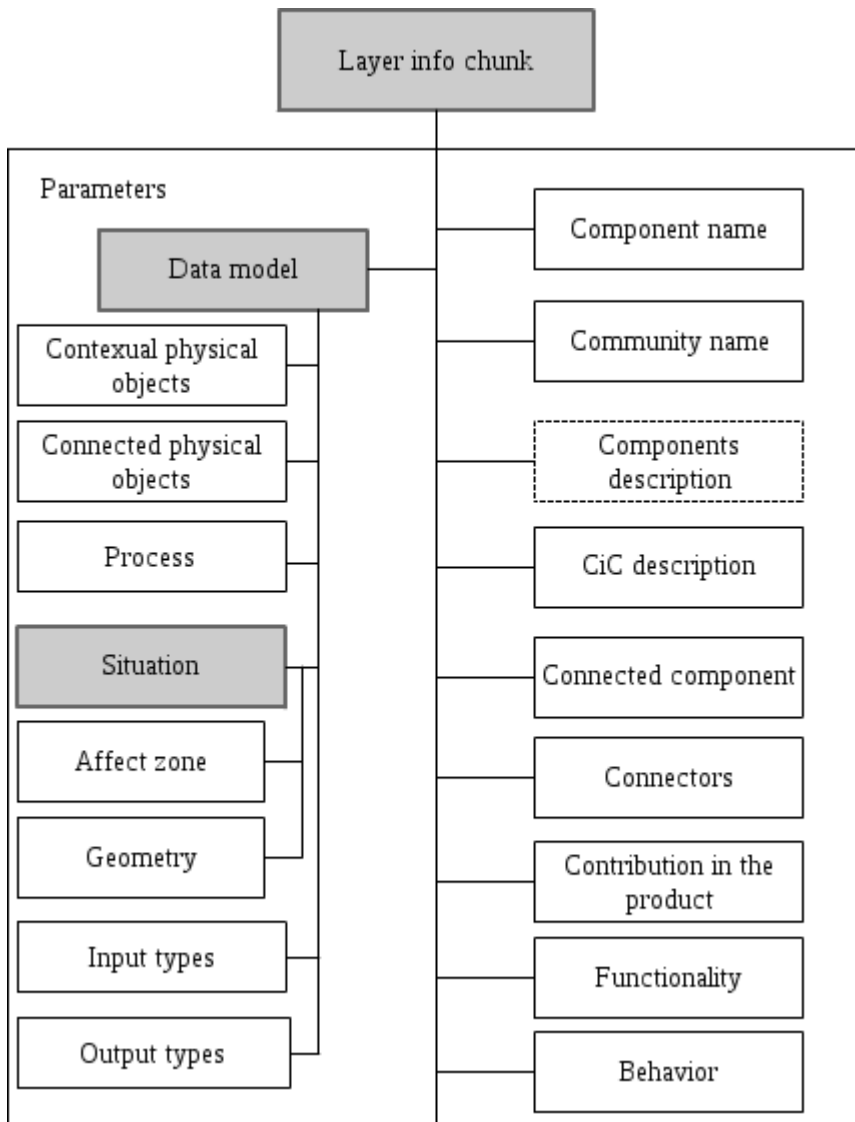
Figure 4
Parameter of Layer Info-Chunk

The input and output type parameters store the knowledge of connection type for input and output port. It depends on the discipline of the connected engineering objects for example if the connected engineering object at the input is a mechanical discipline then the input type parameter will be mechanical. Similarly, the output type parameter will be calculated.

5.2 Layer Info Chunk

Layer Info-Chunk (LiC) is a high-level entity and is placed in logical level of the RFLP structure. The parameters of the LiC are described in Fig. 4. The component name parameter stores the name of the engineering object. Like CiC, the parameters of LiC such as community name, component description, functionality and behavior follow the same steps.
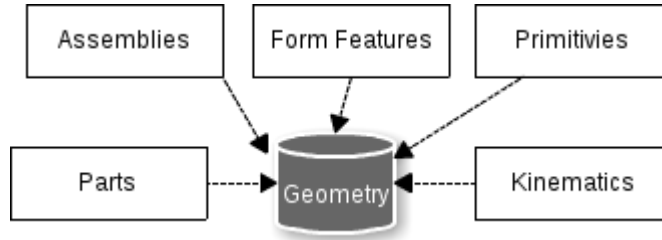
Figure 5

Elements in Geometry entity
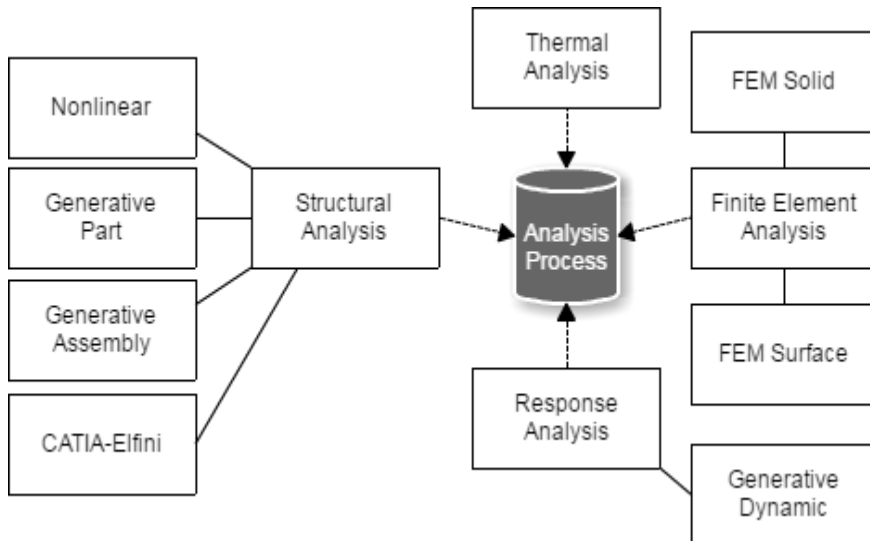
Figure 6

Elements in Analysis Process entity

The connector parameter contains the knowledge of the inner connector and extended connector. The inner connector parameter stores information of the input port and output port type while the extended connector parameter stores information of input and output type of LiC.
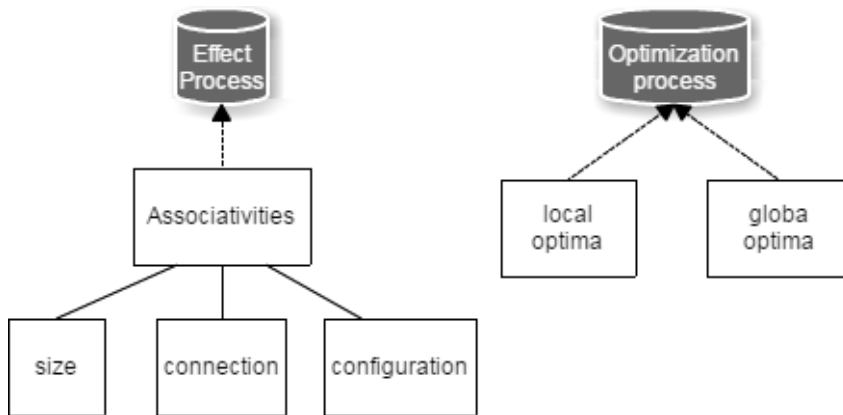
Figure 7
Elements in Effect Process and Optimization Process entity

In case of discipline content, the LiC connector type refers to a discipline while in the case of behavior content, the LiC connector type refers to a behavior. The contribution in the product parameter describes the role of Layer Info-Chunk in logical level of the RFLP structure to deliver the expected result of a system.

a. logical component infochunk   b. representation layer of data model
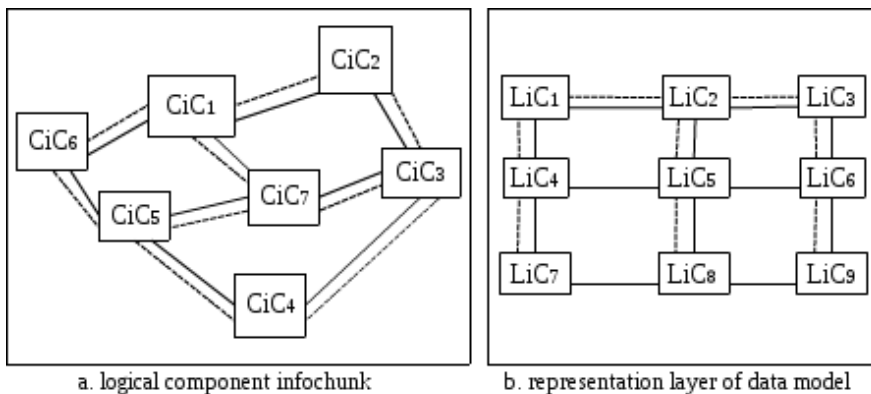
Figure 8
Configuration of Info-Chunk

The data model parameter stores detailed description of the engineering object. The affect zone parameter stores the information of the engineering objects that are influenced due to changes which took place in the analyzed the engineering object. The geometry parameter stores knowledge of the engineering object shape in a situation. It is considered an low-level entity that stores the information of elements like parts, assemblies, form features, and others in this category. The element present in the geometry entity can be assumed as a lower level entity as shown in Fig. 5. The process parameter stores the information of the process

involved in the product modeling. As explained in the paper [6], processes involved in the information content are the analysis process, effect process and optimization process respectively. Like geometry, the process is considered as a low-level entity, which stores the information of the process required by the system design phase. This is explained in Figs. 6 & 7. The input type and output type parameters store the i/o connection of the contextual engineering object.

6   Configuration for Driving the Model

Info-Chunk is placed in the logical component or the logical level of the RFLP structure depending on the type. LiC is collection of the CiC and is connected by the logical and physical connection. The configuration of the LiC is shown in Fig. 8a. The logical connection is the connection between the logical components and is demonstrated by a straight line whereas the physical connection is the connection between the physical components and is demonstrated by a dashed line. Furthermore, structure of the LiC depends on the type of information content. In a similar way, the rest of the LiCs are defined during the product modeling. In order to access the information of a system, LiC are arranged in the representation layer of the data-oriented sector by physical connection and logical connection as shown in Fig. 8b. The CiC is placed in the logical component whereas the LiC is placed at the logical level of the RFLP structure. In Catia V6, the CiC is a low-level entity that extracts information and is represented either corresponding to a modelica component (MC) or to a group of modelica components or the entire graph of a logical component as shown in the Fig. 9a. Engineers can initialize the Info-Chunk as per the system specification. Like CiC, the LiC is represented in the logical component (LC) by same steps shown in Fig. 9b. The logical level of the RFLP structure is mapped to data-oriented sector by the Layer Info-Chunk (LiC) which can transfer the product related knowledge to the information content. The data-oriented sector is connected with the information content to take the correlating decisions during the product modeling.

7   Conceptual Models of Information Content

After evaluating the parameters of Info-Chunk, the final step is to construct conceptual models of information content based on the system behavior and engineering discipline. All the product related decision take place in decision level of the information content. It is important to note that data is accessible in the information content. In other words, it is not possible to make any changes in the data-oriented sector directly. Hence, the interface for HCI (Human Computer

Interaction) is required to access the conceptual model of information content and Info-Chunk. The strategy for the conceptual model of behavior content is concerned with the system behavior while the discipline content is concerned with the engineering discipline.
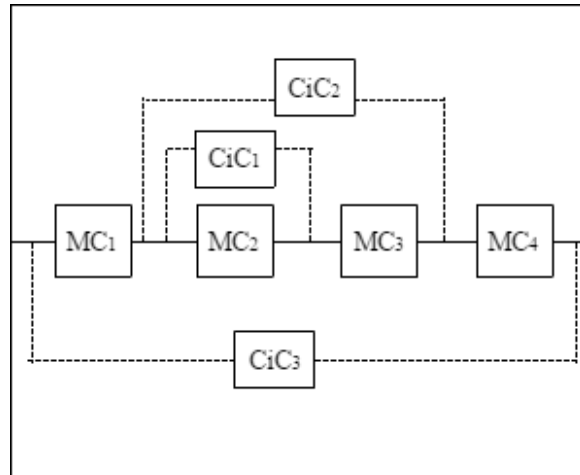
a. logical component
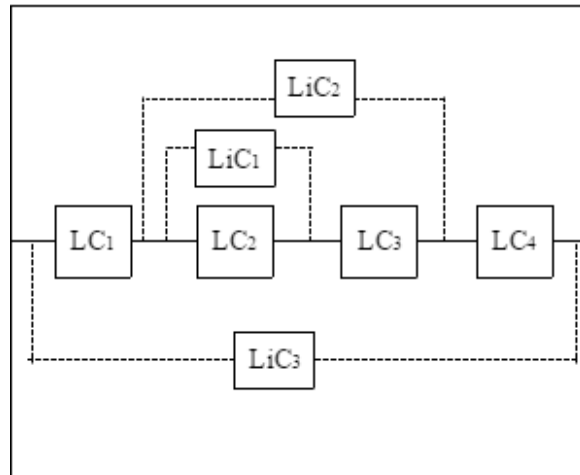
b. logical layer

Figure 9
Representation of Info-Chunk

7.1   Behavior-based Content
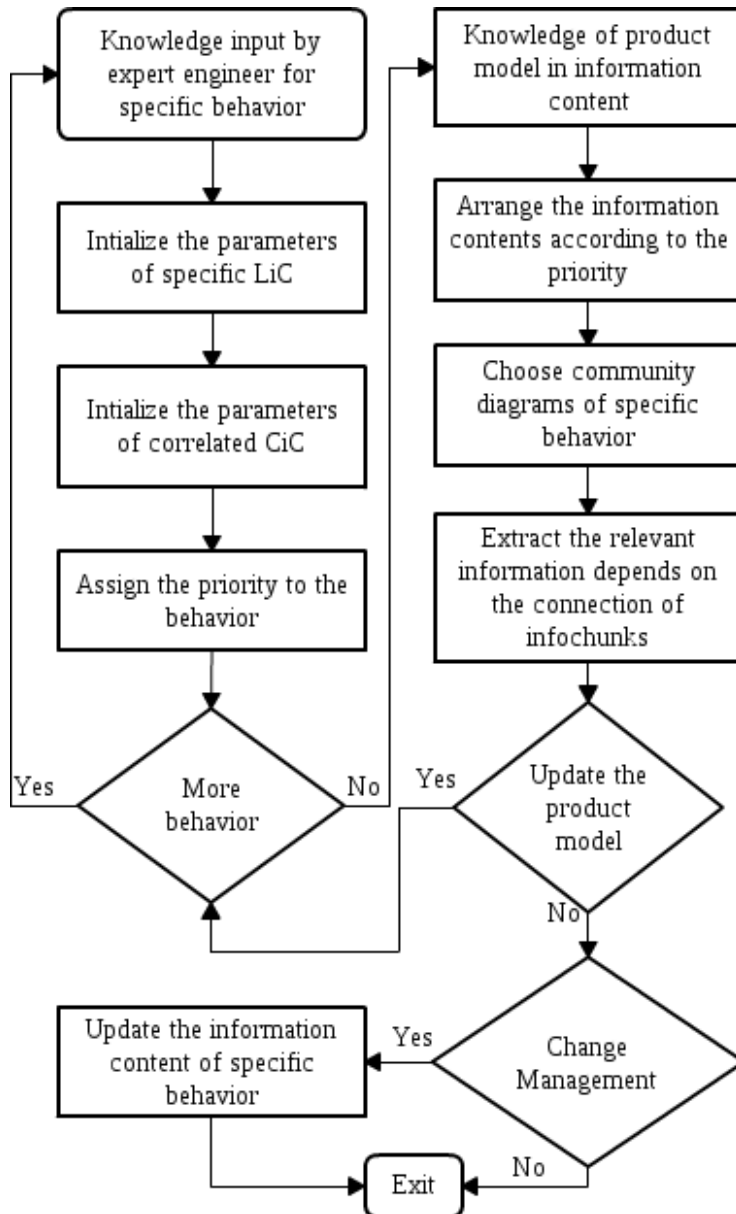
Figure 10
Flow chart of behavior based content

Behavior content is focused on the customer demands. Priority is assigned to the system behavior based on the requirements of customer. Here, some behaviors are more important than others. Therefore, a number of behavior created in a content is based on the priority given to a behavior as explained in Fig. 10. The challenging task is to represent a behavior of a system. It is evaluated and constructed by extracting the mapped parameter of the Component Info-Chunk and Layer Info-Chunk respectively. The logical component with the contextual engineering object of a behavior are initialized. Then, Layer Info-Chunk is proposed and initialized. After that, Component Info-Chunk is proposed and initialized over the Layer Info-Chunk. In a similar way, Layer Info-Chunk is proposed and initialized for the rest of the system behavior. The decision process starts with the community diagram.

To extract the information of a behavior, the community diagram [4] is generated based on the type of Info-Chunk and connection. There are four possible types of community diagrams generated for the behavior content as shown in Fig. 11.
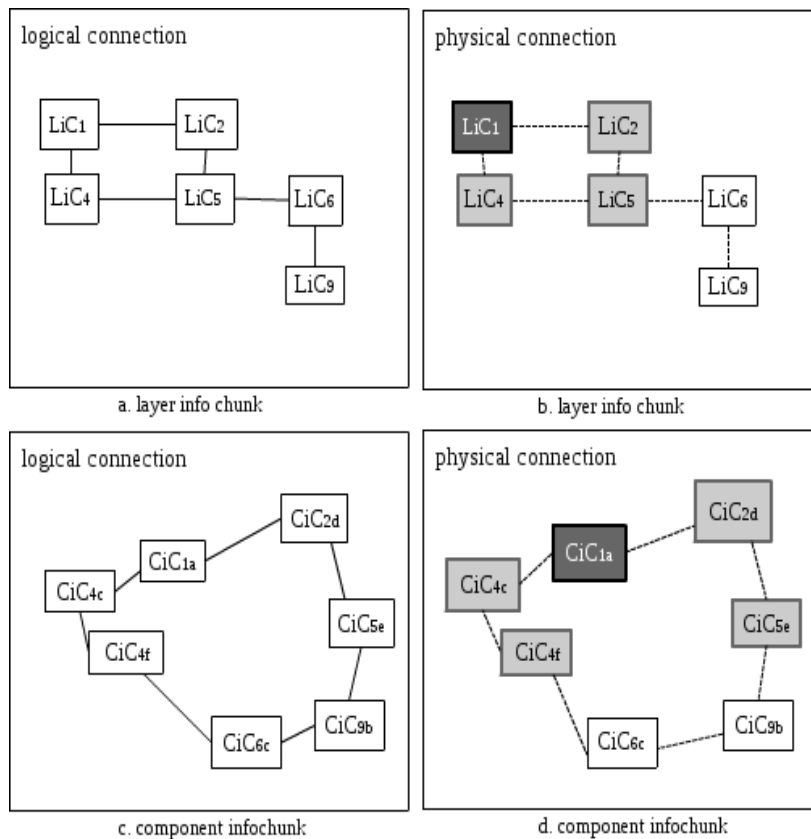
Figure 11
Community diagrams of information content

To express the relation between Info-Chunk in a community diagram, let us assume the following terms: Layer Info-Chunk is represented as LiC, such that $\{LiC_1, LiC_2, LiC_3, \ldots\ldots LiC_m\}$ are the numbers of Layer Info-Chunk present in a logical layer, where m is the total number. Similarly, Component Info-Chunk is represented as CiC, such that $CiC_x = \{CiC_{xa}, CiC_{xb}, CiC_{xc}, \ldots\ldots CiC_{xn}\}$ are the total number of component info chunk present in logical component, where x is the number of Layer Info-Chunk that consists of a specific set of Component Info-Chunk and n is the total number of component in the Info-Chunk. A more detailed description is demonstrated in Fig. 11d, where information of the Component Info-Chunk is extracted which correlates with the Layer Info-Chunk.

To understand a community diagram, it is recommended that the nomenclature of Layer Info-Chunk and Component Info-Chunk are correlated. To analyze the information of a behavior, Info-Chunk is filtered by community names. For example, if any changes occurred in the LiC_1, it can influence the engineering objects of LiC_2, LiC_4 and LiC_5 as shown in Fig. 11b. Based on the information obtained from the community diagram, the contribution of a behavior is evaluated during the product modeling. Later, the product model can be updated by initializing behaviors in the content or making changes in the existing behavior of the content.

7.2   Discipline-based Content

In the present manufacturing world, most products are multi-disciplinary. To define an engineering discipline in discipline content, Component Info-Chunk and Layer Info-Chunk are defined similar to behavior content. The flow chart of a discipline content is shown in Fig. 12. Unlike behavior content, discipline content don't set priority to a discipline. The rest of the steps are similar to the behavior content. The community diagrams are used to extract the relevant information of a discipline by using the Info-Chunk configuration. Later, the product model can be updated by initializing disciplines in the content or making changes in the existing discipline of content.

8   Practical Approach of Conceptual Model

There can be various approaches in taking the conceptual model of information content from concept to reality. In Catia V6, modelica component is used in the logical level of RFLP structure. It is coded using modelica programming language, which is based on the object oriented principles as shown in Fig. 13.
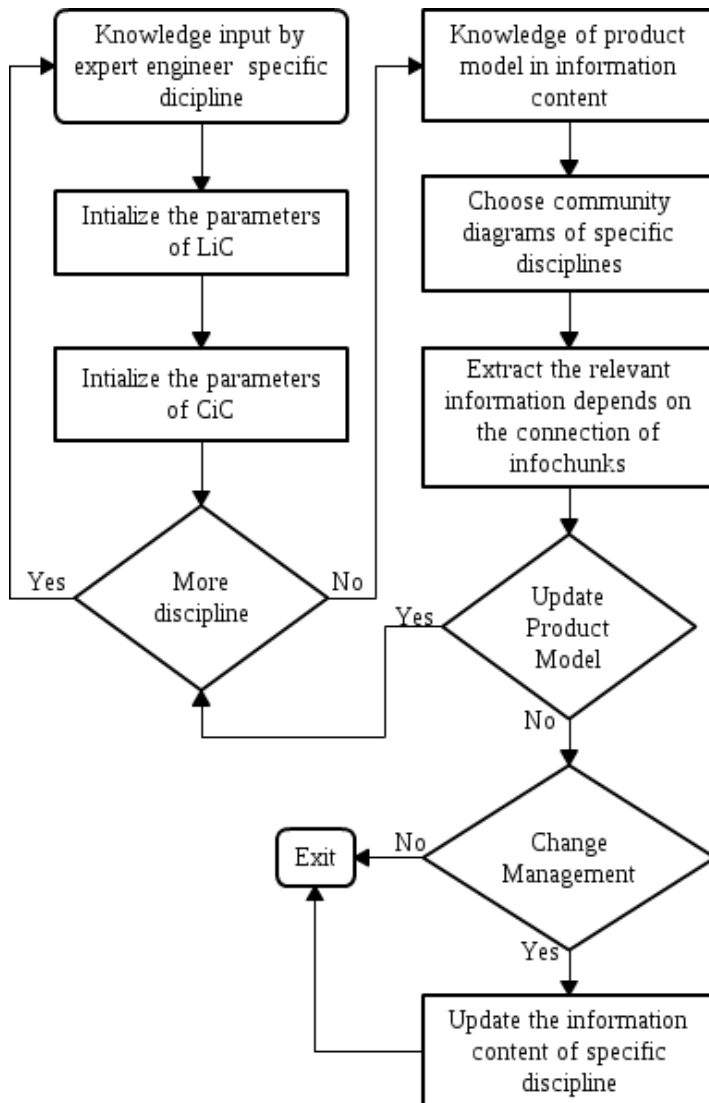
Figure 12
Flow chart of discipline based content

To code an Info-Chunk in the logical level of RFLP structure, it is represented by *InfoChunk* class. It is considered as a base class whose parameters and equations are not yet defined. *ComponentInfo* and *LayerInfo* are the derived class of *InfoChunk* class and is representation of Component Info-Chunk and Layer Info-Chunk respectively.
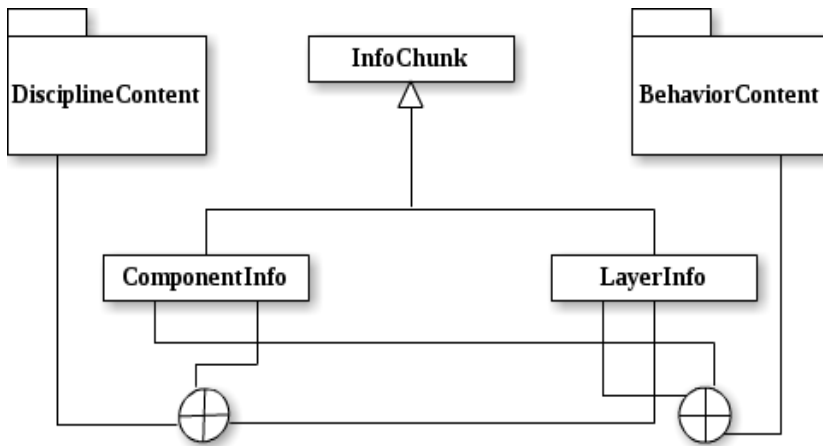
Figure 13

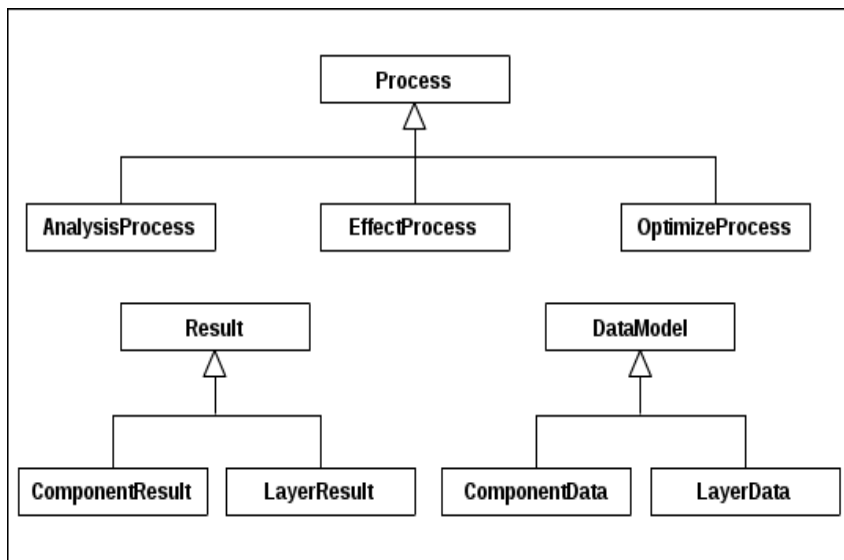Practical approaches for conceptual models of information content

Figure 14

Class diagram for entities in the conceptual model

DisciplineContent and *BehaviorContent* are the package name which can store related *ComponentInfo*, *LayerInfo* and related classes. Furthermore, *ComponentInfo* and *LayerInfo* can initiate the objects of *Process*, *Results* and *DataModel* classes according to the parameters of Info-Chunk. Here, *Process* is the base class and *AnalysisProcess*, *EffectProcess*, *OptimizeProcess* are the derived classes as shown in Fig. 14. Similarly, *Result* is the base class and

ComponentResult, *LayerResult* are the derived classes. *DataModel* is the base class and *ComponentData*, *LayerData* are the derived classes. It is possible to code the Info-Chunk using Simulink component.

Conclusion

This paper proposed conceptual models of information content. The first step is the classification of information content based on the system behavior and engineering discipline. The second step is the introduction of Info-Chunk in the RFLP structure to describe the parameters for the conceptual model of information content. Here, Layer Info-Chunk is placed in the logical level and Component Info-Chunk is placed in the logical component of the RFLP structure. The final step is mapping between Layer Info-Chunk with the Information content to take the correlating decisions. The main purpose of the conceptual model is to store and represent the information of the complex product model into a simplified form so that the engineers can more effectively analyze aspects of the system.

The area of improvements are the parameters of the Info-Chunk, control procedures and integration of information content. Further classification of the information content is also possible. In this paper, the author manually created a conceptual model of information content. The model could be self-adaptive and the Intelligent Virtual space can initialize the parameters of Info-Chunk by algorithms, logic, and rules. In this paper, Info-Chunk is defined for logical and physical level of the RFLP structure. It could be defined for functional level and the next step is to code an API for the conceptual model of information content in the library of modelica.

Acknowledgement

References

[1]   L. Horváth, "New Methods on the Way to Intelligent Modeling in Computer Integrated Engineering," IECON 2010 - 36th Annual Conference on IEEE Industrial Electronics Society, vol., no., pp. 1359-1364, 7-10 Nov. 2010

[2]   L. Horváth and I. J. Rudas, Modeling and Problem Solving Methods for Engineers, ISBN 0-12-602250-X, Elsevier, Academic Press, pp. 46-52, 2004

[3]   L. Horváth and I. J. Rudas, "Supporting Lifecycle Management of Product Data by Organized Descriptions and Behavior Definitions of Engineering Objects," Journal of Advanced Computational Intelligence and Intelligent Informatics, Tokyo, Vol. 11, No. 9, pp. 1-7, 2007

[4]   Yatish Bathla, "Structured Organization of Engineering Objects in the Information Content of PLM System" International Symposium on Applied Computational Intelligence and Informatics (SACI), Timisora, Vol. 11, No. , pp. 473-478, 2016

[5]   Peter Fritzson, Principles of Object-Oriented Modeling and Simulation with Modelica 3.3: A Cyber-Physical Approach, ISBN 978-1-118-85912-4, Wiley-IEEE Press, pp. 3-25, 2015

[6]   Yatish Bathla, "Different Types Of Process Involved In The Information Content Product Model" International Symposium on Intelligent Systems and Informatics (SISY), Subotica, Vol. 14, No. , pp. 99-104, 2016

[7]   L. Horváth, I. J. Rudas, "New Approach to Knowledge Intensive Productmodeling in PLM Systems", International Conference on Systems, Man and Cybernetics, ISBN 978-1-4244-0990-7, Vol ,No. , pp. 668-673, 2007

[8]   Yatish Bathla, Márta Takács "Evaluating Product System Behavior using SoftComputing in Product Structure Modeling" International Symposium on Applied Machine Intelligence and Informatics (SAMI), Herlany, Vol. 15, No. , pp., 2017

[9]   L. Horváth, I. J. Rudas, "Systems Engineering in Product Definition", ISBN 978-1-4799-8221-9, Vol. 13, No. , pp. 181-186, 2015

[10]   Frederic Chauvin, Gauthier Fanmuy "Systems Engineering on 3DEXPERIENCE Platform - UAS Use Case", Dassault systèmes

[11]   Nancy Lesinski "Systems Engineering in Today´s Automative Landscape", http://blogs.3ds.com, December 7, 2015

[12]   Andreas Hofmann, Nils Menager, Issam Belhaj, Lars Mikelsons "Integrated Engineering based on Modelica", International Modelica Conference, Vol, No. 11, pp. 893-901, Sep. 2015

[13]   L. Horváth, I. J. Rudas "Towards the Information Content-driven Product Model," International Conference on System of Systems Engineering , vol., no., pp. 1-6, 2-4 June 2008

[14]   Dassault Systèmes AB, Dymola Dynamic Modeling Laboratory Getting started with Dymola, pp. 5-25, May 2011

[15]   L. Horváth, I. J. Rudas "Product Definition in Virtual Space Using Background information at Description of Engineering Objects," WSEAS TRANSACTIONS on SYSTEMS and CONTROL, Vol. 3, No. 9, pp. 748-758, September 2008

Fault Detection and Isolation of an Aircraft Turbojet Engine Using a Multi-Sensor Network and Multiple Model Approach

Ladislav Nyulászi*, Rudolf Andoga**, Peter Butka*, Ladislav Főző***, Radovan Kovacs***, Tomáš Moravec**

*Department of Cybernetics and Artificial Intelligence, FEEaI, TU Košice
Letná 9, 042 00 Košice, Slovak Republic

**Department of Avionics, Faculty of Aeronautics, TU Košice
Rampová 7, 041 21 Košice, Slovak Republic

***Department of Aviation Engineering, Faculty of Aeronautics, TU Košice
Rampová 7, 041 21 Košice, Slovak Republic

e-mail: {ladislav.nyulaszi, rudolf.andoga, peter.butka, ladislav.fozo, radovan.kovacs, tomas.moravec}@tuke.sk

Abstract: Modern aircraft turbojet engines represent complex systems where it is important to focus on the issues of safety, reliability, efficiency and also the reduction of maintenance costs. Continuous progress in diagnostics brings new possibilities in the implementation of progressive methods instead of traditional based on the use of hardware redundancy. The article deals with the design of the diagnostic and backup system, which uses a voting method and analytical redundancy representing computational models using experimental identification methods (polynomial models, neural networks). Part of the system is also an expert system, which is able to distinguish between engine failure and sensor error. The proposed system for jet engines was tested in laboratory conditions on a small turbojet engine iSTC-21v with positive results.

Keywords: backup; diagnostics; experimental identification; neural networks; turbojet engine; voting method

1   Introduction

The increase in the complexity of aircraft turbojet engines (their structure contains a greater number of elements) also leads to the increased failure probability of engine components. Consequently, any potential failure of an aircraft engine could cause even more extensive damages, therefore the issue of safety and reliability

come to the fore. It is essential to detect faults as fast as possible and to ensure that they do not affect the control of nonlinear systems [1, 2, 3], especially systems like aircraft engines, where failures can be disastrous [4, 5]. Advances in diagnostic systems offer better opportunities for the use of new progressive methods [6, 7]. Today's computers can process back-up controllers and sensor models to create a highly redundant multi-sensor networks with greatly increased efficiency and reliability [8, 9].

Fault detection and isolation (FDI) [10, 11] plays a fundamental role in reducing the maintenance and operating costs and ensuring reliability and safety operation of any system, including a jet engine. A traditional approach to FDI is a hardware redundancy method that is based on the use of multiple sensors. However, this method requires additional equipment which increases cost and weight. That's why we are using analytical redundancy, which uses existing relationships between engine's parameters, so there are no need for extra hardware.

The article deals with the proposal, creation and application of the diagnostic-backup system for small turbojet engines in the software environment MATLAB/Simulink and LabView. The primary focus is oriented on real-time diagnostics of the sensors and engine components using a multi-sensor network [12] and multiple model approach. A voting method, based on results of pair comparison, detects a fault and an expert system determines the type of the fault. The system is able to detect any sensor errors during the engine's operation and to eliminate these errors with the calculated models using other sensors as the backup. These models are created by methods of experimental identification that require the existence of the studied object [13]. In our case, the real object is represented by the small turbojet engine iSTC-21v (see Fig. 1), which undergoes tests in the Laboratory of Intelligent Control Systems of Aircraft Engines [14]. The advantage of using this engine lays mainly in the relatively lower technical complexity compared to normal sized jet engines. But at the same time, the thermodynamic processes ongoing in small and standard jet engines are very similar and the proposed methods are applicable to other types of aircraft engines and systems.
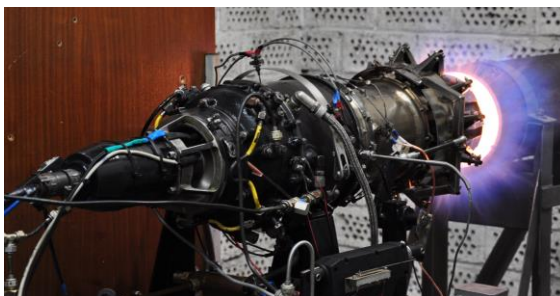
Figure 1
Small turbojet engine iSTC-21v

2 Related Work

The current diagnostic systems that represent a complex of different and unrelated technologies provide only a basic level of monitoring [15]. These systems have limited capabilities and use the obtained information mainly to start maintenance actions, not for decision-making in real time. A lot of promising techniques in the field of fault detection and isolation with good results in simulation environment have been published. Some of them are mentioned in this paper, divided according to the applied methods, together with their limitations, which we try to overcome with our proposed system.

2.1 Kalman Filters

Merrill, Delaat and Bruton in [16] used a bank of Kalman filters (KF) for aircraft engine sensor fault detection and isolation (FDI). They successfully improved the control loop tolerance to the failure of sensors, but did not take the actuator failures into account. Kobayashi and Simon in [17] devised an aircraft engine sensor and actuator FDI system that utilizes a bank of Kalman filters. Based on the results, the designed system is promising for detection of sensor and component faults. Wei and Yingqing in [18] used KF for estimation of engine's health degradation and further fault detection. According to Zedda and Singh [19], the main disadvantages are that Kalman Filters may become unstable if computer calculations have not been sufficiently accurate or include too many small values.

2.2 Linear/Non-Linear Gas Path Analysis

Urban and Volponi in [20] introduced the Gas Path Analysis (GPA) as a method for determining the condition of engine components by using existing aero-thermodynamic relationships between the measured gas path parameters and components. Linear GPA works with the assumption that there are only small changes in health parameters and influence/coefficient matrix (ICM) is invertible. According to Escher in [21] this method does not deal with sensor noise and requires many measurements for the analysis. Escher uses the Newton-Raphson technique to solve the non-linear relationship between the health-parameters and measurements.

2.3 Bayesian Belief Network

Breese et al. in [22] presented a Bayesian Belief Network (BBN) method that uses the statistical data of the engine, for detection of faults on large gas turbines. Romessis and Mathioudakis in [23] introduced a diagnostic BBN that is based on a heuristic approach for determining the network elements. It can be implemented

on any type of engine, but it requires scarce statistical data and BBNs cannot deal with sensor bias.

2.4 Genetic Algorithms

Zedda and Singh in [19] proposed a diagnostic method based on a genetic algorithm (GA). It is used to gain a set of engine parameters which produce a set of predicted dependent parameters through a non-linear model of the gas turbine. The disadvantages are that the method is more computationally demanding than the classic estimation techniques and it is limited to four parameters experiencing parallel degradation. These limitations have been overcome by improving the methods. Kobayashi and Simon in [24] devised the hybrid diagnostic technique that consists of Neural Networks used to estimate the engine internal health and Genetic Algorithms for sensor bias detection and estimation.

3   Experimental Identification

Identification represents the process leading to the compilation of a mathematical model of a certain system by using measured data. We used the measured engine data and experimental identification methods to calculate coefficients and the parameters of the engine's mathematical models.

The basic concepts of the system experimental identification are a real object and its model. A real object represents the original device, in our case the engine iSTC-21v, on which, we can execute certain measurements, to gain knowledge about the systems parametric relationships. System validation is performed through model simulation and the subsequent comparison of each output (measured outputs of a real object are compared with outputs calculated by the model). The process runs until the required similarity of the model, with the real object, is reached [25, 26, 27].

In recent years, there has been substantial progress in the area of experimental identification methods. For these methods, it is essential to have a studied object and the possibility to do experiments with it, but they do not require precise knowledge of the system structure and the description of ongoing processes. To create models of the iSTC-21v engine's parameters, we have chosen 7 methods of experimental identification, which are:

1) Polynomial models
    a. ARX
    b. ARMAX
    c. Output – Error
    d. Box – Jenkins

2) Artificial Neural Networks
   a. Time Delay Neural Network
   b. Distributed Delay Neural Network
   c. NARX Network

3.1 Polynomial Models

3.1.1 ARX Model

ARX model (Auto-Regressive model with eXternal input) [28] estimates parameters using the least squares method provided the measured value is affected only by white noise. It is considered as a simple and highly usable method. ARX model is represented as an equation:

$$y(t) + a_1 y(t-1) + \ldots + a_{n_a} y(t - n_a) = b_1 u(t-1) + b_{n_b} u(t - n_k - n_b + 1) + e(t), \tag{1}$$

where

   $y(t)$ is the system output and t is time

   $a_1 \ldots a_n$ and $b_1 \ldots b_n$ are model parameters for data estimation

   n_a is the order of the polynomial $A(q)$

   n_b is the order of the polynomial $B(q)$

   n_k is the time delay between input u(t) and output $y(t)$

   $y(t-1) \ldots y(t - n_a)$ are previous outputs that depend on current outputs

   $u(t-1) \ldots u(t - n_k - n_b + 1)$ are previous inputs that depend on current inputs

   $e(t)$ is white noise

ARX model can also be represented by a more compact form:

$$A(q)y(t) = B(q)u(t - n_k) + e(t), \tag{2}$$

where

$$A(q) = 1 + a_1 q^{-1} + \ldots + a_{n_a} q^{-n_a}, \tag{3}$$

$$B(q) = b_1 + b_2 q^{-1} + \ldots + b_{n_b} q^{-n_b + 1}, \tag{4}$$

and q^{-1} is the delay operator defined as:

$$q^{-1}u(t) = u(t-1). \tag{5}$$

The ARX model architecture is shown in Fig. 2.
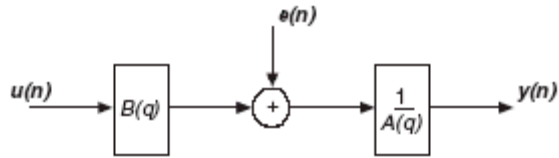
Figure 2
The architecture of the ARX model [29]

3.1.2   ARMAX Model

ARMAX model (Auto-Regressive Moving Average model with eXternal input) [29] is used to estimate parameters by means of the recursive extended least square method. It is able to model stochastic and deterministic parts of the system independently and describes the dynamic behavior of the disturbance variables. The outcome of the ARMAX model is expressed through the idpoly object. This model is defined by an equation:

$$A(q)y(t) = B(q)u(t) + C(q)e(t),$$ (6)

where

$$C(q) = 1 + c_1 q^{-1} + \ldots + c_{n_c} q^{-n_c},$$ (7)

The structure of the ARMAX model can be seen in Fig. 3.
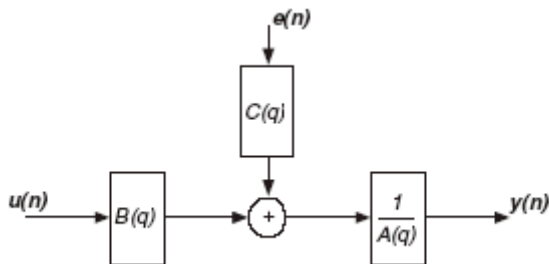
Figure 3
The scheme of the ARMAX model [29]

3.1.3   Output – Error Model

Output – Error (OE) model [30] describes the system dynamics separately from the stochastic dynamics. It does not use any parameters in order to simulate the disturbance characteristics. As the identification method of the OE model is used the prediction error method. This model is defined by an equation:

$$y(t) = \frac{B(q)}{F(q)} u(t - n_k) + e(t),$$ (8)

where

$$F(q) = 1 + f_1 q^{-1} + \dots + f_{n_f} q^{-n_f},$$ (9)

The structure of the OE model can be seen in Fig. 4.
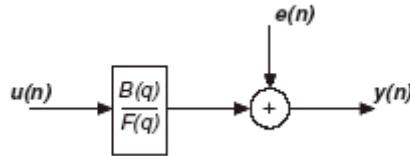
Figure 4
Output - Error model architecture [29]

3.1.4   Box – Jenkins Model

Box – Jenkins (BJ) model [29] is a mathematical model used to predict data within a time series. It is the combination of AR and MA models, where failures are modeled separately from the dynamics of the system:

$$y(t) = \frac{B(q)}{F(q)} u(t - n_k) + \frac{C(q)}{D(q)} e(t),$$ (10)

where

$$D(q) = 1 + d_1 q^{-1} + \dots + d_{n_d} q^{-n_d},$$ (11)

The scheme of the Box – Jenkins model is shown in Fig. 5.
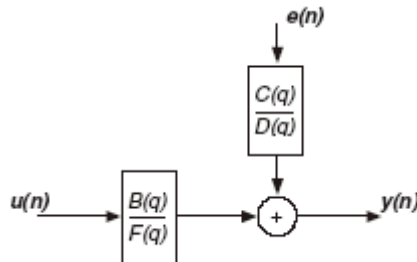
Figure 5
The structure of the Box - Jenkins model [29]

3.2   Artificial Neural Networks

3.2.1   Time Delay Neural Network

Time delay neural networks (TDNNs) [31, 32] represents an architecture which main purpose is to work on sequential data. Their units generally form part of a larger pattern recognition system and are able to recognize characteristics independent of time-shift. A key ability of the TDNNs is to express a relation between inputs in time and so on recognizing patterns between the delayed inputs.

3.2.2   Distributed Delay Neural Network

Distributed delay neural networks (DDNNs) [33] are similar to feed forward networks, with the exception that each input and layer weights have a tap delay line associated with it. This allows the network to have a finite dynamic response to time series input data. This network is also close to the TDNN, with the difference that it only has delays on the input weight.

3.2.3   NARX Neural Network

NARX (Nonlinear Autoregressive models with eXogenous input) neural network [34] is capable of predicting one time series, given past values of the same time series and current and past values of the exogenous or external time series. In addition, the model contains an "error" term, which applies to the fact that knowledge of the other concepts will not enable the present value of the time series to be predicted precisely.

4   Diagnostic and Backup System

The proposed diagnostic and backup architecture is composed of two main blocks. The diagnostic block created in the LabView environment consists of the diagnostic method (voting method) to detect an error and the expert system to determine the type of the error. The backup block contains the calculated mathematical models, obtained by experimental identification methods, in MATLAB/Simulink. Both are interconnected and communicate through the shared variables using OPC server and fully described in this chapter.

4.1   Multi-Sensor Network

Experimental identification [26] is the process that leads to the calculation of the mathematical model of a real system using data obtained by measurement. In our case, these data are represented by ten parameters of the small turbojet engine iSTC-21v. These parameters are:

- T_{2C} – total temperature on the compressor's outlet [°C]

- T_{3C} – total temperature in the combustion chamber [°C]

- T_{4C} – total temperature beyond the gas turbine [°C]

- P_{2C} – total pressure of air beyond the compressor [Pa]

- P_{3C} – total pressure of gas at the inlet to the gas turbine [Pa]

- P_{pal} – fuel pressure [Pa]

- Q_{pal} – fuel flow supply [l/min]

- F_t – thrust of the engine [N],

- n – speed of the turbo-compressor [rpm]

- A_5 – exhaust nozzle diameter [%]

The measured data was divided into training, testing and validation sets. In order to get the most accurate experimental models, we have created over 5000 models in the MATLAB/Simulink environment, using the above mentioned experimental identification methods in different configurations. Then we compared these models, using validation data and selected the best one, based on the values of the mean absolute percentage error (MAPE). The results are shown in Table 1. The simplified structure of the multi-sensor network can be seen in Fig. 6. Each of the inputs to individual models of one parameter is measured by different sensor except exhaust nozzle diameter A_5 which is the essential model input because it influences the thermodynamic properties of the engine and this eliminates the possibility of mutual influence and thus increases the reliability and efficiency of the system.
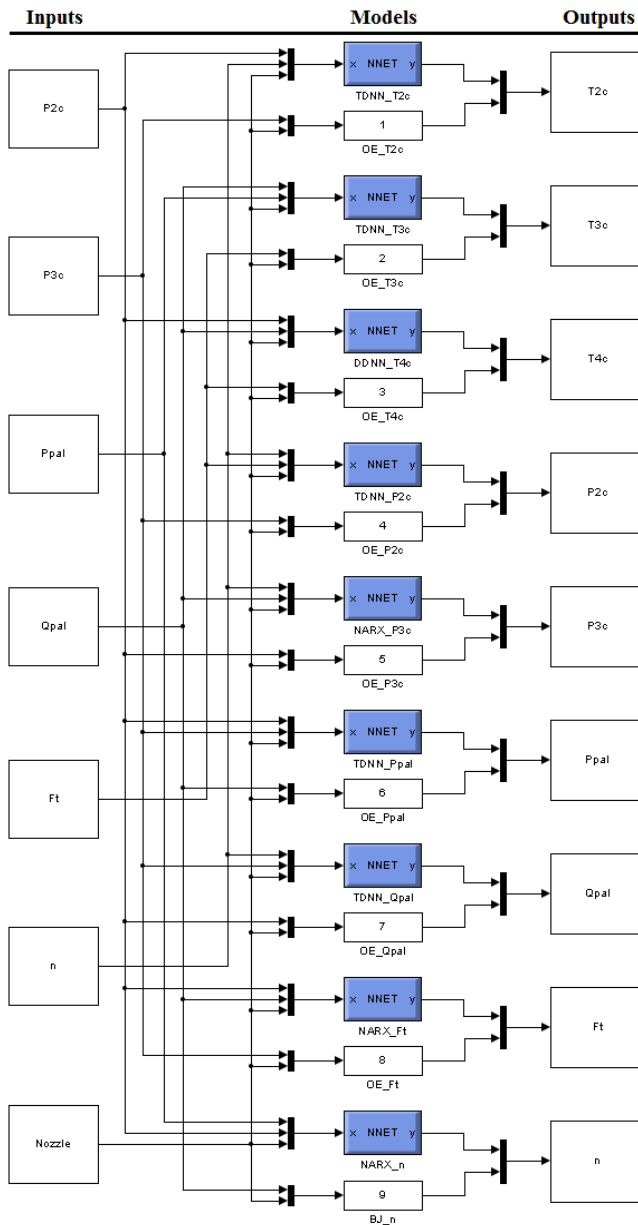
Figure 6
The scheme of multi-sensor network

Table 1
Final experimental models of engine parameters

Outputs	Inputs	Method	MAPE [%]
T_{2C}	P_{2C}, n, A_5	TDNN	7.9784
	P_{3C}, A_5	Output - Error	5.1810
T_{3C}	Q_{pal}, P_{pal}, A_5	TDNN	1.8654
	F_t, A_5	Output - Error	4.0667
T_{4C}	P_{2C}, Q_{pal}, A_5	DDNN	5.1094
	F_t, A_5	Output - Error	4.4707
P_{2C}	n, F_t, A_5	TDNN	1.1303
	P_{3C}, A_5	Output - Error	3.2630
P_{3C}	n, Q_{pal}, A_5	NARX	0.8733
	P_{2C}, A_5	Output - Error	2.7789
P_{pal}	P_{2C}, P_{3C}, A_5	TDNN	4.8581
	Q_{pal}, A_5	Output - Error	10.2502
Q_{pal}	n, P_{3C}, A_5	TDNN	2.0113
	P_{2C}, A_5	Output - Error	7.5757
F_t	P_{2C}, Q_{pal}, A_5	NARX	5.7475
	P_{3C}, A_5	Output - Error	8.0302
n	P_{pal}, P_{2C}, A_5	NARX	0.6436
	Q_{pal}, A_5	Box - Jenkins	2.2926

4.2   Diagnostic Modules

The complete diagnostic and backup system is composed of nine diagnostic modules for each of the chosen iSTC-21v engine's parameters. These modules in monitor engine condition in real time and evaluate whether the sensors provide correct data. If a sensor fault is detected, they can replace it with backup represented by the created experimental model of that parameter whose sensor is faulty. Due to the limited number of pages, for example, the designed architecture of diagnostic module for parameter n (speed of the turbo-compressor) is shown in the Fig. 7.
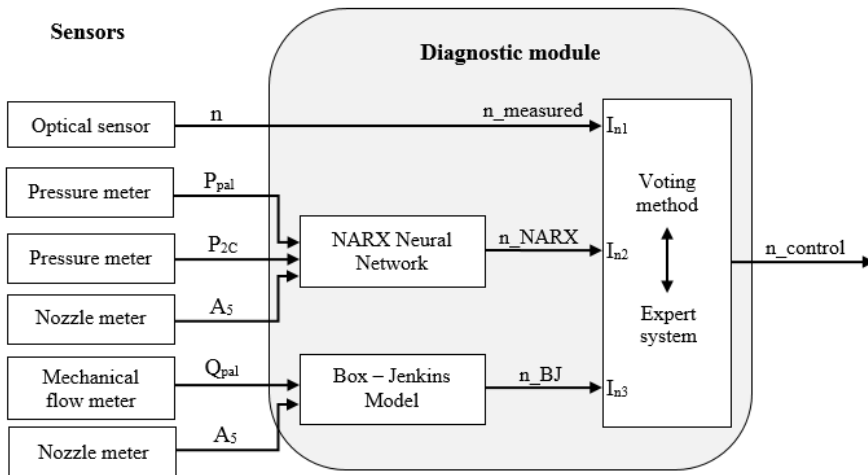
Figure 7
The structure of the diagnostic module for the parameter *n*

The system is based on triple modular redundancy and a dynamic backup which switches between basic and backup elements, depending on the results of the diagnostics. As a diagnostic method the voting method was selected [35, 36]. Inputs to the voting method are the measured data from the sensor and modeled values of parameter computed by experimental models. In our case, for parameter *n* this represents a signal from the optical sensor (I_{n1}) and outputs of the NARX neural network (I_{n2}) and Box – Jenkins model (I_{n3}). These inputs are fed into the block of pair comparisons, where each couple is compared and evaluated depending on the amount of the maximum allowed deviation. The size of this permissible error for each pair is computed as the sum of the allowed deviation values for signals that make up the pair. For the sensors it represents the accuracy with which they work and for experimental models that value is determined as the maximum absolute error (MaxAE), compared to real measured data. The maximum allowed deviation values for parameter *n* are shown in Table 2.

Table 2
Maximum permissible error of inputs

Inputs	Allowed deviation [rpm]	Pair comparison	Sum of allowed deviation [rpm]
I_{n1}	200	I_{n1} and I_{n2}	1252
I_{n2}	1052	I_{n1} and I_{n3}	3363
I_{n3}	3163	I_{n2} and I_{n3}	4215

If two out of the three compared output pairs exceed the sum of the permissible error, then the output parameter, which is present in both of the error exceeding pairs, is declared as faulty. If all three pairs exceed the maximum deviation value,

the system verifies inputs to the models. In the case where the diagnostic/backup system evaluates data from these sensors as accurate, the output of the model is set as correct.

4.3   Expert System

When a fault is detected, the right decision about its type (sensor, actuator or component) is essential. Several methods have been suggested in this area, but most of them were mathematical calculations [37] or were not tested on a real system, only in a simulation environment [38].

We have proposed an effective and low computer resource demanding method to distinguish between a sensor error and a component/engine fault. Due to the complexity of this area, it is difficult and almost impossible to have a hundred percent success, in determining the exact type of failure. So the system always chooses the option with a higher probability. A real-time expert system provides immediate decisions using if-then rules in its knowledge base [39]. This base can contain many rules for all engine sensors, but we could summarize them into three basic rules:

- If only one sensor provides incorrect data, then it is a sensor fault (SF). – This is based on the assumption that an engine fault has an influence on more than just one parameter.

$$\textbf{IF } \sum_{i=1}^{9} E_i = 1 \textbf{ THEN } (\text{SF} = 1 \textbf{ AND } \text{EF} = 0)$$

- If two sensors provide incorrect data, then it is a sensor fault / engine fault. – It depends on exactly which sensors the voting method has evaluated as a fault. If they can be affected by one interference (sensor fault) or if damage to one engine component can affect the values of only these two sensors (component fault).

$$\textbf{IF } \sum_{i=1}^{9} E_i = 2 \textbf{ THEN } (\text{SF} = 1 \textbf{ OR } \text{EF} = 1)$$

- If three or more sensors provide incorrect data, then it is an engine fault (EF). – This is determined by the fact that the probability of failure of the three and more sensors is very small.

$$\textbf{IF } \sum_{i=1}^{9} E_i \in \langle 3,9 \rangle \textbf{ THEN } (\text{SF} = 0 \textbf{ AND } \text{EF} = 1)$$

In the case of fault detection, the results of the voting method E_i are transferred to the expert system. It determines whether a sensor or engine fault is detected. If it is a sensor fault, the output of the diagnostic/backup system is represented by the

most accurate signal (based on the allowed deviation value – see Table 2) which was diagnosed by the voting method as correct. If it is an engine fault, the output of the diagnostic and backup system is set as the signal from the sensor, not the model, so we get the real measured values. Moreover, this signal can be used to parameterize the situational control system and choose appropriate control strategy to handle an engine failure (e.g. overheat). The designed decision making rules of the expert system are simple probability based options and therefore robust, thus not susceptible to changes in sensor network or modifications in the measured parameters. A more complex expert system with further decision making when rules two and three are active can be designed to more precisely evaluate the failure of the engine as well as evaluate the probability of the classification. The link scheme is shown in Fig. 8.
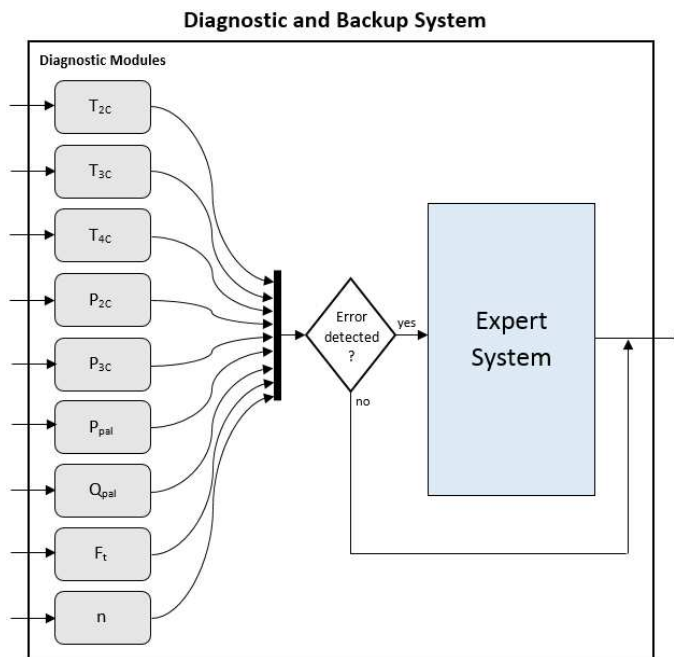
Figure 8
Connection diagram of individual parts of the diagnostic and backup system

5   System Test Results

The functionality of the proposed and implemented system for real-time diagnostics and backup has been tested in the Laboratory of intelligent control systems of jet engines on the small turbojet engine iSTC-21v. The first test

represents a faultless engine operation and the results for the speed of the turbo-compressor *n,* is shown in Fig. 9. The engine was run for 80 seconds and the graph shows the measured data from the optical sensor (blue) and approximate data of the parameter calculated by NARX neural network (red) and Box – Jenkins model (black). The output of the diagnostic/backup system (green) is the most accurate signal, which in the case of faultless operation of the engine represents a signal from the optical sensor. During the test, the mean absolute error of the NARX neural network was MAE = 262.2621 rpm and error of the Box – Jenkins model was MAE = 945.7668 rpm.
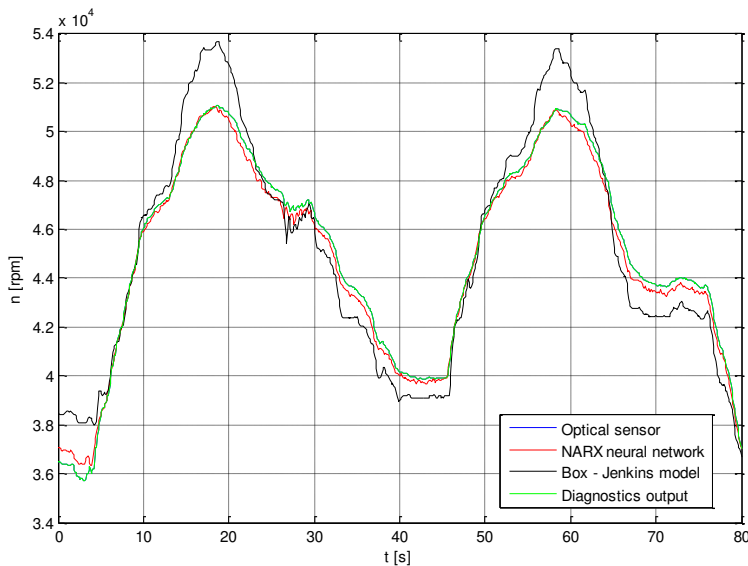
Figure 9

Test of the system for parameter *n* during faultless engine operation

For complete testing of the system response, experiments were also performed when a fault occurs. Two types of sensor errors that are the most common were considered:

- Failure of individual inputs – caused by sudden power loss or loss of the communication channel

- Presence of random input values – caused by electromagnetic interference (noise)

As the sensors cannot be physically damaged, the errors were simulated by influencing input values of the system.

Testing for Failure of Individual Inputs

Failure of individual inputs is represented by a sudden fall of the measured data to zero. This fault was simulated in such a way that at the specific intervals, the real value of the chosen input (signal from the sensor) was set to zero. To generate an error, in the 20th second was measured data from optical sensor (parameter *n*) set to zero. The implemented system diagnosed the sensor error and replaced it with the backup which is the output of the NARX neural network. In the 40th second was the value of the parameter P_{pal} changed to zero, which affected the accuracy of the neural model and thus simulated an error. Only by the pair comparison results, it was impossible to determine which input (I_{n1}, I_{n2}, I_{n3}) is wrong. So the system checked all sensors and model outputs and diagnosed that only the Box – Jenkins model provided correct data. In the 60th second were all data set back to the real values and the diagnostics output was again the most accurate signal from optical sensor. As can be seen in Fig. 10, the designed diagnostic and backup system was able to detect failures and replace them with the backup (data acquired by experimental models).
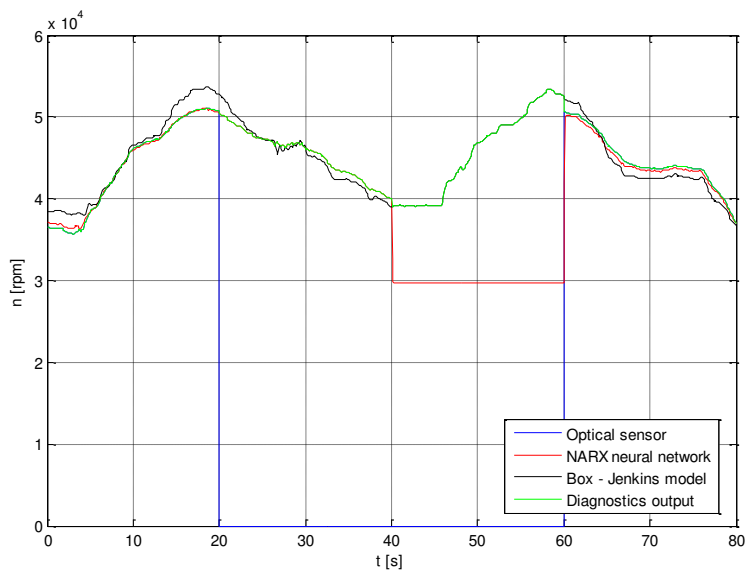
Figure 10
Test of the system for failure of individual inputs

Discrimination Engine/Sensor Failure Test

In this experiment, we tested the ability of the system to distinguish between engine and sensor faults by adding random input values, thus simulating additive errors. The random values appear as a rapid increase or decrease in the size of inputs of the voting method over their real-actual values. It was simulated by adding a certain value to the real values of individual inputs at a certain time.

The response of the system is shown in Fig. 11. Similar to the previous test, the error of the optical sensor was first simulated by adding the speed of 10000 rpm ($20^{th} - 80^{th}$ second). The neural model error was then generated by increasing the value of fuel pressure P_{pal} of 30 Pa ($40^{th} - 80^{th}$ second). In both cases, the system correctly detected the sensor failure and replaced it with a backup. Unlike the previous test, the adjusted values were not returned to true values. In the 60th second 0.5 l/min to the real value of the fuel flow supply Q_{pal} was added. It caused that the expert system diagnosed engine fault because more than two sensors provided the incorrect data and the signal from optical sensor was set as the diagnostic output. This test shows than the implemented diagnostic/backup system is capable of responding to errors caused by random input values and engine faults.
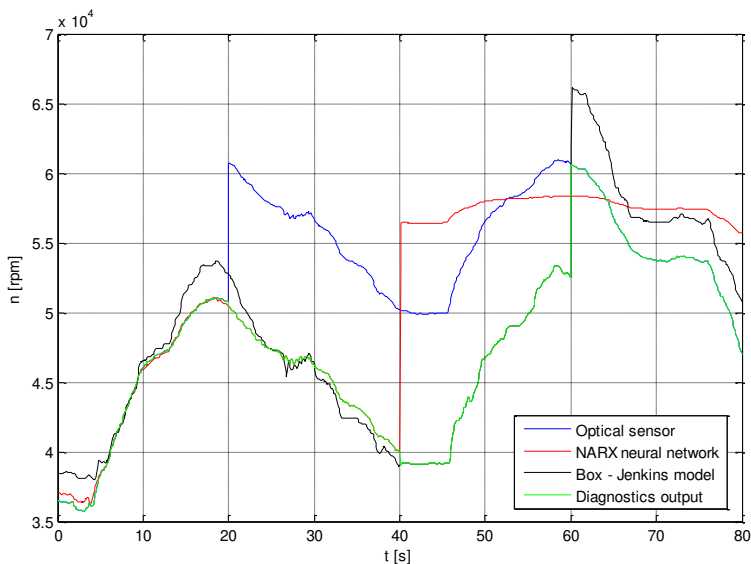
Figure 11
Test of the system for random input values

Conclusions

The issues described in this paper represent the essential components for on-line diagnostics of aircraft turbojet engines. It is made important by the fact, that all aviation systems have to work, without failure, because even a minor failure can have catastrophic consequences. We have designed a diagnostic and backup system using a multi-sensor network and multiple model approach for fault detection and isolation. It utilizes the signals from sensors and approximate values of parameters obtained by polynomial models and neural networks. Using these models as backups, leads to increased redundancy of the system without adding additional sensors, resulting in a cost reduction. The functionality and reliability of

the system was successfully tested on the small turbojet engine, iSTC-21v, under laboratory conditions. The main advantage of the proposed system is the ability to diagnose faults, distinguish between sensor errors and engine faults using the expert system and also to prevent sensor errors that have an impact on engine operation and by timely application of the designed backups. The system can be improved in the future by adding more rules to the expert system, so it will provide more accurate information about the detected faults of the diagnosed object.

Acknowledgement

References

[1]   H. K. Lam, F. H. F. Leung, P. K. S. Tam, "Stable and robust fuzzy control for uncertain nonlinear systems," IEEE Transactions on Systems, Man and Cybernetics, Part A: Systems and Humans, Vol. 30, No. 6, 2000, pp. 825-840

[2]   M.-L. Tomescu, S. Preitl, R.-E. Precup, J. K. Tar, "Stability analysis method for fuzzy control systems dedicated controlling nonlinear processes," Acta Polytechnica Hungarica, Vol. 4, No. 3, 2007, pp. 127-141, ISSN 1785-8860

[3]   J. K. Tar, J. F. Bitó, I. J. Rudas, "Contradiction Resolution in the Adaptive Control of Underactuated Mechanical Systems Evading the Framework of Optimal Controllers," Acta Polytechnica Hungarica, Vol. 13, No. 1, 2016, pp. 97-121, ISSN 1785-8860

[4]   R. Isermann, "Fault-Diagnosis Systems: An Introduction from Fault Detection to Fault Tolerance," Springer – Verlag Berlin Heidelberg, 2006, 475 pp., ISBN 3-540-24112-4

[5]   L. Nyulászi, "Improving the Diagnostic and Backup System Using Experimental Identification Methods," in SCYR 2016: Proceedings from conference: 16th Scientic Conference of Young Researchers, 2016, pp. 148-149, ISBN 978-80-553-2566-8

[6]   A. Linke-Diesinger, "Systems od Commercial Turbofan Engines: An Introducion to Systems Functions," Springer – Verlag Berlin Heidelberg, 2008, 239 pp., ISBN 978-3-540-73619-6

[7]   J. S. Guan, L. Y. Lin, G. L. Ji, Ch. M. Lin, T. L. Le, I. J. Rudas, "Breast tumor computer-aided diagnosis using self-validating cerebellar model neural networks," Acta Polytechnica Hungarica, Vol. 13, No. 4, 2016, pp. 39-52, ISSN 1785-8860

[8]   J. B. Armstrong, D. L. Simon, "Implementation of an Integrated On-Board Aircraft Diagnostic System," NASA/TM-2012-217279, AIAA-2011-5859, 2012

[9]   M. Laššák, K. Draganová, "Improvement of low-cost MEMS gyroscope characteristics by data filtering and fusion", Advances in Military Technology, Vol. 11, No. 2, 2016, pp. 171-178, DOI: 10.3849/aimt.01126

[10]   N. Meskin, K. Khorasani, "Fault Detection and Isolation: Multi-Vehicle Unmanned Systems," Springer – Verlag New York, 2011, 166 pp., ISBN 978-1-4419-8392-3

[11]   J. Bokor, Z. Szabó, "Fault detection and isolation in nonlinear systems," in Annual Reviews in Control, Vol. 33, Issue 2, Elsevier, 2009, pp. 113-123, ISSN 1367-5788

[12]   Y. Mon, Ch. Lin, I. J. Rudas, "Wireless Sensor Network (WSN) Control for Indoor Temperature Monitoring," Acta Polytechnica Hungarica, Vol. 9, No. 7, 2012, ISSN 1785-8860

[13]   L. Nyulászi, L. Madarász, "Experimental Identification of the Small Turbojet Engine MPM-20," in CINTI 2014, 2014, pp. 497-501, ISBN 978-1-4799-5338-7

[14]   L. Főzo, et al., "Description of an intelligent small turbo-compresor engine with variable exhaust nozzle," in SAMI 2015: 13th IEEE International Symposium on Applied Machine Intelligence and Informatics, 2015, pp. 157-160, ISBN 978-1-4799-8220-2

[15]   J. S. Litt, et al., "A Survey of Intelligent Control and Health Management Technologies for Aircraft Propulsion Systems," NASA/TM-2005-213622, ARL-TR-34 13, 2005

[16]   W. C. Merrill, J. C. Delaat, W. M. Bruton, "Advanced detection, isolation, and accommodation of sensor failures – Real-time evaluation," Journal of Guidance, Control, and Dynamics, Vol. 11, No. 6, 1988, pp. 517-526, ISSN 0731-5090

[17]   T. Kobayashi, D. L. Simon, "Evaluation of an Enhanced Bank of Kalman Filters for In-Flight Aircraft Engine Sensor Fault Diagnostics," NASA/TM-2004-213203, ARL-TR-3252, 2004

[18]   X. Wei, G. Yingqing, "Aircraft Engine Sensor Fault Diagnostics Based on Estimation of Engine's Health Degradation," Chinese Journal of Aeronautics, Vol. 22, No. 1, 2009, pp. 18-21, ISSN 1000-9361

[19]   M. Zedda, R. Singh, "Gas turbine engine and sensor fault-diagnosis using optimisation techniques," Journal of Propulsion & Power, Vol. 18, No. 5, pp. 1019-1025, 2002

[20] L. Urban, A. Volponi, "Mathematical methods of relative engine performance diagnostics," SAE 1992 Transactions Journals of Aerospace, Section 1, Vol. 101, SAE Technical Paper No. 922048, 1992

[21] P. C. Escher, "Pythia: An object-oriented gas-path analysis computer program for general applications," PhD thesis, School of Mechanical Engineering, Cranfield University; 1995

[22] J. S. Breese, et al., "Automated Decision-Analytic Diagnosis of Thermal Performance in Gas Turbines," in Proceedings of the ASME International Gas Turbine and Aeroengine Congress and Exposition, Cologne, Germany, 1992

[23] C. Romessis, K. Mathioudakis, "Bayesian Network Approach for Gas Path Fault Diagnosis," ASME. J. Eng. Gas Turbines Power, Vol. 128, No. 1, 2004, pp. 64-72

[24] T. Kobayashi, D. L. Simon, "Aircraft Engine On-Line Diagnostics through Dual-Channel Sensor Measurements: Development of an Enhanced System," In Proceedings of ASME Turbo Expo 2008, Berlin, Germany, 9-13 June 2008, NASA/TM-2008-215229

[25] L. Nyulászi, R. Andoga, P. Butka, V. Gašpar, "Comparison of Experimental Identification Methods Using Measured Data from a Turbojet Engine," in SAMI 2016, 2016, pp. 23-27, ISBN 978-1-4673-8739-2

[26] L. Ljung, "System Identification," New Jersey: PTR Prentice Hall, 1987, 255 pp., ISBN 0-13-881640-9

[27] F. Adamcik, R. Bréda, P. Kurdel, V. Beno, "Modeling of Changes in Flow Air Fuel Effected by Changes in Environmental Conditions," NAŠE MORE: znanstveno-stručni časopis za more i pomorstvo, 61(1-2), 2014, pp. 40-42

[28] M. Rahmat, et al., „Accuracy Comparison of Arx and Anfis Model of an Electro-Hydraulic Actuator System," in International Journal on Smart Sensing and Intelligent Systems, Vol. 4, No. 3, 2011, pp. 440-453

[29] Selecting a Model Structure in the System Identification Process [online] Available on: <http://www.ni.com/white-paper/4028/en/>

[30] M. R. Soumya, S. Bidyadhar, G. Subhojit, "PI Controller Design for a Coupled Tank System Using LMI Approach: An Experimental Study," Journal of Chemical Engineering & Process Technology, Vol. 7, No. 1, 2016, 8 pp., ISSN 2157-7048

[31] C. H. Chen, C. C. Chung, F. Chao, C. M. Lin, I. J. Rudas, "Intelligent Robust Control for Uncertain Nonlinear Multivariable Systems using Recurrent Cerebellar Model Neural Networks," Acta Polytechnica Hungarica, Vol. 12, No. 5, 2015, ISSN 1785-8860

[32]   Y. Kim, Y.-S. Kim, "Optimizing neural network to develop loitering detection scheme for intelligent video surveillance systems," International Journal of Artificial Intelligence, Vol. 15, No. 2, 2017, pp. 30-39

[33]   B. Zhang, J. Lam, S. Xu, "Stability Analysis of Distributed Delay Neural Networks Based on Relaxed Lyapunov–Krasovskii Functionals," in IEEE Transactions on Neural Networks and Learning Systems, Vol. 26, No. 7, 2015, pp. 1480-1492

[34]   Y. Gao, M. J. Er, "NARMAX time series model prediction: feedforward and recurrent fuzzy neural network approaches," Fuzzy Sets and Systems, Vol. 150, No. 2, 2005, pp. 331-350

[35]   T. Lazar, L. Madarász, et al., "Vzájomnosť teoreticko-praktických problémov prognózovania spoľahlivosti MPM (Mutuality of theoretical and practical prolems in reliability of small turbojet engine)," elfa, s.r.o. Košice, 2015, 275 pp., ISBN 978-80-8086-236-7

[36]   R. Andoga, L. Főzo, L. Madarász, T. Karoľ, "A Digital Diagnostic System for a Small Turbojet Engine," Acta Polytechnica Hungarica, Vol. 10, No. 4, 2013, ISSN 1785-8860

[37]   E. Kiyak, A. Kahvecioglu, F. Caliskan, "Aircraft Sensor and Actuator Fault Detection, Isolation, and Accommodation," in Journal of Aerospace Engineering, Vol. 24, No. 1, 2011, pp. 47-58

[38]   Z. N. S. Vanin, N. Meskin, K. Khorasani, "Multiple-Model Sensor and Components Fault Diagnosis in Gas Turbine Engines Using Autoassociative Neural Networks," in Journal of Engineering for Gas Turbines and Power, Vol. 136, No. 9, 2014, p. 16

[39]   E. Tóth-Laufer, M. Takács, I. J. Rudas, "Fuzzy Logic-based Risk Assessment Framework to Evaluate Physiological Parameters," Acta Polytechnica Hungarica, Vol. 12, No. 2, 2015, ISSN 1785-8860

Multi-Directional Image Projections with Fixed Resolution for Object Matching

Gábor Kertész, Sándor Szénási, Zoltán Vámossy

John von Neumann Faculty of Informatics
Óbuda University
H-1034, Budapest, Bécsi str. 96/b
{kertesz.gabor, szenasi.sandor, vamossy.zoltan}@nik.uni-obuda.hu

Abstract: The matching of the visual representations of two objects is a very important task in most computer vision applications. In special cases, when all objects look alike and only small differences occur, the difficulty of the task increases. In this paper, a novel method for matching low-quality images of rear-viewed vehicles is proposed, using multi-directional image projection functions. For GPU-accelerated implementations, a data-parallel algorithm is introduced. It is concluded, that the use of multiple directions with a small fixed resolution number is the most efficient, and more precise than similar techniques with smaller projection dimensions.

Keywords: Computer Vision; Image Projections; Radon Transform; Object Matching; Vehicle Matching

1   Introduction

Closed-circuit television cameras – also known as surveillance cameras – are often applied to monitor traffic. Based on the use-cases, several applications of these traffic cameras are known: congestion-detection and accident-detection systems are popular, speed cameras, safety and various enforcement solutions as well [1]. Most of these solutions require the device to be able to identify or track the vehicle, which could be challenging depending on the brightness and weather conditions. Advanced devices have high resolution cameras with infrared LEDs for night vision [2], also PTZ (pan-tilt-zoom) cameras can be used to track object movement.

On distant locations like public roads, highways, bridges and tunnels simple static cameras are placed with non-overlapping fields of view. These camera-networks are mostly used to measure traffic after crossroads, calculate the average speed of vehicles based on the distance between the cameras and the time of observations [3].

Recognizing a vehicle by using the plate number is not always feasible. In tunnels, where natural light is rare and colors are hard to detect, the usage of such high-level devices is not cost-efficient, giving similar low-quality images as other, less expensive cameras.

1.1 Problem definition

The changes of lighting and vehicle movement can cause difficulties when matching the image representations, as well as different camera settings could reflect in error.

In computer vision, there are simple methods to find objects with specific color or shape [4] [5]. Most methods are based on lines or corners, or other keypoint-based descriptors extracted from template images. In the case of noisy and low-quality pictures, low-level techniques can be applied. For example, template matching is a method which is based on the pixel-level comparison of the reference and the template. The matching process calculates the correspondence of the template image with the reference image [6]. If the sizes of images differ, a sliding window containing the template is moved over the reference. Most methods are able to handle the scaling or the rotation of objects, however template matching is very sensitive to these manipulations, although several additions exist to handle these.

A method introduced by Viola and Jones [7] is able to summarize pixel values into image integrals, in order to accelerate processing of template data for training [8]. A similar, pixel-level approach available is to compare image projections of the reference and the template images.

In this paper we introduce a multi-directional projection calculation method, which is then used to match low-quality images of vehicles (Fig. 1). In Section 2 a brief overview of the related works are given, Subsection 2.1 formally defines image projections and signatures formed from them and in Subsection 2.2 the paradigm of multi-directional projection is presented. Subsection 3.1 contains the declaration of our novel method of projecting images to a fixed number of bins, the parallel implementation of the suggestion is in Subsection 3.2. The matching technique of the signatures are analyzed and the comparison of our results is shown in Section 4.

Figure 1
Sample images from our dataset. The vehicles are viewed from behind on these low quality images.
Resolution goes from 50×50 to 150×150.

2 Related work

Tracking the color information and transforming these data between camera-based models [9] is an appropriate method when objects are tracked in a system of multiple cameras with non-overlapping fields of view. In other relevant work [10], color correlograms are used to match vehicles in different poses. However, these methods are mainly based on color information and assume that the vehicles could show up in different poses.

A matching based on Support Vector Machine (SVM) classification is presented in [11], where the detected edges of the vehicle pairs are used to train the classifier to detect which are the same and the different objects.

Jelača et al. [12] presented a solution for vehicle matching, where object signatures are calculated from projection profiles, and to tolerate potential faults caused by the changing environment and the movement of the object. These projections are joined together in an appearance model. Our work is motivated by this matching technique. Our goal is to increase the precision by using multiple projection directions, and a fixed vector length for all directions.

2.1 Image projection signature

The detection of the vehicles on the image plane could be done several ways: a pre-trained detector based on Haar-features could be applied [13], or even convolutional neural networks seem to perform well on detecting multiple objects on images [14].

After the region of interest is selected, the area is completed to a square and cropped. Since color data are irrelevant, the objects images are grayscaled, meaning that the information is simplified from a RGB structure to a single intensity value. In the case of 8-bit grayscale images the intensity information of one pixel is stored in one single byte.

Each image can be handled as matrix $\mathbf{I} \in \mathbb{N}^{N \times N}$ where $I_{i,j} = [0 \cdots 255]$ denotes the element of the matrix. The horizontal ($\boldsymbol{\pi}_H$) and vertical projections ($\boldsymbol{\pi}_V$) for a squared $N \times N$ matrix results in vectors with the same length:

$$|\boldsymbol{\pi}_H| = |\boldsymbol{\pi}_V| = N. \tag{1}$$

These projections are the averaged sums of the rows and columns of the matrix, normalized to $[0, 1]$ by the value of maximal intensity 255:

$$\boldsymbol{\pi}_H(i) = \frac{1}{N \cdot 255} \sum_{j=1}^{N} I_{i,j},$$
$$\boldsymbol{\pi}_V(j) = \frac{1}{N \cdot 255} \sum_{i=1}^{N} I_{i,j}. \tag{2}$$

The diagonal and antidiagonal projections can be calculated likewise, but it is important to point out that the number of elements for each projected value is not constant. While the length of the diagonal projection vectors are:

$$|\boldsymbol{\pi}_D| = |\boldsymbol{\pi}_A| = 2 \times N - 1, \tag{3}$$

the number of elements in each summarization is based on the distance from the main diagonal:

$$ElemNum(i) = \begin{cases} i & \text{if } i \leq N \\ N - i & \text{otherwise} \end{cases} \tag{4}$$

where i is the index of an element in a diagonal projection, having $i \leq 2 \times N - 1$. The calculation of the diagonal projections $\boldsymbol{\pi}_D$, $\boldsymbol{\pi}_A$ is formalized as:

$$\boldsymbol{\pi}_D(i) = \begin{cases} \frac{1}{ElemNum(i)\cdot 255} \sum\limits_{j=1}^{i} I_{j,N-(i-j)} & \text{if } i \leq N \\ \frac{1}{ElemNum(i)\cdot 255} \sum\limits_{j=1}^{i-N} I_{j+(i-N),j} & \text{otherwise} \end{cases}$$

$$\tag{5}$$

$$\boldsymbol{\pi}_A(i) = \begin{cases} \frac{1}{ElemNum(i)\cdot 255} \sum\limits_{j=1}^{i} I_{j,(i-j)+1} & \text{if } i \leq N \\ \frac{1}{ElemNum(i)\cdot 255} \sum\limits_{j=1}^{i-N} I_{j+(i-N),N-(j-1)} & \text{otherwise} \end{cases}$$

These vectors together provide a so-called signature of the object.

$$\mathbf{S_4} = (\boldsymbol{\pi}_H, \boldsymbol{\pi}_V, \boldsymbol{\pi}_D, \boldsymbol{\pi}_A), \tag{6}$$

as a 4 dimensional signature, while

$$\mathbf{S_2} = (\boldsymbol{\pi}_H, \boldsymbol{\pi}_V), \tag{7}$$

can also be used as a way simpler 2D signature.

2.2 Multi-directional projections

A logical addition to the signatures above is to calculate the projections of the object from more than four directions. There are few methods that provide a mapping from 2D data to its 1D projections. One of them is the Radon transform [15] [16], a formula which is mostly used with the Computer Tomography (CT) CT, Positron Emission Tomography (PET) or Magneto Resonance (MR) scanners to reconstruct images from the obtained data.

It is interesting to point out, that the Hough transform results in a very similar projection vector. The connection between the two is well-known and discussed thoroughly [17] [18].

The common point of both transforms is that if the input is not circular, the length of the projection vectors differ: each projection length depends on the angle.

The visual representations of the results of the transforms are referred as sinograms, where the projection sums are presented for each direction. A sample of a sinogram representation is on Fig. 2. The denomination sinogram comes from the sinusoid representation of the points.

3 Methodology

Our novel method is based on the idea that adding more dimensions to the signature model could provide more accurate results. Another goal is to create a technique with fixed number of bins, where the number of significant elements of the projection vector does not depend on the angle of projection.

3.1 Image Projections with Fixed Resolution

As demonstrated on Fig. 3a, the projection line is placed to the left side of the image (Fig. 3b), and it is rotated by α degrees around point P, which is in the top left corner. In this case, $\alpha \in [0, \frac{\pi}{2}]$.

While rotating the line, the lowest and highest points of the orthogonal projection divide it into two segments around point P. The length of these can be easily given as

$$
\begin{aligned}
LL &= \cos(\alpha) \times N \\
HL &= \sin(\alpha) \times N
\end{aligned}
\tag{8}
$$

To create a fixed number of subsegments for all angles, segment $LL + HL$ is divided into S equal parts, where S stands for the number of bins, resulting in $\frac{LL+HL}{S}$ in the resolution. Finally the $(x; y)$ projection position of each pixel is given as

$$
\begin{aligned}
start &= \sqrt{(x+1)^2 + y^2} \times \cos(\arctan(y, x+1) + \alpha) \\
end &= \sqrt{x^2 + (y+1)^2} \times \cos(\arctan(y+1, x) + \alpha)
\end{aligned}
\tag{9}
$$
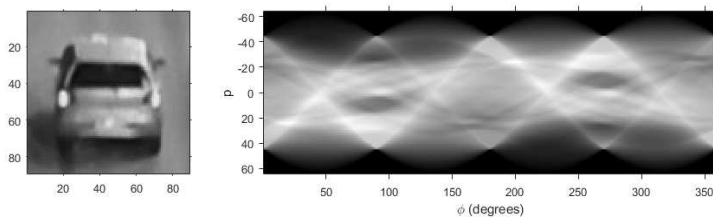
Figure 2
A sample from the dataset and the sinogram of the Radon transform for the same image for $[0; 2\pi]$ degrees

(a)
After the calculation of the projection lengths *HL* and *LL* for rotation angle α is done, the projection line is divided into different number of pieces, according to the projection resolution.

(b)
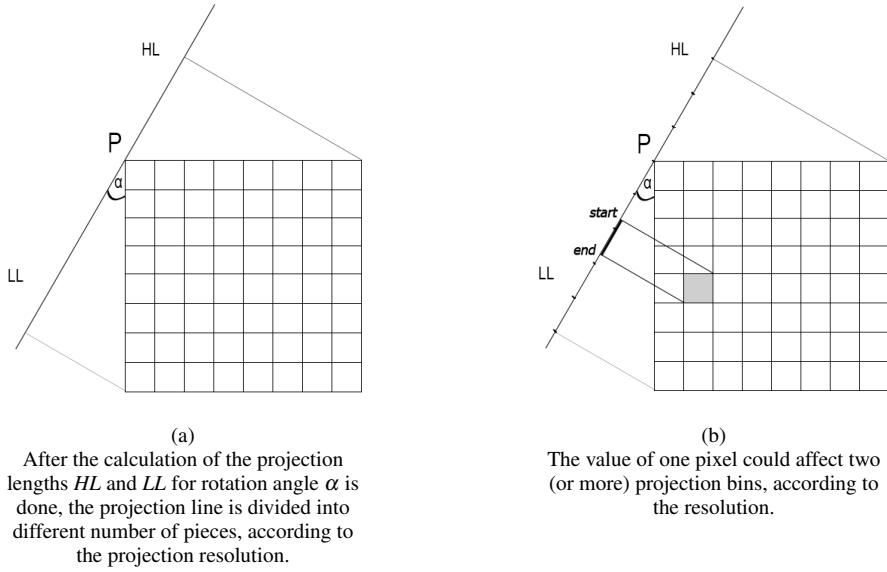The value of one pixel could affect two (or more) projection bins, according to the resolution.

Figure 3

as seen on Fig. 3b.

Based on *S*, each pixel is projected into one or more subsegments of the projection line, each pixel should increase the value of all affected bins, proportionately. Algorithm 1 defines the technique in pseudo language, for the better understanding.

The results for each direction are calculated for angles between 0 and $\frac{\pi}{2}$ for an $N \times N$ sized squared matrix *I*, and collected into *R* resulting matrix. In practice a step size is used at the iteration of α. After *LL* and *HL* is specified, according to Eq. 8, the resolution of the segment *res* is given by dividing the projection line into *S* pieces. Each pixel *p* in image **I** is processed by calculating the position of the projection

---

Algorithm 1 Method to calculate Multi-Directional Projections of an Image

---

procedure MULTIDIRECTIONALPROJECTIONS(*I*, *N*, *R*)
    for $\alpha := 0 \to \frac{\pi}{2}$ **step** *StepSize* **do**
        $LL \leftarrow \cos(\alpha) * N$
        $HL \leftarrow \sin(\alpha) * N$
        $res \leftarrow (LL + HL)/S$
        for all $p \in I$ **do**
            $start, end \leftarrow$ POSITIONOF(*p.X*, *p.Y*, α)
            RATIONALACCUMULATION(*R*, *res*, *start*, *end*, *p*)
        end for
    end for
end procedure

---

using POSITIONOF, which is based on Equation 9, and the correct values of R are increased proportionately, represented as function RATIONALACCUMULATION.

The behavior of RATIONALACCUMULATION procedure can be described as:

- If the number of affected bins is 1, the pixel value is added to the bin entirely

- If the number of affected bins is 2, a ration based on the projection segments is added to each affected bin

- If the number of affected bins is more than 2, fully covered bins are increased by the whole value, and the value of partially affected bins are raised according to the portion of the projection.

The extension of this method to $[0;\pi]$ is done by moving point P to the upper right corner, and rotating HL and LL with it respectively – or the same result could be achieved by rotating the matrix counter-clockwise. Notable, that the method does not need to be extended to a full circle, since the projections are equal on the $[0;\pi]$ and $[2\pi;\pi]$ sections [19].

The resulting matrix of projected values is visualized on Fig. 4. The difference compared to the Radon transform is remarkable: the sinusoids of the picture edges are eliminated.

Although the method provides the necessary results, the performance is questionable. The calculation complexity of the 4D signature is

$$T_1(N) = \mathcal{O}(4 \times N^2) = \mathcal{O}(N^2) \tag{10}$$

which means that the performance is directly proportional to the projection count. The runtime of the proposed method is

$$T_2(N) = \mathcal{O}(StepNumber \times N^2) = \mathcal{O}(N^2) \tag{11}$$

where $StepNumber >> 4$, meaning that the performance of both methods depend on the projection count of the signature. By analyzing the memory cost of the method, we can declare that the original algorithm uses

$$2 \times N + 2 \times (2 \times N - 1) = 6 \times N - 2$$

double-precision floating point numbers to store the results, while our method uses $StepNumber \times S$ doubles, where $StepNumber >> 4$, $N \leq S \leq 2 \times N - 1$.
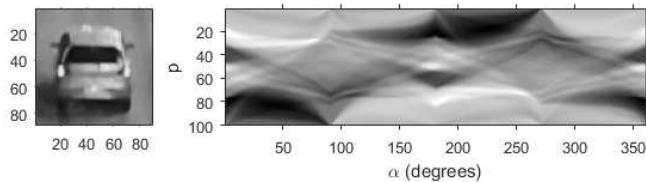

Figure 4
The results of the proposed method, displayed on a sinogram, similar used on Fig. 2.

The value of the total bin number could be defined empirically as N, or constant values could be used. A value less than N causes the compression of the data, resulting in information loss, while greater values result in redundancy.

When using 4D signatures defined in [12], the longest projections are the diagonals, as seen in Eq. 3, while the horizontal and vertical sums are almost half (Eq. 1). The difference of the vector length could cause difficulties storing and handling the data: instead of a matrix an array of different length array should be used.

Software implementations of the Radon transform and Hough transform both use a 2D matrix with the dimension $StepNumber \times (2 \times N - 1)$, meaning that the unused cells of the matrix are filled with empty data. The main advantage of the method presented in this paper is that it does not store any empty values [19], which is useful in data parallel implementations. Since the input matrix is not modified in the iterations, and there is no dependency between calculation steps, multi-level parallelization of the algorithm can be achieved.

3.2   Data parallel solution

The idea of using the architecture of a massive number of processing units in graphical accelerators to solve computationally intense cases created General-Purpose computing on Graphical Processing Units (GPGPU). In practice, these devices perform best on multi-dimensional matrix operations, such as this problem.

When running a calculation on a GPU, the first step must be the transferring of the input data from the memory of the so-called host computer to the device memory. This is the memory transfer time of initializing, which is raised with the time necessary to move the results back from the graphical processor to the memory of the hosting computer. These transfer times should be taken into account when designing the application [20]; it would be wrong to try to access the memory of the computer during the calculation, as it would significantly increase the runtime of the whole procedure.

The code implemented on the GPU is referenced as a compute kernel. The design of the kernel procedures determines the performance of the solution. To achieve the best performance, optimal breakdown of the task is necessary. The aim is to use all multiprocessing units, keeping in mind that access to common variables could cause faults.

The correct usage of the memory architecture [20] of the device is crucial: transfer and access times are present and could have remarkable effects on runtime if designed badly. The main memory of the device – the global memory – could be accessed by the threads, however the access times are better if the less accessible storages, which are assigned to the blocks (shared memory) or the even less accessible registers belonging to the threads themselves (local memory) are used.

A possible solution to achieve a data-parallel solution is to assign singular threads to pixels, and calculate results for every angle, individually (Alg. 2). First, the input matrix is divided into several smaller pieces. These image parts are copied into

---

Algorithm 2 Kernel procedure to calculate the image projection for multiple directions

---

procedure MULTIDIRECTION_KERNEL(blk, I_G, N, S, R_G)
    $I_S \leftarrow$ GETBLOCK($I_G, blk.X, blk.Y$)
    $R_S \leftarrow$ *new array*[]
    $disp_S \leftarrow$ *new array*[]
    for $\alpha := 0 \rightarrow \frac{\pi}{2}$ **step** *StepSize* **do**
        $LL \leftarrow$ COS(α) $* N$
        $HL \leftarrow$ SIN(α) $* N$
        $res \leftarrow (LL + HL)/S$
        $start, end \leftarrow$ POSITIONOF($blk.X, blk.Y + 1, \alpha$)
        $disp_S[\alpha] \leftarrow \lfloor start/res \rfloor$
    end for
    for all $t \in threads$ **do**
        for $\alpha_L := 0 \rightarrow \frac{\pi}{2}$ **step** *StepSize* **do**
            $LL_L \leftarrow$ COS(α_L) $* N$
            $HL_L \leftarrow$ SIN(α_L) $* N$
            $res_L \leftarrow (LL_L + HL_L)/S$
            $start_L, end_L \leftarrow$ GPOS($blk.X, blk.Y, t.X, t.Y, \alpha_L$)
            RATIONALACCUMULATION($R_S, res_L, start_L, end_L, I_S[t.X]$)
        end for
    end for
    SUMMARIZATION($R_S, disp_S, R_G$)
end procedure

---

the shared memory. After the transfer, each thread of the block is assigned to each element of the image section, and after the calculation is done the outcomes are positioned and summarized for each angle. The results are first summarized thread safely in the shared memory, then the results of blocks are accumulated in the global memory, from where the final results are transferred back to the host.

The proposed method in Alg. 2 uses all three mentioned levels from the memory architecture: indexes G, S and L indicate that the variables are stored in the global, shared and local memories, respectively. The following list contains comments and explanations for each member of the procedure:

- blk: image block identifier
- I_G: image in global memory
- N: image size (width & height)
- S: number of bins
- R_G: result container in global memory
- $blk.X, blk.Y$: coordinates of the block
- GETBLOCK($I_G :, x, y$): returns the block starting at x, y from A matrix
- I_S: image in shared memory
- R_S: results in shared memory
- $disp_S$: precalculated dispositions in block memory

- α: rotation angle
- LL, HL: projection line segment lengths
- *res*: resolution: length of each bin
- POSITIONOF(x, y, α): position of a block with the coordinates of x, y on the projection line for α rotation
- *start*, *end*: starting and ending of the projection on the projection line
- *threads*: container representing every thread on a block
- t: a single thread
- α_L: rotation of a single pixel, iterated locally
- LL_L, HL_L: projection line segment lengths used by a thread for a specific rotation
- $t.X, t.Y$: position of a pixel
- GPOS(bx, by, x, y, α): returns the projection position of a pixel referred at x, y relatively to the block bx, by, for α rotation
- $start_L, end_L$: starting and ending position of projection, handled locally
- RATIONALACCUMULATION$(R_S, r_L, start, end, v)$: accumulates R_S with v, having r_L resolution from *start* to *end* using thread safe atomic increment
- SUMMARIZATION$(R_S, disp, R_G)$: R_S values are summarized atomically into R_G based on the dispositions $disp_S$

As earlier measurements [21] indicated (Fig. 5), the method performed with promising numbers in point of time and memory efficiency: while the processing times on CPU increase exponentially, the runtime of the GPU-accelerated solution shows linear behaviour.

4   Results

The dataset used for evaluating the method consists of 253 images of 21 different vehicles, labeled manually. The point of view of the detected vehicles are the same, the width and height of the squared images are in average 100 pixels, sizes vary from 48×48 to 150×150, sparsely with a few larger (200×200, 290×290) instances.

On Fig. 6 the results of the original method are visualized: the horizontal, vertical, diagonal and antidiagonal projections are calculated, divided by the number of elements, and normalized to fit to the $[0; 1]$ interval, for both observations. The visualized projection functions show the same behaviour in cases of the horizontal, vertical, diagonal and antidiagonal angles.

4.1   Matching

To calculate the alignment of the functions, the method suggested by Jelača et al. [12] is to align the projection functions globally, and then fine-tune with a local alignment using a method similar to the Iterative Closest Point [22]. There are a number of other methods to measure similarities [23].

Instead of building up the two-step alignment technique, we chose to apply the Pearson correlation coefficient (PCC) with a shifting technique. Since the size of
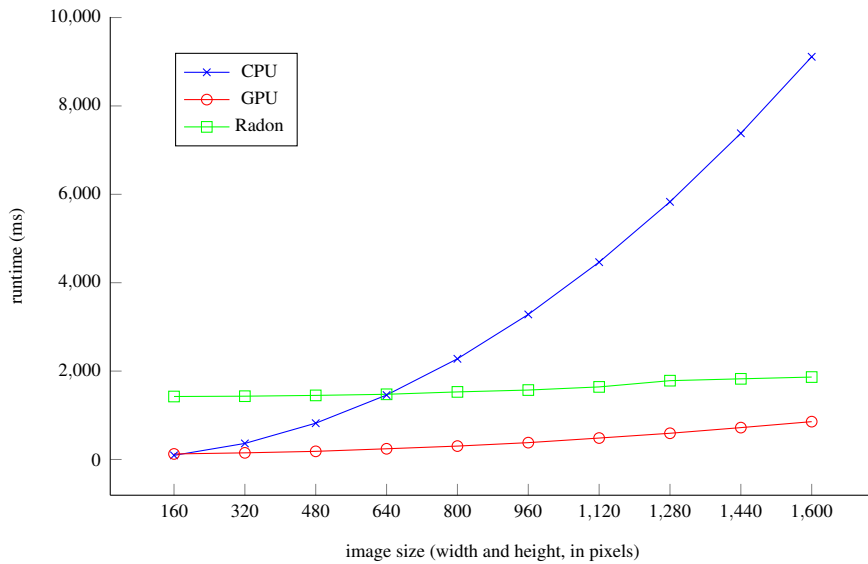
Figure 5
Comparison of runtimes for different image sizes [21]. The horizontal axis displays the width of the squared images in pixels, the vertical axis shows the runtimes in milliseconds. The CPU ad GPU implementation of the presented method was compared with the runtime of Matlab's GPU-accelerated Radon transform.

input images could differ, the projection functions are compared using a shifting window technique: the shorter function is moved over the longer function, and each correlation coefficient is calculated using the PCC formula.

$$\rho(s) = \frac{\text{cov}(\mathbf{x}, \mathbf{y_s})}{\sigma(\mathbf{x})\sigma(\mathbf{y_s})} \tag{12}$$

Basically the $\rho(s)$ correlation coefficients are calculated for each step, where the number of steps is $|\mathbf{y}| - |\mathbf{x}|$, having $|\mathbf{y}| > |\mathbf{x}|$. $\mathbf{y_s}$ stands for the section of $\mathbf{y}$ compared with $\mathbf{x}$ in step s, $\text{cov}()$ means the covariance between the two vectors, and σ indicates the standard deviation.

The range of the values are mapped to $[-1; 1]$, which could be easily handled: the higher the coefficient, the better the match. The highest value $\max_s \rho(s)$ is selected as ρ, defining the similarity of $\mathbf{x}$ and $\mathbf{y}$. After all similarity values are calculated for the projections, the result values are filtered with a rectifier, setting all negative values to zero:

$$r(v) = \begin{cases} v & \text{if } v > 0 \\ 0 & \text{otherwise} \end{cases} = \max(0, v) = v^+ \tag{13}$$

The penalization of the negative correlation is necessary because the projection inverses should not be used at all. Negative correlation values mean that the changes
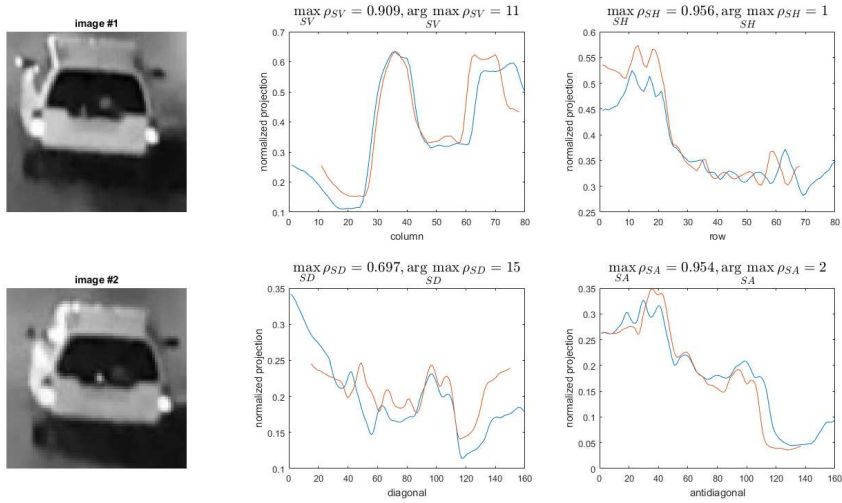
Figure 6

The behavior of the projections of the same vehicle on different observations. In the first column two images of the same object is shown: mind the different sizes and the different lightning conditions, the blink on the side. On the next four diagrams the vertical (top-left), horizontal (top-right), diagonal (bottom-left) and the antidiagonal (bottom-right) projections are visualized, and aligned with the highest calculated correlation.

of one function affects an opposite change on the other function, meaning that the relationship between the two is inverse.

Since each dimension of the data should be equally handled, the suggestion of [12] to use the Euclidean norm is applied here as well. A single value μ is calculated from the 4D signature as

$$\mu = \frac{\sqrt{r(\rho_H)^2 + r(\rho_V)^2 + r(\rho_D)^2 + r(\rho_A)^2}}{2} \tag{14}$$

where 2 is the square root of the dimension number. The measured similarities of the 4D signature are visualized on Fig. 7.

The same method could be applied to evaluate the method presented in this paper: the correlation of each fixed length projection function could be calculated, and the results of the shifted PCC could be united using the Euclidean norm, defined above.

4.2   Evaluation

As already seen on Fig. 7, for the same vehicles the lowest similarity μ is 0.6, while the largest value is 0.98, which is quite convincing. However, when comparing all different vehicles with each other, the results show great spread, represented on Fig. 8.

If a simple classification is done, where it is desired that 50% of the true matches should pass, the line should be drawn to 0.82. However, using this threshold,
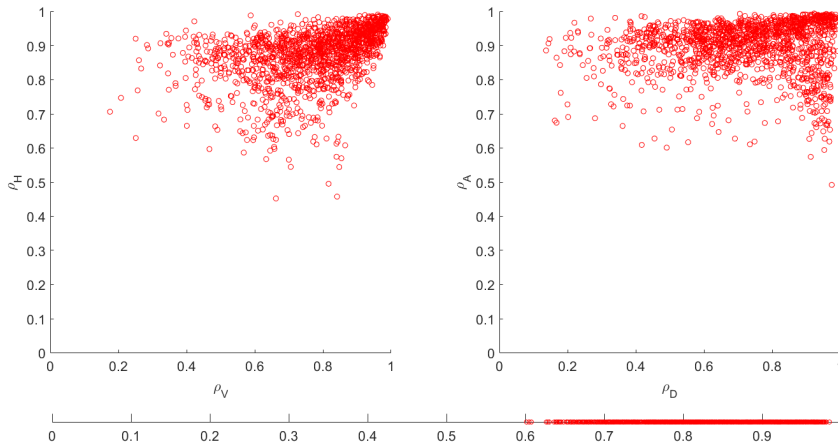
Figure 7

The measured correlations and the calculated similarities in the case of comparing the same instances with different observations. On the left a scatter diagram of the values of horizontal and vertical coefficients ρ_H-ρ_V, and on the right is the same with diagonal and antidiagonal values ρ_A-ρ_D. Below them is the μ similarity value calculated by the Euclidean norm of these, according to Eq. 14.

19.29% of the different vehicles would also pass as false positives, which is way too high.

This is caused by the high variance between the similarity values calculated for different vehicles: while the minimum value is 0.27, the highest calculated similarity is 97.69, with a 10.43% standard deviation. The application of the 2D signature show the same low results: the threshold should be set to $\mu \geq 0.833$, resulting in 22.79% false positives.

When applying the proposed method, several variables could be set: first, the *StepSize* between each projection angle should be set. Our experiments are done with *StepSize* = 5 degrees, $\frac{\pi}{36}$.

The resolution of the projection line is also a significant tradeoff variable. By setting it to N for all images, every projection will be set to N number of bins. If the setting is a constant, for example 100, as the average of the image sizes, will compress less of the data, also some redundancy will come up on smaller images. Notable, that the runtime for the calculation of correlation shortens significantly, as no sliding window is needed, since the vector sizes are equal.

The method with the least compression of the data is the application of $2 \times N - 1$ resolution, which is the exact length of the diagonal. The results for these three different settings are shown in Table 1.

When the proposed method is used with relative bin numbers, and results are matched with the technique described before, the pass-rate and the portion of false positives are closely the same.
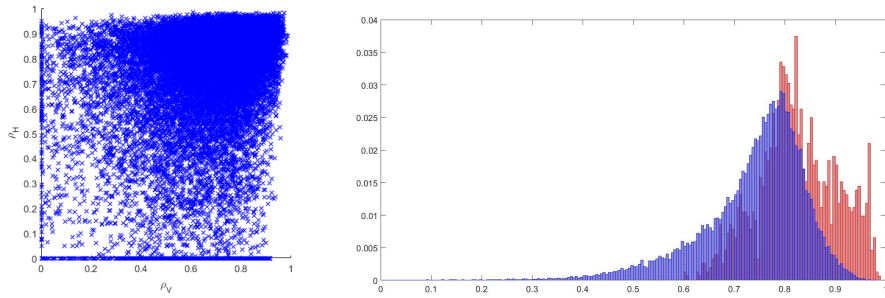
Figure 8

The high rate of false positives using a 4-dimensional signature. On the left side a scatter diagram of measured ρ_H horizontal and ρ_V vertical correlations. On the right is a histogram of the distribution of the similarities calculated for the same (red) and different (blue) objects.

	2D	4D	Multi-directional with bin number:					
			N	2N-1	25	50	100	300
Threshold to pass 50% of true matches	0.833	0.820	0.819	0.819	0.881	0.875	0.873	0.872
Portion of false matches above this	22.79%	19.29%	19.94%	19.84%	5.06%	5.22%	5.24%	5.25%
Threshold to pass 80% of true matches	0.740	0.763	0.769	0.768	0.804	0.795	0.793	0.792
Portion of false matches above this	56.75%	48.85%	48.40%	48.67%	21.26%	21.64%	21.82%	21.85%
Median of the similarity values of true matches	0.833	0.820	0.819	0.819	0.882	0.875	0.873	0.872
Median of the similarity values of false matches	0.760	0.761	0.766	0.766	0.697	0.691	0.689	0.688
Minimum of the similarity on true matches	0.479	0.601	0.573	0.571	0.566	0.557	0.554	0.553
Maximum of the similarity on false matches	0.978	0.976	0.970	0.970	0.968	0.964	0.962	0.962

Table 1

2D, 4D, fixed multi directional with bin number set as N, 2N-1, 25, 50, 100 and 300

However, when using a fixed number as the projection length for all input images, results show that the number of false positives reduces significantly. For example for bin number 25, the limit which passes through 50% of the true matches is drawn at $\mu \geq 0.881$, which is higher than the border set at the two and four dimensional signatures. The portion of false matches is only 5.06%, which is around four times better than the false positives counted using the 2D and 4D signatures.

The difference between the results of the 4D signatures and our method with bin number 25 is visualized on histograms (Fig. 9) generated from the similarity values measured for true and false matches. The high false match rate is caused by the moving window: the best similarity is handled as the final similarity, which leads to high values. A possible solution would be to stretch the different length vectors to the same size, and calculate the correlation correspondingly.

In our research, the optimal resolution number begins at a minimum of 10 bins for all projections (Fig. 10). We understand, that in case of low numbers, the small details are removed, and by the compression a small tolerance to changes is developed.

It might be interesting to present the top false positives and negatives of the method: on Fig. 11a the falsely excluded vehicle pairs with the lowest similarity rate are shown, while the couples of different vehicles with the highest calculated similarity are on Fig. 11b. As Fig. 11a shows, the low similarity values measured for the same vehicles are caused by different poses. By empirically evaluating the calcu-
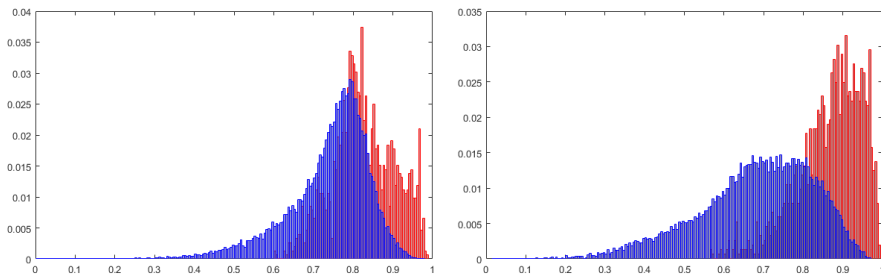
Figure 9

Histograms of the similarities measured using the 4D and the proposed method, red columns show the percentage for the comparison of the same, and blue columns present the calculated values for different objects. The diagram on the left presents the distribution of similarities using the 4D image projection signature, while on the right side, the results of the proposed method is shown, with $\pi/36$ step size, and the projection bin number set to 25.
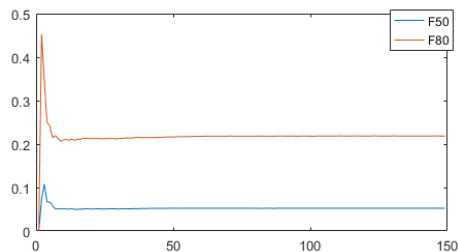

Figure 10

The rate of false positives if the threshold is adjusted to a limit where 50% (F50) or 80% (F80) of true matches should pass, for different number of projection bins.

lated similarities, we learned that the correlation of each projection change as the projection angle diverts from the vertical direction. The highest false positives are caused by similar vehicles, blinks, or in few cases the same or similar type of a vehicle is falsely recognized as the same instance.

Conclusions

In this paper, we defined a novel method to calculate image projections, similar to the Radon transform. To increase the efficiency of the algorithm, we introduced a data-parallel solution, which could be applied on graphical processors. After evaluating the results, we concluded that in case of a simple Euclidean norm-based matching method the precision of the proposed method exceeds the rates given by previously studied techniques.

As an overall procedure, other possibilities should be examined in each different phase (Fig. 12): the image of the detected vehicle could be preprocessed (noise removal, background subtraction).

Our future plans include the redesign of the matching procedure: a method regarding the angle and the orientation of the vehicle, could lead to more precise predictions
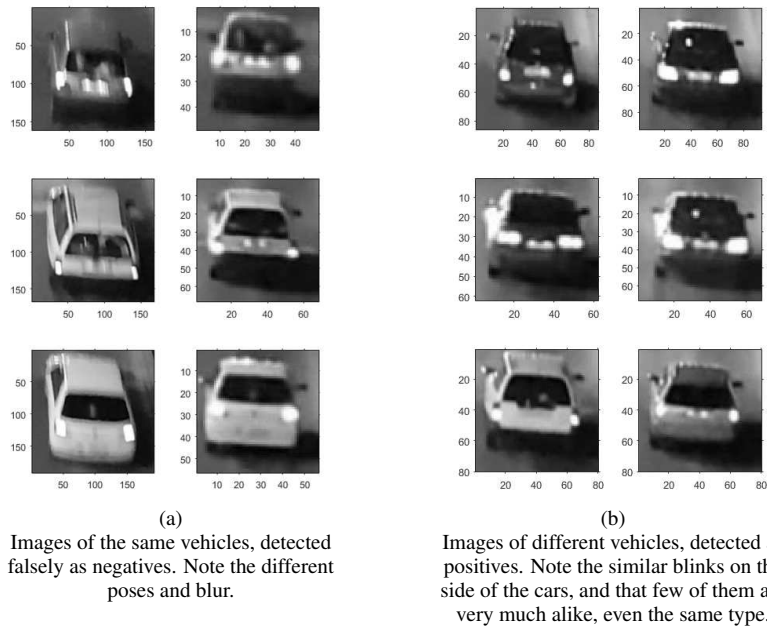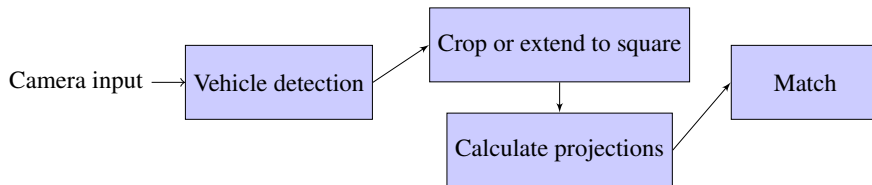
(a)
Images of the same vehicles, detected falsely as negatives. Note the different poses and blur.

(b)
Images of different vehicles, detected as positives. Note the similar blinks on the side of the cars, and that few of them are very much alike, even the same type.

Figure 11

Camera input → Vehicle detection → Crop or extend to square → Calculate projections → Match

Figure 12
The overall approach as a block diagram: the method described in this paper discusses the last three phases.

for the same or different vehicles. If the current Euclidean norm is to be used, different weights should be rendered to each projections, based on their direction, or more sophisticated classification methods should be applied.

Acknowledgement

Notations and abbrevations

In this study we consequently used the following notations and abbreviations:

$N, start, end, LL, HL, S, \dots$	scalars
$\mathbf{I}$	image matrix
$\mathbf{S_2}, \mathbf{S_4}$	object signatures
$\boldsymbol{\pi}_H, \boldsymbol{\pi}_V, \boldsymbol{\pi}_D, \boldsymbol{\pi}_A$	projection vectors
σ	standard deviation
$\mathrm{cov}()$	covariance between two vectors
ρ	correlation coefficient
μ	similarity

References

[1]   B. Rinner and W. Wolf, "An Introduction to Distributed Smart Cameras," *Proceedings of the IEEE*, vol. 96, no. 10, pp. 1565–1575, 2008.

[2]   C.-C. Yu, H.-Y. Cheng, and Y.-F. Jian, "Raindrop-Tampered Scene Detection and Traffic Flow Estimation for Nighttime Traffic Surveillance," *IEEE Transactions on Intelligent Transportation Systems*, vol. 16, pp. 1518–1527, 2015.

[3]   A. Sanchez, P. D. Suarez, A. Conci, and E. Nunes, "Video-Based Distance Traffic Analysis: Application to Vehicle Tracking and Counting," *Computing in Science and Engg.*, vol. 13, no. 3, pp. 38–45, 2011.

[4]   A. E. Abdel-Hakim and A. A. Farag, "Color segmentation using an Eigen color representation," *2005 8th International Conference on Information Fusion*, vol. 2, 2005.

[5]   M. Azodinia and A. Hajdu, "A Novel Combinational Relevance Feedback Based Method for Content-based Image Retrieval," *Acta Polytechnica Hungarica*, vol. 13, no. 5, pp. 121–134, 2016.

[6]   G. Kertész, S. Szénási, and Z. Vámossy, "Parallelization Methods of the Template Matching Method on Graphics Accelerators," *CINTI 2015 - 16th IEEE International Symposium on Computational Intelligence and Informatics*, pp. 161–164, 2015.

[7]   P. Viola and M. Jones, "Robust Real-time Object Detection," in *International Journal of Computer Vision*, 2001.

[8]   P. Viola and M. Jones, "Rapid Object Detection using a Boosted Cascade of Simple Features," in *Computer Vision and Pattern Recognition, 2001. CVPR 2001. Proceedings of the 2001 IEEE Computer Society Conference on*, vol. 1, pp. 511–518, IEEE, 2001.

[9]   O. Javed, K. Shafique, and M. Shah, "Appearance Modeling for Tracking in Multiple Non-Overlapping Cameras," in *Proceedings of the 2005 IEEE Computer Society Conference on Computer Vision and Pattern Recognition (CVPR'05) - Volume 2 - Volume 02*, CVPR '05, (Washington, DC, USA), pp. 26–33, IEEE Computer Society, 2005.

[10] T. E. Choe, M. W. Lee, and N. Haering, "Traffic Analysis with Low Frame Rate Camera Networks," in *Computer Vision and Pattern Recognition Work-*

shops (CVPRW), 2010 IEEE Computer Society Conference on, pp. 9–16, IEEE, 2010.

[11] Y. Shan, H. S. Sawhney, and R. Kumar, "Vehicle Identification between Non-Overlapping Cameras without Direct Feature Matching," *Tenth IEEE International Conference on Computer Vision (ICCV'05) Volume 1*, vol. 1, pp. 378–385 Vol. 1, 2005.

[12] V. Jelača, A. Pižurica, J. O. Niño-Castañeda, A. Frías-Velazquez, and W. Philips, "Vehicle matching in smart camera networks using image projection profiles at multiple instances," *Image and Vision Computing*, vol. 31, pp. 673–685, 2013.

[13] R. Rios-Cabrera, T. Tuytelaars, and L. Van Gool, "Efficient Multi-camera Vehicle Detection, Tracking, and Identification in a Tunnel Surveillance Application," *Comput. Vis. Image Underst.*, vol. 116, no. 6, pp. 742–753, 2012.

[14] A. Krizhevsky, I. Sutskever, and G. E. Hinton, "ImageNet Classification with Deep Convolutional Neural Networks," in *Proceedings of the 25th International Conference on Neural Information Processing Systems*, NIPS'12, (USA), pp. 1097–1105, Curran Associates Inc., 2012.

[15] J. Radon, "Über die Bestimmung von Funktionen durch ihre Integralwerte längs gewisser Mannigfaltigkeiten," *Berichte über die Verhandlungen der Königlich-Sächsischen Akademie der Wissenschaften zu Leipzig, Mathematisch-Physische Klasse*, pp. 262–277, 1917.

[16] J. Radon, "On the Determination of Functions from Their Integral Values along Certain Manifolds," *Medical Imaging, IEEE Transactions on*, vol. 5, pp. 170–176, 1986.

[17] S. R. Deans, *The Radon Transform and Some of Its Applications*. New York: John Wiley and Sons, 1983.

[18] M. van Ginkel, C. L. Hendriks, and L. van Vliet, "A short introduction to the Radon and Hough transforms and how they relate to each other," 2004.

[19] G. Kertész, S. Szénási, and Z. Vámossy, "Application and properties of the Radon transform for object image matching," *SAMI 2017: IEEE 14th International Symposium on Applied Machine Intelligence and Informatics*, pp. 353–358, 2017.

[20] D. B. Kirk and W. W. Hwu, *Programming Massively Parallel Processors: A Hands-on approach*. Morgan Kaufmann, 2010.

[21] G. Kertész, S. Szénási, and Z. Vámossy, "A Novel Method for Robust Multi-Directional Image Projection Computation," *INES 2016 - 20th IEEE International Conference on Intelligent Engineering Systems*, pp. 239–243, 2016.

[22] R. A. Newcombe, S. Izadi, O. Hilliges, D. Molyneaux, D. Kim, A. J. Davison, P. Kohli, J. Shotton, S. Hodges, and A. Fitzgibbon, "KinectFusion: Real-time Dense Surface Mapping and Tracking," in *Proceedings of the 2011 10th*

IEEE International Symposium on Mixed and Augmented Reality, ISMAR '11, (Washington, DC, USA), pp. 127–136, IEEE Computer Society, 2011.

[23] G. Németh, G. Kovács, A. Fazekas, and K. Palágyi, "A Method for Quantitative Comparison of 2D Skeletons," *Acta Polytechnica Hungarica*, vol. 13, no. 7, pp. 123–142, 2016.

Robot Coverage Path Planning Based on Iterative Structured Orientation

Ernő Horváth[a], Claudiu Pozna[a, b], Radu-Emil Precup[c]

herno@sze.hu, cp@unitbv.ro, radu.precup@upt.ro

[a] Department of Computer Engineering, Széchenyi István University,
Egyetem tér 1, 9026 Győr, Hungary

[b] Department of Automation and Information Technology, Transilvania University
of Brasov, Str. Mihai Viteazu 5, Corp V, et. 3, 500174 Brasov, Romania

[c] Department of Automation and Applied Informatics, Politehnica University of
Timisoara, Bd. V. Parvan 2, 300223 Timisoara, Romania

Abstract: Coverage path planning for mobile robots aims to compute the shortest path that ensures the overlap of a given area, with applications in various domains. This paper proposes a coverage path planning strategy, referred to as Iterative Structured Orientation Coverage, which has two main advantages over the state-of-the-art, namely it is it versatile and it is capable to handle complex environments. The path planning strategy is expressed as three new approaches to coverage path planning. The suggested approaches are validated by simulation and experimental results. The source codes along with the test set are available in a public repository.

Keywords: Auxiliary lines; Coverage path planning; Iterative Structure Orientation Coverage; Main lines; Mobile

1 Introduction

As shown in [1] and [2], robot coverage path planning (CPP) deals with the problem of covering a certain area with a movable object as, for example, with a mobile robot (MR). CPP makes use of two classes [3]: it is complete if it guarantees complete coverage or heuristic in other cases. There are also two main CPP strategies: offline if there is an a priori known map, otherwise online if the robot needs to discover the environment.

The most widely used approaches to CPP are Random Path Planning (RPP) [4], Exact Cellular Decomposition (ECD) [1], Boustrophedon Cellular DeComposition (BCDC) [1] [38], Backtracking Spiral Algorithm (BSA) [4], Internal Spiral Search

(ISS) [5], U-turn A* Path Planning (UAPP) [5] and Neural Network (NN)-based CPP [6]. A critical analysis of these approaches is presented as follows.

RPP imposes the MR to move on several random trajectories. Each time when the current trajectories are obstructed a new one is chosen and next repeated. RPP is a simple but not effective approach. Combining RPP with preprogrammed trajectory patterns such as spirals and serpentines and/or a wall following mechanism the algorithm may increase efficiency [4]. Due to its simplicity, the path planning algorithms specific to RPP are used in nowadays popular autonomous robotic vacuum cleaners.

ECD uses cells to fill the whole map. Usually the MR covers each cell using simple back-and-forth motions. After the current cell is covered, the robot moves to another cell. Finally the whole map will be covered. The Trapezoidal Decomposition is a particular case of ECD given in [1], and characterized by the decomposition of the map into trapezoids, which are covered with simple back-and-forth motions.

BCDC has been introduced in [4] and the path planning algorithms based on BCDC became popular as highlighted in [5]. The word boustrophedon literally means "the way of the ox" in Greek [4]. The original supposition is that the map is composed from polygons, so it is a line map [6]. BCDC exploits this hypothesis and generates cells (easy to be covered) and finally generates the connection between these cells. BCDC performs an exact cellular decomposition, and each cell in the boustrophedon is covered with back and forth motions [4].

The drawback of the polygonal decomposition is the big number of cells. This problem has been corrected by merging cells [7]. Fig. 1 illustrates an example of BCDC-based solution where four cells are produced. The cells are generated using a beam of parallel lines because of intersection with obstacles. These cells are actually convex polygons that do not have any holes. Consequently, the cells are covered with back and forth motions. This aspect is also illustrated in Fig. 1. Finally, the thick path shows how each cell is connected to ensure a complete coverage.
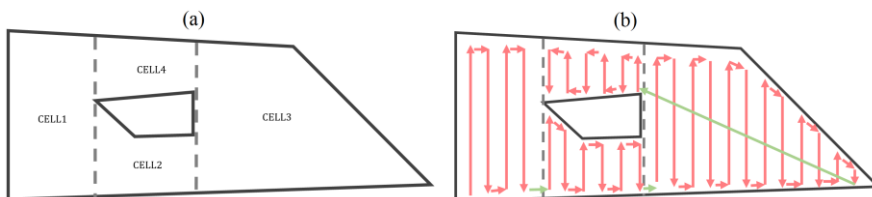

Figure 1
The cells (a) and the path (b) generated by BCDC

BSA is similar to ISS. The MR traverses the area in a certain direction. If the area is free, i.e., not covered, the MR will move forward. If it is already covered or there is an obstacle in the way, the MR will turn perpendicularly [5].

UAPP combines the heuristic feature of A* algorithm with the U-turn search algorithm [5]. The MR moves from the origin point using a U-turn algorithm, and next plans the shortest path in term of an A* algorithm [5].

The NN-based approach generates collision-free complete coverage paths in known environments by producing shunting equations [6]. Several features specific to NNs that offer convenient input-output maps to model complex systems [7–13] can be included and combined with the NN-based CPP approach.

Some recent applications of CPP are reported in [14–18]. The path planning approaches can be applied to various categories and applications of MRs [19–27].

This paper proposes a novel CPP strategy, which is referred to as Iterative Structured Orientation Coverage (ISOC). ISOC uses discrete grid maps and targets the complete coverage. The specific feature of our approach is the combination of two ideas, considering the whole area as one unit and using the BCDC-based motion.

The ISOC approach uses the concept of main lines. These main lines are actually a beam of parallel lines, which have a particular orientation in the map. This orientation ensures a set of straight lines with maximum length, surrounded by the map and interrupted by the obstacles. By composing (or linking) these lines we obtain the minimum length path. The composition stage relates our solution with optimization problems as, for example, the traveling salesman problem (TSP) or other problems in different applications treated with classical or evolutionary-based algorithms [9, 11, 28–36], and also represents the advantage of the ISOC approach with respect to the state-of-the-art reported in [1–6, 14–19].

Three solutions to obtain the main lines are proposed. These solutions are inserted in the ISOC strategy resulting in three new ISOC approaches.

The paper is organized as follow: the main contribution of the paper, which is the ISOC approaches, is discussed in the next section and presented in a unified formulation. Section 3 deals with the validation of the proposed approaches by simulation and experimental results for the Khepera III differential drive robot, and a comparative study is included. Section 4 is dedicated to concluding and summarizing remarks and to outlining the future research directions.

2   Iterative Structured Orientation Coverage Approaches

As mentioned in Section 1, the map (domain) coverage in ISOC uses the main lines concept. The main lines represent a beam of parallel lines, which are trimmed by the map boundary in segments. The final path is obtained by composing these segments with additional segments. The additional segments ensure the path continuity. The main lines have a particular orientation, which ensures the minimum length of the path, i.e., the goal to make the MR navigate on long straight lines. Fig. 2 illustrates this concept by means of Fig. 2 (a) that illustrates the map and the main lines and Fig. 2 (b) that illustrates the main segments (lines) and the auxiliary segments.
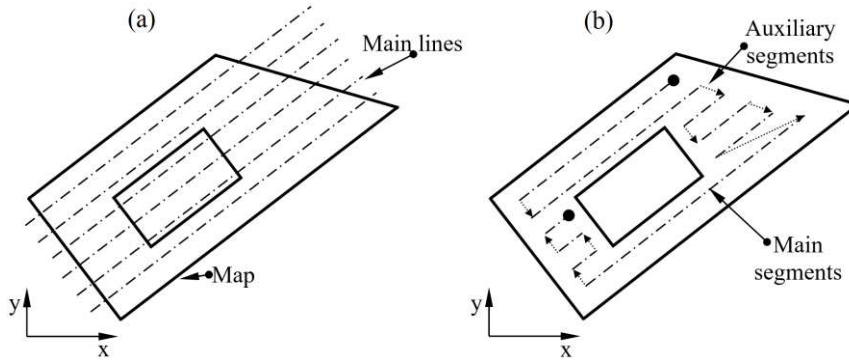
Figure 2

The map and the main lines (a), the main segments (lines) and the auxiliary ones (b)

The initial data of the CPP approach is the map. The map is generated from a picture and modeled by the map matrix $M = [M_{ij}]_{i=1\dots n, j=1\dots m} \in \Re^{n \times m}$ with the elements

$$M_{ij} = \begin{cases} 1, & \text{if pixel } (i,j) \text{ is black,} \\ 0, & \text{if pixel } (i,j) \text{ is white,} \end{cases} \tag{1}$$

where n is the number of horizontal pixels and m is the number of vertical pixels.

Using the main lines concept, the problem of finding a minimum length path, which covers the whole map, reduces to the following steps, 1, 2 and 3:

1. Find the appropriate main line, i.e., the orientation of the beam of parallel lines.
2. Obtain the main segments.
3. Link these segments with auxiliary segments such that the final (continuous) path has a minimum length.

These steps will be described in the next sub-sections, and next organized as a unified algorithm specific to the ISOC approaches.

2.1 Finding the Main Lines (the Orientation of the Beam of Parallel Lines)

The equation of the beam of parallel lines expressed in the discrete domain is

$$\begin{cases} L_{q_1k_1} \equiv i = \left\lfloor j\frac{q_1}{(m+1)} \right\rfloor + k_1 + 1, & \text{if } \alpha \in \left[-\frac{\pi}{4}, \frac{\pi}{4}\right], \\ L_{q_2k_2} j = \left\lfloor i\frac{q_2}{(n+1)} \right\rfloor + k_2 + 1, & \text{if } \alpha \in \left[-\frac{\pi}{2}, -\frac{\pi}{4}\right) \cup \left(\frac{\pi}{4}, \frac{\pi}{2}\right] \end{cases} \tag{2}$$

where α is the line slope in the continuous domain, $\alpha = \tan^{-1}\left(\frac{q_1}{m+1}\right)$ or $\alpha = \tan^{-1}\left(\frac{q_2}{n+1}\right)$, $q_1 = 1...m$ or $q_2 = 1...n$ have a direct effect on the slope in the discrete domain, with the unified notation $q \in \{q_1, q_2\}$, $\lfloor x \rfloor$ indicates generally the integer part of $x \in \Re$, $k_1 = \beta_1\delta_1$ or $k_2 = \beta_2\delta_2$ is the intercept with the unified notation $k \in \{k_1, k_2\}$ for both horizontal and vertical axes, $\beta_1 = 0...(n-1)/\delta_1$, $\beta_2 = 0...(m-1)/\delta_2$ the integer steps δ_1 and δ_2 are computed in terms of

$$\delta_1 = \left\lfloor b\frac{\sqrt{q_1^2+(m+1)^2}}{m+1} \right\rfloor, \quad \delta_2 = \left\lfloor b\frac{\sqrt{q_2^2+(n+1)^2}}{n+1} \right\rfloor, \tag{3}$$

b is the distance between the lines (the robot width), $L_{q_1k_1}$ and $L_{q_2k_2}$ are the lines that belong to the beam with the unified notation $L_{qk} \in \{L_{q_1k_1}, L_{q_2k_2}\}$ for both axes. Fig. 3 illustrates several examples of lines for different slopes.
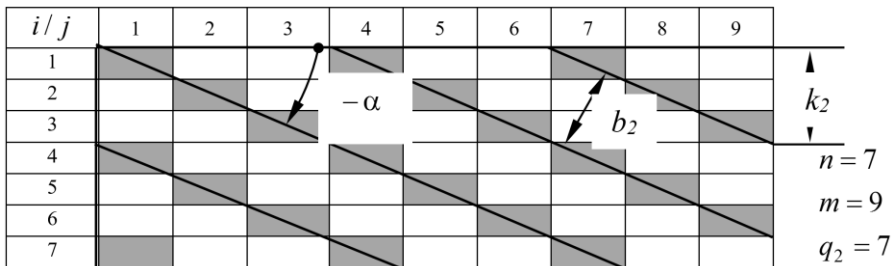

Figure 3

Examples of lines in the discrete domain

Each line can be associated with a matrix $\Lambda^{qk} = [\Lambda_{ij}^{qk}]_{i=1...n, j=1...m} \in \Re^{n \times m}$ with the elements Λ_{ij}^{qk}

$$\Lambda_{ij}^{qk} = \begin{cases} 1, & \text{if } (i,j) = (L_{q_1k_1}, j) \wedge (i,j) = (i, L_{q_2k_2}), \\ 0, & \text{otherwise.} \end{cases} \tag{4}$$

Three solutions for the computation of the main lines are proposed in this paper. The first two solutions generate a beam of lines and define the main segments as the intersection between the map and the beam of lines, compute the segments length and compute (or approximate) the path length in terms of the sum of these lengths. An iterative process is conduced to compute the slope of the beam of lines, which generates a set of path lengths. The result, represented the main segments, is related to the minimum length path as the solution to the optimization problem

$$q^* = \arg\min_{q \in D_q} \sum_{k \in D_k} \Gamma(\Lambda^{qk}, M) \tag{5}$$

where q^* gives the optimum slope in the discrete domain, D_q is the discrete domain of slope, D_k is the intercept domain, the general notation $\Gamma(\Lambda^{qk}, M)$ is the general notation for the path length:

$$\Gamma(\Lambda^{qk}, M) = \lambda \sum_{i=1}^{n} \sum_{j=1}^{m} p_{ij}, \quad p_{ij} = \begin{cases} 0, & \text{if } M_{ij} = 1, \\ 1, & \text{if } \Lambda_{ij}^{qk} = 1, \end{cases} \tag{6}$$

where the general notation $\lambda \in \{\lambda_1, \lambda_2\}$ is used for the distance between the points calculated as

$$\begin{aligned} \lambda_1 &= \sqrt{\frac{(m+1)^2 + q_1^2}{m+1}}, \\ \lambda_2 &= \sqrt{\frac{(n+1)^2 + q_2^2}{n+1}}. \end{aligned} \tag{7}$$

The first solution consists of the following steps:

Step 1.1. The lines expressed in (2), which depend on q and k, are generated.

Step 1.2. The matrices Λ^{qk} with the elements Λ_{ij}^{qk} expressed in (4) are generated.

Step 1.3. The path length $\Gamma(\Lambda^{qk}, M)$ is computed according to (6).

Step 1.4. The objective function in (5) is computed in terms of the sum $\sum_{k \in D_k} \Gamma(\Lambda^{qk}, M)$ for $q = \text{const}$ and variable k, $k \in D_k$.

Step 1.5. The optimization problem defined in (5) is solved considering that the objective function in the right-hand term of (4) depends on the variable q, $q \in D_q$, and the solution to this optimization problem, i.e., the variable that gives the minimum path length, is q^*.

The first two solutions differ by the slope domain and by the map definition. The first solution preserves the initial map and defines a continuous domain of slope $D = [0, \pi]$ in order to include all possible orientations of the beam of parallel lines. Fig. 4 illustrates an example of beam of parallel lines used in the first solution.
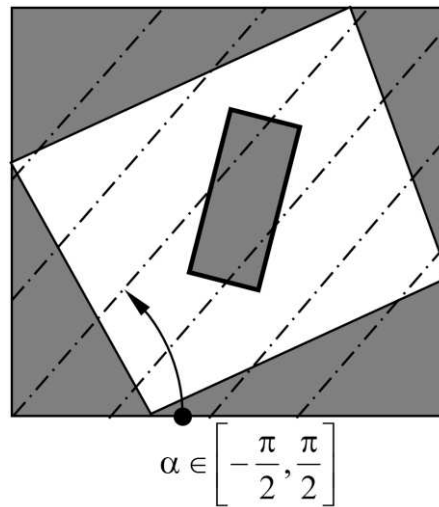
Figure 4
Example of beam of parallel lines used in the first solution

The second solution defines a new map using a composition of the initial map and uses a smaller domain of slope, i.e. $D = [0, \pi/4]$. Fig. 5 exemplifies a beam of parallel lines used in the second solution.
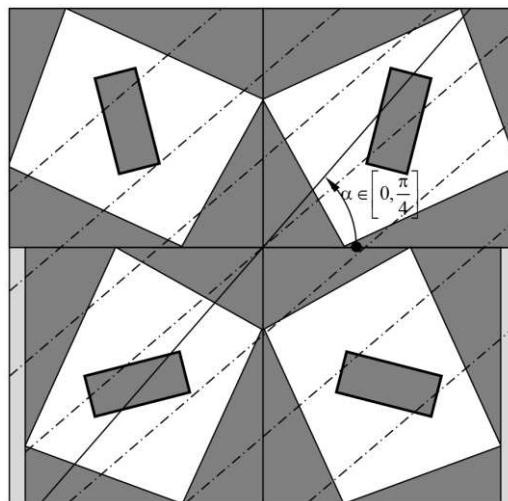

Figure 5
Example of beam of parallel lines used in the second solution

The second solution is based on the generation of a new map by the union of four maps that are rotated as shown in Fig. 5. These four maps correspond to the four quadrants I, II, III and IV, obtained as follows.

The map in the quadrant I is $M_I = [M_{I,\text{ij}}]_{i=1...n, j=1...m} \in \Re^{n \times m}$, with the map matrix elements:

$$M_{I,\text{ij}} = M_{\text{ij}}, i = 1...n, j = 1...m \tag{8}$$

The map in the quadrant II is $M_{\text{II}} = [M_{\text{II,ij}}]_{i=1...n, j=1...m} \in \Re^{n \times m}$, with the map matrix elements:

$$M_{I,\text{ij}} = M_{\text{im}-j+1}, i = 1...n, j = 1...m \tag{9}$$

The map in the quadrant III is M_{III}, obtained in terms of the composition

$$M_{\text{III}} = [P|M^T] \in \Re^{m \times m}, \ P = [P_{\text{ij}}]_{i=1...m, j=1...m-n}, \ P_{\text{ij}} = 1 \tag{10}$$

where the subscript T indicates matrix transposition.

The map in the quadrant IV is $M_{\text{IV}} = [M_{\text{IV,ij}}]_{i=1...n, j=1...m} \in \Re^{n \times m}$, with the map matrix elements:

$$M_{I,\text{ij}} = M_{\text{in}-j+1}, i = 1...n, j = 1...m \tag{11}$$

The second solution consists of the following steps:

Step 2.1. The map matrix in the four quadrants is computed using (8) to (11).

Steps 2.2 to 2.6. These are the steps 1.1 to 1.5 in the first solution.

The third solution approximates the main lines with the map axis, which is inspired from the properties specific to mechanical inertia. The map axis slope is obtained in terms of

$$\alpha = \frac{1}{2} \tan^{-1} \left(\frac{2I_{\text{xy}}}{I_y - I_x} \right) \tag{12}$$

where the following center of gravity-type relationships are employed:

$$I_{\text{xy}} = \sum_{i=1}^{n} \sum_{j=1}^{m} i_c j_c M_{\text{ij}}, \ I_x = \sum_{i=1}^{n} \sum_{j=1}^{m} j_c^2 M_{\text{ij}}, \ I_y = \sum_{i=1}^{n} \sum_{j=1}^{m} i_c^2 M_{\text{ij}}$$

$$x = \frac{\sum_{i=1}^{n} \sum_{j=1}^{m} j M_{\text{ij}}}{\sum_{i=1}^{n} \sum_{j=1}^{m} M_{\text{ij}}}, \ y = \frac{\sum_{i=1}^{n} \sum_{j=1}^{m} i M_{\text{ij}}}{\sum_{i=1}^{n} \sum_{j=1}^{m} M_{\text{ij}}} \tag{13}$$

$$i_c = i - y, \ j_c = j - x, \ i = 1...n, \ j = 1...m$$

and M_{ij} are the elements of the map matrix M defined in (1). The beam of parallel lines is next computed using (2).

The third solution consists of the following steps:

Step 3.1. The map axis slope is computed using (12) and (13).

Steps 3.2 to 3.6. These are the steps 1.1 to 1.5 in the first solution.

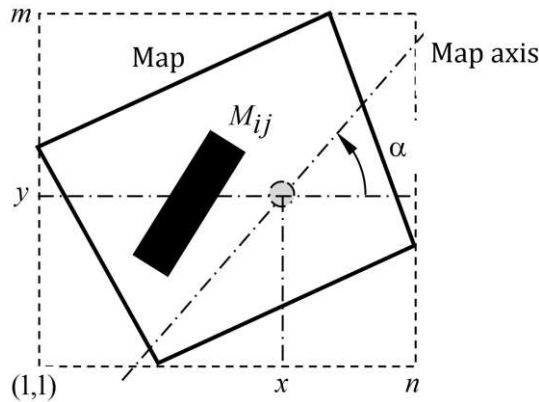An example of application of the third solution is given in Fig. 6.

Figure 6
Example of map and map axis in used in the third solution

2.2 Finding the Auxiliary Lines

The result of the three solutions presented in the previous sub-section is an ordered beam of segments. The lines order has been defined in the process of definition of the main lines using the intercept of each line expressed in (2). The definition of the main segments splits the lines in several segments producing a list of segments ordered (in their turn) using a left to right convention. This means that each segment has two kinds of neighborhoods, i.e., the segments that belong to the lists of neighbor main lines and the segments that do not belong to the same list. The second type of segments is eluded because of the obstacles between these segments. An ordered beam of segments is illustrated in Fig. 7.
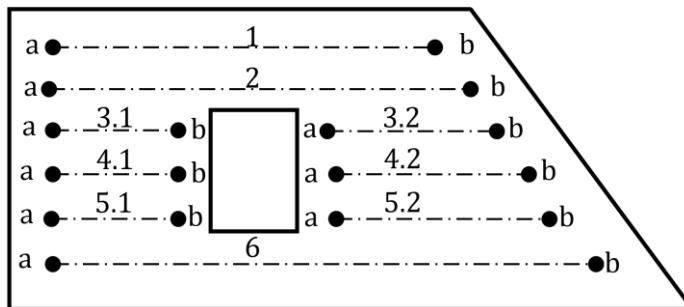
Figure 7
Example of ordered beam of segments

Each segment defines two nodes, a and b. The graph G is defined between the nodes of the main segments:

$$G = (V, E), \tag{14}$$

where the set of nodes (vertices) is V:

$$V = \{i.j.k | i = 1...n_s, \; j = 1...n_i, \; k = a \text{ or } b\} \tag{15}$$

n_s is the number of main segments, and n_i is the number segments generated from i^{th} main line, and the set of edges is E:

$$E(i.j.k, p.r.l) = \begin{cases} 1 & \text{if } p = i + 1 \text{ or } i.j = p.r, \\ 0 & \text{otherwise.} \end{cases} \tag{16}$$

Equation (16) evaluates the existence of the edge between two nodes. The edge exists if $E(i.j.k, p.r.l) = 1$, that means if either $p = i + 1$, i.e. between the segments of two successive lines (the lines are not skipped) or $i.j = p.r$, i.e. between the points of the same segment.

This idea assigns a segment to a node. At the first glance each node can be connected with any other node. In order to avoid this complexity, a heuristic is proposed in this paper to connect only neighbor segments.

The graph related to the segments illustrated in Fig. 7 is presented in Fig. 8 (a).
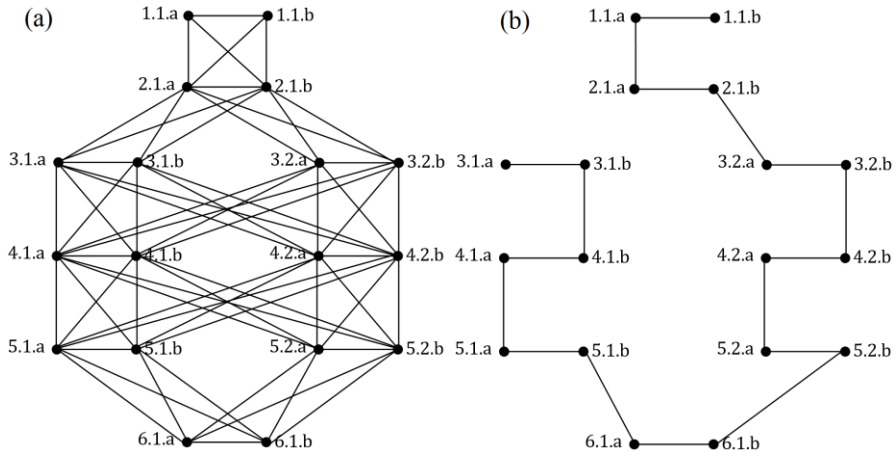

Figure 8

The graph (a) and its solution (b)

Each edge of the graph is associated to a cost function. The simplest cost function definition is the distance between the nodes. If the nodes can be linked with a straight line, the computation of the distance is simple. Contrarily, if obstacles interfere, a trajectory between nodes must be defined. The graph can be further simplified by trimming these edges in order to fulfill the objective to minimize the cost function, i.e., to minimize the path length.

The problem of visiting all segments (nodes) is related to the TSP [32]. In contrast to the classical TSP approach, which assumes that all of them need to be visited once, the ISOC approach proposed in this paper does not have this constraint. The only constraint imposed here is that after a node is reached it is mandatory to visit the second node of the segment so the covering of the main segments is ensured. Fig. 8 (b) points out a possible solution that starts with the node 1.1.b and ends with the node 3.1.a.

Concluding, the auxiliary segments are the lines (or trajectories) that connect the main segments and ensure a minimum path length.

2.3 The Algorithm Specific to the Iterative Structured Orientation Coverage Approaches

Using the steps 1, 2 and 3 related to finding a minimum length path specified at the beginning of Section 2 and the two previous sub-sections, the algorithm specific to the ISOC approaches to robot CPP is referred to as the ISOC algorithm and consists of the following steps:

Step A. The initial data regarding the robot CPP is provided in terms of:

- The map (1), i.e., a discrete representation of the boundaries and the obstacles
- The overall dimensions of the robot

Step B. The main lines are defined and the main segments are found using one of the three solutions presented in Sub-section 2.1, which lead to the minimum length path as the solution to the optimization problem defined in (5), expressed as the optimum slope q^* of the main segments.

Step C. The auxiliary lines are obtained using the results presented in sub-section 2.2 by:

- Computing the visiting order between the main segments
- Computing the path between the main segments using the graph G defined in (14), (15) and (16)

Concluding, the three ISOC approaches are characterized in a unified presentation by the ISOC algorithm. The difference between the three approaches is in the step B, where one of the three solutions to obtain the minimum length path presented in Sub-section 2.1 is included, and leads to one of the three new ISOC approaches. The ISOC approach with the first solution to obtain the minimum length path is next referred to as the first ISOC approach, the ISOC approach with the second solution to obtain the minimum length path is next referred to as the second ISOC approach, and the ISOC approach with the third solution to obtain the minimum length path is next referred to as the third ISOC approach.
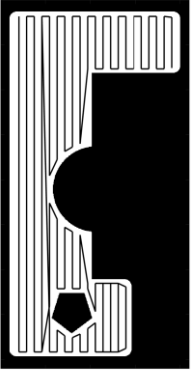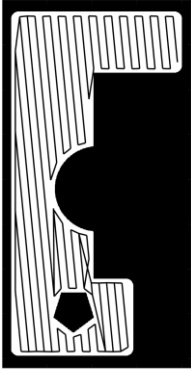
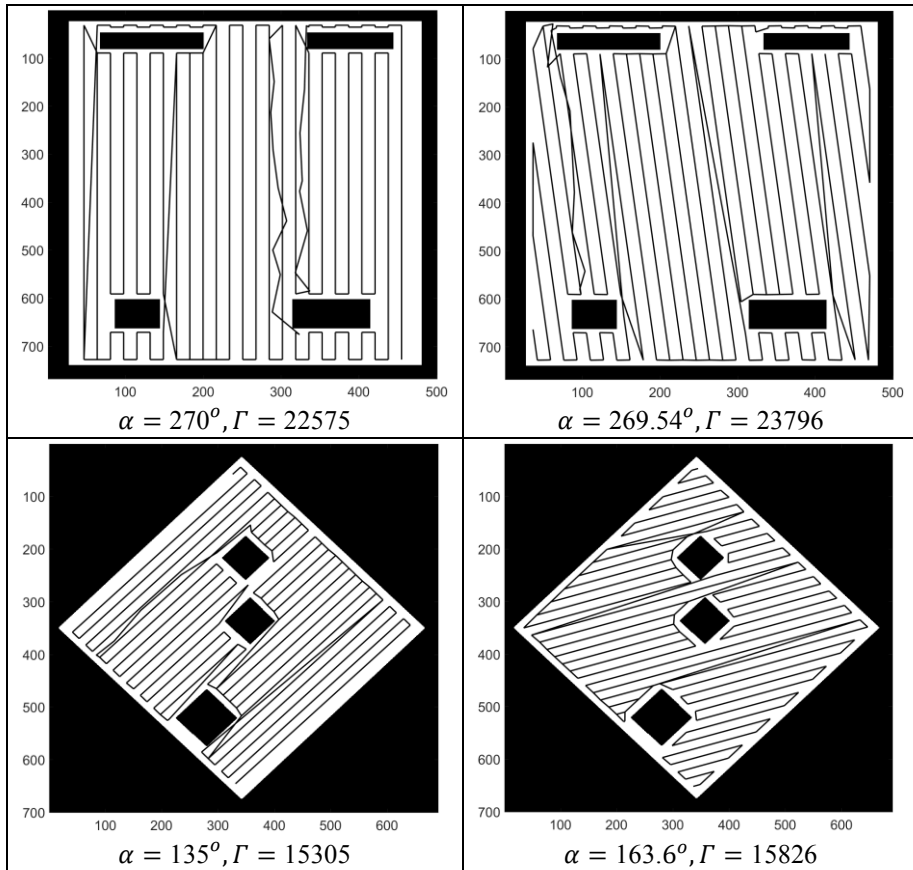# 3   Validation by Simulation and Experiments

This section validates the ISOC approaches presented in the previous section by simulations and experiments conducted on mobile robots. The validation by simulation includes a comparison between the proposed approaches, and of the proposed approaches with another well-known approach discussed in Section 1, namely the BCDC approach. The validation by experiments is focused on a Khepera mobile robot.

3.1   Simulation Results

The comparison between the ISOC approaches has been carried out for artificial (generated) maps. The results are illustrated in Table 1. Although the first two ISOC approaches use optimal solutions and the third ISOC approach is heuristic, the results are close. As shown in the first row, the third ISOC approach gives a better result because of the discretization errors.

Table 1

Comparison between the proposed approaches

Results using the first two approaches	Results using the third approach
$\alpha = 90^o, \Gamma = 14443$	$\alpha = 84.52^o, \Gamma = 13684$

$$\alpha = 270^{o}, \Gamma = 22575 \qquad\qquad \alpha = 269.54^{o}, \Gamma = 23796$$

$$\alpha = 135^{o}, \Gamma = 15305 \qquad\qquad \alpha = 163.6^{o}, \Gamma = 15826$$

Three types of maps have been used to validate the ISOC algorithm presented in the previous section: a simulated map obtained from V-REP [2], a real-life measurement map [37], and an artificially generated map. The maps developed in V-REP and imported to Matlab are called simulation maps. The real-world measurement maps are available datasets, which we have been downloaded from [37]. These maps represent the third floor common area of the MIT Stata Center (Dreyfoos Center) [38]. The artificially generated maps have been obtained by either hand drawing or randomly using Matlab. These maps are illustrated in Fig. 9 as follows: three artificial maps in Fig. 9 (a), (b) and (d), and a real-world map, i.e. the test bench taken from our laboratory snapshot in Fig. 9 (c).
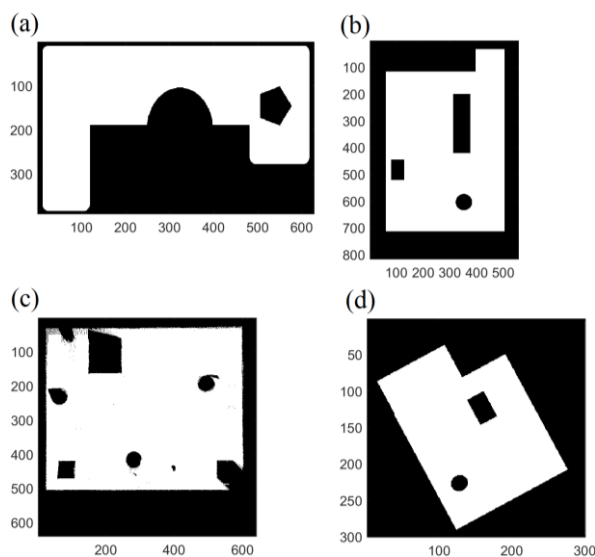
Figure 9
Real-world and artificially generated maps

The proposed approaches are next compared to the BCDC approach, and the results are presented in Table 2. The comparison shows that the ISOC algorithm is always slower than the BCDC algorithm, but most of the time it generates a shorter path. This confirms the results that have been foreseen at the very beginning of the creation of the ISOC approaches and algorithm: ISOC deals with complex maps better, meaning that it generates shorter paths, but this is reflected in its increased computational complexity.

Table 2
Comparison between the proposed approaches and the BCDC approach

Map size (pixel)	Number of holes	Occupied ratio (%)	BCDC-based path length (mm)	ISOC-based path length (mm)	BCDC-based computation time (s)	ISOC-based computation time (s)	Image
435600	1	73.04	9984.41	9625.15	15.65	32.17	Fig. 9 (a)
453696	3	55.77	21392.96	18449.71	10.79	45.65	Fig. 9 (b)
409600	5	60.06	27214.68	22278.05	14.82	96.97	Fig. 9 (c)
90000	2	39.23	2879.35	2880.04	10.54	49.48	Fig. 9 (d)

The comparison was done with an i7 processor, clock rate of 3.7 GHz and 16 GB memory. The comparison of the three proposed approaches from the point of view of the computation time shows that the first approach is the most time consuming, and the second approach reduces the computation time if a parallel computing (for each quadrant) is considered and the approximation is made faster.

3.2   Experimental Results

A Khepera III differential drive robot has been used in the experiments. The map has been previously known, and after the path commutation, an open loop control was applied for the robot. The first phase of the experiments consists of a simulation, and the result is given in Fig. 10.
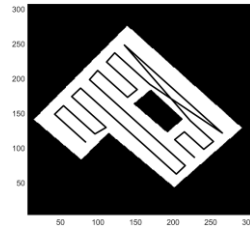

Figure 10

Simulation result of the known map and the robot path

A map was evolved in the second phase and highlighted with yellow marker in order to visualize the real-world experiments as shown in Fig. 11 (a). The robot path was measured with a camera applied above the robot path. This camera took photos in approximately equivalent periods of time. Fig. 11 (b) shows a merge of several images that were taken during the experiments, and suggestively illustrates that the robot covers the path. The entire commented source code is available at the repository https://github.com/horverno/sze-academic-robotics-projects in order to test the presented results.
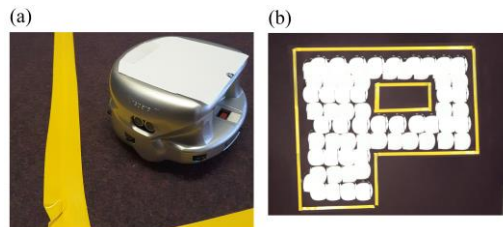

Figure 11

Image that shows the Khepera robot (a) and merged images illustrating the robot path (b)

Conclusions

This paper has proposed three approaches to coverage path planning expressed in a unified manner in terms of the ISOC algorithm. This algorithm starts with the initial data of the map and computes a collection of parallel segments named the main segments. These segments are linked with auxiliary segments into continuous paths. The ISOC strategy to coverage path planning links two ideas: the minimum length beam of parallel lines computed by means of three solutions that lead to the three ISOC approaches, plus the minimum length auxiliary lines that are based on a solution to the traveling salesman problem.

Future research will focus on performance enhancement of the ISOC algorithm by means of four approaches. First, the parallelization of certain sections of code will be carried out by means of a GPGPU-based approach. Second, the use of abstract data types as lists, trees or graphs will be also considered. Third, own targeted functions will be written instead of the used general-purpose functions of an API or a toolbox. And last, the generated path can be executed with a help of a nonlinear model and controller [40-43].

Acknowledgement

References

[1]   H. Choset, "Coverage for robotics – A survey of recent results, Annals of Mathematics and Artificial Intelligence" Vol. 31, No. 1, pp. 113-126, 2001

[2]   M. Freese, S. Singh, F. Ozaki, N. Matsuhira, Virtual Robot Experimentation Platform V-REP: A versatile 3D robot simulator, in: N. Ando, S. Balakirsky, T. Hemker, M. Reggiani, O. von Stryk (Eds.), Simulation, Modeling, and Programming for Autonomous Robots, Springer-Verlag, Berlin, Heidelberg, Lecture Notes in Computer Science, Vol. 6472, pp. 51-62, 2010

[3]   E. Galceran, M. Carreras, A survey on coverage path planning for robotics, Robotics and Autonomous Systems Vol. 61, No. 12, pp. 1258-1276, 2013

[4]   M. Waanders, Coverage path planning for mobile cleaning robots, in: Proc. 15th Twente Student Conference on IT, Twente, The Netherlands, pp. 1-10, 2011

[5]   Z.-Y. Cai, S.-X. Li, Y. Gan, R. Zhang, Q.-K. Zhang, Research on complete coverage path planning algorithms based on A* algorithms, The Open Cybernetics & Systemics Journal Vol. 8, pp. 418-426, 2014

[6]   S. X. Yang, C. Luo, A neural network approach to complete coverage path planning, IEEE Transactions on Systems, Man, and Cybernetics, Part B: Cybernetics Vol. 34, No. 1, pp. 718-724, 2004

[7]   I. Škrjanc, S. Blažič, O. E. Agamennoni, Identification of dynamical systems with a robust interval fuzzy model, Automatica Vol. 41, No. 2, pp. 327-332, 2005

[8]   A. G. Martin, R. E. Haber Guerra, Internal Model Control Based on a Neurofuzzy System for Network Applications. A Case Study on the High-

Performance Drilling Process, IEEE Transactions on Automation Science and Engineering, Vol. 6, No. 2, pp. 367-372, 2009

[9]   J. Vaščák, M. Paľa, Adaptation of fuzzy cognitive maps for navigation purposes by migration algorithms, International Journal of Artificial Intelligence Vol. 8, No. 12, pp. 20-37, 2012

[10]   R.-E. Precup, R.-C. David, E. M. Petriu, Grey Wolf Optimizer Algorithm-Based Tuning of Fuzzy Control Systems With Reduced Parametric Sensitivity, IEEE Transactions on Industrial Electronics, Vol. 64, No. 1, pp. 527-534, 2017

[11]   R.-E. Precup, P. Angelov, B. S. J. Costa, M. Sayed-Mouchaweh, An overview on fault diagnosis and nature-inspired optimal control of industrial process applications, Computers in Industry Vol. 74, pp. 75-94, 2015

[12]   T. T. Mac, C. Copot, D. T. Tran, R. De Keyser, Heuristic approaches in robot path planning: A survey, Robotics and Autonomous Systems Vol. 86, pp. 13-28, 2016

[13]   K. Sasaki, K. Noda, T. Ogata, Visual motor integration of robot's drawing behavior using recurrent neural network, Robotics and Autonomous Systems Vol. 86, pp. 184-195, 2016

[14]   J. Conesa-Muñoz, G. Pajares, A. Ribeiro, Mix-opt: A new route operator for optimal coverage path planning for a fleet in an agricultural environment, Expert Systems with Applications Vol. 54, pp. 364-378, 2016

[15]   I. A. Hameed, A. la Cour-Harbo, O. L. Osen, Side-to-side 3D coverage path planning approach for agricultural robots to minimize skip/overlap areas between swaths, Robotics and Autonomous Systems Vol. 76, pp. 36-45, 2016

[16]   M. Torres, D. A. Pelta, J. L. Verdegay, J. C. Torres, Coverage path planning with unmanned aerial vehicles for 3D terrain reconstruction, Expert Systems with Applications Vol. 55, pp. 441-451, 2016

[17]   D. S. Li, X. L. Wang, T. Sun, Energy-optimal coverage path planning on topographic map for environment survey with unmanned aerial vehicles, Electronics Letters Vol. 52, No. 9, pp. 699-701, 2016

[18]   J. Granna, I. S. S. Godage, R. Wirz, K. D. Weaver, R. J. Webster, J. Burgner-Kahrs, A 3-D volume coverage path planning algorithm with application to intracerebral hemorrhage evacuation, IEEE Robotics and Automation Letters Vol. 1, No. 2, pp. 876-883, 2016

[19]   J. K. Tar, I. J. Rudas, J. F. Bitó, Group theoretical approach in using canonical transformations and symplectic geometry in the control of approximately modelled mechanical systems interacting with an unmodelled environment, Robotica Vol. 15, pp. 163-179, 1997

[20]   J. K. Tar, I. J. Rudas, K. R. Kozłowski, Fixed point transformations-based approach in adaptive control of smooth systems, in: K. R. Kozłowski (Ed.),

Robot Motion and Control 2007, Springer-Verlag, London, Lecture Notes in Control and Information Sciences, Vol. 360, pp. 157-166, 2007

[21]   S. Blažič, A novel trajectory-tracking control law for wheeled mobile robots, Robotics and Autonomous Systems Vol. 59, No. 11, pp. 1001-1007, 2011

[22]   M. Arndt, S. Wille, L. de Souza, V. Fortes Rey, N. Wehn, K. Berns, Performance evaluation of ambient services by combining robotic frameworks and a smart environment platform, Robotics and Autonomous Systems Vol. 61, No. 11, pp. 1173-1185, 2013

[23]   K. Bolla, Zs. Cs. Johanyák, T. Kovács, G. Fazekas, Local center of gravity based gathering algorithm for fat robots, in: L. T. Kóczy, C. R. Pozna, J. Kacprzyk (Eds.), Issues and Challenges of Intelligent Systems and Computational Intelligence, Springer-Verlag, Berlin, Heidelberg, Studies in Computational Intelligence, Vol. 530, pp. 175-183, 2014

[24]   J. Vaščák, N. H. Reyes, Use and perspectives of fuzzy cognitive maps in robotics, in: E. I. Papageorgiou (Ed.), Fuzzy Cognitive Maps for Applied Sciences and Engineering: From Fundamentals to Extensions and Learning Algorithms, Springer-Verlag, Berlin, Heidelberg, Intelligent Systems Reference Library, Vol. 54, pp. 253-266, 2014

[25]   M. Reichardt, T. Föhst, K. Berns, An overview on framework design for autonomous robots, it – Information Technology Vol. 57, No. 2, pp. 75-84, 2015

[26]   C. Pozna, R.-E. Precup, P. Földesi, A novel pose estimation algorithm for robotic navigation, Robotics and Autonomous Systems Vol. 63, pp. 10-21, 2015

[27]   B. Kovács, G. Szayer, F. Tajti, M. Burdelis, P. Korondi, A novel potential field method for path planning of mobile robots by adapting animal motion attributes, Robotics and Autonomous Systems Vol. 82, pp. 24-34, 2016

[28]   F. G. Filip, Decision support and control for large-scale complex systems, Annual Reviews in Control Vol. 32, No. 1, pp. 61-70, 2008

[29]   J.-S. Chiou, S.-H. Tsai, M.-T. Liu, A PSO-based adaptive fuzzy PID-controllers, Simulation Modelling Practice and Theory Vol. 26, pp. 49-59, 2012

[30]   D. Wijayasekara, O. Linda, M. Manic, C. G. Rieger, FN-DFE: Fuzzy-Neural Data Fusion Engine for enhanced resilient state-awareness of hybrid energy systems, IEEE Transactions on Cybernetics Vol. 44, No. 11, pp. 2065-2075, 2014

[31]   R.-E. Precup, M.-C. Sabau, E. M. Petriu, Nature-inspired optimal tuning of input membership functions of Takagi-Sugeno-Kang fuzzy models for anti-lock braking systems, Applied Soft Computing Vol. 27, pp. 575-589, 2015

[32]   E. Osaba, R. Carballedo, F. Diaz, E. Onieva, A. Masegosa, A. Perallos, Good Practice Proposal for the Implementation, Presentation, and

Comparison of Metaheuristics for Solving Routing Problems, Neurocomputing, Vol. 271, pp. 2-8, 2018

[33]   S. B. Ghosn, F. Drouby, H. M. Harmanani, A parallel genetic algorithm for the open-shop scheduling problem using deterministic and random moves, International Journal of Artificial Intelligence Vol. 14, No. 1, pp. 130-144, 2016

[34]   D. Azar, K. Fayad, C. Daoud, A combined ant colony optimization and simulated annealing algorithm to assess stability and fault-proneness of classes based on internal software quality attributes, International Journal of Artificial Intelligence Vol. 12, No. 2, pp. 137-156, 2016

[35]   P. Cabrera-Guerrero, A. Moltedo-Perfetti, E. Cabrera, F. Paredes, Comparing two heuristic local search algorithms for a complex routing problem, Studies in Informatics and Control Vol. 25, No. 4, pp. 411-420, 2016

[36]   F. Gaxiola, P. Melin, F. Valdez, J. R. Castro, O. Castillo, Optimization of type-2 fuzzy weights in backpropagation learning for neural networks using GAs and PSO, Applied Soft Computing Vol. 38, pp. 860-871, 2016

[38]   H. Choset, P. Pignon, Coverage path planning: The boustrophedon decomposition, in: A. Zelinsky (Ed.), Field and Service Robotics, Springer-Verlag, London, pp. 203-209, 2008

[39]   Maps of common areas of 3rd floor Stata Center (Dreyfoos Section) provided by P. E. Missiuro, posted at http://cres.usc.edu/radishrepository/view-one.php?name=mitstata3rdfloordreyfoos and accessed in March 2017

[40]   C. Pozna, F. Troester, R.-E. Precup, J. K. Tar, S. Preitl, On the Design of an Obstacle Avoiding Trajectory: Method and Simulation, Mathematics and Computers in Simulation, Vol. 79, No. 7, pp. 2211-2226, 2009

[41]   R.-E. Precup, M. L. Tomescu, S. Preitl, E. M. Petriu, J. Fodor, C. Pozna, Stability Analysis and Design of a Class of MIMO Fuzzy Control Systems, Journal of Intelligent and Fuzzy Systems, Vol. 25, No. 1, pp. 145-155, 2013

[42]   J. K. Tar, J. F. Bitó, I. J. Rudas, Contradiction Resolution in the Adaptive Control of Underactuated Mechanical Systems Evading the Framework of Optimal Controllers, Acta Polytechnica Hungarica, Vol. 13, No. 1, pp. 97-121, 2016

[43]   A. Ürmös, Z. Farkas, M. Farkas, T. Sándor, L. T. Kóczy, A. Nemcsics, Application of Self-Organizing Maps for Technological Support of Droplet Epitaxy, Acta Polytechnica Hungarica, Vol. 14, No. 4, pp. 207-224, 2017